Rochester Institute of Technology

RIT Digital Institutional Repository

Theses

4-12-2024

A New Vicarious Technique for Radiometric and Spatial Calibration of Drone-based Multispectral and Hyperspectral Imaging Systems

David N. Conran
dnc7309@rit.edu

Follow this and additional works at: https://repository.rit.edu/theses

Recommended Citation

Conran, David N., "A New Vicarious Technique for Radiometric and Spatial Calibration of Drone-based Multispectral and Hyperspectral Imaging Systems" (2024). Thesis. Rochester Institute of Technology. Accessed from

This Dissertation is brought to you for free and open access by the RIT Libraries. For more information, please contact repository@rit.edu.

ROCHESTER INSTITUTE OF TECHNOLOGY

DOCTORAL THESIS

A New Vicarious Technique for Radiometric and Spatial Calibration of Drone-based Multispectral and Hyperspectral Imaging Systems

---

Author:
David N. CONRAN

Advisor:
Dr. Emmett J. IENTILUCCI

A dissertation submitted in fulfillment of the requirements
for the degree of Doctor of Philosophy

in the

Digital Imaging and Remote Sensing Lab (DIRS)
Chester F. Carlson Center for Imaging Science

April 12, 2024

Signature Page

We approve the thesis of David N. CONRAN

Date of Signature

Dr. Emmett J. IENTILUCCI, Thesis Advisor

Associate Professor, Chester F. Carlson Center for Imaging Science

Dr. Agamemnon L. CRASSIDIS, External Chair

Professor, Department of Mechanical Engineering

Dr. Carl N. SALVAGGIO

Professor, Chester F. Carlson Center for Imaging Science

Dr. Michael G. GARTLEY

Research Faculty, Chester F. Carlson Center for Imaging Science

Dr. Brandon J. RUSSELL

Technical Staff, MIT Lincoln Laboratory

"Sometimes I'll start a sentence and I don't even know where it's going. I just hope I find it along the way."

Michael G. Scott

ROCHESTER INSTITUTE OF TECHNOLOGY

A New Vicarious Technique for Radiometric and Spatial Calibration of Drone-based Multispectral and Hyperspectral Imaging Systems

Abstract

A new technology (convex mirrors) used for radiometric and spatial characterization of remote sensing imaging systems has demonstrated equal, but unique results when compared to Lambertian targets for vicarious calibration. Using convex mirrors to characterize the radiometric and spatial response of hyperspectral and multispectral imaging systems has yet to be thoroughly investigated for drone-based platforms. When imaged, a convex mirror produces a known radiant intensity source that can characterizes the radiometric and spatial performance of an imaging system. The simultaneous assessment supports a unique understanding of the hyperspectral and multispectral instrument's response for vicarious characterization.

Assessing a new technique for vicarious characterization of imaging systems requires thorough comparison to traditional methods. The Empirical Line Method (ELM) uses Lambertian panels to characterize an imaging systems response to varying surface reflectances for radiometric calibration. The slanted edge method for extracting the spatial response of imaging systems also uses Lambertian panels to form a high contrast edge. Spatial performance characterization defines the smallest spatial feature that can be observed and assists in the discovery of poorly focused or highly distorted optical configurations.

The research findings indicate that convex mirrors provide a novel technique to extract new information when deployed for drone-based field experiments. The reflected sunlight produces a broadband point source for characterizing the spatial misregistration of HSI systems without the need to oversample an edge target. More importantly, the reflected sunlight from a convex mirror is defined in a closed-form radiometric expression that can easily be used to validate the small target radiometric performance of imaging systems. Small target performance of HSI systems has drastic consequences for sub-pixel target detection and spectral unmixing. Further discoveries unveiled the inconsistent radiometric performance of a well-calibrated HSI system to point targets in the presence of platform motion and orthorectification.

Contents

Title Page i

Signature Page iii

Abstract vii

1 Introduction 1

2 Literature Review 5

2.1 Hyperspectral Imaging 5
  2.1.1 Spectral 5
  2.1.2 Radiometric 10
  2.1.3 Spatial 11
2.2 Field Calibration Methods 15
  2.2.1 Field Reflectance Measurements 16
  2.2.2 Empirical Line Method - Radiometric Calibration 21
  2.2.3 Slanted Edge Method - Spatial Characterization 24
    Slanted Edge Theory 24
    ESF Construction 29
2.3 Convex Mirror Targets (SPARC) 33
  2.3.1 SPARC Geometry 34
  2.3.2 SPARC Radiometry 37
  2.3.3 Equivalent Lambertian Reflectance Factor 42
  2.3.4 Mirror-based Empirical Line Method 42

3 Methodology 45

3.1 Experimental Planning . . . 45

3.1.1 Practical Considerations . . . 45

3.1.2 Preflight Planning . . . 49

3.2 Data Analysis and Computational Techniques . . . 51

3.2.1 Point Target - Radiometric Analysis . . . 51

3.2.2 Point Target - Spatial Analysis . . . 54

Single-Point Analysis . . . 54

Multi-Point Analysis . . . 56

4 Results 59

4.1 Spatial Target Comparison Study . . . 59

4.2 Appendix A Summary . . . 63

4.2.1 Laboratory Investigation . . . 64

4.2.2 Field Re-Investigation . . . 71

4.3 Appendix B Summary . . . 76

4.4 Appendix C Summary . . . 76

4.5 Appendix D Summary . . . 77

5 Conclusion 79

6 Future Work 81

A Interrogating UAV Image and Data Quality using Convex Mirrors 89

B A Vicarious Technique for Understanding and Diagnosing Hyperspectral Spatial Misregistration 95

C Small Target Radiometric Performance of Drone-based Hyperspectral Imaging Systems 119

D A New Technique to Define the Spatial Resolution of Imaging Sensors 143

Bibliography **149**

List of Figures

2.1 Basic optical design for a push-broom hyperspectral imaging system. 6
2.2 A pictorial illustration of the three primary spectral characterization parameters of an HSI system. 7
2.3 Measured SRF's (by the author) from the Headwall Nano-Hyperspec are the orange dots and the Gaussian fit are the blue curves. The SRF at 436 nm can not be accurately represented by the Gaussian fit whereas the SRF at 750 nm is more Gaussian in shape. These plots were derived from laboratory testing in the Optical Calibration Facility within the Digital Imagery and Remote Sensing (DIRS) department at RIT. 8
2.4 The spectral profiles of emission lamps used in the Optical Calibration Facility for wavelength calibration. The spectral emission lines were measured by a high resolution laboratory spectrometer (i.e., Ocean SR2 VIS-NIR) to show all the known emission lines. 9
2.5 (A) An example of spectral smile estimate across all spatial channels of an HSI system. (B) Wavelength calibration using a third-order polynomial (blue curve) to map spectral channels to physical units of nanometers for various emission line centers (orange dots). 10
2.6 A pictorial illustration of the two primary spatial characterization parameters of an HSI system. 13
2.7 The variable scale of resolution demonstrates the need to balance optic or detector limited imaging based on the application needs [Fiete, 2010]. 16
2.8 Pictorial examples of BRDF and HRDF measurements [Schaepman-Strub et al., 2006]. 17

2.9 The total downwelling irradiance (A) and sky irradiance (B) were measured during the experiment at 1 second intervals. The black curves are variation estimates of both signals and demonstrate atmospheric stability over an 8 minute time interval. 19

2.10 (A) The HRF of $Spectralon_{TM}$ and (B) BRF of $Spectralon_{TM}$. Each measurement has the source at nadir and the detector at 8 and 40 degree inclination, respectively. The HRF is typically measured within an integrating whereas the BRF is a point measurement. 20

2.11 (A) An example of the Global-to-Diffuse ratio during a field experiment where the majority of the energy is at the blue end of the spectrum. (B) Incorporating the Global-to-Diffuse ratio and the field reflectance of the reference panel, $Spectralon_{TM}$, increases the perceived reflectance of other Lambertian panels. . . 21

2.12 A simplistic illustration of the two-point ELM for a dark and bright target. The linear fit between spectral radiance and reflectance has a positive intercept which has a physical interpretation tied back the path radiance. 22

2.13 The inter-relationship between the various spatial response functions for imaging systems. 26

2.14 This illustration demonstrates how an tilted edge target is oversampled by projecting onto a perpendicular axis defined by the edge location and tilt angle [Viallefont-Robinet et al., 2018]. 27

2.15 (A) Broadband satellite image of an edge target where the red box is the ROI for edge assessment. (B) Estimated edge location per row (red dots) with a linear fit (black line) within the ROI. 30

2.16 (A) Oversampled SESF after axis projection with nonuniform sampling. (B) SESF binned to 1/4 pixel intervals. 32

2.17 This example demonstrates the slanted edge method and the extracted results. (A) Example SLSF with a FWHM estimate of 1.62 pixels. (B) 1D MTF estimate with a value at Nyquist of 0.132. 33

2.18 Illustrating various properties of convex mirrors when stimulated with plane waves originating from the solar irradiance. 35

3.1 Experimental images of various mirror arrays and black felt background. (Left) Convex mirrors arranged in a line creating an ideal line source. (Right) Various mirror arrays configurations for different signal levels. 47

3.2 Sample phasing example from a field experiment conducted by the author. (A) Point target landing in the center where majority of energy is in the central pixel. (B) Point target landing in the top right of the central pixel where energy is shared between the four surrounding pixels. 48

3.3 An example of 4 different ELRF's predictions. Single mirrors are represented by solid curves whereas two mirror arrays are represented by dotted curves. The blue curves are mirrors with R_m = 25 mm and the orange curves are mirrors with R_m = 50 mm. 50

3.4 Two preflight alignment graphs demonstrate the elevation angle needed for nadir viewing instruments. Mirrors of the same diameter but different radius of curvature demonstrate how the FOR impacts elevation angle has for similar solar zenith angles. 52

3.5 The image on the left is a visualization of the pixels used to estimate the background signal (shaded green) and the isolated SPSF signal (shaded red). The graph on the right is the result of background subtraction and pixel summing. This is used to estimate the point target siganl. 53

3.6 An example of single-point analysis performed on an HS image at wavelength 550nm. (A) An isolated SPSF containing 7x7 pixels. (B) The resulting 2D Gaussian fit when optimized to the SPSF. 55

3.7 A multi-point analysis example performed on a MS image. (A) 20 individual SPSF's with varying sample phasing. (B) The optimized SPSF using the oversampling technique defined by Stephen J. Schiller and Silny, 2010. 56

3.8 Stephen J. Schiller and Silny, 2010 defined a double loop technique as an oversampling technique for point targets. Inner and outer loops independently optimize the x and y centroids and FWHM respectively. 58

4.1 Images used for the analyses between edge and point targets based on the green channel where the red boxe indicates edge extraction. (A) Field experiment with the edge target placed besides 16 point targets for comparison. (B) Laboratory experiment, using a collimator system, showing the edge target for comparison to field measurements. 60

4.2 Results when comparing edge vs. point targets. (A) Results represented in the spatial domain where the SPSF and SLSF are not directly comparable. (B) Results defined in the frequency domain where direct comparisons can be made based on the MTF relationship between the SLSF and SPSF. 62

4.3 RGB rendered image of Lambertian calibration panels with a graph of overall digital signal levels. The digital signals on the calibration panels are far lower than anticipated and this system is not optimized for remote sensing applications. 65

4.4 (A) Various mirror configurations (yellow, red and white boxes) were deployed for both VNIR and SWIR HSI systems. The mirrors highlighted in smaller blue and orange boxes had the highest SNR for further examination. (B) A comparison between predicted and extracted mirror reflectance signals demonstrate correlation within the estimated uncertainty. 67

4.5 To examine the difference between HSI fore-optics, (A) the HSI system is placed in front of an integrating sphere. (B) For each fore-optic, the integrating sphere's spectral radiance was measured by an internal, calibrated, spectrometer. 68

4.6 (A) The digital signals were optimized to the integrating sphere's illumination. The MX1 Lens required 4x the integration time to achieve the same signal as the MX2 Lens. (B) Using Eq. (4.3), the f/# of the MX1 Lens was estimated. The throughput differences between the tested lenses create a slight various in the f/# as a function of wavelength. 69

4.7 Images of the apertures within the fore-optics provides visual evidence that the MX1 Lens reduced incomming signal more than anticipated. The smaller aperture caused the f/# to be larger where the light throughput was drastically reduced. 70

4.8 Imagery from (A) G-SCALE and (B) MMRC. Within each image is a orange box that highlights the point target used in this analysis. Image quality, SNR and GSD differences are apparent between the images. 72

4.9 Point target differences between the data sets extracted from G-SCALE and MMRC. (A) The ensquared digital signal and (B) predicted radiant intensity of both point targets. 74

4.10 A comparison between estimate of the G-SCALE lens f/# from two different experimental methodologies. The blue curve represents the results from a laboratory controlled experiment with an integrating sphere. The orange curve is the result from extracting the f/# from two field experiments using convex mirrors. . 75

6.1 (A) A roof-top experiment can be achieved from the Chester F. Carlson building. The horizontal distance marked by the “X” (45m and 70m) indicate an experimental area for centimeter level GSD. The solar path is indicate as the orange curve with the horizons in red and yellow. (B) Pointing configuration for an imaging system with respect to the black background panel. This is based on specific configurations of the convex mirror’s FOR and solar zenith angle. 84

6.2 Three scenarios where the underlying optical PSF is sampled at different rates in the along-track direction or in the direction of motion. The sampling rate is as follows: (A) undersampled, (B) ideally sampled, and (C) oversampled. 86

List of Tables

2.1 This table displays the minimum height requirements for the hyperspectral (HS) and multispectral (MS) imaging systems used for all drone experiments. 37

3.1 Mirror configurations used in all field experiments. Various geometrical parameters highlighting the differing properties. 46

4.1 Final results from the spatial comparison study between edge and point targets. 63

4.2 Parameter values for the non-spectral terms of Eq. (4.6). 73

Dedicated to my Grandmom

Chapter 1

Introduction

Lambertian panels continue to be an important part in the Empirical Line Method (ELM) for reflectance calibration and atmospheric correction of remote sensing imaging systems [Smith and Milton, 1999]. Extended targets has been shown to provide an accurate and well established calibration method to derive the gain and offset for convert entrance aperture reaching quantities to surface reflectance over the imaging systems dynamic range [Baugh and Groeneveld, 2008]. Vicarious calibration allows for the characterization of an imaging system during operation, but not one method can extract all the fundamental properties of an imaging system.

A research area that lacks experimental investigation is small target calibration methods [S. Schiller and Silny, 2016]. Lambertian panels offer the best target for surface reflectance retrieval, but extended targets can not provide information about the imaging systems response to small targets (i.e., scales of a pixel). More specifically for hyperspectral imaging systems (HSI), Lambertian panels do not correlate with scene acquisition of small targets that are spatially unresolved [Eismann, 2012]. Most HSI systems use motion to acquire the second spatial dimension when creating the 3D image cube. Small targets can be missed or re-imaged over multiple images when compared to extended targets (Appendix C). Investigating an imaging systems response to a small target requires knowledge of both the spatial and radiometric properties and can be very difficult, if not impossible, for naturally occurring targets. The only vicarious calibration method that stress an imaging system to a small target is the SPecular Array for Radiometric Calibration (SPARC) technique [S. J. Schiller, 2012].

In this thesis, the use of convex mirrors to interrogate the spatial and radiometric response of imaging systems will be studied. An emphasis on HSI systems highlights the novel research performed to understand the reflectance calibration comparison to Lambertian targets (Appendix A), spatial misregistration errors (Appendix B) and small target radiometric performance (Appendix C) for drone-based platforms. Drone-based imaging opens new research areas for applying convex mirrors to estimate properties of hyperspectral systems that have been exclusively studied in laboratories. In addition, critical questions regarding the post-processing of hyperspectral data opens further research opportunities that have yet to be investigated. Future research opportunities will be discussed in Section 5.

The thesis is structured around four peer-reviewed research articles in Appendices A, B, C, and D with the primary focus on the use of convex mirrors to characterize HSI systems during field experiments. The literature review (Chapter 2) outlines a basic structure of HSI systems with original results from technical investigations using laboratory equipment. A discussion on standard processes for vicarious calibration, both radiometric and spatial. Then a formal description of the SPARC techniques finalizes the literature. The methodology section (Chapter 3) outlines various preflight and analysis techniques in more detail than the research articles. More specially, the preflight planning is critical because this defines how to use the convex mirrors due to saturation risk and ensuring the solar disk is visible to the imaging systems. All results from the multi-year investigation into imaging systems, both laboratory and field experiments, are presented in Chapter 4. A summary of all peer-reviewed papers outlines the main contributions to the scientific community. The final section (Chapter 5) highlights future work that can be pursed based on the scientific discovered covered in the thesis. There are various unanswered questions that stem from the research that has already been conducted, but was out of scope for the initial investigation into the use of convex mirrors for drone-based HSI systems.

The first three appendices encompass the primary research for the thesis and progress into more complex investigations into the use of convex mirrors to extract HSI properties during field experiments. Appendix A is an initial examination of the reflectance properties of convex mirrors and a comparison to Lambertian targets. Convex mirrors can provide an known reference signal for surface reflectance calibration and is similar to the ELM. Appendix B is a unique approach to extracting spatial misregistration from HSI systems by convex mirrors as an ideal point target. The analysis of spatial misregistration is typically performed in a laboratory experiment, but this approach demonstrates the strength of knowing how well-behaved the imaging system is during flight. Appendix C is the most recent study into the radiometric performance of drone-based HSI systems to small targets. Due to the complex scene acquisition of pushbroom HSI systems, small targets were shown to be influenced more than Lambertian targets. The papers described above demonstrate the novel research published into scientific journals and the progress of research maturity as the examinations discovered more problems to investigate.

Appendix D was the first published research article about estimating the spatial resolution of an multispectral imaging system by observing convex mirrors. This was performed for a fleet of satellites and supported the development of *python*-based spatial characterization software for Labpshere Inc. Even though this paper does not fit in the scope of the thesis statement, the analysis and use of convex mirrors is universal to any imaging system. The investigation for using convex mirrors for drone-based imaging proved to be an unexplored area of research where novel results could be derived.

Chapter 2

Literature Review

2.1 Hyperspectral Imaging

The main characteristics that define a hyperspectral imaging (HSI) system include radiometric, spectral and spatial parameters. This information stems directly from discussions in the Testing Group defining test methods and procedures for Hyperspectral Camera Characterization in the P4001 Standards Development Committee [Gilchrist, Torbjorn Skauli, and Durell, 2018]. Figure 2.1 is a simplistic optical design for a push-broom hyperspectral imaging system. Push-broom HSI systems captures 1D spatial information defined by the scan line (cross-track) and requires movement to capture the second dimension (along-track) to create a 2D image where each pixel contains unique spectral information of the scene. The 2D image pixels is defined by the integration time, frame rate (time between images) and the projection of the slit onto the ground. The focus of the following sections will be to understand the static performance of HSI systems and the black-box approach used to measure the key parameters [Ientilucci, D. N. Conran, et al., 2022].

2.1.1 Spectral

HSI systems take advantage of sampling the scene both spatially and spectrally to extract information about the underlying materials for scientific application such as object target detection, for example. Typical HSI designs incorporate small entrance slits (e.g., 25 μm) restricting the spatial dimension and defining the spectral resolution, but ultimately reduce radiometric throughput. In addition, HSI systems tend to have multi-element optical designs to deposit a

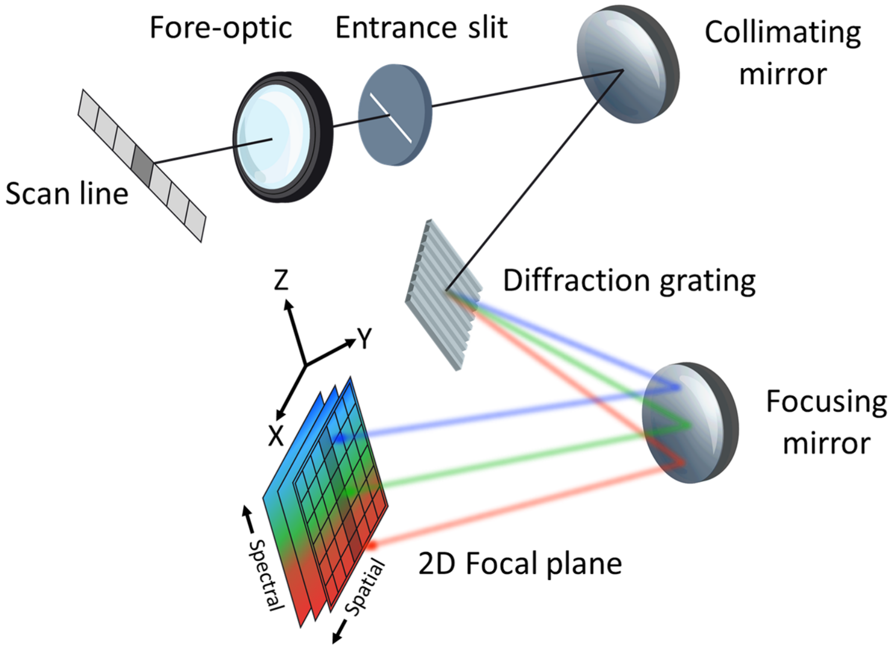

FIGURE 2.1: Basic optical design for a push-broom hyperspectral imaging system.

spatial/spectral image onto a 2D focal plane array, as seen in Figure 2.1. Throughout the path length of the optical system, an introduction of various aberrations and inherent optical phenomenology can lead to imperfect projection of the spatial/spectral image onto the focal plane [Eismann, 2012]. In the spectral domain, these imperfections include spectral smile, wavelength dependent spectral response functions and 2D wavelength calibration requirements (Figure 2.2).

The Spectral Response Function (SRF), as shown in Figure 2.2, is the wavelength response of a spectrograph defined by the entrance slit, grating diffraction and optical aberrations [Trim, Mason, and Hueni, 2021]. Over a small wavelength range, the SRF is assumed to be consistent but can be dynamic over the full wavelength range of the spectrograph. A common metric used to define the spectral resolution is the full-width at half maximum (FWHM) of the peak normalized SRF. For example, experimental data taken with the Headwall Nano-Hyperspec (VNIR 400-1000 nm) HSI system has a FWHM change of roughly 11% from 436 nm (Figure 2.3a) to 750 nm (Figure 2.3b). Complexities within HSI systems requires a measurement of the SRF at 49 evenly space spatial/spectral positions over the entire focal plane to understand the

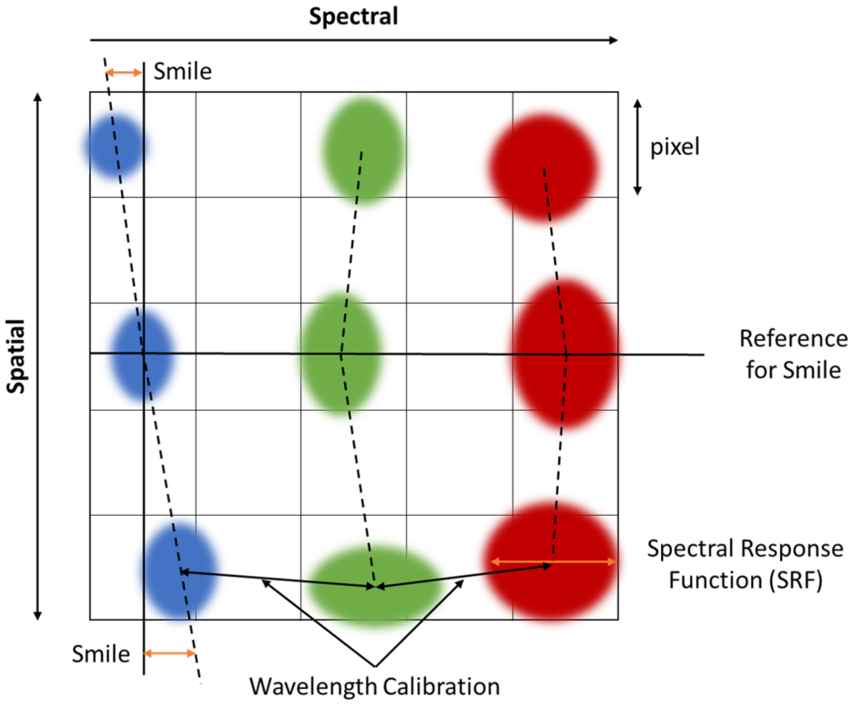

FIGURE 2.2: A pictorial illustration of the three primary spectral characterization parameters of an HSI system.

SRF shape and size [Ientilucci, D. N. Conran, et al., 2022]. The uniqueness of the SRF is critical to understand how an observed material is tarnished by the instruments spectral imperfections and has real world ramifications when using hyperspectral imagery to solve scientific problems such as monitoring vegetation health/stress and mapping land cover change [Teillet, Staenz, and William, 1997]. Further investigations have been conducted under the P4001 Testing Group to utilize the measured SRF to estimate the center positions of the spectral emission lamps for more precision and accurate wavelength calibration. Initial results demonstrate that a measured SRF outperforms any analytical function such as a Gaussian distribution for center position estimates and also extends to spectral smile estimates [Ientilucci, D. N. Conran, et al., 2022].

Wavelength calibration is the process of defining the absolute position of the spectral channels (i.e., the physical spacing between CCD/CMOS pixels) and defines the gratings linear dispersion (nm/pixel) at the focal plane. Since HSI systems are designed for spectroscopy,

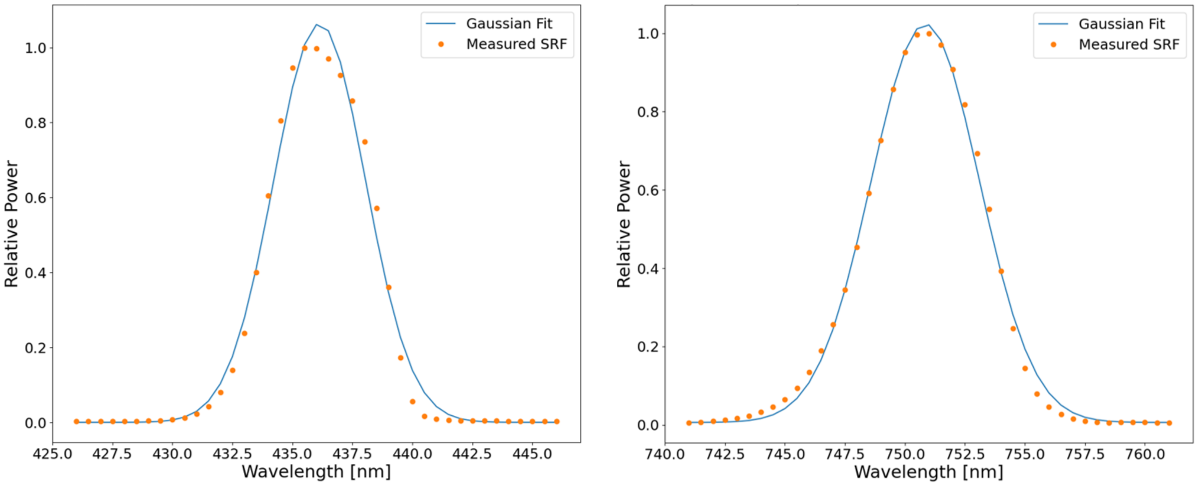

(A) SRF @ 436 nm

(B) SRF @ 750 nm

FIGURE 2.3: Measured SRF's (by the author) from the Headwall Nano-Hyperspec are the orange dots and the Gaussian fit are the blue curves. The SRF at 436 nm can not be accurately represented by the Gaussian fit whereas the SRF at 750 nm is more Gaussian in shape. These plots were derived from laboratory testing in the Optical Calibration Facility within the Digital Imagery and Remote Sensing (DIRS) department at RIT.

it is critically important that a thorough investigation and continued quality checks are practiced to ensure absolute wavelength accuracy of the measured spectrum. Wavelength shifts will misrepresent the spectral energy deposited onto the focal plane and will cause detrimental errors in any analyses that use high resolution spectral libraries or other well-calibrated spectrometers in ground truth measurements. Wavelength shifts as small as 1-2 nm will cause spikes where false absorption lines can be introduced into retrieved data during field calibration efforts and in comparative measurements from other instruments [Bachmann et al., 2012]. Figures 2.4a and 2.4b illustrates emission line plots from emission lamps such as Mercury-Neon, Argon, and Krypton. The lamps are used to for spectral calibration, can be found in Optical Calibration Facility in the Center for Imaging Science, and cover the VNIR/SWIR regions [Trim, Mason, and Hueni, 2021]. The inert gas that fills the lamps emit very sharp, NIST traceable spectral features (i.e., spectral delta functions) at very precise wavelengths [Kramida, 2009]. When incorporating a small integrating sphere to overfill the entrance aperture, the spectral lamps can be used for wavelength calibration and spectral smile estimates (Figures 2.5a and 2.5b).

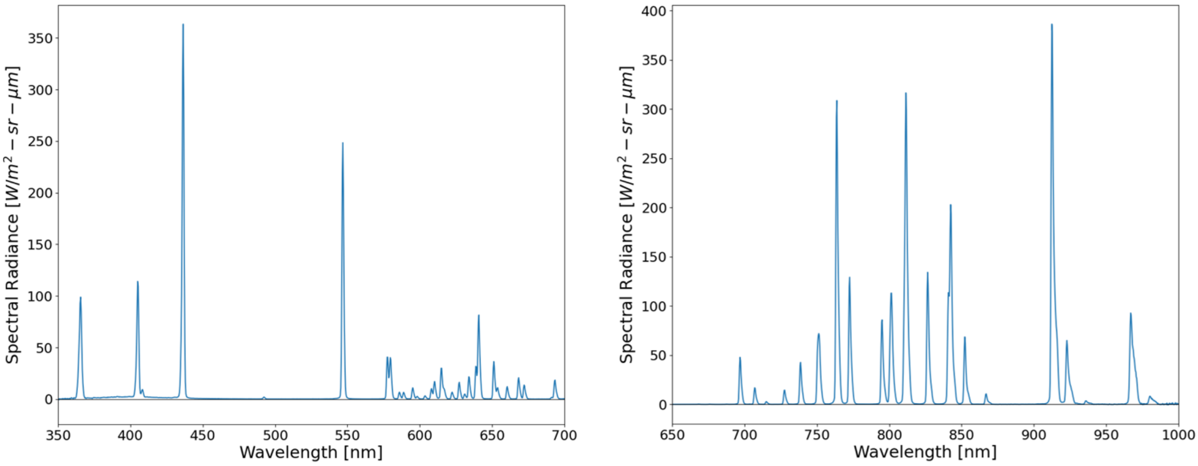

(A) Mercury-Neon

(B) Argon

FIGURE 2.4: The spectral profiles of emission lamps used in the Optical Calibration Facility for wavelength calibration. The spectral emission lines were measured by a high resolution laboratory spectrometer (i.e., Ocean SR2 VIS-NIR) to show all the known emission lines.

Hyperspectral smile distortion is defined as a wavelength shift in the gratings dispersion as a function of spatial position. In other words, as one traverses the slit in the cross-track direction, the grating does not equally disperse the light onto the focal plane with small wavelength shifts on the order of tenths of a pixel [Jablonski et al., 2016]. Estimate the center position as a function of the spatial domain derives the spectral smile estimate with an emphasis on an accurate center position using the measured SRF. Estimating the spectral smile within an HSI system requires spatial homogenized spectral emission lines or monochromatic light with a bandwidth of roughly 1/7th a spectral channel [Ientilucci, D. N. Conran, et al., 2022]. Understanding smile distortion is vital for collecting accurate data because as previously mentioned small shifts in the spectrum can cause unwanted errors and spectral smile creates these small shifts in wavelength calibration across the focal plane.

Figure 2.5a is an estimate (by the author) of spectral smile in the Headwall Nano-Hyperspec at wavelength 436 nm. The dotted black line indicates the reference spatial position (i.e., spatial channel 320) such that spectral smile is in terms of sub-pixel units. Because spectral smile is a characteristic of the instrument, there is no expected shape, but values approaching 1/2 pixel is not desired due to the spectral sampling interval of 2.23 nm/pixel (e.g., 1/2 pixel offset is a 1.1 nm wavelength shift). In addition, wavelength calibration could be restricted or minimized to the center spatial position and spectral smile corrections can define the wavelength calibration for all other spatial positions. An example of wavelength calibration can be seen in Figure 2.5b where a third-order polynomial is used to extract the linear dispersion properties (i.e., nm/pixel).

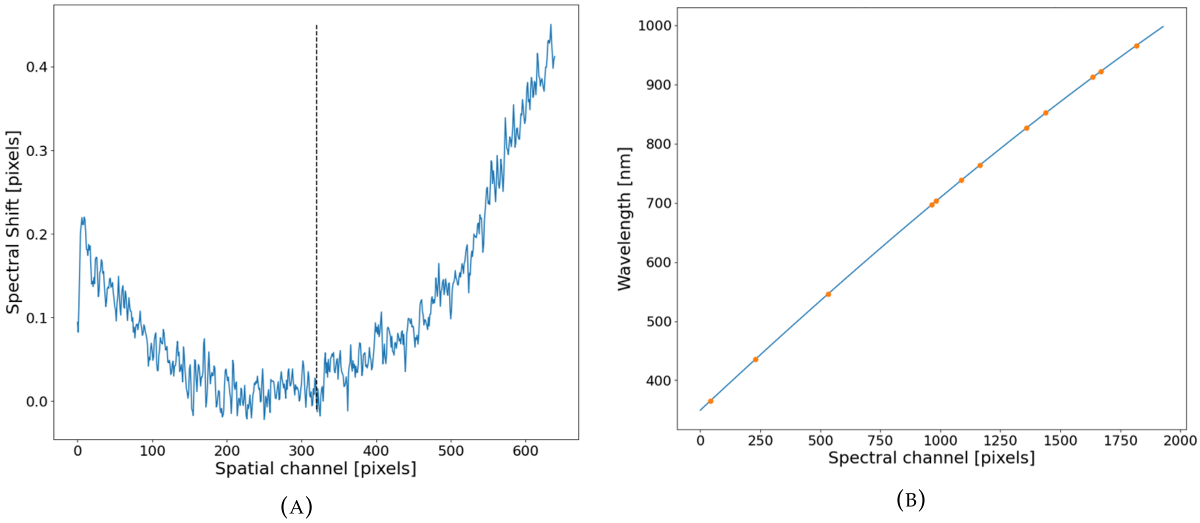

FIGURE 2.5: (A) An example of spectral smile estimate across all spatial channels of an HSI system. (B) Wavelength calibration using a third-order polynomial (blue curve) to map spectral channels to physical units of nanometers for various emission line centers (orange dots).

2.1.2 Radiometric

A radiometric representation of a scene is important for understanding a scene in physical units for scientific exploration, rectifying system étendueb, and sensor dependent artifacts. A radiometric assessment of HSI systems can be performed simplistically or more rigorously depending on the application and uncertainty requirements. All of this analysis requires accurate wavelength calibration such that the matching of integrating sphere spectral radiance to hyperspectral instruments digital signal contains no biases. Furthermore, it is recommended that the illumination source used for hyperspectral calibration is spectrally smooth (e.g., Quartz Tungsten Halogen (QTH) illumination) and spatially homogeneous (i.e., integrating sphere exit port).

Characterizing the radiometric response requires dark signal subtraction, non-uniform correction (NUC) and a multi-illumination radiometric calibration. Dark signal subtraction includes effects from electronic offset or bias, read noise, dark current and dark signal non-uniformity (DSNU). A non-uniform correction or NUC includes fixed-pattern noise or Photon-Response Non-Uniformity (PRNU), irradiance and optical falloff [Janesick, 2007]. A multi-illumination radiometric calibration derives a relationship between the electronic signal (Digital Numbers or DN) and a NIST-traceable spectral radiance quantity such as that found using an integrating sphere. Typically, this is done for a variety of illumination levels that are physically tied to illumination levels outdoors. This simplistic approach provides a reasonable representation of the physical world; however, many assumptions are made.

A major assumption that is typically made is sensor linearity during radiometric calibration. Assessing this artifact pushes the ultimate understanding of nonlinear behaviors and absolute radiometric response of an HSI system [Ewald et al., 2016]. Sensor linearity can be examined with respect to integration time or noise as a function of signal. Nonlinearity associated to integration time dictates that a signal captured at short exposure is not one-to-one with a signal captured at a long exposure. This form of nonlinearity is tied back to the radiometric response of the instrument. Nonlinearity related to noise characteristics is a more complex problem to solve and requires extensive knowledge of photon transfer theory [Janesick, 2007]. For example, CMOS sensors can exhibit sub-Poisson noise at high signal levels resulting in nonlinear behavior as the full well depth is approached. This form of nonlinearity is tied back to the photon response (or gain) of the sensor changing as a function of signal [Bohndiek et al., 2008]. Both forms of nonlinearity requires tedious characterization for an accurate radiometric correction. Assuming a linear response between digital signal and input spectral radiance has many ramifications during field experiments when various signal levels are present in the scene.

2.1.3 Spatial

Inherent to all imaging systems is the spatial blur induced by fore-optics, focusing/collimating components, entrance slit diffraction and the diffraction grating that defines the optical Point

Spread Function (PSF). An image can only be recorded by depositing the optical PSF onto a focal plane array where rectangular pixels contribute to the blur and discretely sample the final spatial response. The focal plane can contribute greatly to the spatial response of any imaging system based on the size of the optical PSF, detector pixel size and sampling rate. Imaging systems with small optical PSF's compared to the detector pixel is said to be *aliased*. The pixel size contributes more to the spatial response then an imaging system that is consisted Nyquist sampled [Fiete, 2010]. The spatial response that culminates all elements within an imaging system and discretely sampled by the detector is defined as the sampled PSF (SPSF) which describes the end-to-end spatial performance of any imaging system. The SPSF can be undersampled (e.g., HSI systems) or oversampled by techniques discussed in this section and in Section 3.2.2.

HSI systems require large apertures to increase energy density per pixel because light throughput is reduced by the entrance slit and grating diffraction efficiency. This design consideration typically leads to a narrow optical PSF which prioritizes the signal-to-noise ratio (SNR) and spectral bandwidth rather than spatial acuity. Moreover, HSI systems have the advantage of identifying objects through their spectral signatures rather than visually acuity [Mouroulis et al., 1998]. Typically, SNR requirements and integration time limitations can drive imaging system design even in multispectral instruments such as the Landsat missions [Stephen J. Schiller and Puschell, 2017].

In summary, the main advantage of spatially aliasing an imaging system is to force the majority of the energy from ideal spatial targets into the fewest number of pixels as possible. A large optical PSF will spread energy out over many more pixels, reducing the energy per pixel and inherently lower the SNR. This is an important property that will be discussed throughout the Findings chapter where all the imaging systems used in the experiments are spatially aliased.

Examining an HSI systems SPSF is much more complex than typical multispectral imaging systems because motion and ortho-rectification can corrupt the imaged scene and produce unrealistic reconstructions of spatial targets (see authors publication in Appendix B). To counteract the problem of motion and image ortho-rectification issues, laboratory experiments using precise rotation or linear stages can accurately move spatial targets across the focal plane to test spatial performance [Ientilucci, D. N. Conran, et al., 2022]. Ideally, the SPSF can be estimated by sliding a point source over the pixel under test and measure its response as a function of position. However, creating a point source using a broadband light source, circular target and a collimator is impractical because circular targets severely limit flux through the system. An approximation to this technique replaces the circular target with a slit which greatly increases the flux throughput, but no longer directly measures the SPSF. This compromise must be made to keep performance estimates reasonable in time, effort and equipment (e.g., QTH-based illumination sources instead of bright laser sources). With this modified technique, the SPSF can only be approximated from two directional scans (cross and along-track) of the sampled Line Spread Function (SLSF) [Torkildsen and Torbjørn Skauli, 2018]. More discussion on the the inter-connectivity of the various spatial responses of imaging systems can be found in Section 2.2.3.

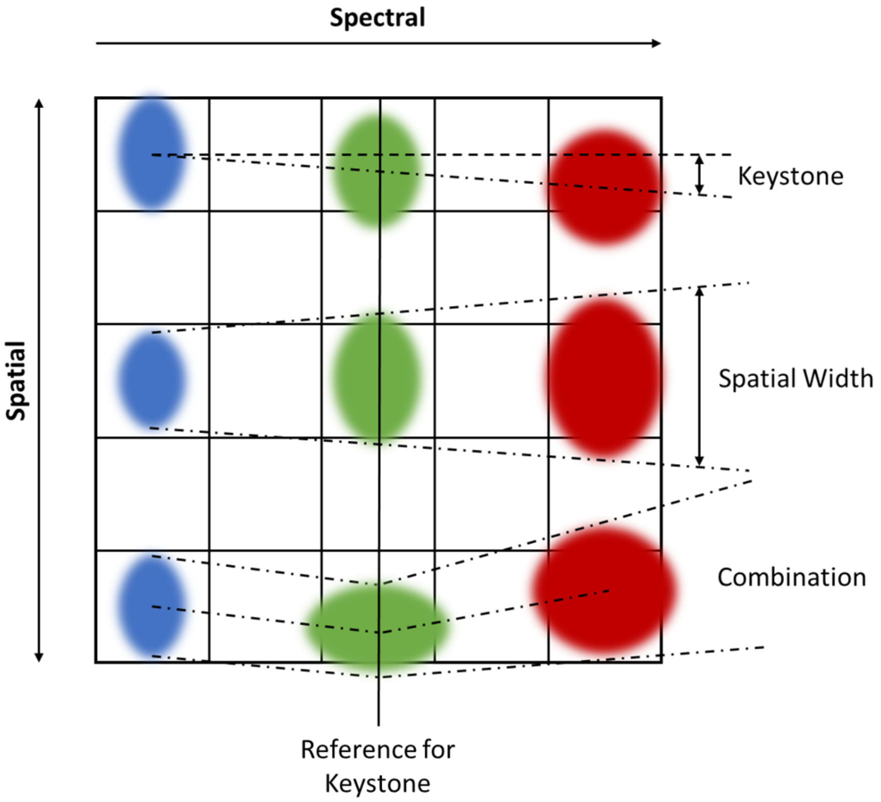

FIGURE 2.6: A pictorial illustration of the two primary spatial characterization parameters of an HSI system.

Keystone distortion, as seen in Figure 2.6, is a variation in the entrance slits magnification as a function of wavelength and includes field-of-view (FOV) dependencies. Using the SLSF measurement technique, keystone can be summarized as a wavelength dependent displacement (from a reference wavelength, typically midpoint of the full spectral range) of the spatial responses centroid position. This displacement is unique in structure and is assumed to be smoothly varying across the entire FOV [Ientilucci, D. N. Conran, et al., 2022]. It will be demonstrated that the center FOV will have the best keystone metric when compared to the edge's and this can be typical for low-cost systems with large apertures and poor off-axis optical performance. Optical designs (i.e., three-mirror anastigmat) prioritizes the minimization of off-axis artifacts such as spherical aberrations, coma and astigmatism [Bentley and Olson, 2012]. These systems are large and can not be used for low-cost compact imaging systems such as one's used on drone-based imaging platforms.

The variation in SPSF width (i.e., SPSF FWHM) as a function of wavelength is observed when a single aperture is used to image scenes containing a wide spectral range such as in HSI (see Figure 2.6). The theoretical limit of imaging systems is known as the diffraction limit and is defined by the entrance aperture and specifically for HSI systems, the entrance slit. Aberrations further complicate the theoretical diffraction limit by adding various wavelength and FOV dependent distortions that combine into the optical PSF defined above. Ideally, if an imaging system is diffraction limited the width of the optical PSF should vary linearly with wavelength at a minimum [Bentley and Olson, 2012]. From the Section 2.1.2, HSI designs gravitate towards optimizing high SNR. This is achieved by a small F-number fore-optic (e.g., Headwall Nano-Hyperspec is optimized for F/2.5). Situations where the aperture is not optimized, very low SNR is experienced and high integration times are required, but drastically induce motion blur. A small F-number achieves two advantages in HSI designs (assuming fixed focal length), large entrance aperture for collecting as many photons as possible and producing a tight optical PSF when compared to the detector element size [Fiete, 2010]. Naturally, the optical PSF and inherently the SPSF will always have some form of width variability which is demonstrated in Appendix B with further demonstrations in future publications derived from the Spatial Testing Group's activities in the P4001 Standards Committee [Ientilucci,

D. N. Conran, et al., 2022].

The typical descriptors used in resolution metrics can be estimated from the SLSF or SPSF and the Modulation Transfer Function (MTF) which provide insight to the instruments spatial performance. The SLSF's FWHM is a metric for estimating the spread of energy directly observed at the focal plane. This metric stays in the spatial domain and can provide minimum resolvability similar to the Rayleigh Criteria. David Conran, Ientilucci, et al., 2021 and J. Holt and D. Conran, 2022 demonstrated a technique using convex mirrors for testing an imaging systems resolution with a direct connection to the Rayleigh Criteria. The MTF value at Nyquist frequency is the other performance metric for understanding an imaging systems spatial performance. An MTF curve supplies information about contrast preservation of imaged spatial frequencies and more specifically how aliased an imaging system is. If the MTF value at the Nyquist frequency is nonzero, the imaging system is aliased with larger values indicating a more aliased system and the resolution is detector limited. An imaging system with a nonzero MTF value at Nyquist requires oversampling to get an accurate estimate of the SPSF/MTF or sample phasing will impact results. If the MTF value at the Nyquist frequency is zero, the imaging system is said to be Nyquist sampled persevering all spatial information without the requirement of oversampling and the resolution is optics limited [Valenzuela and Reyes, 2019].

Figure 2.7 illustrates the variation in resolution based on optical and detector limited imaging and requires proper balancing for imaging system design and application requirements. For example, optical limited imaging spatially perseveres the optical PSF, but lowers the energy per pixel (i.e., lower SNR) whereas detector limited imaging spatially undersamples the scene, but puts more energy into a single pixel (i.e., higher SNR).

2.2 Field Calibration Methods

Characterizing an instrument in both laboratory and field conditions is always recommended for a thorough understanding of the imaging system performance. Field calibration and characterization is particularly important because scientific applications require knowledge on the quality of data collects and the imperfections that may corrupt results. There are two traditional techniques used for assessing an imaging systems calibration and performance in the

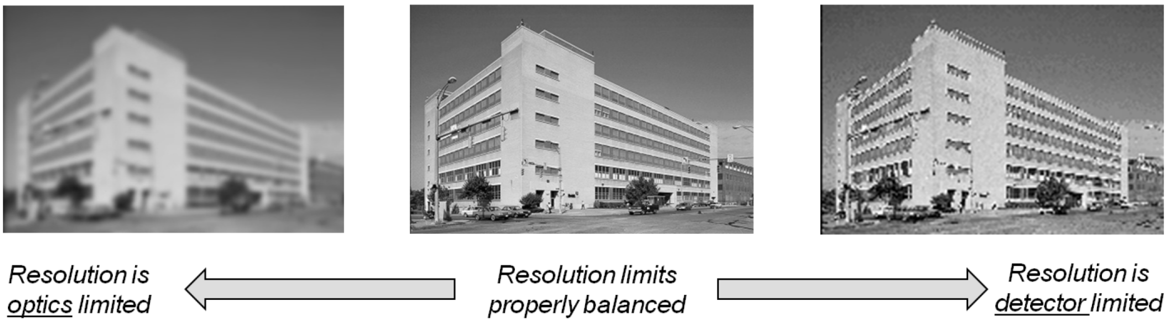
Resolution is optics limited
Resolution limits properly balanced
Resolution is detector limited

FIGURE 2.7: The variable scale of resolution demonstrates the need to balance optic or detector limited imaging based on the application needs [Fiete, 2010].

field: the Empirical Line Method (ELM) (for in-scene reflectance calibration) and the slant edge method (for spatial characterization). In-scene reflectance calibration requires a more thorough analysis due to the complexity of radiometric properties of the environment (i.e., atmosphere and local objects impacting how a material is perceived) whereas spatial characterization is far more forgiving since absolute signal levels are disregarded in the analysis (i.e., normalized out by modelling or computational techniques). b

2.2.1 Field Reflectance Measurements

A reflectance estimate of in-scene calibration targets is typically a relative measurement to that of a $Spectralon_{TM}$ (reference panel) due to its near perfect Lambertian characteristic with a diffuse reflectance of roughly 99% across the VNIR spectrum. However, both assumptions are not entirely true and $Spectralon_{TM}$ falls from ideal when used in the field where multiple illuminations impacts the perceived reflectance. Lab characterization of $Spectralon_{TM}$ typically ends with a hemispherical reflectance factor (HRF) estimated from Labsphere, Inc. (i.e., 8^o Hemispherical reflectance calibration) and only describes $Spectralon_{TM}$ when illuminated by hemispherical sources (e.g., diffuse sky irradiance) [Storm, 1998]. An important property to consider when measuring the reflectance of a material is the bi-directional reflectance factor (BRF) describing the reflectance when illuminated by a point source with directional components (e.g., direct solar irradiance as a function of time). Note that HRF and BRF are representations of the bi-directional reflectance distribution function (BRDF) and hemispherical reflectance distribution function (HRDF) respectively, but are scaled by π steradians such that materials are compared to a perfect Lambertian reflector. Below, we can see these representations as, Eq. (2.1), where θ_{sun} is the solar zenith angle of the sun. It is often convenient to describe the reflectance of a material in terms of a reflectance factor since it is unitless quantity that can be easily applied to both field and laboratory measurements with only nadir viewing geometry [Schaepman-Strub et al., 2006]. Figure 2.8 illustrate the theoretical description of BRDF and HDRF.

$$\rho_{BRDF}(\theta_{sun}, \lambda) = \frac{\rho_{BRF}(\theta_{sun}, \lambda)}{\pi}, \qquad \rho_{HRDF}(\lambda) = \frac{\rho_{HRF}(\lambda)}{\pi} \tag{2.1}$$

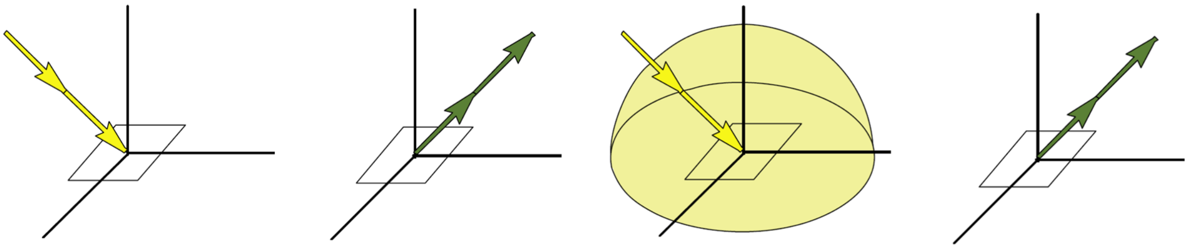

(A) BRDF

(B) HRDF

FIGURE 2.8: Pictorial examples of BRDF and HRDF measurements [Schaepman-Strub et al., 2006].

There are two primary sources of illumination that affects the perceived field reflectance of all materials, the solar and sky irradiances, with their respective reflectance factors, ρ_{BRF} and ρ_{HRF}. A connection between laboratory measurements of reference materials (i.e., $Spectralon_{TM}$) and the illumination sources observed during daylight conditions is critical for extracting the absolute reflectance of the materials in field campaigns [Schaepman-Strub et al., 2006]. Laboratory measurements of the reference panel, ρ_{BRF} and ρ_{HRF}, are estimated prior to the field campaign where a connection to the atmosphere and illumination sources during the experiment are required to fully understand the absolute reflectance of calibration panels. The Digital Imaging and Remote Sensing (DIRS) laboratory at RIT has the unique capability of measuring the BRDF within the GRIT Laboratory [Harms, 2016]. These measurements will be utilized in the presented research.

Performing field measurements with a calibrated spectroradiometer with a cosine corrector (*i.e.,* measuring downwelling irradiances) optimizes the field collection process when using mirrors as calibration targets. The predicted entrance aperture-reaching spectral radiance of a convex mirror relies on the downwelling irradiance from the sun, $E_{sun}(\lambda)$ and sky, $E_{sky}(\lambda)$. If the field spectroradiometer is placed in a cleared area, the total downwelling irradiance, $E_T(\lambda)$ can be described as

$$E_T(\lambda) = E_{sun}(\lambda) + E_{sky}(\lambda) \tag{2.2}$$

A very robust and simple method for characterizing the illumination sources during field experiments is the Global-to-Diffuse ratio, $G(\lambda)$. This measurement characterizes the contribution of diffuse sky to total downwelling irradiance as a dimensionless quantity and provides with additional information about the atmospheric scattering properties over the duration of the experiment [Stephen J. Schiller, 2019]. The definition of the Global-to-Diffuse ratio is

$$G(\lambda) = \frac{E_{sky}(\lambda)}{E_T(\lambda)} \tag{2.3}$$

The Global-to-Diffuse ratio can be readily measured throughout the day using a well-behaved spectrometer in two standard configurations: a cosine corrector (irradiance) or a nadir viewing spectrometer observing a $Spectralon_{TM}$ reference panel (radiance) [Ruddick et al., 2019]. Predicting the radiometric signal of convex mirrors, to be discussed in Section 2.3, requires the measurement of the field irradiance. Naturally, estimating the field irradiance directly is easier than converting the radiance off a $Spectralon_{TM}$ to irradiance. The only measurements required to evaluate the Global-to-Diffuse ratio is the total downwelling irradiance (i.e., denominator of Eq. (2.3)) and a shaded view by eclipsing the solar disk (i.e., numerator of Eq. (2.3)). Figure 2.11a illustrates an example of the Global-to-Diffuse ratio from a recent experiment conducted at the Tait Preserve. Eq. (2.3) can be rearranged to describe the direct solar component to the total downwelling irradiance downwelling, Eq. (2.4).

$$1 - G(\lambda) = \frac{E_{sun}(\lambda)}{E_T(\lambda)} \tag{2.4}$$

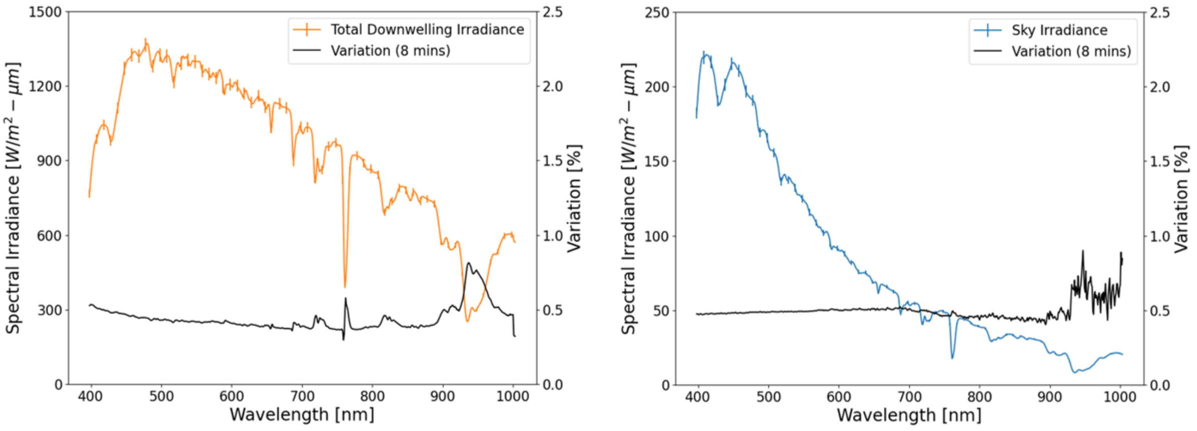

(A) (B)

FIGURE 2.9: The total downwelling irradiance (A) and sky irradiance (B) were measured during the experiment at 1 second intervals. The black curves are variation estimates of both signals and demonstrate atmospheric stability over an 8 minute time interval.

Eq. (2.3) and Eq. (2.4) provide information about the diffuse and direct illumination sources in field measurements, respectively. These quantities can be used as a weighting factor with the laboratory measurement of ρ_{HRF} (Figure 2.10a) and ρ_{BRF} (Figure 2.10b) to extract the true reflectance of Lambertian panels under field conditions. The will be referred to as the field reflectance factor. An important quantity that requires special attention is the reference panels ρ_{BRF}. This factor has solar zenith angle dependency as ρ_{HRF} is assumed to be independent of the solar zenith angle. In general, estimating the reflectance of a material in the field is simply not just the ratio of the target to reference panel signal and requires the incorporation of the reference panels field reflectance factor. There is a misconception that $Spectralon_{TM}$ has a 99% reflectance across the VNIR spectrum and may suffice for general estimates, but the reflectance begins to vary significantly in the short-wave infrared (SWIR) making the assumption invalid for estimates outside the VNIR (see Figure 2.10).

The field reflectance factor of $Spectralon_{TM}$ requires laboratory measurements of ρ_{BRF} to supplement ρ_{HRF} provided by Labsphere, Inc. Field measurements of the Global-to-Diffuse ratio ($G(\lambda)$) and solar zenith angle are required to extract the proper BRF spectrum. The Global-to-Diffuse ratio will then be used as a weighting factor for understanding the differing contributions of the reference panel. The field reflectance factor of any reference panel (i.e., $Spectralon_{TM}$) can be written as Eq. (2.5) and used for further calculations [Stephen J. Schiller,

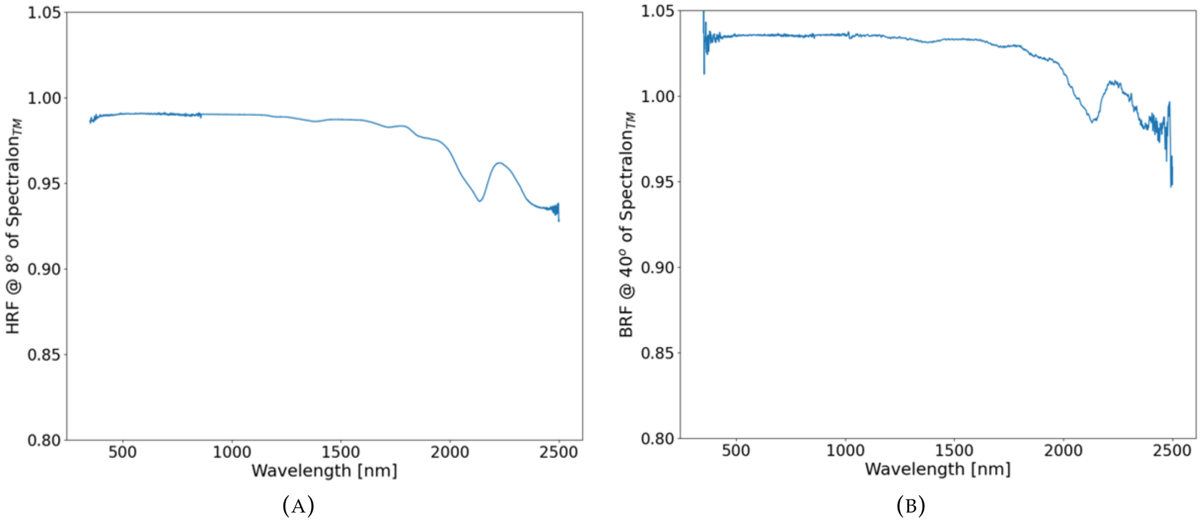

(A)

(B)

FIGURE 2.10: (A) The HRF of $Spectralon_{TM}$ and (B) BRF of $Spectralon_{TM}$. Each measurement has the source at nadir and the detector at 8 and 40 degree inclination, respectively. The HRF is typically measured within an integrating whereas the BRF is a point measurement.

2019].

$$\rho^{ref}_{FRF}(\theta_{sun}, \lambda) = (1 - G(\lambda))\rho^{ref}_{BRF}(\theta_{sun}, \lambda) + G(\lambda)\rho^{ref}_{HRF}(\lambda) \tag{2.5}$$

Since $Spectralon_{TM}$ can vary up to 10% based on the solar zenith angle, the assumption of merely using the HRF or not even considering this factor can lead to the reflectance measurement of targets in the field being unreliable or misleading [Stephen J. Schiller, 2019]. The absolute reflectance of calibration panels, accounting for all illumination factors, when using a $Spectralon_{TM}$ reference panel require the following equation

$$\rho^{target}_{FRF}(\theta_{sun}, \lambda) = \left(\frac{A_{target}}{A_{ref}}\right)\rho^{ref}_{FRF}(\theta_{sun}, \lambda) \tag{2.6}$$

where A defines a measurement of the target and reference panel under full illumination. Any measurements taken with this methodology will account for all BRDF effects embedded in any measurement of the target materials (see Figure 2.11b). This will hold true for any measurement taken in quick succession after the reference panel measurement as long as the atmosphere is not varying under atmospheric and environmental conditions. Eq. (2.6) will be used rigorously for in-scene reflectance calibration using the ELM (Section 2.2.3) and SPARC (Section 2.3) techniques.

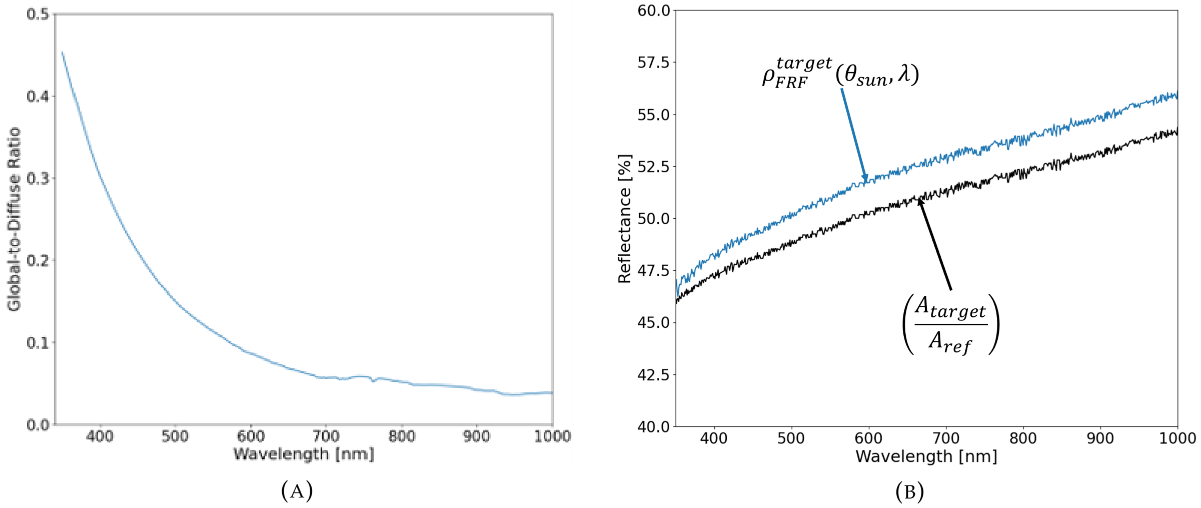

FIGURE 2.11: (A) An example of the Global-to-Diffuse ratio during a field experiment where the majority of the energy is at the blue end of the spectrum. (B) Incorporating the Global-to-Diffuse ratio and the field reflectance of the reference panel, $Spectralon_{TM}$, increases the perceived reflectance of other Lambertian panels.

2.2.2 Empirical Line Method - Radiometric Calibration

The current technique for validating radiometric performance and converting image data to surface reflectance is to use various shades of gray Lambertian calibration panels. Varying the shades provides multiple signal levels to build a look-up-table (LUT) for converting entrance aperture-reaching spectral radiance or digital signal to surface reflectance. It is important that the calibration panels cover the desired reflectance and sensor dynamic range, such that low reflectances are not buried in instrument noise and high reflectances are not saturating. The following discussion is generalized for all imaging systems (i.e., from drones to satellites), but greatly simplifies for drone-based collections because upwelling atmospheric transmission and path radiance can be negated [Mamaghani et al., 2018].

The Empirical Line Method (ELM) is the standard approach for calibrating a imaging system data to surface reflectance [Smith and Milton, 1999; Baugh and Groeneveld, 2008]. This approach completely relies on in-situ calibration targets and measurement equipment/procedure for accurately estimating their reflectance. Field measurements are typically done in quick succession to the collected imagery in order to directly relate observed image data to the measured reflectance factors. A minimum of two calibration targets, as seen in Figure 2.12, are required to extract these parameters if and only if the contrast between the calibration targets spans the appropriate dynamic range of the imaging system and/or for the scientific application [Baugh and Groeneveld, 2008].

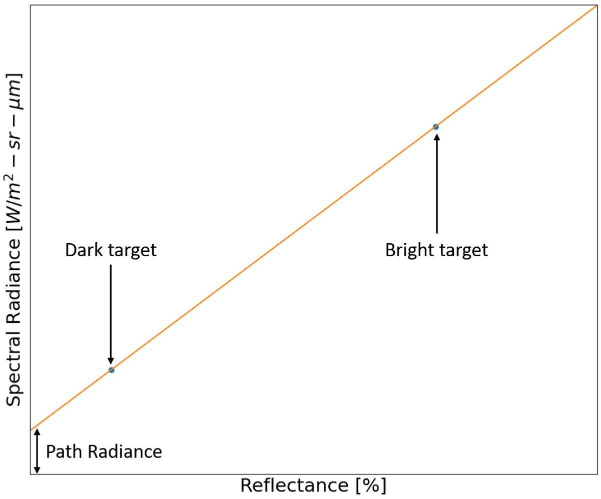

FIGURE 2.12: A simplistic illustration of the two-point ELM for a dark and bright target. The linear fit between spectral radiance and reflectance has a positive intercept which has a physical interpretation tied back the path radiance.

The propagation of radiation reflecting off Lambertian surfaces in ideal daylight conditions begins with the understanding of the various illumination sources including direct solar irradiance, indirect downwelling radiance, upwelling path radiance. Indirect downwelling radiance is a combined source of radiation that stems from diffuse sky illumination, local objects scattering light onto the target and adjacency effects from surrounding objects. Upwelling path radiance is classified as radiation scattered by the atmosphere directly into the imaging systems without reflecting off the targets surface [Eismann, 2012; Ientilucci and Adler-Golden, 2019]. For a Lambertian panel, simplifying assumptions are required to model the observed radiance at the entrance of an imaging system. These assumptions include describing the Lambertian panel by its diffuse reflectance component only, diffuse sky irradiance is uniform in all directions and all other radiation grouped into a single term. The entrance aperture-reaching spectral radiance for a Lambertian panel can be modeled as,

$$L_{EAR}^{panel}(\lambda) = \frac{\tau_{\uparrow}(\lambda)\rho_d(\lambda)}{\pi}[E_{sun}(\lambda) + E_{sky}(\lambda)] + L_a(\lambda) \tag{2.7}$$

where $\tau_{\uparrow}(\lambda)$ is the upwelling atmospheric transmission, $\rho_d(\lambda)$ is the targets diffuse hemispherical reflectance, $E_{sun}(\lambda)$ and $E_{sky}(\lambda)$ are the direct solar and downwelling sky irradiance components at the targets surface and $L_a(\lambda)$ includes path radiance, adjacency effects and scattering from surrounding objects. It should be noted here that $E_{sun}(\lambda)$ is measured at Earth's surface and incorporates the solar zenith angle dependence. Through projection of area, $E_{sun}(\lambda)$ can be written as $\tau_{\downarrow}(\lambda)E_0(\lambda)cos(\theta_{sun})$ where $E_0(\lambda)$ is the exoatmospheric solar irradiance, θ_{sun} is the solar zenith angle and $\tau_{\downarrow}(\lambda)$ is the downwelling atmospheric transmission. However, field measurements readily record $E_{sun}(\lambda)$ at the Earth's surface that contain all unique signatures of the downwelling atmospheric transmission loss including the Global-to-Diffuse estimate. Eq. (2.7) defines all contributions an imaging system instantaneous field-of-view (IFOV) when observing Lambertian targets through the Earth's atmosphere. The mathematical basis behind the ELM approach emerges from Eq. (2.7) when rewritten in the following form

$$L_{EAR}^{panel}(\lambda) = a(\lambda)\rho_{FRF}(\lambda) + b(\lambda) \tag{2.8}$$

where a linear relationship between entrance aperture-reaching spectral radiance and field reflectance factor is derived through empirical parameters, $a(\lambda)$ and $b(\lambda)$. The gain parameter, $a(\lambda)$, defines the differential relationship between the surface reflectance and spectral radiance whilst containing all atmospheric conditions whereas the offset term, $b(\lambda)$, contains all upwelling path radiance and adjacency effects. At-sensor spectral radiance is easily converted to surface reflectance for all scene pixels by inverting Eq. (2.8) and solving for $\rho_{FRF}(\lambda)$ [Smith and Milton, 1999; Baugh and Groeneveld, 2008]. It should be noted that the reflectance in Eq. (2.8) is the field reflectance factor as measured by a spectrometer and is different than the assumption of a diffuse reflectance defined in Eq. (2.7). The empirical relationship can not be applied liberally to all imagery over large area swaths because of the uniqueness of atmospheric composition. Water vapor column amount and atmospheric scattering properties can vary significantly from one location to another including seasonal dependencies. Atmospheric differences impacts the parameters derived from ELM and thus, can only be applied to imagery taken within the vicinity of the calibration targets and within a strict time window [Ientilucci and Adler-Golden, 2019].

Challenges faced when using ELM to atmospherically compensate and convert imagery data to surface reflectance originates from the assumptions in Eq. (2.7) and in the calibration targets reflectance. The Lambertian assumption made about the calibration targets allows for the simplification of complex radiometric interactions between light and matter and a more comprehensive physics-based approach can be found in Ientilucci and Adler-Golden, 2019. Calibration target BRDF is typically assumed to be diffuse and equivalent to the hemispherical reflectance ($\rho_{HRF}(\lambda)$) only, but more rigorous methods can provide more accurate results in extracting true reflectances of remotely sensed materials [Yeom et al., 2017]. BRDF estimates of calibration targets can be hard to measure and typically require complex assemblies to ensure angular information is as accurate as possible. Because of this complexity, implementing BRDF estimates in field calibration experiments can only be done by institutions and partnerships with BRDF measurement facilities or paid services provided by national labs or accredited institutions (e.g., GRIT Lab at RIT [Harms, 2016]). Further assumptions include a uniform Lambertian sky such that there is no angular dependence to the diffuse sky irradiance. In reality, this is never the case and the surrounding environment (large buildings or vegetation) can greatly affect this assumption [Eismann, 2012].

2.2.3 Slanted Edge Method - Spatial Characterization

Slanted Edge Theory

Spatial characterization of an imaging system involves the measurement of the overall system level blur while defining the spatial resolution (i.e., smallest observable feature) within imagery. From aerial imagery, the simplest way spatial resolution can be defined is by the projected distance between two pixels onto the ground (i.e., ground sampling distance or GSD). However, this simplistic definition completely disregards diffraction and all other optical distortions discussed in Section 2.1.3. The underlying physics of image formation in real systems relies heavily on Fourier mathematics and diffraction theory to define how light is focused through an aperture. For imaging systems, the ideal descriptor of spatial response is the optical PSF and is a 2D representation of the optical blur when simulated by a point source such as a star. Other forms of spatial characterization descriptors, includes the optical line spread function (LSF) and edge spread function (ESF). Mathematically these spatial responses originate from the PSF as 1D integral projections (Figure 2.13). Because the LSF and ESF are 1D integral projections of the PSF, multiple directional measurements are required to fully describe the imaging system. For remote sensing applications, two orthogonal measurements (x and y) of the ESF provides enough information to describe the imaging systems spatial resolution [Fiete, 2010]. The sampled version of the optical LSF and ESF (i.e., sampled LSF (SLSF) and ESF (SESF)) define the imaging systems end-to-end spatial performance including the detector pixel blur. Technological advancements in calibration targets for remote sensing (i.e., convex mirrors) has allowed direct measurements of the PSF, but standard practices in this community were built on ESF measurements and the Fourier relationships outlined in Figure 2.13. Future discussions will focus on the inter-relationship between the PSF, Modulation Transfer Function (MTF) and LSF because the PSF is not directly measured by the ESF.

A spatial response model for an imaging system can be thought of as simple convolutions and multiplications of blurring and sampling functions. Real imaging systems have various blur sources and for simplicity all blurring contributions will be combined into a single function, $h(x, y, \lambda)$ that define the end-to-end spatial performance. The scene to be imaged will be defined as $f(x, y, \lambda)$ and the output image defined as $g(x, y, \lambda)$. That is,

$$g(x, y, \lambda) = (f(x, y, \lambda) * h(x, y, \lambda))\, COMB\left(\frac{x}{p_x}, \frac{y}{p_y}\right) \tag{2.9}$$

where COMB is a series of Dirac delta functions spaced at an equal intervals defined by the pixel pitch of the detector. From Eq. (2.9), it can be shown that $g(x, y, \lambda)$ will represent a sampled version of $h(x, y, \lambda)$ if and only if $f(x, y, \lambda)$ is a 2D Dirac delta function (i.e., $\delta(x, y)$). If not, $f(x, y, \lambda)$ will be contaminated with spatial artifacts induced by the targets physical extent and further processing is required to extract the imaging systems spatial response. Furthermore, the COMB function complicates the estimate of $h(x, y, \lambda)$ since most imaging systems

$$\begin{tikzcd}
PSF(x,y) \arrow[rr, "\text{One-sided 1D Integration}"'] \arrow[d, leftrightarrow, "\text{2D Fourier Transform}"'] \arrow[drr, "\text{1D Integration}"'] & & ESF_x(x) \arrow[d, shift right, "\text{1D Derivative}"'] \\
MTF(\xi,\eta) \arrow[r, "\text{1D Profile}"'] & MTF(\xi,0) \arrow[r, leftrightarrow, "\text{1D Fourier Transform}"'] & LSF_x(x) \arrow[u, shift right, "\text{One-sided 1D Integration}"']
\end{tikzcd}$$

FIGURE 2.13: The inter-relationship between the various spatial response functions for imaging systems.

within the remote sensing field undersample the spatial domain. This requires multiple variations of $h(x, y, \lambda)$ that are sampled differently where this is referred to as sample phasing. Retrieving different phases of the spatial response function virtually fills in the missing spatial information that was lost from undersampling [Easton Jr, 2010].

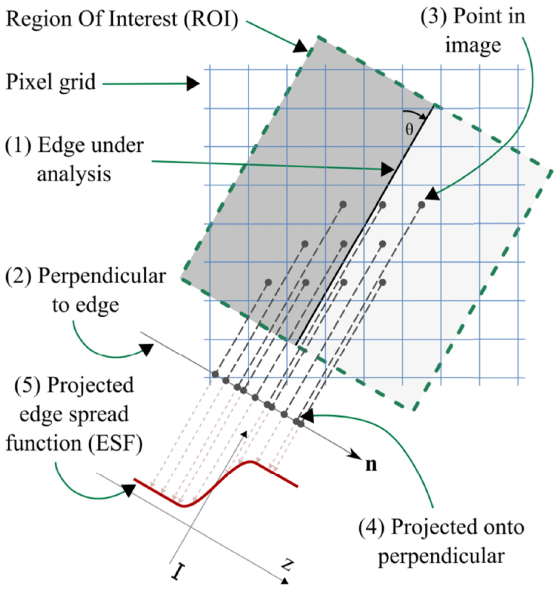
Region Of Interest (ROI)
Pixel grid
(1) Edge under analysis
(2) Perpendicular to edge
(3) Point in image
(4) Projected onto perpendicular
(5) Projected edge spread function (ESF)
θ
n
I
z

FIGURE 2.14: This illustration demonstrates how an tilted edge target is oversampled by projecting onto a perpendicular axis defined by the edge location and tilt angle [Viallefont-Robinet et al., 2018].

The following derivation of the slanted edge method was inspired by Viallefont-Robinet et al., 2018 and Easton Jr, 2010. The slanted edge method considers an imaging system as linear and shift invariant such that the spatial response can be easily described with Eq. (2.9). The observation of the scene, $f(x, y, \lambda)$, is convolved with the system PSF, $h(x, y, \lambda)$, then sampled at intervals defined by the pixel pitch (p_x, p_y) in two directions. Figure 2.14 illustrates how an edge target is oversampled (non-uniformly) by projecting data onto a perpendicular axis to the edge. The edge target, $f_{edge}(x, y, \lambda)$, can be mathematically represented as a step function with arbitrary amplitude and offset and extents infinitely in the y-direction (along-track). That is,

$$f_{edge}(x, y, \lambda) = a \cdot STEP(x) 1(y) + b \cdot 1(x, y) \tag{2.10}$$

where a is the edge's amplitude, $STEP(x)1(y)$ is 2D representation of the Heaviside step function and b is a constant offset value. The edge function (Eq. (2.10)) replaces the scene function and Eq. (2.9) becomes

$$g_{edge}(x,y,\lambda) = \left(f_{edge}(x,y,\lambda) * h(x,y,\lambda)\right) COMB\left(\frac{x}{p_x}, \frac{y}{p_y}\right) \tag{2.11}$$

Without showing every step in the derivation, Eq. (2.11) can be easily simplified with Fourier mathematics where the sampling function has been excluded for clarity. Thus we have,

$$G_{edge}(\xi,\eta,\lambda) = a \cdot \mathcal{F}\{STEP(x)\} \cdot MTF(\xi,0) + b \cdot MTF(0,0) \tag{2.12}$$

The edge method culminates within Eq. (2.12) and illustrates future post-processing steps needed to evaluate the ESF. First, $MTF(\xi,0)$ is, by definition, the 1D profile of the 2D MTF highlighted in Figure 2.13 and can be directly tied to the LSF in the x-direction (i.e., $\mathcal{F}^{-1}\{MTF(\xi,0)\} = LSF_x(x)$) after an inverse Fourier transform. The MTF is peak normalized to unity and the offset equates to the constant b. An inverse Fourier transform of Eq. (2.12) then becomes

$$g_{edge}(x,y,\lambda) = (a \cdot STEP(x) * LSF_x(x) + b)\, COMB\left(\frac{x}{p_x}, \frac{y}{p_y}\right) \tag{2.13}$$

Eq. (2.13) describes the sampled edge target blurred by the system LSF and further post-processing is required before the SLSF can be estimated. To rid all impacts from sampling (i.e., aliasing artifacts), the edge target requires specific orientation (tilted by 6-8 degrees) during deployment. The construction of an SESF will be discussed later in this section, but for this mathematical derivation the main assumption is that the oversampled ESF is uniformly sampled across the spatial axis such that the frequency axis of the MTF is linear. To isolate the SLSF, Eq. (2.13) is differentiated with respect to the spatial axis defined by projecting all data points onto the z-axis (i.e., a perpendicular axis to the edge). We can compute the derivative as

$$\frac{d}{dz}\left[g_{edge}(z,\lambda)\right] = \frac{d}{dz}\left[(a \cdot STEP(z) * LSF_x(z) + b)\right] \tag{2.14}$$

The derivative operator when applied to the convolution in Eq. (2.14) can either be distributed to the STEP function or the LSF. It is trivial to show that the derivative of the STEP function is a Dirac delta centered at zero and this justifies applying it to the STEP function. By use of the shift theorem, it can be shown that a Dirac delta function, center at zero, convolved with any function equates to the function itself and Eq. (2.14) reduces to

$$\frac{d}{dz}\left[g_{edge}(z,\lambda)\right] = a \cdot LSF_x(z) \tag{2.15}$$

The expression above defines a linearly scaled SLSF that was derived from a slanted edge target under a specific orientation. The mathematical theory is only as good as the practical limitations experienced in real scenarios. There are many subtitles involved in the construction of the oversampled ESF and this procedure follows the ISO 12233 standard for evaluating the spatial frequency response of digital cameras [Burns, 2000].

ESF Construction

The main steps in constructing an SESF is: identify a region of interest (ROI) within the edge image, estimate the edge location and angle, project data onto an axis perpendicular to the defined edge, bin oversampled ESF to uniform spacing to at least 1/4 pixel intervals (i.e., results in the SESF), differentiate to extract the SLSF then perform a discrete Fast Fourier Transform (FFT) to estimate the 1D profile of the MTF. The following procedures will use the geospatial quality reference dataset established by the MTF project team of CEOS/WGCV/IVOS : `http://calvalportal.ceos.org` to illustrate the various algorithms, processing steps, highlighting advantages and challenges used by different satellite companies [Viallefont-Robinet et al., 2018].

Understanding the edge target includes subtle details in orientation and overall target extent which are important properties to consider for creating a sampled ESF or SESF. Figure 2.15a is an example satellite image of an ideal edge target for both an x and y directional measurements of the SESF. As previously mentioned, a slight rotation in the edge target as projected onto a square focal plane permits proper oversampling of the SESF if and only if the tilt is close to 6 to 8 degrees and if not, the SESF's can not be tied directly to the cross or

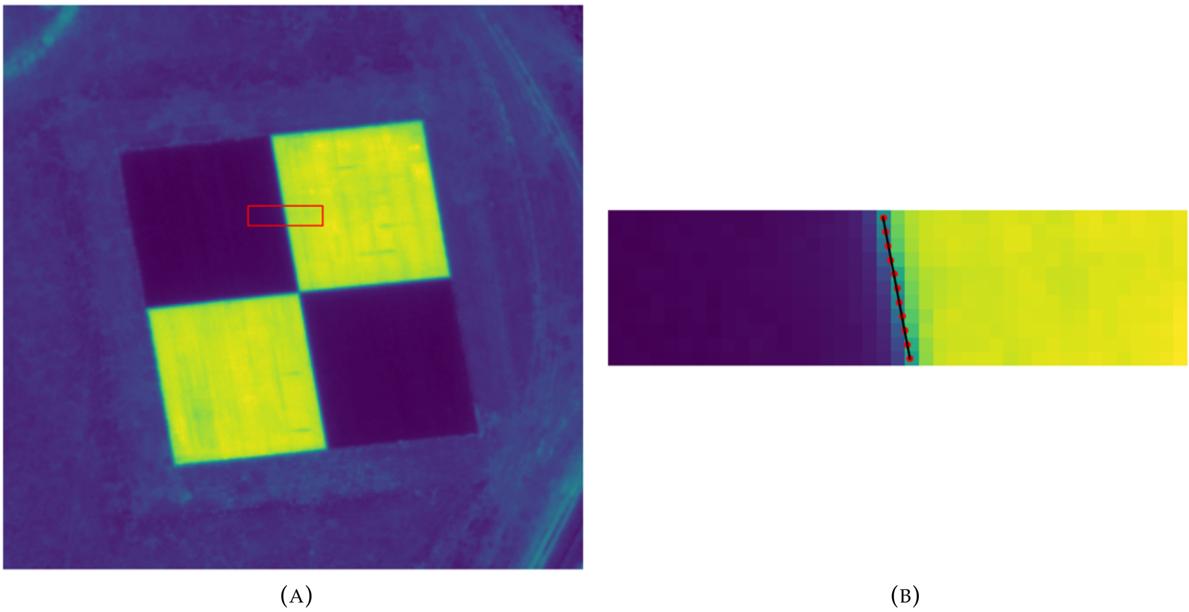
(A) (B)

FIGURE 2.15: (A) Broadband satellite image of an edge target where the red box is the ROI for edge assessment. (B) Estimated edge location per row (red dots) with a linear fit (black line) within the ROI.

along-track directions [Burns, 2000]. The red box in Figure 2.15a is an isolated region on the edge target with adequate buffering zones around the ROI to mitigate any background effects (i.e., spatial blurring of background material on the target) and spatial pattern transition zones. Figure 2.15b shows the isolated edge from the red ROI in Figure 2.15a with an estimate of the edge location (fitted black line). The length (number of rows) and width (number of columns) of Figure 2.15b has a dominant role in the development of an accurate SESF. If the length of the edge is not long enough, oversampling will not be complete. If the width is not large enough, enclosed energy will not be fully captured in the analysis and will impact the MTF calculation (i.e., area under the curve). Journal articles Kabir, Leigh, and Helder, 2020 and Kohm, 2004 suggested an overall extent of the edge image to be 6 to 10 rows (length) and at least 20 columns (width) to accommodate the excess noise and edge blur, respectively. However, these rules can be modified if the sample phasing is too sparse and gaps in the 1/4 pixel binning step or the imaging system has a very large PSF (i.e., optical PSF is close to Nyquist sampled).

Constructing an SESF starts with Figure 2.15b and requires two key steps: estimating the sub-pixel edge location per row (i.e., red dots) and projecting all image data points onto an axis perpendicular to the derived linear fit that define the sub-pixel edge locations (i.e., black line). Locating the sub-pixel edge is achieved by breaking up the edge image into row vectors corresponding to a 1D undersampled SESF. A well-known method for locating edges in digital imagery is the Tabatabai Method [Tabatabai and Mitchell, 1984]. This method is invariant to additive noise that can plaque sub-pixel edge locations and is more desirable than a simple center of mass calculation. In fact, the Tabatabai Method uses the the first three sample moments of input data to estimate the sub-pixel edge location without introducing any interpolation processes. After all edge locations are estimated (red dots in Figure 2.15b), a linear fit can be applied to the red dots. The edge location can be seen in Figure 2.15b as the black line. The linear fit accomplishes two tasks: further reduction of systematic errors and noise contained in the edge image and extracting key parameters for projecting the data onto a perpendicular axis. Parameters estimated from the linear fit can be applied directly to every pixel using

$$z = [x - e(y)] \cdot \cos\theta_e \tag{2.16}$$

where z defines the projected spatial axis, x is an arbitrary array of column indices (e.g., 0, 1,..., 19), $e(y)$ is a sub-pixel edge location for row y derived from the linear fit and the edge angle, θ_e [Viallefont-Robinet et al., 2018]. When Eq. (2.16) is applied to Figure 2.15b, an oversampled ESF is constructed centered around zero with non-uniform intervals, as seen in Figure 2.16a. Before a uniformly sampled ESF (i.e., SESF) can be differentiated, the oversampled ESF requires uniform intervals such that a FFT can be applied. Burns, 2000 specifies a binning procedure where data is averaged within $1/4$ pixel intervals (see Figure 2.16b) and from basic Fourier mathematics the highest observable frequency would then be 4x the Nyquist sampling frequency. The subtlety of this step can be greatly overlooked, but it is important to understand that imaging systems can only resolve spatial frequencies up to Nyquist (i.e., Δx = 1 pixel or $f_{Ny} = 0.5$ pixels^{-1}). This restriction in resolution can only be resolved by methods (i.e., oversampling, super-resolving or pan-sharpening) using extra information to avoid aliasing and increasing the apparent sampling frequency [Easton Jr, 2010].

Performing a 2- or 3-point numerical derivative on the SESF extracts a peak normalized

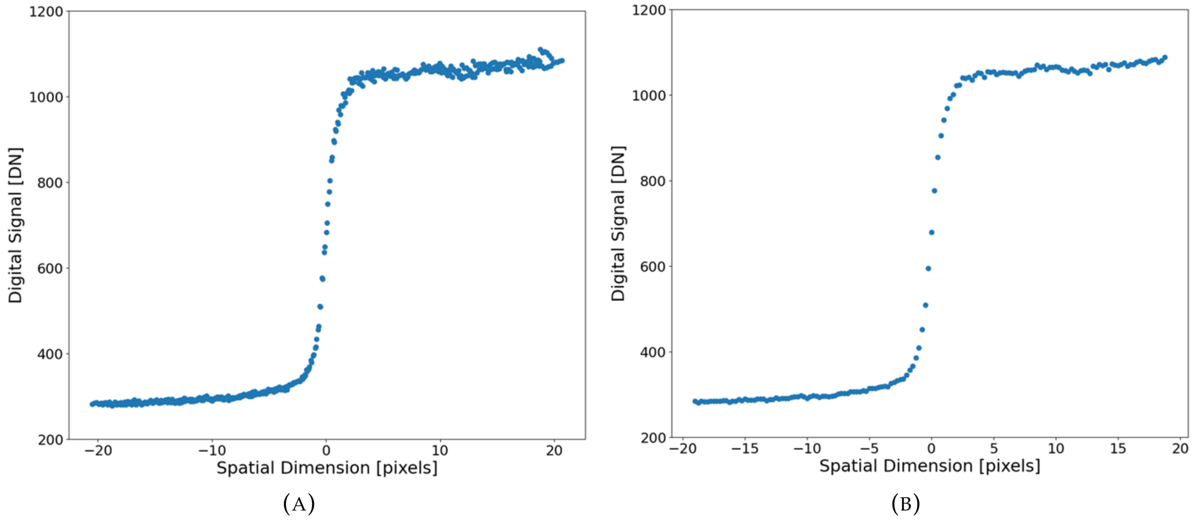

(A)

(B)

FIGURE 2.16: (A) Oversampled SESF after axis projection with nonuniform sampling. (B) SESF binned to 1/4 pixel intervals.

SLSF as shown in Figure 2.17a. The overall spatial axis was cropped to 20 pixels as previously discussed. Even though a Hamming window function was applied to the SLSF, noise is still apparent in the data. Asymmetry in the noise surrounding the SLSF peak is a direct result of photon noise, spatial non-uniformity within the edge target and the numerical differentiation. This is a major pitfall of the slanted edge method because the bright side of the edge will always contain more noise than the dark side and this will causes uncertainty in the oversampled LSF shape. This flaw can be mitigated by reducing overall signal level (i.e., reduce integration time) during imaging, but this has diminishing returns until the dark side approaches the sensors noise floor. Furthermore, differentiation exacerbates all noise acting as a high pass filter causing an increase in noise from post-processing. As elegant as the slanted edge method proof is, physics and required computation steps will limit the extracted shape and accuracy of performance metrics defined in Section 2.1.3.

The final step is to perform an FFT on the uniformly sampled LSF or SLSF and define the frequency axis. The frequency axis is defined by the pixel sampling interval (e.g., $\Delta x = 1/4$ pixel) and the total number of data points (e.g., $N = 80$). Eq. (2.17) defines the spacing in the

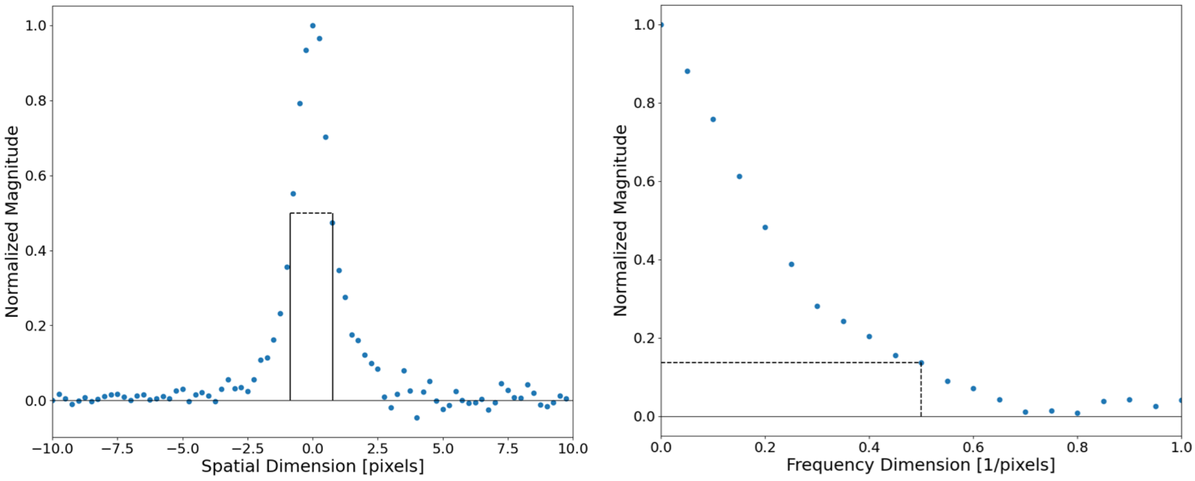

(A) (B)

FIGURE 2.17: This example demonstrates the slanted edge method and the extracted results. (A) Example SLSF with a FWHM estimate of 1.62 pixels. (B) 1D MTF estimate with a value at Nyquist of 0.132.

Fourier domain as

$$\frac{-1}{2\,\Delta x} \leq \Delta f = \frac{1}{N\,\Delta x} \leq \frac{1}{2\,\Delta x} - \Delta f \tag{2.17}$$

where Δx is the spatial sampling interval, Δf is the frequency sampling interval, N is the total data points within the SLSF, and the Nyquist frequency is defined by $\frac{1}{2\,\Delta x}$. This finalizes the slant edge method for extracting the spatial response of an imaging system. Since the MTF derived from the slanted edge method only provides 1D information about the SPSF, a minimum of two orthogonal directions (cross and along track) is required to fully understand the 2D MTF. If all these parameters are met, the SESF can be differentiated into the SLSF for the cross and along track directions. This can complicate the measurement process and targets like Figure 2.15a are best to observe both directional SLSF's in one image.

2.3 Convex Mirror Targets (SPARC)

A SPecular Array for Radiometric Calibration (SPARC) method utilizes convex mirrors to redirect solar radiation striking the ground to Earth remote sensing systems for radiometric calibration and spatial characterization [Stephen J. Schiller and Silny, 2010]. The convex mirrors re-image the solar disk providing an imaging system with an ideal point source defined by the radius of curvature (i.e., proportional to the focal length) and the mirrors reflectance factor. The discuss of the SPARC method begins with the basic radiometric description of an ideal point source and follows a theoretical path towards defining radiometric properties useful for remote sensing applications such as entrance aperture-reaching spectral radiance and surface reflectance factors for calibration [S. J. Schiller, 2012].

A spherical, convex mirror focuses plane waves (i.e., solar irradiance) at the focal point, the reflected image (virtual) is best represented as a spectral radiant intensity source ($I_m(\lambda)$) with dependence's on the mirror's geometry (i.e., projected area and solid angle). Eq. (2.18) is the radiometric description of energy reflecting off the mirrors surface with spectral reflectance ($\rho_m(\lambda)$), projected area (A_m), solid angle (Ω_i) and downwelling spectral irradiance ($E_d(\lambda)$).

$$I_m(\lambda) = \frac{\rho_m(\lambda)E(\lambda)A_m}{\Omega_i} \tag{2.18}$$

Propagating the radiometry from downwelling irradiance to an entrance aperture-reaching reaching quantity (e.g., spectral radiance) requires understanding the geometric properties that transform Eq. (2.18) into easily measurable and traceable radiometric quantities for remote sensing systems. Furthermore, the mirrors geometric extent will highlight their use for spatial quality assessment [Silney and S. J. Schiller, 2013]. The focus of the next section will be to break down the $\left(\frac{A_m}{\Omega_i}\right)$ components into an easily measurable quantity having a direct relationship to the geometric property of spherical, convex mirrors.

2.3.1 SPARC Geometry

The geometry of a convex mirror is critical for understanding the image formation and radiometric properties. Geometric optics and simple ray tracing can easily describe image formation of spherical, convex mirrors. Geometry of spherical surfaces outlines the $\left(\frac{A_m}{\Omega_i}\right)$ term which is critical for the radiometric description transformation.

The primary descriptors for a conical section of a spherical surface is the Radius of Curvature (R_m) and the projected diameter (D_m), as seen in Figure 2.18. Geometrical optics states that

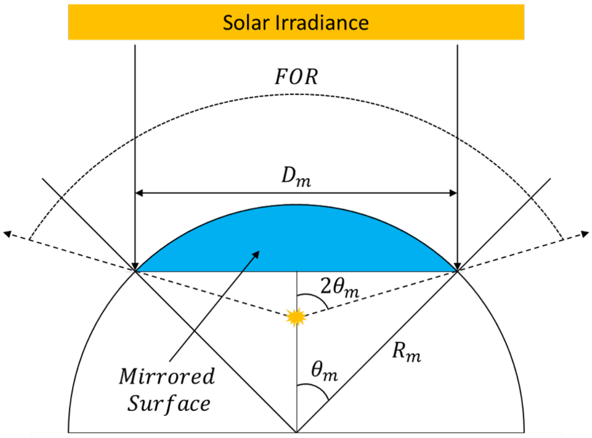

FIGURE 2.18: Illustrating various properties of convex mirrors when stimulated with plane waves originating from the solar irradiance.

a spherical, convex mirror has a focal length related to half of R_m when illuminated by plane waves. When the mirrors are used in the field, plane waves originating from the sun create a virtual image of the solar disk at the mirrors focal length. An important note to highlight is that the solar disks image is formed at half the radius of curvature (R_m). This is critical for understanding the mirrors solid angle, (Ω_i). The solid angle is related to the solar disks image and not exclusively related to the physical geometry (i.e., the projected area, A_m).

Figure 2.18, illustrates the projected area and the physical geometric relationship. The projected area can be written as

$$A_m = {}^1\!/_4 \pi D_m^2 = \pi R_m^2 sin^2(\theta_m) = {}^1\!/_2 \pi R_m^2 (1 - cos(2\theta_m)) \tag{2.19}$$

where θ_m is the half-angle of the cone formed by the center of the sphere and the edges of the mirror.

Figure 2.18 also demonstrates the solid angle created from the virtual image. If we define the angle created from this position to the edge of the mirror, the angle subtended to $2\theta_m$ and can easily be proved by the law of reflection. The solid angle can be evaluated through the following integral

$$\Omega_i = \int_0^{2\pi} d\phi \int_0^{2\theta_m} sin\theta \, d\theta = 2\pi(1 - cos(2\theta_m)) \tag{2.20}$$

Another important property is the total viewing angle at which the virtual image is observable and is referred to as the Field of Regard (FOR). The FOR for the convex mirror is $4\theta_m$ based on the geometric image formation principles of the convex mirrors defined above. With the understanding of both the projected area and solid angle created by the mirrors, the $\left(\frac{A_m}{\Omega_i}\right)$ term can be simplified to the following

$$\left(\frac{A_m}{\Omega_i}\right) = \frac{{}^1\!/\!{}_2\pi R_m^2(1 - cos(2\theta_m))}{2\pi(1 - cos(2\theta_m))} = {}^1\!/\!{}_4 R_m^2 \tag{2.21}$$

This demonstrates that the geometric term in Eq. (2.18) can be simplified to just a R_m dependence which can be readily measured in the laboratory. This further simplifies Eq. (2.18) which will be investigation in Section 2.3.2 [S. J. Schiller, 2012].

To ensure that the convex mirrors create an ideal point source for spatial analysis, the point source criteria needs to be met which relates the solar disk image to the imaging systems GSD. A general rule adopted from the P4001 Standards Committee is that the size of the spatial source should not exceed 0.25 pixels [Ientilucci, D. N. Conran, et al., 2022]. A simple geometric analysis can show that Eq. (2.22) expresses a measure of altitude at which the imaged solar disk is considered a point source. That is,

$$H > \frac{f_m}{n_c} \cdot \frac{\alpha_{sun}}{IFOV_i} \tag{2.22}$$

where H is the altitude, f_m is the mirror focal length, n_c is the 0.25 pixel criteria and $IFOV_i$ is the imaging systems IFOV and α_{sun} is the solar disks angular diameter. It should be noted that H will have equivalent units as f_m with $IFOV_i$ and α_{sun} are in units of radians or milli-radians. Table 2.1 displays a few configurations that illustrate the argument that under most UAS flight conditions, the mirrors provide an ideal spatial point source. Most of the drone flights conducted with the mirrors were greater than 30 meters and even for the largest mirror, this is roughly 10x the height requirement. In Table 2.1, the hyperspectral (HS) systems IFOV was 0.6167 milli-radians and the multispectral (MS) systems IFOV was 0.6944 milli-radians.

TABLE 2.1: This table displays the minimum height requirements for the hyperspectral (HS) and multispectral (MS) imaging systems used for all drone experiments.

f_m	d_{sun}	H (HS)	H (MS)
12.5 mm	0.11 mm	0.71 m	0.63 m
25 mm	0.22 mm	1.42 m	1.26 m
50 mm	0.44 mm	2.83 m	2.51 m

2.3.2 SPARC Radiometry

The radiometric response from a SPARC target is unique because as perceived by an imaging system, the signal originates from a sub-pixel location and the energy spreads over the SPSF. The mirrors signal resides on top of the background material and effectively is turned off when not within the FOR. Since the image of a SPARC target represents the mirror(s) plus background signal, the background signal needs to be subtracted such that the mirrors signal is isolated. The following derivation stems from Stephen J. Schiller and Silny, 2010 and S. J. Schiller, 2012.

The simplified version of Eq. (2.18) describing the spectral radiant intensity off the surface of N convex mirrors is

$$I_m(\lambda) = {}^1\!/_4\rho_m(\lambda)NR_m^2E_d(\lambda) \tag{2.23}$$

Eq. (2.23) has an elegant form with all mirror properties being easily measured in a laboratory and an added benefit of linearly scaling perceived the signal by incorporating more mirrors into an array. To extract entrance aperture-reaching quantities with Eq. (2.23), the $E_d(\lambda)$ term requires two respective quantities corresponding to the two types of radiation striking the surface under ideal daylight conditions. Under these conditions, direct solar irradiance and hemispherical sky irradiance are simultaneously observed by the imaging system; however, the mirrors solid angle (Eq. (2.20)) directly affects the amount of sky irradiance propagated into the IFOV. By definition, the solid angle of diffuse hemispherical sky irradiance is 2π steradians (assuming no surrounding objects) and the fractional amount of sky irradiance reflected into the imaging system is defined as

$$f_{sky} = \frac{\Omega_i}{2\pi} = (1 - cos(2\theta_m)) \tag{2.24}$$

Eq. (2.24) has a direct relationship to the solid angle created by the image of the solar disk and has two limiting factors having a direct affect on the total reflected energy. If mirrors with θ_m = 45 degrees are used, all diffuse sky irradiance is reflected up into nadir viewing imaging system (e.g., $\Omega_i = 2\pi$ sr and $f_{sky} = 1$). If the mirror diameter is small and the R_m approaches a few degrees, the fractional amount of reflected sky irradiance is drastically reduced and Eq. (2.24) approaches zero. Practically, this can be achieved by making mirrors with a small diameter and a large R_m or create small flat mirrors which exclusively reflect the solar disk only. However, this ultimately affects the amount of reflected radiation (i.e., both solar and sky) and pointing accuracy is required for small FOR mirrors. All experiments conducted with the drone-based imaging systems, in this research, used mirrors with large FOR's (see Section 3.1.2, Table 3.1).

All energy reflected off the surface of a convex mirror originating from the solar and sky irradiance can be expressed as

$$I_m(\lambda) = {}^1\!/_4 \rho_m(\lambda) N R_m^2 \left[E_{sun}(\lambda) + f_{sky} E_{sky}(\lambda)\right] \tag{2.25}$$

with the direct solar irradiance, $E_{sun}(\lambda)$, and diffuse sky irradiance, $E_{sky}(\lambda)$, striking the surface of the mirror and includes downwelling atmospheric transmission (i.e., $E_{sun}(\lambda) = \tau_{\downarrow}(\lambda) E_o(\lambda)$ where $E_o(\lambda)$ is the exoatmospheric solar irradiance). Note the differences between $E_{sun}(\lambda)$ for convex mirrors compared to Lambertian surfaces discussed in Section 2.2.2 (i.e., no projected area for convex mirrors). Further rearrangement of Eq. (2.25) is required such that standard measurements in the field can be used to estimate the irradiance parameters (e.g., Global-to-Diffuse ratio discussed in Section 2.2.1). Eq. (2.25) can be rewritten with the Global-to-Diffuse ratio and describes the radiation reflected off the mirrors surface including unique atmospheric properties as

$$I_m(\lambda) = {}^1\!/_4 \rho_m(\lambda) N R_m^2 \left[1 + f_{sky} \frac{G(\lambda)}{1 - G(\lambda)}\right] E_{sun}(\lambda) \tag{2.26}$$

where $G(\lambda)$ is the Global-to-Diffuse ratio mentioned previously. Remote sensing instruments are radiometrically calibrated in laboratory settings from a digital signal to entrance aperture-reaching spectral radiance and should be verified in field experiments using targets of known spectral radiance (i.e., convex mirrors). Propagating a single mirrors radiant intensity source to the imaging system requires an estimate of the upwelling atmospheric transmission, $\tau_{\uparrow}(\lambda)$, imaging system slant range, H, and the sensors IFOV Ω_{IFOV}. Thus, the entrance aperture reaching spectral radiance is

$$L_{EAR}^{mirror}(\lambda) = {}^{1}\!/\!_{4}\rho_m(\lambda)NR_m^2\tau_{\uparrow}(\lambda)\left[1 + f_{sky}\frac{G(\lambda)}{1 - G(\lambda)}\right]\frac{E_{sun}(\lambda)}{\Omega_{IFOV}\,H^2} \tag{2.27}$$

It is often more convenient to express the $\Omega_{IFOV}H^2$ term as a multiplicative form of the cross and along-track ground sample distances, $GSD_x\,GSD_y$, based on the following definition.

$$GSD = \frac{p}{f}H \tag{2.28}$$

Eq. (2.28) defines p as the pixel pitch, f as the effective focal length of the imaging system and the line-of-sight or slant range, H. This greatly simplifies Eq. (2.27) to quantities that are normally known and measurable at the mirror deployment site. Note that when observing a convex mirror, the GSD is not one projected in world coordinates and is simply the GSD normal to the line-of-sight to the mirrors. This difference is unique to convex mirrors since they are a sub-pixel point source having no physical area. This is not the case when imaging Lambertian targets (i.e., extended target having a physical area) where the pixel covers a physical area on the targets surface and viewing off-nadir induces a projected area. Eq. (2.29) the complete entrance aperture-reaching spectral radiance within an IFOV of the imaging system including path radiance, adjacency effects and scattering from surrounding objects expressed in a single term, $L_a(\lambda)$.

$$L_{EAR}^{mirror}(\lambda) = {}^{1}\!/\!_{4}\rho_m(\lambda)NR_m^2\tau_{\uparrow}(\lambda)\left[1 + f_{sky}\frac{G(\lambda)}{1 - G(\lambda)}\right]\frac{E_{sun}(\lambda)}{GSD_x\,GSD_y} + L_a(\lambda) \tag{2.29}$$

For satellite-based imaging, the upwelling atmospheric transmission ($\tau_{\uparrow}(\lambda)$) is required and

MODTRAN can provide the most accurate estimate of this parameter. Further field measurements can aid in the accuracy of MODTRAN's prediction of atmospheric path transmission and include estimates of the aerosol optical depth, altitude dependent pressure and temperature profiles, etc [SSI and AFRL, 2016].

Eq. (2.29) can be reduced to *scalar values* for imaging systems with a known relative spectral response (RSR). The RSR an imaging systems spectral sensitivity that reduces a spectral quantity into a single value (e.g., multispectral imaging). The RSR can also be defined for an HSI system (see Section 2.1.1), but is more complex and time consuming to measure for all the spectral channels. Thus, using the RSR and entrance aperture-reaching spectral radiance, we can compute the band-effective spectral radiance as,

$$L_{eff}(\lambda_c) = \frac{\int_{\lambda_1}^{\lambda_2} RSR(\lambda)\, L_{at-sensor}(\lambda)\, d\lambda}{\int_{\lambda_1}^{\lambda_2} RSR(\lambda)\, d\lambda} \tag{2.30}$$

Note that Eq. 2.30 is defined at an effective wavelength center, λ_c, and is still consisted to be a spectral quantity. A band-effective quantity can be derived from any spectral equation such as the quantities defined in the following section.

The spectral radiance can be estimated by integrating all pixels within a small box around the mirrors signal (Figure 3.5) and ensuring all energy is captured in this process (see Section 3.2 for more details). In addition, the background signal must be estimated and subtracted from all pixels before integrating the mirrors signal. The most accurate estimate of the background signal comes from perimeter pixels exterior to the pixels containing the mirrors signal. It is very important that the background is uniform over this area and the enclosed mirror energy is not in the background estimate. The following equation demonstrates the discrete summation (over N pixels) to estimate the mirrors spectral radiance signal.

$$L_{EAR}^{mirror}(\lambda) = \sum_{n=1}^{N} \left(L_{mirror}(n, \lambda) - \overline{L_{bkg}(\lambda)} \right) \tag{2.31}$$

where $L_{mirror}(n, \lambda)$ is the mirror spectral radiance for N pixels within the summation box and $\overline{L_{bkg}(\lambda)}$ is the averaged background spectral radiance. A unique advantage and consequence is hidden within Eq. (2.31). When mirrors are placed on uniform backgrounds, the path radiance contribution (L_p) from the mirror and background are equal. Thus, when the averaged background signal is subtracted from the mirrors signal, the path radiance is negated.

When mirrors are deployed in the field, spectroradiometer measurements inherently measures the total downwelling irradiance ($E_T(\lambda)$) and the Global-to-Diffuse Ratio ($G(\lambda)$). Eq. (2.26) can be rearranged to utilize the primary measurements performed in the field. The modified version of the mirror's radiant intensity (Eq. (2.32)) now provides the most direct way to predict the mirror's signal in the field from spectroradiometer measurements.

$$I_m(\lambda) = {}^1\!/\!_4\rho_m(\lambda)NR_m^2\left[1 - G(\lambda)\cos(2\theta_m)\right]E_T(\lambda) \tag{2.32}$$

The term $E_T(\lambda)$ defined the total downwelling irradiance (Eq. (2.2)) and the $2\theta_m$ defines the angle formed by the virtual image of the solar disk. The mirror's spectral radiance can be calculated in the same way as Eq. (2.27). For drone-based applications, the atmosphere transmission to the sensor is negligible [Mamaghani et al., 2018] and the path radiance is negated through background subtraction. Thus, Eq. (2.33) is optimal for drone-based imaging experiments when the total downwelling irradiance is measured by a spectroradiometer with a cosine-corrector. The entrance aperture reach spectral radiance for drone-based experiment can be defined as,

$$L_{EAR}^{mirror}(\lambda) = {}^1\!/\!_4\rho_m(\lambda)NR_m^2\left[1 - G(\lambda)\cos(2\theta_m)\right]\frac{E_T(\lambda)}{GSD_x\,GSD_y} \tag{2.33}$$

where $E_T(\lambda)$ defined the total downwelling irradiance (Eq. (2.2)) and the $2\theta_m$ defines the angle formed by the virtual image of the solar disk. Note that when $\theta_m = 45$, the mirror reflects the entire visual hemisphere up to the sensor. This means the sky irradiance, modelled by $G(\lambda)$, is contained within the measured total downwelling irradiance. However, the solid angle alignment between the cosine corrector on the spectroradiometer and mirror becomes more important [Jeff Holt et al., 2021].

2.3.3 Equivalent Lambertian Reflectance Factor

As previously mentioned, the convex mirror(s) are inherently described as a radiant intensity source. Convex mirrors provide an absolute radiometric signal, which can be expressed as an Equivalent Lambertian Reflectance Factor (ELRF), $\rho^{mirror}_{FRF}(\lambda)$ [Stephen J. Schiller, 2019]. Convex mirrors have a unique reflectance spectrum comparable to an ideal Lambertian surface when both direct (solar) and indirect (atmosphere) illumination sources are accounted for in the reflected spectrum. The derivation can be easily evaluated by equating Eq. (2.7) to Eq. (2.29) and solving for the Lambertian reflectance component ($\rho^{mirror}_{FRF}(\lambda)$). The convex mirror surface reflectance can now be described as a signal originating from a flat diffuse surface as,

$$\rho^{mirror}_{FRF}(\lambda) = \left[\frac{1}{cos(\theta_{sun})} + \left(f - \frac{1}{cos(\theta_{sun})}\right) G(\lambda)\right] \frac{\pi N R_m^2}{4\, GSD_x\, GSD_y} \rho_m(\lambda) \tag{2.34}$$

An important result that greatly affects, $\rho^{mirror}_{FRF}(\lambda)$, is the foreshortening affect of flat, Lambertian surfaces. The foreshortening affect is a result of Lambert's cosine law and describes the cosine dependence on reflected light from a Lambertian target illuminated by an irradiance source (i.e., solar radiation). Since this property is only related to Lambertian targets, convex mirrors do not have this affect and when deriving the ELRF for a convex mirror, it shows up in the denominator. This leads to an interesting and sometimes confusing property of the ELRF, mirrors reflecting more light at low solar angles when compared to a high solar angle. However, this is not the case and the real reason is because of the foreshortening affect of Lambertian targets (i.e., inverse projected area). In reality, the mirror signal is staying constant whereas the Lambertian target is dimming at low solar angles when compared to higher solar angles. In other words, the ELRF has a inverse dependency on the solar zenith angle because the reflected energy of a Lambertian target changes as a function of solar zenith angle [S. J. Schiller, 2012; Stephen J. Schiller, 2019; Stephen J. Schiller and Silny, 2010].

2.3.4 Mirror-based Empirical Line Method

The use of convex mirrors as field calibration targets has multiple path ways for extracting the radiometric performance of an imaging system. The closed-formed equations describe the mirrors as either a spectral radiance or a reflectance source. As a spectral radiance source, an imaging systems digital signal (in DN) can be calibrated to entrance aperture-reaching spectral radiance (Eq. (2.29)) or the imaging systems radiometric calibration can be field tested for accuracy. As a reflectance source, the imaging system can be calibrated from the digital signal or spectral radiance to surface reflectance using Eq. (2.34) where a linear fit is extracted and applied to all scene pixels. For the following discussion, spectral radiance will be the observed quantity from the HSI system to be converted to surface reflectance. It is should be noted that digital signals may contain non-linear behavior or other sensor dependent artifacts and care must be taken when uncorrected digital signals are used for calibrating imaging systems. All derivations stem from S. J. Schiller, 2012, Stephen J. Schiller and Silny, 2010 and Stephen J. Schiller, 2019. The mirror-based ELM or MELM can be expressed as,

$$\rho_{FRF}^{mirror}(\lambda) = m(\lambda) L_{EAR}^{mirror}(\lambda) + b(\lambda) \tag{2.35}$$

It has two components to discuss: estimating the differential reflectance relationship (i.e., $m(\lambda)$) and obtaining an absolute reflectance transformation for the entire scene. Estimating the differential reflectance relationship requires isolating at least two different mirror signals (i.e., a low and high radiometric signal) from the imagery. Isolating the mirrors enclosed energy rids all measurements from the added background signal (assuming background spatial uniformity) and simplifies Eq. (2.35) such that the differential reflectance relationship only remains. The simplified equations is seen as,

$$\rho_{FRF}^{mirror}(\lambda) = m(\lambda) L_{EAR}^{mirror}(\lambda) \tag{2.36}$$

Note that this expression is only used to generate the slope coefficient and does not provide the absolute scene transformation from spectral radiance to reflectance. Extracting the slope, $m(\lambda)$, from HSI imagery can be achieved by applying a linear fit with zero intercept between the observed spectral radiance and predicted mirror reflectance. As mentioned before, the mirrors signal sits on top of the background such that if no mirror signal is observed the only signal arriving at the aperture is from the background material.

Each mirror signal has a corresponding spectral radiance (Eq. (2.31)) and reflectance (Eq. (2.34)) to build the linear relationship stated in Eq. (2.36). When the differential reflectance relationship is known, a scene transformation equation, $\rho_{FRF}^{scene}(\lambda)$, can be derived for pixel-to-pixel conversion of spectral radiance to reflectance. That is,

$$\rho_{FRF}^{scene}(\lambda) = m(\lambda)\left(L_{scene}(\lambda) - \overline{L_{bkg}(\lambda)}\right) + \rho_{bkg}(\lambda) \tag{2.37}$$

where $m(\lambda)$ is the differential reflectance relationship in Eq. (2.36), $L_{scene}(\lambda)$ is the observed spectral radiance of all pixels in the HSI imagery, $\overline{L_{bkg}(\lambda)}$ is the average background spectral radiance that was used in Eq. (2.31), and $\rho_{bkg}(\lambda)$ is the measured field reflectance factor of the background where mirrors were deployed on.

There are a few subtle details that manifest from Eq. (2.37) that require further discussion. First off, Eq. (2.37) atmospherically corrects all scene pixels to an absolute field reflectance factor by adding back in the in-situ background reflectance. Verification of the scene transformation (i.e., $\rho_{FRF}^{scene}(\lambda)$) can be assessed by selecting pixels within the background and comparing these values to $\rho_{bkg}(\lambda)$. Because the background spectral radiance is subtracted from all scene pixels, Eq. (2.37) reduces to the $\rho_{bkg}(\lambda)$. Instrument noise and background non-uniformity can violate this condition, but an estimate of this error can be assessed using the verification process.

Chapter 3

Methodology

3.1 Experimental Planning

To fully assess the new use of convex mirrors for field calibration and characterization of drone-based imaging systems, various field experiments were conducted to build knowledge on this new technique. In this section, practical considerations, preflight planning and data processing will highlight how convex mirrors are used during field experiments and the processing required to test the radiometric and spatial properties of imaging systems in response to point targets. Practical considerations highlight the lessons learned during field deployments of convex mirrors and various impacts from perceived mirror signal and background choices.

Table 3.1 displays the three different mirror configurations used for all drone experiments conducted for this thesis. The mirror configurations list in Table 3.1 were off-the-shelf convex mirrors from Edmund Optics. Labsphere Inc. validated the radius of curvature and measured the mirror's reflectance (i.e., $\rho_m(\lambda)$). The mirrors can be arranged into mirror arrays, as seen in Figure 3.1, to stimulate the imaging system with varying signal levels. This can be achieved by adding similar mirrors into groups for a linear increase in signal or single mirrors, with different radius of curvatures, can be arranged to achieve a quadratic increase in signal (refer to Eq. (2.29) or (2.34)).

3.1.1 Practical Considerations

Investigating how an imaging system responded to a point target (i.e., convex mirror) required a lot of trail and error because multispectral and hyperspectral systems have different spectral

TABLE 3.1: Mirror configurations used in all field experiments. Various geometrical parameters highlighting the differing properties.

R_m	D_m	FOR	d_{sun}
25 mm	22.9 mm	108.8°	0.11 mm
50 mm	22.9 mm	52.9°	0.22 mm
100 mm	45.7 mm	52.9°	0.44 mm

and spatial responses. Various experimental testing was completed to understand the relationship between perceived and predicted signals of point targets. Since point targets provide both a radiometric and spatial source to an imaging system, the spatial response has a direct impact on the perceived mirror signal. In addition, the background material where the mirrors are deployed can disrupt the radiometric and spatial response of an imaging system to a point target. For drone-based imaging, there were many advantages and disadvantages discovered in this initial phase of testing which lead to specific choices for future experiments.

The first lesson learned when using convex mirrors as a calibration source is that the background, as seen in Figure 3.1, has a large impact on the SPSF structure and perceived mirror signal. As previously discussed in Section 2.3.4, the total energy arriving to the sensor from a point target is spread over the SPSF where the contrast between background/mirror and sensor noise defines the measurable SPSF structure (i.e., where the background dominates the overall signal). Because background photon noise can impact the measurability of the SPSF structure, very dark materials were used to reduce background photon noise. However, sensor noise will ultimately limit the measurability of the SPSF wings even with the darkest materials. Background non-uniformity drastically impacts the overall measurability of the SPSF structure because the background signal is an additive factor to the overall perceived signal. Since drone imaging is usually on the scale of a few centimeters, background uniformity is minimal at this scale compared to satellite imagery with GSD's on the order of meters.

The mirror's perceived signal can be affected by three major variables: background reflectance, the sub-pixel location of the point source on the sensor (i.e., sample phasing) and the SPSF sharpness. As discussed in the previous paragraph, the overall perceived signal stems from the mirror and background signal. Even though the mirror's signal alone will not cause

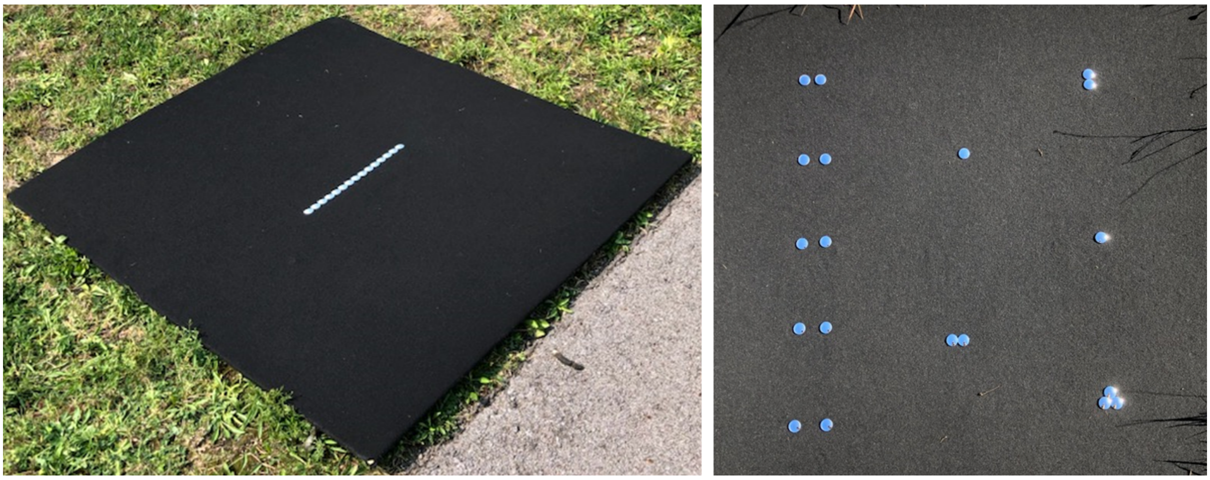

FIGURE 3.1: Experimental images of various mirror arrays and black felt background. (Left) Convex mirrors arranged in a line creating an ideal line source. (Right) Various mirror arrays configurations for different signal levels.

saturation, mirror and background signal can. Although the enclosed mirror energy is conserved, the sample phasing and SPSF size can impact the amount of energy deposited into a single pixel. The sample phasing, as seen in Figure 3.2, impacts how much energy is spread to surrounding pixels where the majority of the energy is contained in one pixel (i.e., lands exactly centered) or shared between four pixels (i.e., lands a corner). Peak pixel value between Figures 3.2a and 3.2b is roughly 2.6x where target/background contrast can also be observed in Figure 3.2 because of energy sharing.

Initial experiments demonstrated this fact when the sensor saturated when the point target landed exactly in the center of the pixel compared to landing at the corner. This situation can be minimized by predicting the mirror's ELRF and understanding when saturation occurs with Lambertian panels. The SPSF sharpness also impacts the perceived signal from a mirror because this defines how much energy is spread to surrounding pixels (i.e., energy density). If the SPSF is well-behaved, signal predictability can be quickly understood, but if the SPSF is very blurry, sample phasing may not exist and the mirror's signal can easily be lost in the background. Understanding the relationship between recorded mirror signal and SPSF has very important practical applications because it can easily define problems within the optical system such as defocus or misaligned optics during field operations.

An interesting radiometric property that requires further discussion is the foreshortening

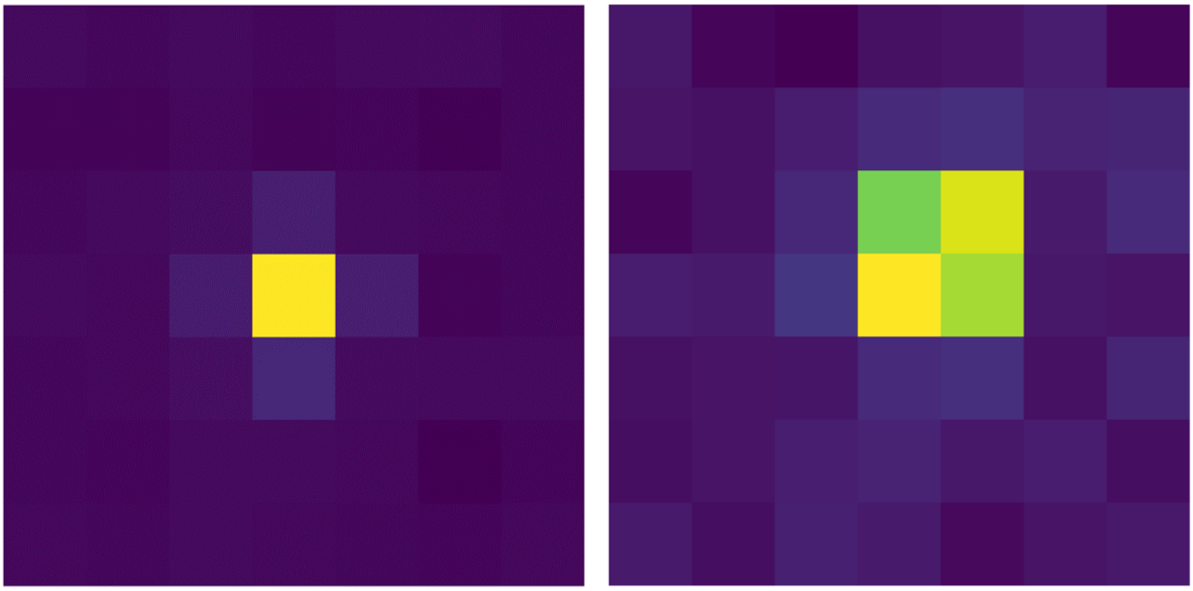

(A) Center

(B) Corner

FIGURE 3.2: Sample phasing example from a field experiment conducted by the author. (A) Point target landing in the center where majority of energy is in the central pixel. (B) Point target landing in the top right of the central pixel where energy is shared between the four surrounding pixels.

effect seen in Eq. (2.34) and is a direct consequence of equating at-senor radiance from a point target to a Lambertian surface. This means that $\rho_{FRF}^{mirror}(\lambda)$ has an inverse cosine dependence on solar zenith angle and results in $\rho_{FRF}^{mirror}(\lambda)$ being significantly brighter at high solar zenith angles compared to nadir angles. In fact, the mirror's brightness never changes with zenith angle, but it's the Lambertian surface dimming at higher solar zenith angles causing the illusion that the mirror is changing in brightness. This has to be accounted for when deploying mirrors since the inverse cosine dependence drastically increases the perceived mirror signal at high zenith angles.

Because most drone-based imaging is nadir, pointing accuracy is static when mirrors with a large FOR are used (see Table 3.1). Accurate pointing accuracy and object tracking are required to ensure the solar radiation reaches the sensor when the mirror has a very narrow FOR (e.g., FOR < 5 degrees). For all drone experiments, the mirrors were placed on large, black felt covered plywood and only required slight elevation angle changes in the event the solar zenith angle changed significantly. The pointing process can be simplified if the background faces the sun and the only component to tune is the background elevation angle. A more detailed discussion on mirror pointing can be found in Section 3.1.2.

3.1.2 Preflight Planning

Deploying convex mirrors requires preflight planning to ensure the reflectance is adequate such that mirror signals will not saturate the sensor. Spatial characterization requires the least amount of planning because the absolute radiometry is not required and estimates of the ELRF are sufficient. Predicting mirror ELRF can be easily tied back to laboratory calibration or previous field experiments conducted with Lambertian panels.

Other considerations in preflight planning include SPSF sharpness since this directly impacts the energy density recorded by each pixel. For well-behaved SPSF's, ELRF predictions (Eq. (2.34)) should be reduced by 70% this will ensure the brightest perceived mirror signal will not saturate. Based on the limited selection of mirrors (see Table 3.1), priority should be to span the appropriate reflectance range without saturation and tune the GSD to achieve this.

Predicting the ELRF for various mirror configurations with an optimized GSD is the first step when planning to deploy mirrors for a field experiment. Figure 3.3 shows an example of a preflight ELRF prediction for a GSD of 6.5 cm using a previously measured Global-to-Diffuse ratio. Additionally, one can derive a Global-to-Diffuse ratio using MODTRAN, as previously stated in Section 2.2.1. As discussed in Section 2.2.1, the Global-to-Diffuse ratio is unique to the time of experiment, but for preflight planning, a typical understanding is all that is needed for this step.

After predicting the ELRF, pointing angle estimates are required to ensure mirror signals will reach the imaging system. Mirror pointing for nadir viewing instruments will only be discussed since most drone-based imaging is performed using this configuration. Based on the law of reflection and the mirror's FOR, mirror background pointing angles can be evaluated for various solar zenith angles over the duration of the experiment. The most important estimate is the mirror background elevation angle (i.e., black felt covered plywood). The following equation, ϕ, defines an upper bound such that a nadir viewing instrument can observe the

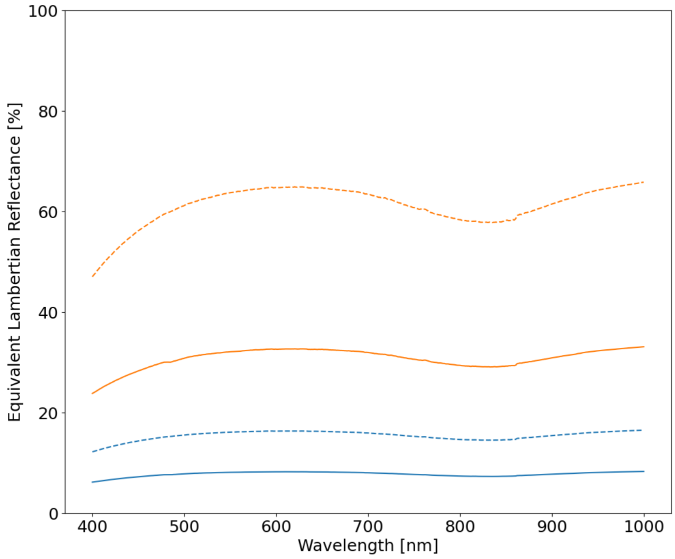

FIGURE 3.3: An example of 4 different ELRF's predictions. Single mirrors are represented by solid curves whereas two mirror arrays are represented by dotted curves. The blue curves are mirrors with R_m = 25 mm and the orange curves are mirrors with R_m = 50 mm.

reflected solar image from a convex mirror with a specific FOR. That is,

$$\phi = \theta_{sun} - \theta_{el} - 1/2FOR \tag{3.1}$$

where θ_{el} is the background elevation angle towards the sun and θ_{sun} is the solar zenith angle. A nadir viewing imaging system can only observe the solar image when the following criteria is met, $\phi \leq 0$. Solving Eq. (3.1) for θ_{el} when $\phi = 0$ provides the lower limit on the backgrounds elevation angle (θ_{el}) such that a nadir viewing imaging system can observe the reflected solar image. That is,

$$\theta_{el} = \theta_{sun} - 1/2FOR \tag{3.2}$$

Eq. (3.2) defines the needed background elevation angle for a nadir viewing instrument. If $\theta_{el} \leq 0$, the background can remain flat on the ground and the reflected light can be observed from a nadir viewing instrument. Figure 3.4 shows examples of Eq. (3.2) implemented for two mirror configurations with a fixed solar zenith angle. Mirror's with a large FOR (Figure 3.4a) usually results in background elevation angles of zero and thus requiring no pointing for nadir viewing instruments. Whereas Figure 3.4b requires pointing due to the reduction in the FOR for this scenario. The azimuth alignment is of lesser importance because the background can be pointed into the direction of the sun or slightly to the west when accounting for the solar trajectory over the experiment duration. Field alignment can be verified by visually observing the mirrors from a nadir viewing position without looking directly at the solar disk.

3.2 Data Analysis and Computational Techniques

Data assessment diverges into two pathways depending on mirror deployment (single or multiple mirror arrays) and if the analysis is radiometric or spatially driven. Radiometric analysis relies on enclosed energy and background estimates whereas a spatial analysis requires a defined model and fitting routines. Depending on the required spatial assessment (i.e., rough or accurate estimates), the spatial analysis can be further split into two categories: single- or multi-point estimates. A spatial response estimate using a single-point uses a 2D Gaussian distribution to assess the centroid and FWHM of a single SPSF whereas the multi-point analysis uses a similar 2D Gaussian distribution to assemble multiple SPSF responses into a common reference frame to achieve oversampling. A multi-point analysis provides the best estimate of the SPSF's shape because any loss of information due to aliasing is recovered in the oversampling process. In this thesis, an oversampled SPSF will be limited to multispectral imaging systems whereas HSI systems will be restricted to single-point analysis.

3.2.1 Point Target - Radiometric Analysis

Extracting the digital signal from an image with a point target for radiometric assessment is a straight forward process when a uniform, dark background is used. In all experiments, the mirrors were deployed far enough away such that the SPSF signal could be isolated from the background. Figure 3.5 demonstrates actual pixels from an image used to estimate the signal and background. The mirror's signal (shaded in red) is isolated by defining a bounding box

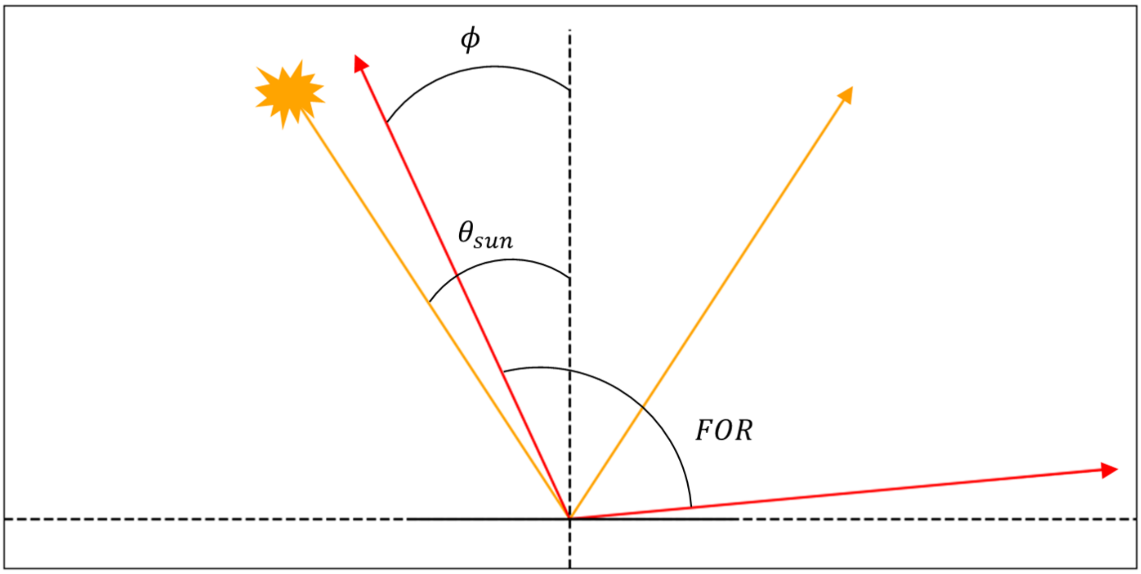

ϕ
θ_{sun}
FOR

(A) R_m = 25 mm

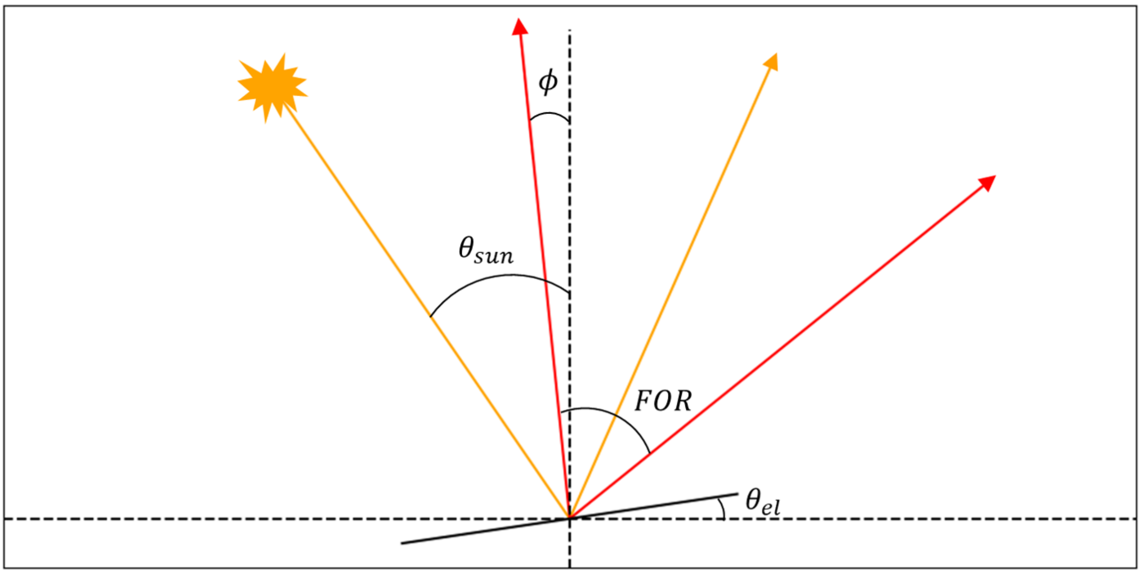

ϕ
θ_{sun}
FOR
θ_{el}

(B) R_m = 50 mm

FIGURE 3.4: Two preflight alignment graphs demonstrate the elevation angle needed for nadir viewing instruments. Mirrors of the same diameter but different radius of curvature demonstrate how the FOR impacts elevation angle has for similar solar zenith angles.

around the SPSF peak and should contain all enclosed energy. A one pixel annulus (shaded in green) around the SPSF is used to estimate the average background signal.

The size of the annulus is chosen by the sharpness of the SPSF, but it should be noted that instrument noise and/or background photon noise can corrupt SPSF tails and energy loss is inevitable. The mirror signal can then be isolated by subtracting the average background value from every pixel shaded in red. The enclosed energy is estimated by summing all pixels shaded red and represents only the mirror's signal that's tied back to the physical quantities described in Sections 2.3.2 and 2.3.3. This method allows for a quick and easy assessment of the radiometric response from a sub-pixel calibration target without assuming any SPSF shape as long as the background material is uniform and consistent across the red and green shaded pixels in Figure 3.5.

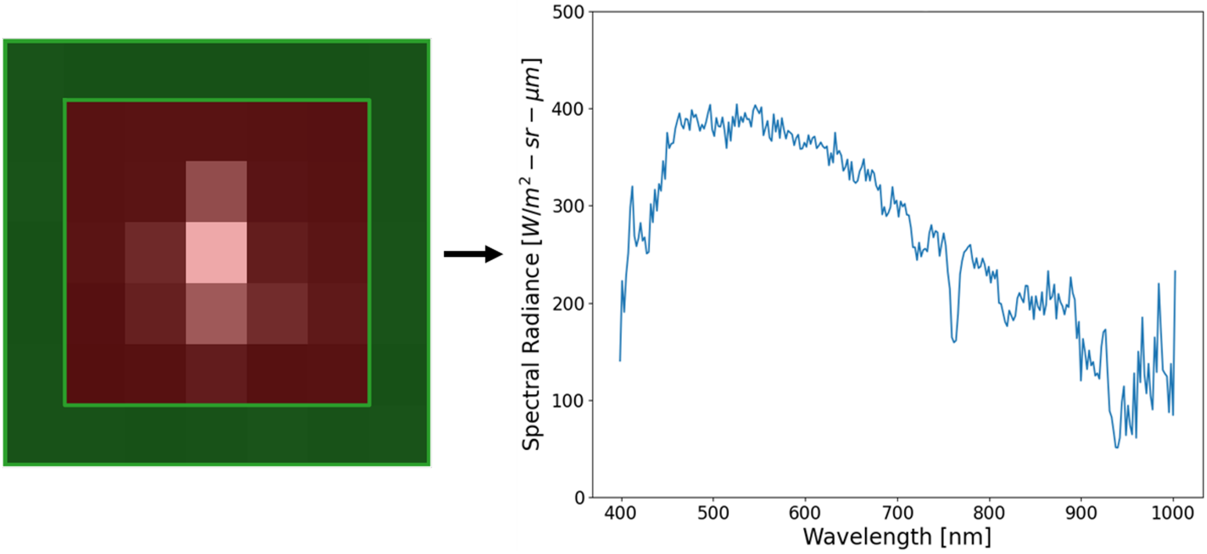

FIGURE 3.5: The image on the left is a visualization of the pixels used to estimate the background signal (shaded green) and the isolated SPSF signal (shaded red). The graph on the right is the result of background subtraction and pixel summing. This is used to estimate the point target siganl.

After extracting the mirror's signal from the imagery (Eq. (2.31)), the steps for field calibration is similar to ELM using Lambertian panels. Assuming the mirror's signal is extracted as a spectral radiance, Eq. (2.34) can be used to calibrate the data to a field reflectance factor (see Figure 3.3) with field measurements defined in Section 2.2.1. As discussed in Section 2.2.2, a minimum of at least two mirror signals, a bright and dark point, are required to form the linear relationship between spectral radiance and a field reflectance factor. An important deviation from the ELM is the measurement of the mirror's background reflectance such that imagery can be calibrated to absolute reflectances (see Section 2.3.4). Accurate measurements of the mirror's background reflectance is critical because this is an additive factor where BRDF can become significant especially when the background is a natural target like vegetation.

3.2.2 Point Target - Spatial Analysis

Extracting spatial information from a point target is separated into two categories: a single-point analysis where only one SPSF is assessed and multi-point analysis where multiple SPSF's are assembled into a common reference frame such that oversampling is achieved. This section highlights important computational techniques, developed in *python* by the author, used in both analyses.

Single-Point Analysis

Single-point analysis is a simple and fast technique for a rough estimates of spatial performance of imaging systems. The main assumption here is that the SPSF has a similar shape to a 2D Gaussian distribution where a first order approximation to the spatial performance can be evaluated. The simplicity of the single-point analysis has the benefit of extracting parameters used to estimate spatial parameters in scenarios where a multi-point analysis is too complex or not feasible. This can include fixed mounted HSI systems where ortho-rectification changes the SPSF consistently or as a diagnostic tool for determining problem areas across the FOV. Such observations across a sensors FOV were published, by the author, in 2022 [David Conran and Ientilucci, 2022] and included in Appendix A.

Figure 3.6 demonstrates a single wavelength example of the single-point analysis from data used in Appendix A and B. Figure 3.6a is an isolated HS image of the point target at 550 nm. Figure 3.6b is a 3D plot of the optimized Gaussian surface fit to the SPSF data points using the technique developed in this thesis.

Single-point analysis uses scipy.optimize.curve_fit, a *python* function, to perform a non-linear curve fitting routine between a 2D Gaussian distribution and the SPSF data. The 2D

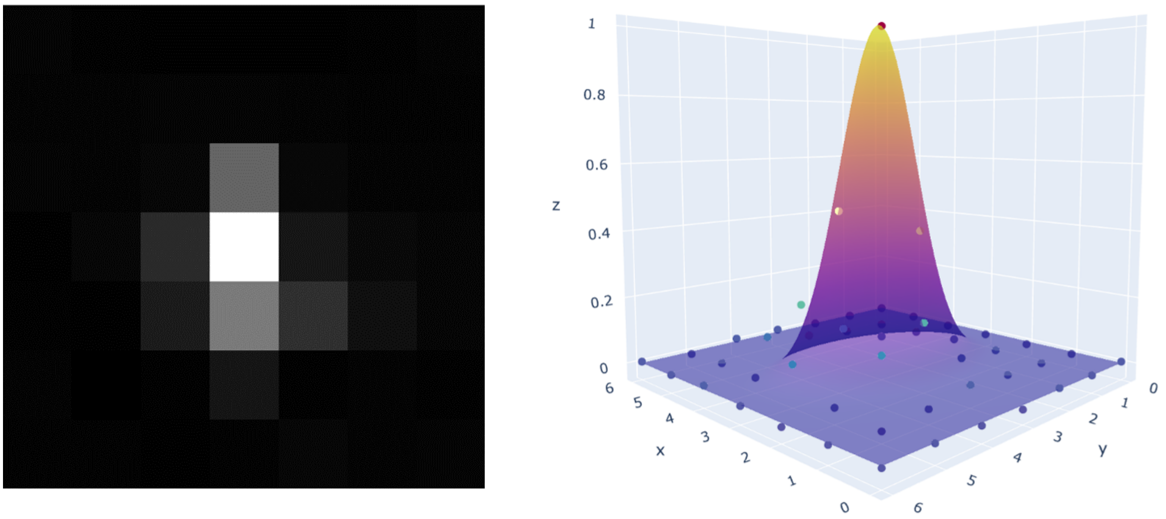

(A)

(B)

FIGURE 3.6: An example of single-point analysis performed on an HS image at wavelength 550nm. (A) An isolated SPSF containing 7x7 pixels. (B) The resulting 2D Gaussian fit when optimized to the SPSF.

Gaussian distribution has six degrees of freedom and includes the following: baseline, amplitude, an x and y centroid and FWHM. To extract a realistic solution between the Gaussian distribution and data, bounds are defined for all six degrees of freedom to restrict over-fitting. The degrees of freedom that require more intelligent bounds are the x and y centroid and FWHM. Under the assumption that the SPSF is well-behaved and contains only a single peak, the x and y centroid solution can be restricted to a single pixel around the largest pixel value.

The bounds defined for the x and y FWHM have more of a physical interpretation that can be easily explained through Fourier logic. For example, if an imaging system has a very sharp optical PSF that is smaller than the sensor pixel (i.e., a rectangular pixel), the limiting blur factor is the rectangular pixel and the FWHM will have a minimum of one pixel. Thus, in the curve fitting routine the minimum FWHM solution will be bounded to one pixel. There is only one caveat for the FWHM bounds and that is tied back to the errors associated with HS ortho-rectification. For fixed mounted HSI systems, ortho-rectification errors can reconstruct inaccurate representations of the SPSF which is demonstrated in our up-and-coming publication included in Appendix B. Here, the FWHM bound should be slightly lower than one pixel to account for this (i.e., x and y FWHM > 0.8 pixel).

Multi-Point Analysis

Multi-point analysis takes advantage of multiple observations of undersampled data to recover lost information from spatial aliasing. Recovering the aliased information can be easily achieved by having multiple observations of the SPSF with random sample phasing (Figure 3.7a) where they are assembled into a common reference frame by estimating sub-pixel centroids. Figure 3.7a, collected by the author in a field experiment, show that the SPSF is sampled at different positions and collectively contain more information than just one SPSF. As long as the phasing (i.e., the point target landing in different position within a pixel) is randomized in all directions, a more complex optimization routine, than the single-point analysis, is required to assemble all SPSF's into a common reference frame (Figure 3.7b).

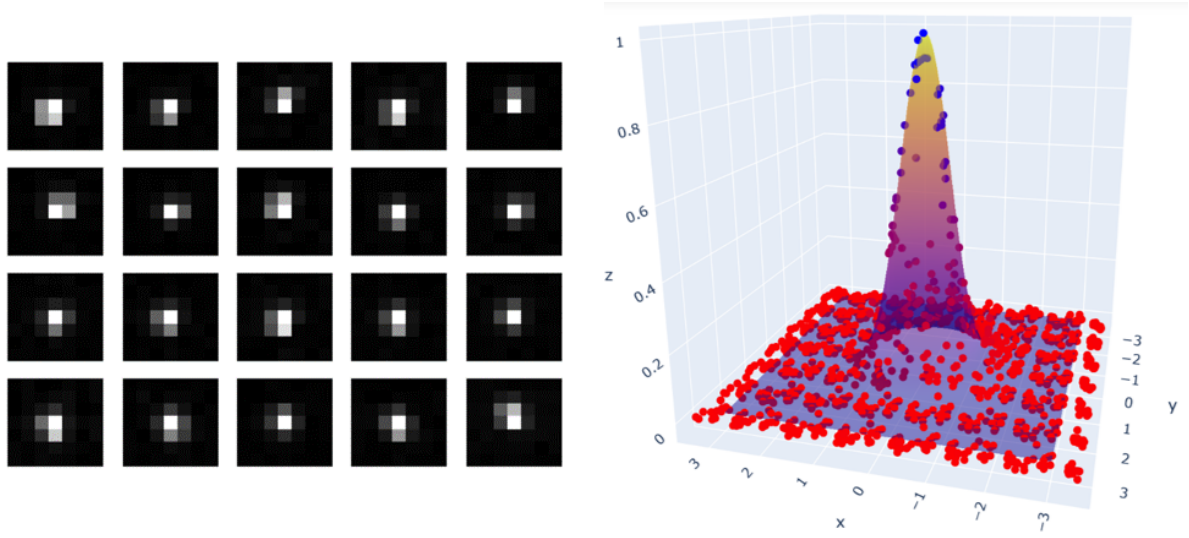

(A) (B)

FIGURE 3.7: A multi-point analysis example performed on a MS image. (A) 20 individual SPSF's with varying sample phasing. (B) The optimized SPSF using the oversampling technique defined by Stephen J. Schiller and Silny, 2010.

An oversampling technique used to derive a more accurate SPSF originated from research done by Stephen J. Schiller and Silny, 2010 at Raytheon Technologies and implemented in *MATLAB*. Because of Raytheon IP control, the oversampling technique was not available and was recreated, by the author, in *python* for Labsphere Inc. and used in this thesis. Figure

3.8 is a graphic that illustrates the double-loop optimization routine used for deriving a more accurate SPSF (Figure 3.7b) from a collection of N cropped SPSF's (Figure 3.7a). The double-loop algorithm has two branches that work together to derive a single solution to the x and y FWHM that minimizes the sum of the RMSE's. The single x and y FWHM solution can be used to estimate the spatial performance and the oversampled data can be directly transformed into a 2D MTF after 1/4 pixel binning (see Section 4.1). In order to reduce the degrees of freedom in the double-loop algorithm, all SPSF's have the baseline subtracted and amplitude normalized by the curve fitting routine stated in the single-point analysis.

The outer loop can only vary the x and y FWHM where as the inner loop varies the x and y centroid for a fixed x and y FWHM set by the outer loop. The inner loop is simply the single-point analysis defined in the previous section, but with only two degrees of freedom, the x and y centroid. When all cropped SPSF's are optimized for a fixed x and y FWHM, the sum of the RMSE's defines the value to be minimized in the outer loop. The outer loop uses scipy.optimize.minimize, a *python* function, for minimizing a multi-variate scalar (i.e., the sum of RMSE's for a specific x and y FWHM). The minimization function finds a solution by using the Quasi-Newton method to find a local minima and achieves this through approximations to the Jacobian matrix. The solution of the double-loop algorithm then defines a single x and y FWHM that fits all SPSF data and recovers lost information from spatial aliasing.

A major disadvantage with the minimization routine is its inability to distinguish between local and global minima when finding a solution. Providing an accurate and logical initial guess to the solution is one way of avoiding local minima; however, only one solution for this problem will be found because of the assumption that all aliased SPSF's originate from the shape. More importantly, the bounds placed on the directional FWHM (i.e., x and y FWHM > 0.8 pixel) will restrict further over-fitting.

Because point targets are readily available in Astronomy (i.e., stars), estimating an accurate SPSF in telescopes has been studied since 1987 with the computer program, DAOPHOT [Stetson, 1987]. The computer program uses thousands of stars to oversample the SPSF such that accurate stellar photometry can be achieved in crowded stellar fields were multiple stars can overlap. Further improvements have been developed over the years by Anderson and King,

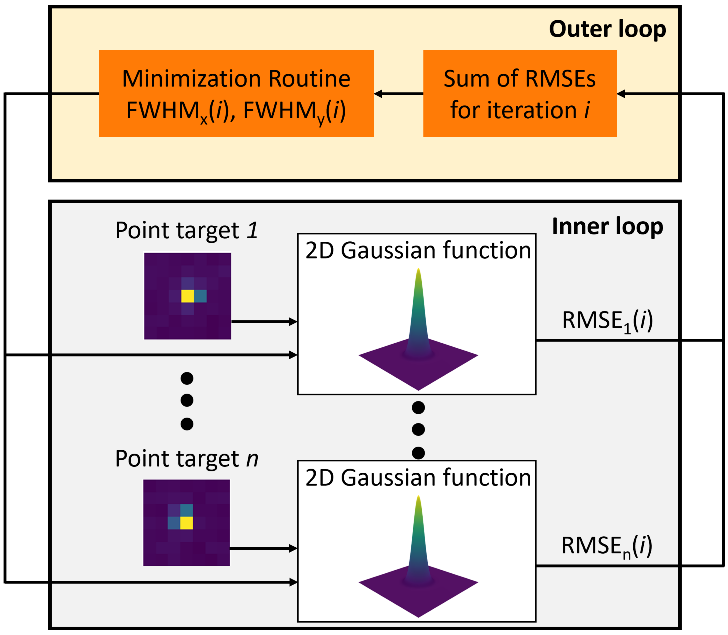
Outer loop
Minimization Routine
FWHM$_x$(i), FWHM$_y$(i)
Sum of RMSEs
for iteration i
Inner loop
Point target 1
2D Gaussian function
RMSE$_1$(i)
Point target n
2D Gaussian function
RMSE$_n$(i)

FIGURE 3.8: Stephen J. Schiller and Silny, 2010 defined a double loop technique as an oversampling technique for point targets. Inner and outer loops independently optimize the x and y centroids and FWHM respectively.

2000 and is the standard method for deriving an accurate SPSF in Astronomy. Lauer, 1999 proposed a Fourier-based method for deriving an accurate estimate of the SPSF, but requires more accurate sub-pixel maneuverability from the telescope.

All these methods demonstrate the ability to use point targets as a field method for deriving an accurate SPSF, but in the case of Earth observing satellites, thousands of stars can not be imaged without taking time away from remote sensing applications. Faran et al., 2009 has demonstrated the use of celestial bodies in assessing a remote sensing satellites SPSF and the instruments focus, but this requires complex maneuvers to observe space objects. Thus, convex mirrors used for Earth observing satellites is the next best method for extracting the SPSF without complex maneuvers while observing at the same viewing distance as the targets of interest.

Chapter 4

Results

4.1 Spatial Target Comparison Study

This thesis revolves around the use of convex mirrors as an ideal spatial target which can provide results similar to traditional calibration techniques such as using slanted edge targets. Demonstrating comparative results between the two methods for vicarious spatial analysis will not only build confidence in this technique, but will also allow for simplifying assumptions in future experiments when ideal mirror deployment can not be achieved (e.g., using only one mirror to estimate spatial performance). In Section 3.2.2, the computational technique related to the multi-point analysis was discussed and it was noted that this technique is best performed with a multispectral imaging systems because 2D spatial information is captured instantly unlike HSI systems. For all experiments conducted here, all imagery was flat-field corrected to reduce the fixed-pattern noise (defined in Section 2.1.2) over the edge target which will reduce noise within the construction of the SLSF.

This experiment was conducted at the Tait Preserve in Rochester, New York where a multispectral imaging system observed both point and edge targets in close proximity to each other. Figure 4.1a shows an overview image of the field experiment where the results were only analyzed based on the green channel (i.e., wavelength center of 560 nm). The drone altitude was set to acquire imagery at a GSD of 4 cm where the integration time was tuned such that the edge target and the mirrors had adequate SNR. More importantly, the 4 cm GSD was selected with the intention that the bright side of the edge target and peak value off the mirrors had comparative signal levels. The dark side of the edge target and the mirror background were similar in brightness as well (i.e., both were black felt).

A secondary experiment was conducted in the lab using a collimating system (i.e., Electro Optical Industries (EOI) Laboratory Collimator) which included a small integrating sphere with a QTH lamp and a slanted knife edge target (Figure 4.1b). The purpose was to compare lab results to the field experiments. Since the lab experiment uses a subtractive method to form an ideal edge target (i.e., the edge blocks light on one side) and collimating system projects the edge to infinity, slight differences in the spatial performance may exist. The collimating system has its own spatial imperfections (i.e., aberrations, edge roughness, edge focus, etc.) and may impact the spatial quality extracted in this method. Without high precision measurements of wave-front error, it can be assumed that these effects are negligible. The lab edge target was placed at the center of the FOV and more importantly, replicated the edge placement experienced in the field experiment. This analysis provides further validation between field and lab experiments using edge targets. Again, integration time in the lab experiment was tuned with the aim that the bright side of the edge target was above 50% saturation in the green channel.

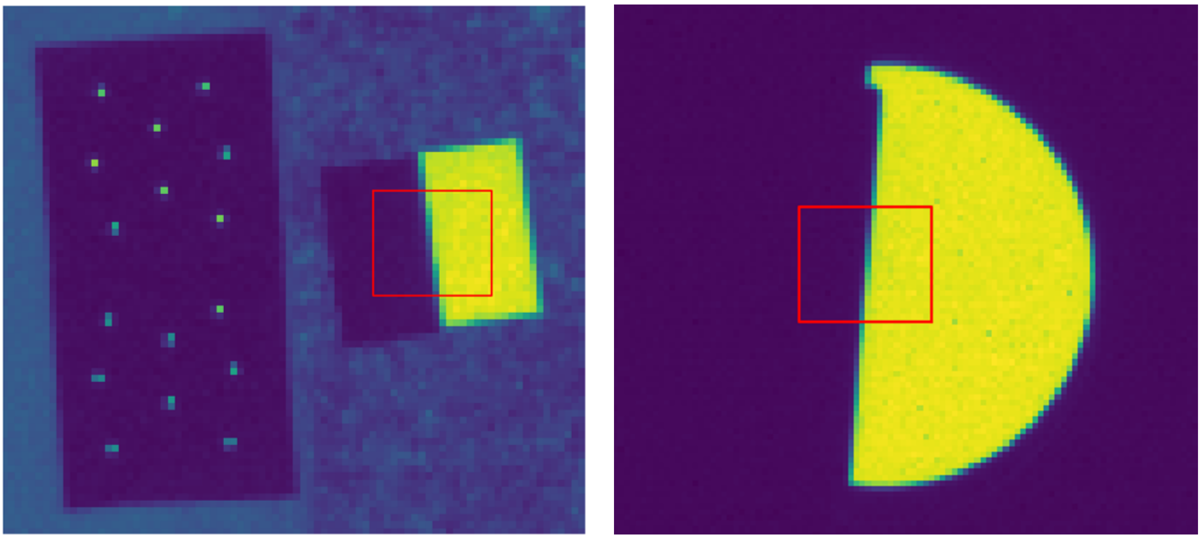
(A) (B)

FIGURE 4.1: Images used for the analyses between edge and point targets based on the green channel where the red boxe indicates edge extraction. (A) Field experiment with the edge target placed besides 16 point targets for comparison. (B) Laboratory experiment, using a collimator system, showing the edge target for comparison to field measurements.

The results from this study can be seen in Figure 4.2. In Figure 4.2a, the spatial cross-track SLSF and SPSF can be observed. The black dots correspond to the SPSF data points binned to 1/4 pixel sampling and the blue line corresponds to the 1D Gaussian fit from the multi-point analysis described in Section 3.2.2. Due to the 1/4 pixel binning and the gaps in the non-uniform sampling, the measured SPSF (i.e, black data points) are slightly lower than the rest and is merely a processing error. The Gaussian fit and measured SPSF data are in good agreement based on the 1.81% RSME with a FWHM of approximately 1.10 pixels. The SPSF and Gaussian fit are slight wider than the SLSF's, but the measured SPSF is far less noisy and with the base falling to zero faster than the SLSF's.

The orange squares are related to the result of evaluating the edge target in Figure 4.1a where the green line is from evaluating the lab-based edge target. The edge targets were evaluated in a similar manner discussed in Section 2.2.3 and the overall extent of the red boxes were matched. A comparative discussion is not adequate in this domain because the SLSF measured from an edge is not directly related to the SPSF measured from the mirrors. This was discussed in Section 2.2.3 where the SLSF is the one-sided integral of the SPSF, but similar size and structure is easily observed in Figure 4.2a. The SLSF's both have slight narrower peaks that begin to flare out towards the base and both experience more noise on the right side that corresponds to the brighter side of the edge target.

The true comparison of this study can be observed by transforming all curves into their corresponding MTF. In the frequency domain, the comparison between using an edge and point target is valid based on the discussion from Section 2.2.3 and Figure 2.13. Here, the 1D MTF extracted from the SLSF is a sliced version of the 2D MTF created from the SPSF. Figure 4.2b presents all the methods in the Fourier space where the black dotted line indicates the Nyquist sampling frequency (i.e., 0.5 1/pixels). The value at Nyquist can be used as a comparative metric for evaluating the similarity between all the methods used for extracting the spatial performance of the imaging system. Since all imagers can not observe greater than Nyquist, unless oversampling techniques are implemented, this value defines the contrast at which a spatial frequency can be observed without influence from aliasing.

Interesting features can be observed from the MTF plot that warrant further discussion

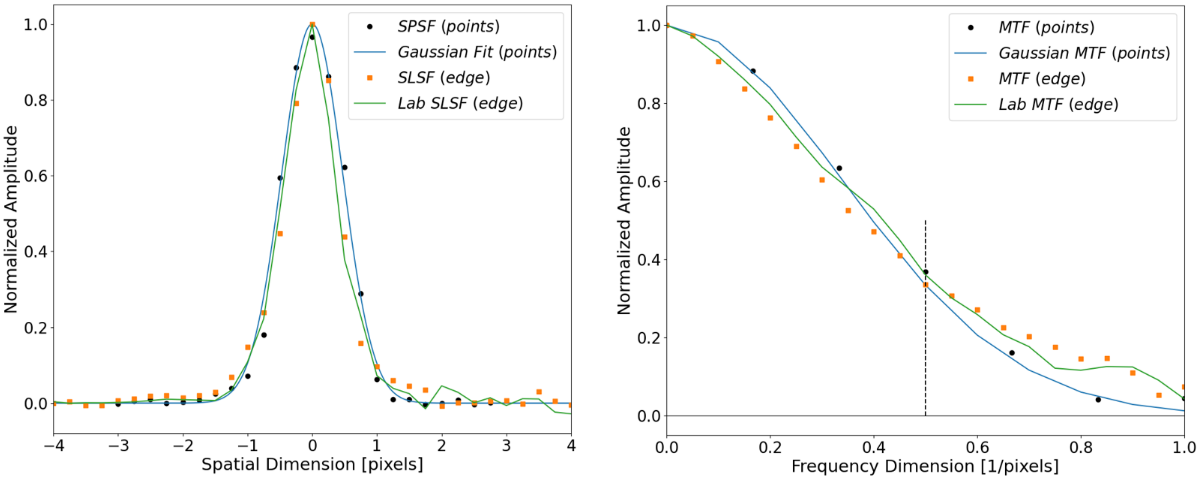

(A)

(B)

FIGURE 4.2: Results when comparing edge vs. point targets. (A) Results represented in the spatial domain where the SPSF and SLSF are not directly comparable. (B) Results defined in the frequency domain where direct comparisons can be made based on the MTF relationship between the SLSF and SPSF.

on their causes and impacts to the spatial performance. The MTF plot can be broken up into two halves: before and after the Nyquist frequency. Before the Nyquist frequency, both MTF's from the edge targets are lower than the Gaussian MTF and measured SPSF. This feature can be attributed to the larger spread of the SLSF at the base and indicates a mid-frequency degradation in the spatial performance when compared to the mirror-based MTF's. After the Nyquist frequency, the edge derived MTF's show better performance compared to the mirror-based MTF's and can be attributed to SLSF's being more narrow about the peak which enhances spatial performance for higher frequency spatial patterns. Keep in mind that contributions from noise, especially from right side of the SLSF's, can corrupt the MTF results at these higher frequencies. This leads one to conclude that this information is *not as reliable as the mirror-based MTF's.*

In conclusion, this spatial target comparison study has demonstrated that comparative results can be extracted from either an edge or point target for assessing an imaging systems spatial performance. Both lab and field-based experiments were conducted using similar targets to provide confidence in the extraction of edge derived MTF's from an localized region on the focal plane. The deviations in Table 4.1 are comparable to results observed in Viallefont-Robinet et al., 2018 where only the slanted edge method was tested using various algorithms from different satellite companies. Even when the same edge target was analyzed using the different algorithms, MTF results (at Nyquist) had values with standard deviations of 0.01 to 0.04 and max-min values ranging from 0.01 to 0.11. This further demonstrates the success of the comparison study between point and edge targets conducted here where the sample mean was 0.35, sample standard deviation was 0.018 and the max-min value of 0.034.

TABLE 4.1: Final results from the spatial comparison study between edge and point targets.

Method	*MTF @ Nyquist*
Points	0.368
Gaussian	0.334
Edge (Field)	0.335
Edge (Lab)	0.361

New insight that came from this study was the similarity between a Gaussian derived profile from point targets and an edge derived SLSF. This is used in Appendix A and B where a multi-point analysis can not be achieved because of the orthorectification errors an HSI system experiences over a small localized region within an image. In these studies, the simplifying assumption that a 2D Gaussian distribution can provide rough estimates of an HSI systems spatial performance, especially for highly aliased systems, is the key insight for the use of convex mirrors over edge targets.

4.2 Appendix A Summary

In Appendix A, a review on the use of convex mirrors as *field calibration targets for drone-based HSI systems.* “Interrogating UAV Image and Data Quality using Convex Mirrors” was accepted and presented virtually at *IGARSS* 2022. The primary goal was to analyze the radiometric performance of convex mirrors using Eq. (2.34) (i.e., a predicted mirror reflectance) and reflectance calibrated HS imagery using Lambertian panels. This initial assessment of the reflectance retrieval demonstrated, within an estimated uncertainty, that an extracted mirror signal, when calibrated to reflectance using Lambertian panels, had comparative results to the predicted ELRF. Mirror parameters such as the radius of curvature and mirror reflectance were measured by Labsphere Inc. and provided the means to evaluate a first order approximation to the uncertainty. Investigations into spatial misregistration and orthorectification errors was the first observation of this kind for drone-based HSI systems. These observations lead to the next paper in this thesis where spatial misregistration was more formally assessed.

4.2.1 Laboratory Investigation

Critical discoveries about RIT's VNIR HSI systems performance were found after the G-SCALE campaign [Russell et al., 2023] concluded and were out of the scope of the paper (Appendix A). To summarize the drone component of the G-SCALE campaign, RIT's VNIR and SWIR HSI systems were flown over a field of Lambertian and SPARC targets. The VNIR and SWIR systems had GSD's of 6.5 cm and 10.2 cm respectively and these values were targeted based on preflight predictions of the mirror's ELRF.

This section will highlight the problems discovered in the HSI imagery, the lab-based experiments conducted and the simple solution. The problem was discovered during a data quality check of the HSI data before it was calibrated to spectral radiance. Intrinsically, the HSI system collects 12-bit digital numbers (0-4095 DN) and acceptable peak signals should not exceed roughly 80-90% saturation (i.e., 3300-3700 DN). This general rule is important because most electronic sensors have non-linear behavior (i.e., linear increase in radiance does no equal a linear increase in DN) as saturation is approach and balancing signal levels for the scientific application is required.

The initial problem in the HSI data was overall signal level (with reasonable integration time of 6 ms) throughout the scene and more importantly, on the calibration problems used for in-scene radiance-to-reflectance conversion. Since the whole scene was impacted and exhibited low signal, diagnosing the problem could only be achieved by re-scaling the image or manually investigating the imagery by extracting signal levels from various calibration panels (Figure 4.3). As Figure 4.3 demonstrates, the brightest signal is from the very large white panel (in the lower left part of the image), peaks around 800 DN and represents a 50% Lambertian reflector. The darkest signal is from the small black panel (at the top of the image) and peaks just above the noise floor (∼ 155 DN) of the sensor. Any signal close to the sensors noise floor exhibits a ruffled spectrum and is indicative of sensor artifacts at low signal. For in-scene radiance-to-reflectance conversion, the ideal signal off a 50% calibration panel should be around 75% saturation (i.e., ∼ 3000 DN). This signal level allows for brighter targets to be imaged without saturation (i.e., typical vegetation reflectances are less than 65% [Eismann, 2012]) and for dark targets to have enough signal over the noise floor. An initial reaction to solving this problem would be to increase the integration time; however, this only mitigates the problem and enhances motion blur throughout the scene.

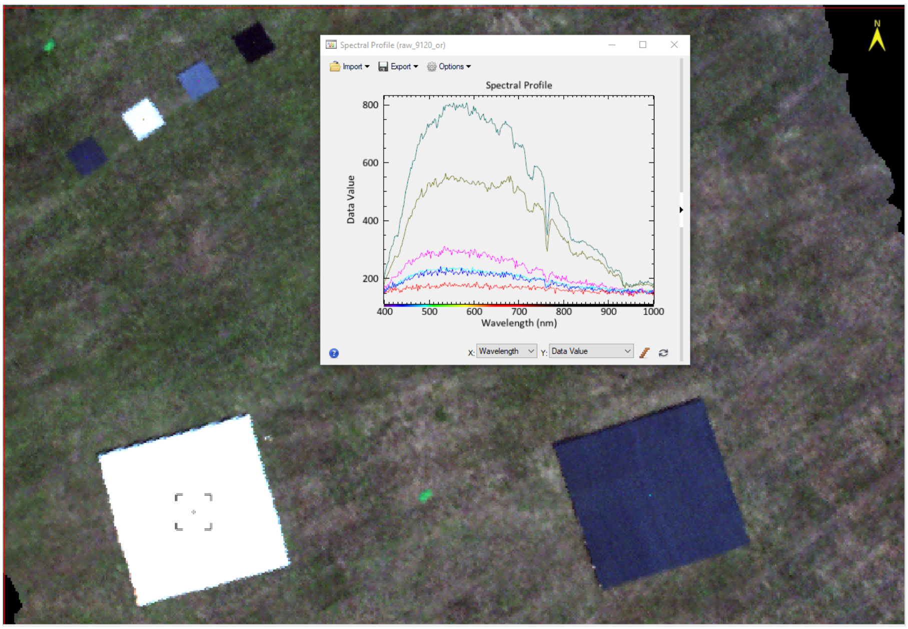

FIGURE 4.3: RGB rendered image of Lambertian calibration panels with a graph of overall digital signal levels. The digital signals on the calibration panels are far lower than anticipated and this system is not optimized for remote sensing applications.

The G-SCALE campaign was a demonstration for the use of SPARC targets with drone, airplane and satellite-based imaging. Figure 4.4a is a RGB image extracted from the drone-based HSI system and shows three backgrounds containing all the mirror configurations outlined in Table 3.1. What makes this image more valuable is the signal dependent SPSF's highlighted in the white, yellow and red boxes. The G-SCALE experiment plan designated the white box

(R_m = 25 mm) for spatial analysis and the yellow box (R_m = 50 mm) for radiometric analysis of the VNIR HSI system whereas the red box (R_m = 100 mm) was exclusively designed for RIT's SWIR HSI system and was purely experimental. However, due to the problem with the VNIR HSI system, the targets in the white box were much dimmer in digital signal than expected and could not be used. The targets in the yellow box were designed to stimulate the VNIR HSI system with reflectance values similar to the deployed Lambertian panels, but the digital signals were again far lower than expected and the 3-mirror array was not reconstructed properly and was too close to the 2-mirror array, causing issues with extracting the signal.

If it wasn't for testing the SWIR HSI system with targets designed for a much larger GSD, this field campaign would have been far less useful. The red box is further highlighted in Figure 4.4b where the peak signal was plotted representing the 1- and 2-mirror array. As can be seen in the plot of signal levels, the mirrors designed for the SWIR system provided perfect digital signal on the VNIR system. This was very unexpected for the VNIR system because the ELRF of these mirrors were roughly 175% and 350% where saturation was anticipated. Because of the signal dependent SPSF, the VNIR HSI systems problem is much more visually apparent than the Lambertian panels.

To find the root cause of the problems experienced during G-SCALE, a laboratory experiment was conducted using the DIRS Labs 20-inch integrating sphere with a broadband plasma illumination source. Extracting the fore-optics F-number can only be achieved if two similar fore-optics were available to compare recorded signals under constant illumination. Luckily, the DIRS group had the same hyperspectral imaging systems with equivalent fore-optics. The experiment consisted of observing an integrating sphere with the same HSI system (MX1 payload) used in G-SCALE, but interchanging the fore-optics and recording the digital signal. The fore-optics had fixed focal lengths with a variable aperture that control the f/#. Since the variable aperture impacts the signal through the HSI system, this was perceived to be the problem with low signal at reasonable integration times. The main assumptions for this investigation was that the fore-optics have similar transmission profiles, focal length and focusing power. More importantly, the secondary lens (defined as the MX2 Lens) needs to be working perfectly such that the primary lens (defined as the MX1 Lens) f/# can be estimated. If the primary lens

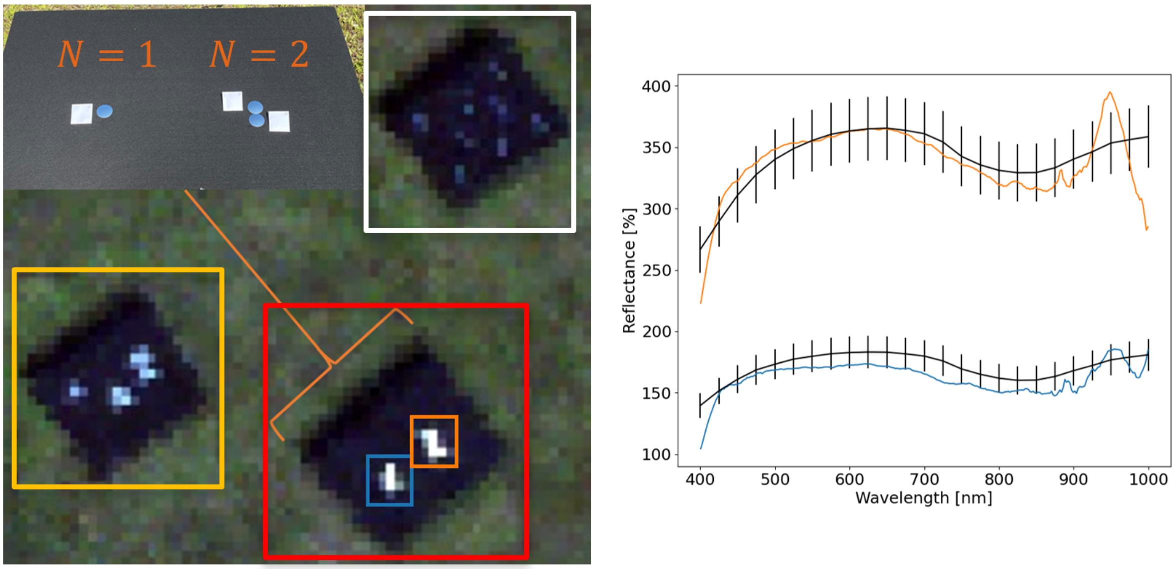

(A) (B)

FIGURE 4.4: (A) Various mirror configurations (yellow, red and white boxes) were deployed for both VNIR and SWIR HSI systems. The mirrors highlighted in smaller blue and orange boxes had the highest SNR for further examination. (B) A comparison between predicted and extracted mirror reflectance signals demonstrate correlation within the estimated uncertainty.

is not at the correct f/#, both the radiometric calibration and derived flat-field would be no longer valid.

Figure 4.5a is the instrument setup for testing the impacts of interchanging the fore-optic. Once the HSI system is aligned and leveled, the system does not need to be touched in order to change out the fore-optic. To reduce any sphere loading (*i.e.*, light reflecting back into the sphere) black felt covered everything except the HSI system (not shown in Figure 4.5a). Figure 4.5b shows the spectral radiance levels within the integrating sphere for both fore-optic measurements. The integrating sphere measurements were used in the signal modeling for estimating the primary lens f/#.

An end-to-end radiometric model, Eq. (4.1) for an extended target (*i.e.*, an integrating sphere) will allow for the extraction of the primary lens f/#. The digital signal, $S(\lambda)$ at the focal plane can be described by

$$S(\lambda) = \frac{\pi}{4(f/\#)^2}\,\tau_{sys}(\lambda)\,p^2\,\Delta t\,\frac{QE_{max}}{QSE}\,\mathcal{O}[L_{EAR}(\lambda)] \tag{4.1}$$

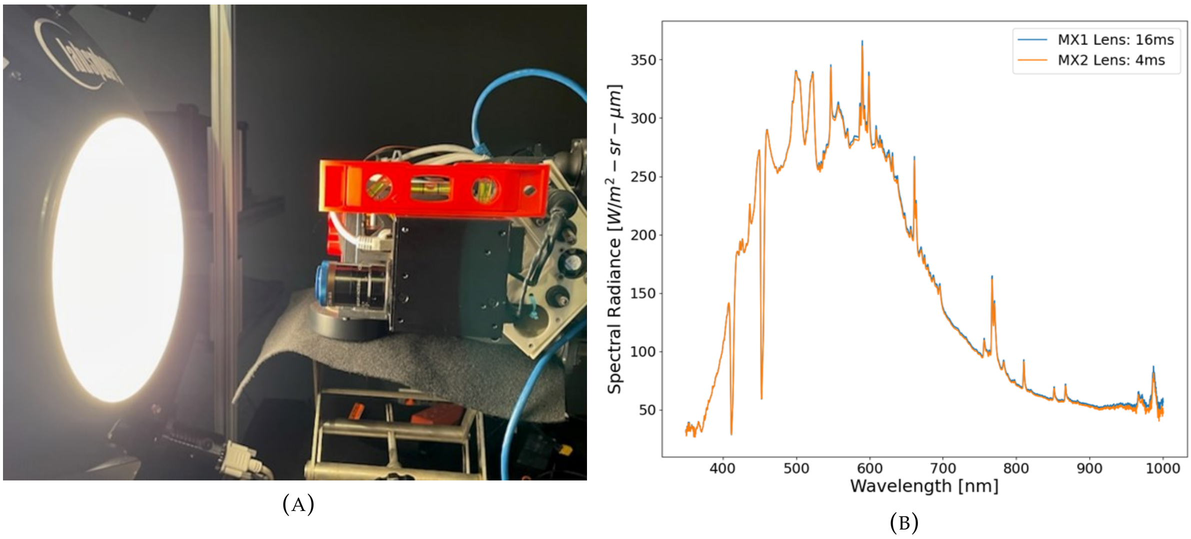

(A)

(B)

FIGURE 4.5: To examine the difference between HSI fore-optics, (A) the HSI system is placed in front of an integrating sphere. (B) For each fore-optic, the integrating sphere's spectral radiance was measured by an internal, calibrated, spectrometer.

and includes the following terms from left to right: the optical systems solid angle prescribed by the $f/\#$, the pixel pitch, p squared, the integration time, Δt, the system transmission function, $\tau_{sys}(\lambda)$ containing all optical elements and relative detector responsively, the maximum quantum efficiency, QE_{max}, and the quantization step equivalence, QSE. The final term defines a two step operation for transforming the observed spectral radiance between two different spectral instruments. The first operation is a convolution with a kernel that would transform the spectral response of one instrument into another. The second operation is an interpolation step where downsampling is the preferred direction. The integrating sphere has a higher spectral sampling interval and spectral resolution compared to the hyperspectral instrument. Thus, the operation ($\mathcal{O}[L_{EAR}(\lambda)]$) would transform the entrance aperture reaching spectral radiance ($L_{EAR}(\lambda)$) of the integrating sphere to the hyperspectral instrument.

Eq. (4.1) can be reduced to a simplified equation because a ratio of signals from the same instrument will be used in the estimate. The only assumption here is that the transmission profile through both lenses and the ratio of the integrating sphere is spectrally smooth (*i.e.,* only interpolation is needed). The following equation is a simplified radiometric model used for the estimation.

$$S(\lambda) \sim \frac{\pi}{4(f/\#)^2}\,\Delta t\, L_{intsph}(\lambda) \tag{4.2}$$

where $L_{EAR}(\lambda)$ was replaced with the integrating sphere spectra radiance, $L_{intsph}(\lambda)$. It should be noted that the only dependence here that defines the differences between the two f/# is the integration time, the digital signal and spectral radiance of the integrating sphere. A ratio can be formed between the two measurements and solved for the primary lens f/# (*i.e.*, $(f/\#)_{MX1}$).

$$(f/\#)_{MX1} = (f/\#)_{MX2}\sqrt{\frac{\Delta t_{MX1}}{\Delta t_{MX2}}\frac{L(\lambda)_{MX1}}{L(\lambda)_{MX2}}\frac{S(\lambda)_{MX2}}{S(\lambda)_{MX1}}} \tag{4.3}$$

Within Eq. (4.3) each term is specified for either the MX1 Lens or the MX2 Lens. Both integrating sphere spectral radiance measurements ($L(\lambda)_{MX1}$ and $L(\lambda)_{MX2}$) were plotted in Figure 4.5b. The digital signals ($S(\lambda)_{MX1}$ and $S(\lambda)_{MX2}$) are plotted in Figure 4.6a. The integration times (Δt_{MX1} and Δt_{MX2}) were 16 ms and 4 ms respectively.

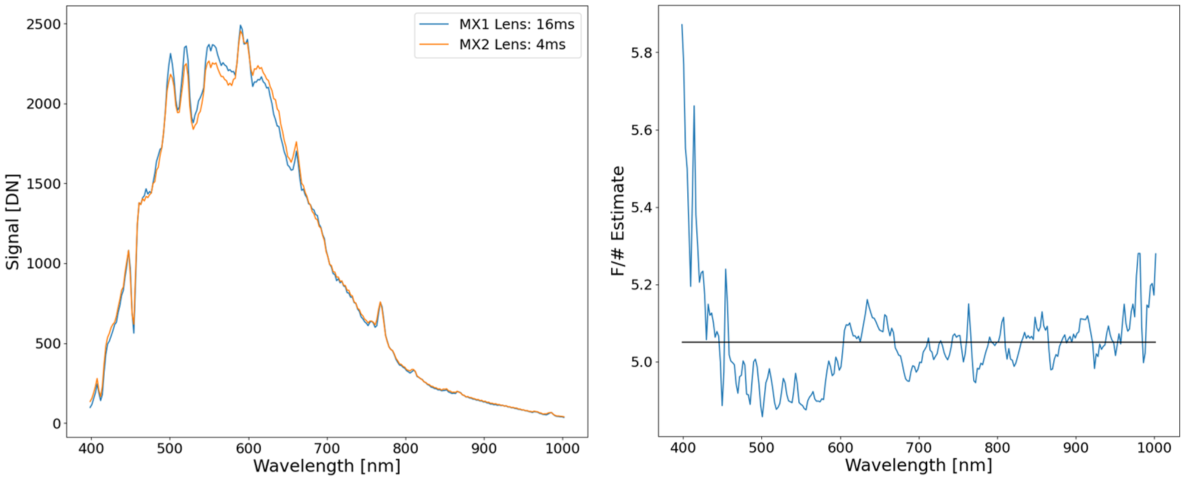

(A) (B)

FIGURE 4.6: (A) The digital signals were optimized to the integrating sphere's illumination. The MX1 Lens required 4x the integration time to achieve the same signal as the MX2 Lens. (B) Using Eq. (4.3), the f/# of the MX1 Lens was estimated. The throughput differences between the tested lenses create a slight various in the f/# as a function of wavelength.

With only the knowledge of the integration time difference, a guess that the f/# is roughly twice as large for the primary lens would provide a reasonable guess. An estimate of the f/# can be seen in Figure 4.6b where the blue line is a spectral estimate and the black is the average. From this figure, the estimate is slightly above 5.0, but clearly highlights why the signals were low in G-SCALE. Furthermore, the smaller aperture in the primary lens inherently lowered the amount of light through the instrument and this required the higher integration time to achieve a similar signal as the secondary lens.

After all experiments concluded both fore-optics were visually inspected to confirm the results. When angled under over head lights, the aperture size difference between both fore-optics was clearly visible and confirms the results from the experiment. The low signal observed in G-SCALE was caused by the fore-optic aperture being smaller than expected. This problem went undiscovered for many experiments because the markings along the lens barrel that tune the f/# was set to the appreciate value of 2.5, but the *internal springs were damaged.* This resulted in the aperture closing without any external indication!

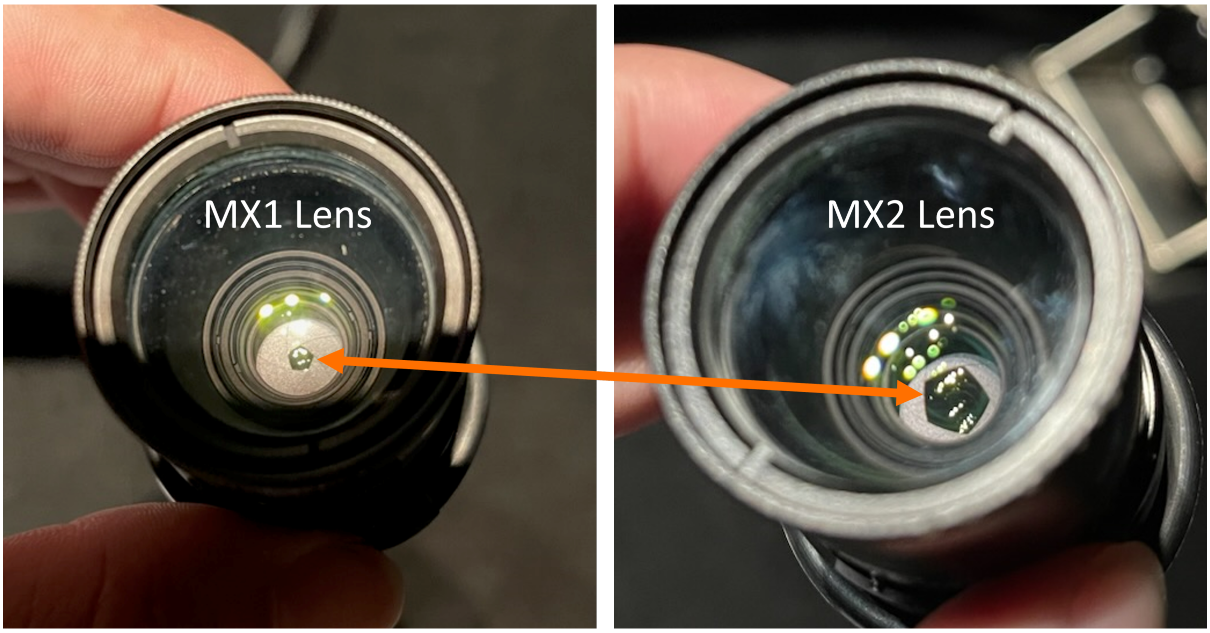

FIGURE 4.7: Images of the apertures within the fore-optics provides visual evidence that the MX1 Lens reduced incomming signal more than anticipated. The smaller aperture caused the f/# to be larger where the light throughput was drastically reduced.

4.2.2 Field Re-Investigation

An effort similar to the laboratory experiment was conducted on field data that contained mirror targets to estimate the f/#. This investigation lends itself to confirm the findings from the laboratory experiment, but also the use of the mirror targets to extract physical properties of the imaging system. In the process of this exercise, the point target radiometric model will be tested and compared to results found when using an integrating sphere.

G-SCALE was conducted in July 2021 while the integrating sphere analysis was conducted a few months later. In this investigation two field experiments were used to estimate the f/#: the G-SCALE data set conducted on 07/23/2021 (Figure 4.8a) and the Multi-Mirror Radiometric Collect (MMRC) data set conducted on 04/14/2023 (Figure 4.8b). The time between G-SCALE and MMRC was almost 21 months apart with both data sets containing more instrument variations than the laboratory experiment. Between the two experiments, the HSI system under investigation had a major refurbishment from the manufacturer. This included replacing the defective fore-optic, replacing the detector (and electronics) and re-calibrating the instrument. All the changes to the instrument will not make the investigation a one-to-one comparison, but can provide reasonable estimates of the aperture differences between the data sets.

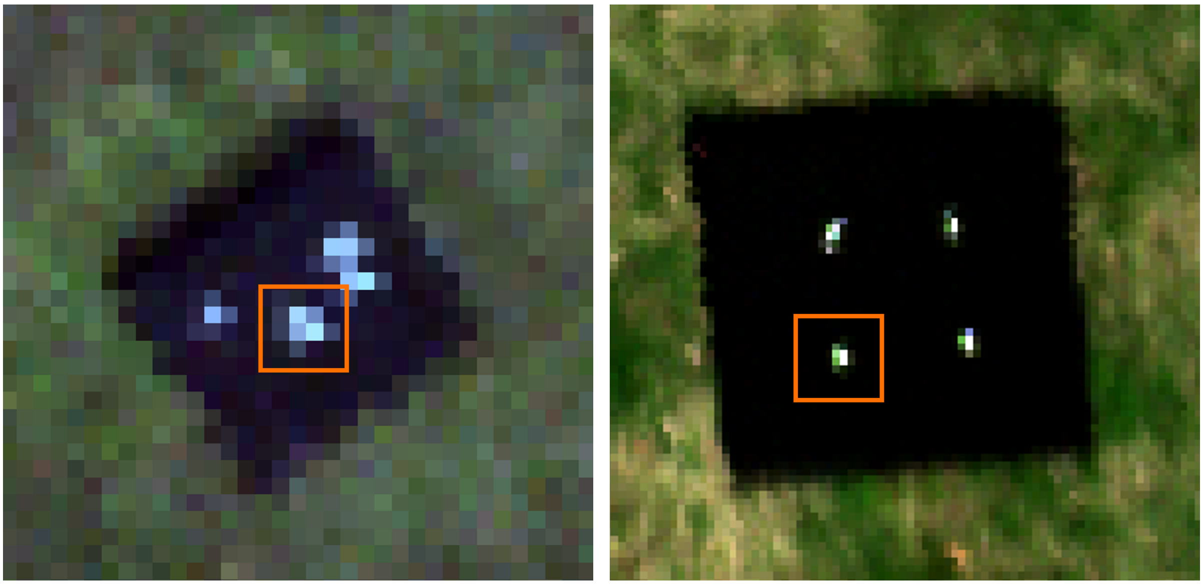
(A) (B)

FIGURE 4.8: Imagery from (A) G-SCALE and (B) MMRC. Within each image is a orange box that highlights the point target used in this analysis. Image quality, SNR and GSD differences are apparent between the images.

An end-to-end radiometric model (Eq. (4.4)) for a point target (*i.e.*, a convex mirrors) allows for the extraction of the primary lens aperture area. The f/# can be calculated after the aperture area is estimated. The digital signal, $S(\lambda)$ at the focal plane can be described by

$$S(\lambda) = \frac{A_{ap}}{SR^2}\, \Delta t\, \tau_{sys}(\lambda)\, \frac{QE_{max}}{QSE}\, \mathcal{O}[I_{tgt}(\lambda)] \tag{4.4}$$

The only difference between Eq. (4.1) and Eq. (4.4) are the terms that define receiving apertures area and solid angle (A_{ap} and SR) and targets radiant intensity, $I_{tgt}(\lambda)$. The solid angle is defined by the entrance aperture area, A_{ap} and the slant range to the target, SR. In the field experiments, convex mirrors naturally produce a point source and Eq. (2.32) defines the targets radiant intensity. Using Eq. (2.32), the radiometric signal model for imaging a point source originating from a convex mirror can be defined as

$$S(\lambda) = \frac{A_{ap}}{SR^2}\, \tau_{sys}(\lambda)\, \Delta t\, \frac{QE_{max}}{QSE}\, \mathcal{O}\left[{}^{1}\!/\!{}_{4}\, \rho_m(\lambda)\, N\, R_m^2\, \left[1 - G(\lambda)\cos(2\theta_m)\right] E_t(\lambda)\right] \tag{4.5}$$

where the same operation ($\mathcal{O}$) is applied to the spectral radiant intensity term. The digital signals used to estimate the aperture area came from G-SCALE and MMRC data sets. Due to the point target distributing its energy over the SPSF, both signals must be the ensquared energy. A simplified model can be defined since the instrument is assumed to be consistent between experiments. We now see that Eq. (4.6) only contains terms that are different between the experiments. That is,

$$S(\lambda) \sim \frac{A_{ap}}{SR^2}\,\Delta t\,\rho_m(\lambda)\,N\,R_m^2\,\left[1 - G(\lambda)\cos(2\theta_m)\right]E_t(\lambda) \tag{4.6}$$

The terms left in Eq. (4.6) not only account for the different mirrors, but also the different atmospheric conditions between G-SCALE and MMRC. Table 4.2 outlines the difference between the mirrors and flight configurations between the experiments. Both mirrors have the same diameter (D_m = 25.4 mm), but have different radii of curvature. This influences the reflect skylight and is dependent on the virtual images solid angle formed by the mirror ($2\theta_m$). Deriving the f/# from the field data is more complex than the laboratory experiment because the mirrors radiant intensity is dependent on the atmospheric conditions and flight configuration. The radiant intensity is a closed form equation compared to the spectral radiance out of an integrating sphere. By forming a ratio of signals between point targets within G-SCALE ($S_1(\lambda)$) and MMRC ($S_2(\lambda)$) data sets, the entrance aperture area can be estimated from Eq. (4.7). The entrance aperture of the MMRC lens is assumed to be working properly with a similar focal length to the lens used in G-SCALE. The entrance aperture of the MMRC lens is $A_{ap,2}$ = 19.63 mm^2. The entrance aperture area of the G-SCALE lens can be defined as

TABLE 4.2: Parameter values for the non-spectral terms of Eq. (4.6).

Collect	$SR[m]$	$\Delta t[ms]$	$R_m[mm]$	θ_m	N
(1) G-SCALE	105.41	5.995	49.77	13.08°	2
(2) MMRC	34.05	5.499	24.99	26.76°	1

$$\begin{aligned} A_{ap,1} &= \left(\frac{S_1(\lambda)}{S_2(\lambda)}\right)\left(\frac{SR_1}{SR_2}\right)^2\left(\frac{\Delta t_2}{\Delta t_1}\right)\left(\frac{N_2}{N_1}\right)\left(\frac{R_{m,2}}{R_{m,1}}\right)^2 \\ &\cdot \left(\frac{\rho_{m,2}(\lambda)}{\rho_{m,1}(\lambda)}\right)\left(\frac{1 - G_2(\lambda)\cos(2\theta_{m,2})}{1 - G_1(\lambda)\cos(2\theta_{m,1})}\right)\left(\frac{E_{t,2}(\lambda)}{E_{t,1}(\lambda)}\right) A_{ap,2} \end{aligned} \tag{4.7}$$

with G-SCALE and MMRC defined with subscripts 1 and 2, respectively. The point target signals are shown in Figure 4.9a and a large signal discrepancy can be observed caused by the difference in entrance aperture area. Even though the signals are recorded by the same instrument, the sensor was replaced after G-SCALE and slight differences in how the sensor performs at different areas of the dynamic range will impact the ratio of signals. The G-SCALE signal was closer to the noise floor whereas the mirror signal in MMRC is slightly over half the dynamic range.

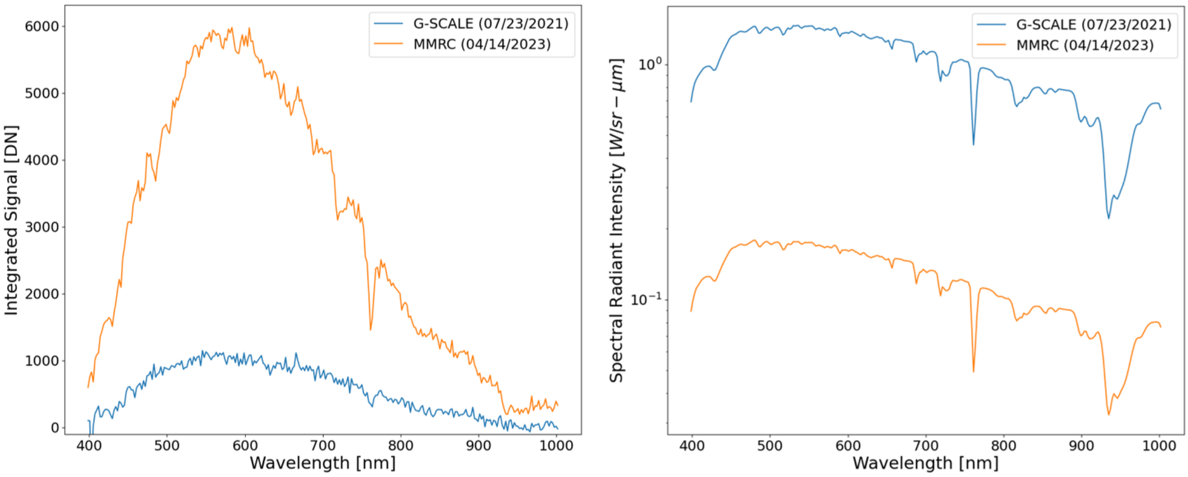

(A)

(B)

FIGURE 4.9: Point target differences between the data sets extracted from G-SCALE and MMRC. (A) The ensquared digital signal and (B) predicted radiant intensity of both point targets.

The predicted spectral radiant intensity of the point targets for each experiment is plotted in Figure 4.9b. There is roughly a 10x difference in radiant intensity between the point targets used in the experiments. The point target examined in G-SCALE is roughly 10x higher than the MMRC point target. Even though the G-SCALE point target is brighter, the restricted entrance aperture area and slant range difference causes the digital signal to be lower than the digital signal from MMRC. Using simple geometric relationships between the entrance aperture area (from Eq. (4.7)) and focal length (fl = 12.5 mm) of an imaging system, the f/# can be evaluated by Eq. (4.8) after calculating the entrance aperture area from Eq. (4.7). That is,

$$(f/\#)_1 = \sqrt{\frac{\pi}{4}\frac{fl^2}{A_{ap,1}}} \tag{4.8}$$

An estimate of the lens used in G-SCALE is shown in Figure 4.10 with a comparison to the f/# estimated from the laboratory investigation (Section 4.2.1). Despite extracting the f/# from two dissimilar methods (integrating sphere vs. convex mirrors), the results provided evidence that the G-SCALE lens had an aperture that was on average 2x smaller. The change in aperture configuration drastically impacted the signal reaching the detector, but also impacted the radiometric calibration and flat-fielding operations. The slight differences between the results can be traced to the assumptions used in the analysis used to estimate the f/# from the field experiments. The primary assumption was that the instrument did not change in-between G-SCALE and MMRC (roughly 21 months). As previously stated, this is not true because the HSI system was refurbished in June of 2022 and key components (fore-optic and detector) were replaced. Even though the field experiment was not perfect, it demonstrated the radiometric response of convex mirrors from Eq. (2.26) and the ability to extract the intrinsic properties of an imaging system (i.e, entrance aperture area).

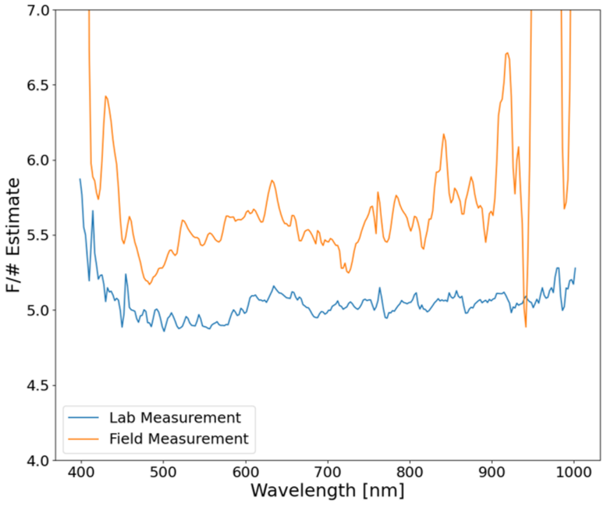

FIGURE 4.10: A comparison between estimate of the G-SCALE lens f/# from two different experimental methodologies. The blue curve represents the results from a laboratory controlled experiment with an integrating sphere. The orange curve is the result from extracting the f/# from two field experiments using convex mirrors.

4.3 Appendix B Summary

In Appendix B, the *extraction of spatial misregistration* was examined during field experiments using convex mirrors for drone-based HSI systems across the FOV. "A Vicarious Technique for Understanding and Diagnosing Hyperspectral Spatial Misregistration" was accepted into MDPI - *Sensors*. The analysis of spatial misregistration is traditionally performed in laboratory scenarios where controlled experiments can accurately estimate the parameters that formulate spatial misregistration. Estimating SPSF width, shape and keystone can be used to calculate the spatial coregistration error that defines a metric for spatial misregistration. The research revealed the various components that can be extracted from SPSF measurements of convex mirrors; however, only SPSF width and keystone can be extracted under the assumption that the spatial response can be accurately modelled by a 2D Gaussian distribution. Thus, a first order approximation to the spatial coregistration error for HSI systems was assessed and two areas within the FOV were compared to demonstrate the uniqueness of spatial misregistration.

4.4 Appendix C Summary

In Appendix C, the *small target radiometric performance* of drone-based HSI systems were investigated using convex mirrors. "Small Target Radiometric Performance of Drone-based Hyperspectral Imaging Systems" was be submitted to MDPI, *Remote Sensing*. The performance of HSI systems to conserve radiometry after orthorectification was shown to be unreliable and inexact for point targets compared to Lambertian panels. The investigation revealed that platform motion from a fix mounted HSI system and the orthorectification process lead to over-estimates of the point targets spectral radiance. Out of the 144 individual point target observations, only 18.1% were radiometrically accurate to the 8% predicted uncertainty. Large deviations of the spectral radiance's observed by the HSI system indicate significant dependence on the interpolation used within the orthorectification process. Nearest neighbor interpolation would add or eliminate signal energy over the high contrast point targets where the bilinear interpolation scheme could spectrally modify the point targets signal.

4.5 Appendix D Summary

In Appendix D, a new approach was developed to *characterize the spatial resolution* of an imaging system by observing convex mirrors. “A New Technique to Define the Spatial Resolution of Imaging Sensors” was accepted and presented virtually at *IGARSS* 2021. By oversampling the SPSF and interpolating to equidistant spacing, spatial resolution criteria could be analyzed by simulating overlapping point targets. This methodology was validated off real imagery where convex mirrors were separated by known distances and formed point target pairs. The validation showed high statistical agreement between the simulated and real point target pairs from a collection of 17 images for the along and across-track directions.

Chapter 5

Conclusion

Using convex mirrors to characterize the radiometric and spatial response of hyper- spectral and multispectral imaging systems has yet to be thoroughly investigated for drone-based platforms. When convex mirrors are deployed in field experiments, a radiometrically accurate point source can be imaged by remote sensing systems. When imaged, a convex mirror produces a known radiant intensity source that can be transformed into aperture reaching quantities such as radiance or reflectance.

The research findings indicate that convex mirrors provide a novel technique to extract new information when deployed for drone-based field experiments. The reflected sunlight produces a broadband point source for characterizing the spatial misregistration of HSI systems without the need to oversample an edge target. More importantly, the reflected sunlight from a convex mirror is defined in a closed-form radiometric expression that can easily be used to validate the small target radiometric performance of imaging systems. Small target performance of HSI systems has drastic consequences for sub-pixel target detection and spectral unmixing. Further discoveries unveiled the inconsistent radiometric performance of a well-calibrated HSI system to point targets in the presence of platform motion and orthorectification compared to Lambertian panels.

An initial study on the radiometric properties of convex mirrors when com- pared to Lambertian panels was investigated and published for drone-based HSI systems [David Conran and Ientilucci, 2022]. An analysis on the Equivalent Lambertian Reflectance Factor (ELRF) of convex mirrors (i.e., Section 2.3.3) demonstrates results within the uncertainty to Lambertian targets for in-scene reflectance calibration. An examination into small target radiometric performance of drone-based HSI systems highlights major inconsistencies in orthorectification when compared to Lambertian panels [In Review: MDPI - Remote Sensing]. Large radiometric variations were observed over point targets from image to image and demonstrates major inconsistencies in the interpolation schemes used in the orthorectification process.

The inherent response of an imaging system to a point source is the sampled point spread function (SPSF) that characterizes the spatial performance. The simultaneous radio- metric and spatial response from convex mirrors creates a multiplex advantage that support a unique understanding of the hyperspectral and multispectral instrument's response for vicarious characterization. Early work has demonstrated convex mirrors can provide a unique estimate of spatial resolution for multispectral satellite imagery [David Conran, Ientilucci, et al., 2021]. The spatial analysis is based on the Rayleigh Criteria, but the resolution is found experimentally estimating the spatial response from convex mirrors. To validate the results, point target pairs were formed from convex mirrors and compared to the analysis.

An investigation into HSI spatial misregistration for drone-based field experiments demonstrates unique property of convex mirrors [D. N. Conran and Ientilucci, 2023]. Using two field experiments, G-SCALE [Russell et al., 2023] and BigMAC [Hedler et al., 2023], various point target responses were assessed across the imaging systems FOV. Major discoverers include the comparison of on and off-axis performance through the misregistration error. These errors impact the ability to spatially separate small targets on the ground through there spectral signature. During G-SCALE, signal discrepancies were discovered and further assessment was done in a laboratory experiment. Under illumination from an integrating sphere, the HSI's fore-optic was damaged from past field experiments and the aperture was smaller than anticipated (Section 4.2.1). A re-evaluation of point targets from G-SCALE and the most recent field experiment from Appendix C found similar results (Section 4.2.2).

Chapter 6

Future Work

For each published research article, specifically Appendix A and B, future work was identified related to each research article. Within Appendix A, the primary research focus was an initial surface reflectance retrieval from convex mirrors and comparison to Lambertian targets. Secondary discoveries were found when the data set was examined for spatial response inconsistencies. Initial results showed that spectral separation was seen within point targets that were imaged at the edge of the FOV. This discovery initiated a reevaluation of all field experiments where point targets were imaged across the FOV and lead to the second published research article (Appendix B).

The discoveries of spatial inconsistencies within the first research article lead to the second research article about hyperspectral spatial misregistration. Appendix B outlines an evaluation of spatial misregistration for HSI systems during two field experiments. Point targets were deployed for radiometric and spatial analysis in G-SCALE [Russell et al., 2023] and Big-MAC [Hedler et al., 2023]. Both data sets contained examples of spatial misregistration errors and provided enough objective evidence for the second published research article. Key characteristics of spatial misregistration are keystone and spatial width variations across the spectral range. The concluding sections within Appendix B highlight orthorectification impacts on point targets. Initial observations demonstrated enough supporting evidence to warrant a final field experiment to examine any correlations between orthorectification and radiometric performance of point targets (Appendix C).

The final research paper (Appendix C) focused on the radiometric inconsistencies within drone-based HSI data over small targets (i.e., point targets). Large variations in the observed spectral radiance of point targets were observed over multiple images correlated to the orthorectification process. In general, the spectral radiance of point targets tends to be overestimated after orthorectification. The radiometric performance of drone-based HSI systems demonstrates the need to fully understand post-processing artifacts in order to trust the collected data in the absence of calibration targets. From Appendix C, major concerns were observed on the fidelity of the collected scene and true accuracy of what is collected during a flight. Without examining the radiometric performance issues within post-processing, hidden biases can never be uncovered and accounted for. The dynamic connection between platform motion and orthorectification is far too complex to separate during flight. Thus, warranting more controlled experiments.

The proposed future work should examine the relationship between orthorectification and along-track sampling over point targets. The primary focus of this experiment would be to recreate field conditions similar to drone-based campaigns, but control the platform motion with a translation stage. Limiting the platform motion to the along-track direction will provide a method for extracting the true correlation between orthorectification and small target radiometric performance for different along-track sampling rates. Ideally, the experiment would be conducted outside with convex mirrors and a precision linear translation stage. It is important to note that a linear stage is ideal because this will keep the GSD consistent during scanning. However, this adds complexity to the experimental set-up since the linear translation stage needs to cover the physical length of the black background panel that the mirrors are deployed on (e.g., 36in). In addition, the precision of the linear translation stage needs to be sub-pixel such that accurate along-track step sizes can be achieved. Linear translation stages from ZABER can achieve physical lengths up to 137in, micron level accuracy and repeatability with high speed translation rates. Not only can this translation stage be used for this investigation, but other research experiments that prioritize controlled scanning can use this translation stage (e.g., high resolution HSI of plants).

A roof-top experiment, where an imaging system is attached to a linear translation stage observing convex mirrors in a slant range configuration would simulate a drone-based experiment. For a roof-top experiment to be successful, a few experimental setup conditions are required: centimeter level GSD's, targets to be placed directly north of the imaging system and perpendicular imaging over the mirror background. The first condition, centimeter level GSD, can be easily achieved from most roof-top locations with appropriate slant ranges. The second condition is more critical because the imaging system will be observing the targets at a high zenith angle and needs to see reflected sunlight. The third condition can be easily met by ensuring the target background and imaging platform are parallel.

Figure 6.1 illustrates how these conditions could be meant by performing an experiment on the roof of the Chester F. Carlson building, at RIT. To meet the first condition, targets can be placed at various locations within parking lot F and are marked with an "X" (see Figure 6.1a). The distances are also specified and where estimated based on the distance from the edge of the building. With an estimate of the buildings height, the slant range and GSD can be calculated. It would be recommended that the slant range distance is measured with a LIDAR system to get the most accurate estimate. In Figure 6.1a, it can be seen that the Chester F. Carlson building naturally satisfies the second condition where proposed target placement is directly north of the imaging system (direction of black arrow).

Figure 6.1b depicts an imaging system observing a convex mirror for a specific solar zenith angle. If the convex mirror has a large FOR (red arrows), the mirror background elevation angle will be constrained to buildings elevation angle and required GSD. The building's elevation angle, θ_b can be defined as follows

$$\theta_b = sin^{-1}\left(\frac{IFOV}{GSD}H_b\right) \tag{6.1}$$

where $IFOV$ is the imaging systems pixel instantaneous field of view in radians, GSD is the target ground sample distance in meters and H_b is the buildings height in meters. For completeness, an angular quantity, ϕ was derived for determining if an imaging system can observe the reflect sunlight in the situation depicted in Figure 6.1b. That is, if ϕ equates to a negative value, the reflected sunlight can be observed whereas a positive value means the

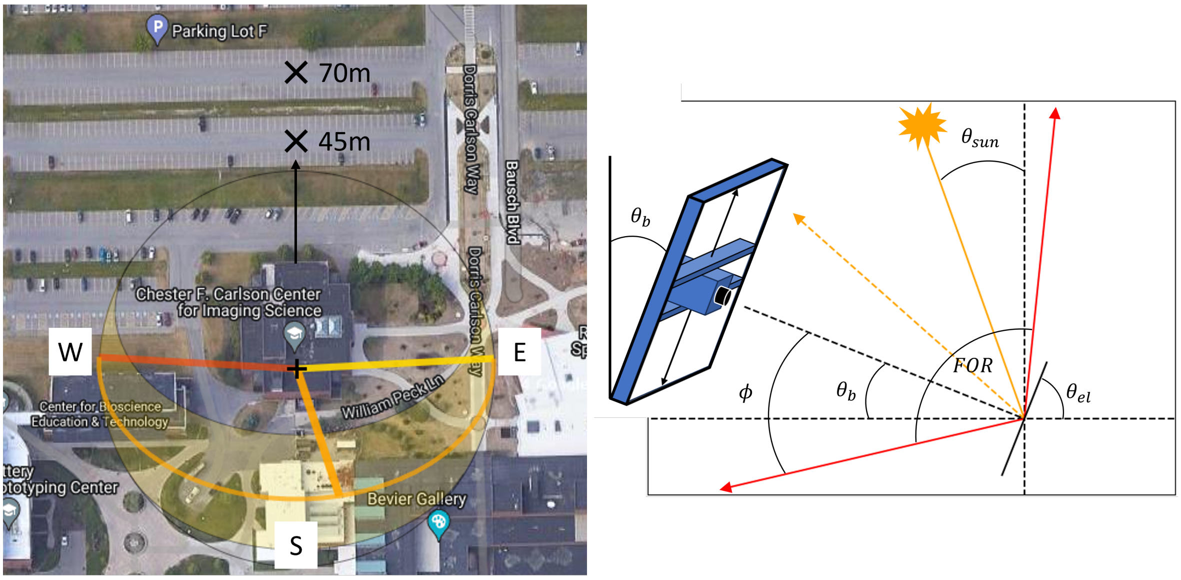
Parking Lot F
70m
45m
Doris Carlson Way
Bausch Blvd
Chester F. Carlson Center for Imaging Science
W
E
S
Center for Bioscience Education & Technology
William Peck Ln
Bevier Gallery
θsun
θb
FOR
ϕ
θel

(A) (B)

FIGURE 6.1: (A) A roof-top experiment can be achieved from the Chester F. Carlson building. The horizontal distance marked by the “X” (45m and 70m) indicate an experimental area for centimeter level GSD. The solar path is indicate as the orange curve with the horizons in red and yellow. (B) Pointing configuration for an imaging system with respect to the black background panel. This is based on specific configurations of the convex mirror’s FOR and solar zenith angle.

sunlight is not getting to the imaging system. Therefore, ϕ is defined as

$$\phi = (90 - \theta_b) + \theta_{sun} - \theta_{el} - {}^1\!/_2 FOR \tag{6.2}$$

where θ_{sun} is the solar zenith angle, ${}^1\!/_2 FOR$ is half of the convex mirror's FOR, and θ_b and θ_{el} are the elevation angle of the building and mirror background, respectively. If require the GSD to be consistent across the mirror background as the HSI system scans, the mirror background and imaging axis of the HSI system must be perpendicular. This means that $\theta_{el} = 90 - \theta_b$ and Eq. (6.2) can be reduced to the following,

$$\phi = \theta_{sun} - {}^1\!/_2 FOR \tag{6.3}$$

and the reflected sunlight will always be observable if $\phi \leq 0$. Note that this condition can be easily met during the summer time in Rochester when the solar zenith angle is at its smallest.

Figure 6.2 depicts three along-track sampling cases overlaid on the optical PSF: undersampling (Figure 6.2a), ideal sampling (Figure 6.2b) and oversampling (Figure 6.2c). Within Figure 6.2a, the cross- and along-track directions are indicated where the spectral component is left out for clarity. A 2D spatial image is acquired instantaneously in the cross-track direction whereas the along-track component requires movement to precess the slit image forward. The progression of the slit image in the along-track direction is critical in the orthorectification process because any missing information (i.e., Figure 6.2c) will be interpolated to replaced missed spatial information. Due to the interpolation, the radiometric uncertainty can be explored by varying the along-track sampling rate.

In theory, the depictions in Figure 6.2 will have different radiometric estimates of the spectral radiance from a convex mirror. The radiometric accuracy can be summarized as follows: under-estimates (Figure 6.2a), perfectly estimates (Figure 6.2b) and over-estimates (Figure 6.2c). The amount of under or over-estimates of the spectral radiance will depend on the gaps or overlap of the along-track sampling. However, the above theory only considers energy loss from an improper along-track sampling of the scene. Further issues and complexities

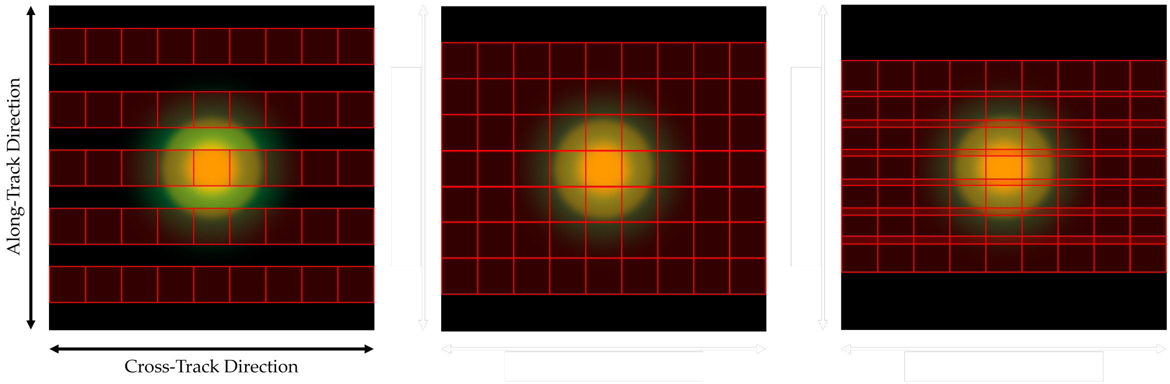

(A) (B) (C)

FIGURE 6.2: Three scenarios where the underlying optical PSF is sampled at different rates in the along-track direction or in the direction of motion. The sampling rate is as follows: (A) undersampled, (B) ideally sampled, and (C) oversampled.

arise when considering the radiometric effects from orthorectifying (with a fixed interpolation scheme) the data set depicted in Figure 6.2. A correlation between along-track sampling and orthorectification could provide further objective evidence for the results observed in Appendix C.

Further investigations could be studied by applying different interpolation schemes to the data set depicted in Figure 6.2. A trade study could be examined where the radiometric accuracy is assessed as a function of along-track sampling and interpolation used in the orthorectification. It has been shown that interpolation within the orthorectification process can add and/or eliminate energy within the imagery over the HSI's systems response to a point target (i.e., SPSF). This further complicates the radiometric performance of HSI systems because interpolation can act on individual pixels or entire rows as discussed in Appendix C.

Additional studies could help define how the 2D SPSF is propagated through an orthorectification process. As stated in the finding within Appendix C, the wavelength dependent SPSF sharpness is greatly affected by orthorectification and more specifically, the interpolation method. The high contrast of the SPSF causes significant signal gradients over a few pixels and interpolation was shown to eliminate, duplicate or fabricate pixels with large radiometric energy. More importantly, if the 2D SPSF is used within the interpolation, this could provide conservation of energy constraints on small targets within the orthorectification process. This has the potential to define a new standard for orthorectifying HS imagery where radiometric accuracy of small targets is conserved. This relies on the ability to fully characterize the 2D SPSF of an HS instrument in the laboratory [Ientilucci, D. N. Conran, et al., 2022].

Appendix A

Interrogating UAV Image and Data Quality using Convex Mirrors

INTERROGATING UAV IMAGE AND DATA QUALITY USING CONVEX MIRRORS

David Conran and Emmett J. Ientilucci

Rochester Institute of Technology, Center for Imaging Science, Rochester NY, 14623

ABSTRACT

The Digital Imaging and Remote Sensing (DIRS) lab in the Chester F. Carlson Center for Imaging Science at the Rochester Institute of Technology (RIT) focuses on the development of tools to extract information about the Earth from aerial and satellite imaging systems. Recent focus has been in the area of drone-based hyperspectral imaging and data acquisition. A strong in-lab and in-field calibration capability has allowed for the precise characterization of many aspects of hyperspectral imaging (HSI) performance, particularly in the *field* (*i.e.,* vicarious calibration). This paper discusses our innovative approaches to in-field calibration along with our observations of hyperspectral (HS) instruments and data processing effects related to radiometric calibration, the sampled point spread function (SPSF), and geo-rectification.

Index Terms— radiometry, SPSF, mirrors, UAS

1. INTRODUCTION AND BACKGROUND

The use of drone-based HSI systems to remotely sense the Earth has been increasing in popularity due to the ease of acquiring the technology with a relatively small budget. Because of this ease of accessibility from manufactures, most research groups can easily purchase an HSI camera integrated on to a drone with a GPS/IMU system as a completed package. Many systems are advertised as "turn key" with little effort or expertise required to collect, calibrate, and produce a geo-rectified data product.

Within the last six years, the DIRS has lab acquired multiple fixed mounted drone based imaging platforms including three HSI systems covering the visible (VNIR) to short-wave infrared (SWIR) portion of the EM spectrum (*i.e.,* 400-2500 nm). Research applications include sub-pixel target detection, vegetative health and disease analysis, fundamental properties of soils, and calibration/validation applications for aerial and space-based imaging platforms.

The Unmanned Aerial Systems (UAS) lab seeks to provide high quality HSI-collected data products (*i.e.,* raw DN, radiance, reflectance, etc.). To meet this goal, we collect ground truth measurements during every drone flight. These include surface reflectance estimates of all calibration/validation panels, downwelling irradiance monitoring, and GPS ground control points. All of these measurements ensure the imagery and data collected are accurate and analysis ready. However, recent experimental studies with *convex mirrors* have illustrated pixel-level artifacts that can greatly impact image and data quality, which is the focus of this paper.

Understanding the response of a drone-based HSI system to a point source provides critical performance information and highlights limitations of the imaging system under test. Both radiometric integrity and spatial quality are key components when assessing pixel-level targets and imaged convex mirrors. We use the SPecular Array Radiometric Calibration (SPARC) method [1], a novel technology for absolute vicarious calibration, to assess the image quality of our imagers' response to small targets and point sources.

SPARC is the technology that defines the use of convex mirrors for radiometric and spatial assessment of remote sensing systems. Radiometrically, the convex mirrors create a radiant intensity source (*i.e.,* a point source) by specular reflection of the sun. Spatially, a convex mirror forms a virtual image of the solar disk at the appropriate focal length for an imager to observe [1]. When the imaging system observes this point source, the inherent spatio-optical response (*i.e.,* the sampled point spread function or SPSF) is measured. More importantly, it not only reveals the response of the imaging system to an ideal point source, but also highlights any induced blurring or artifacts from platform motion and/or post-processing (*e.g.,* geo-rectification).

As previously mentioned, the convex mirror(s) are inherently described as a radiant intensity source. These mirrors can provide an absolute radiometric signal, which may also be expressed as an equivalent Lambertian reflectance factor, $\rho_F(\lambda)$ [1]. In other words, the mirrors have a unique reflectance spectrum comparable to an ideal Lambertian surface while accounting for both direct (solar) and indirect (atmosphere) illumination sources. That is,

$$\begin{aligned}\rho_F(\lambda) \;&=\; \left[\frac{1}{cos(\theta_s)} + \left(f - \frac{1}{cos(\theta_s)}\right) G(\lambda)\right] \cdot \\ &\quad \frac{\pi N R_m^2}{4\, GSD_x\, GSD_y} \rho_m(\lambda)\end{aligned} \tag{1}$$

where θ_s is the solar zenith angle, f is the fraction of indirect illumination contribution, $G(\lambda)$ is the Global-to-Diffuse Ratio, N is the number of mirrors, R_m is the mirrors radius of curvature, GSD is the directional Ground Sampling Distance, and $\rho_m(\lambda)$ is the mirrors spectral reflectance.

A first-order approximation of the uncertainty in Eq. (1) is determined to understand the confidence in the estimated surface reflectance $\rho_F(\lambda)$. A full uncertainty analysis of Eq. (1) is beyond the scope of this paper and would require a Monte Carlo approach to handle the non-linear terms. By inspection, there are only a few parameters within Eq. (1) that will dominant the uncertainty. We will consider the GSD to be the same in both x and y directions. Additionally, the uncertainty in $\rho_m(\lambda)$ will not have wavelength dependence here. This may not always be the case, but these assumption will provide an upper limit to the combined uncertainty of $\rho_F(\lambda)$. This approximation to the uncertainty will be assessed in terms of percent with each term having a corresponding percent uncertainty. We express the uncertainty in $\rho_m(\lambda)$ as,

$$\frac{\delta\rho_F}{\rho_F} = \sqrt{4\left(\frac{\delta R_m}{R_m}\right)^2 + 4\left(\frac{\delta GSD}{GSD}\right)^2 + \left(\frac{\delta\rho_m}{\rho_m}\right)^2}. \qquad (2)$$

When using traditional Lambertian panels or targets, pixel level discrepancies can go completely unnoticed or can be ignored due to the large aerial footprint of the panels. Major issues can include HS camera design artifacts such as keystone and spectral misregistration, geo-rectification errors due to inaccurate GPS/IMU data, inadequate mounting techniques (*e.g.,* fixed mounting), a lack of understanding on the SPSF across the field-of-view (FOV) which can include complex blurring factors induced by platform motion, and any post-processing errors such as interpolation schemes used when fusing the raw imagery into final data products [2].

Convex mirrors provide an easy to use alternative to Lambertian panels when assessing the image and data quality of HS imagery. Problems can be easily observed and quantified by assessing the vicarious SPSF during scientific missions. The ultimate limit of an HSI systems can be thoroughly tested with SPARC technology. From the flight path, to the HS instrument, to any post-processing done to the imagery. In other words, convex mirrors allow for the end-to-end performance testing of HSI systems with omni-directional, sub-pixel targets for image and data quality assessment. In this paper, we flew a drone-based HS imager (VNIR) and observed *sub-pixel* artifacts unique to the spatial and radiometric performance of the HS system. This paper discusses our findings and the utility of deploying mirrors to assess system performance.

2. METHODOLOGY

A large scale, multi-agency ground to space calibration and validation experiment (G-SCALE) was conducted on July 23, 2020 at RIT's Tait Preserve in Rochester, New York. This experiment was designed to validate the use of convex mirrors, for radiometric calibration, when imaged by drones, crewed aerial platforms, and Low Earth Orbit satellites (Fig. 1). A multitude of calibration and validation panels were placed out in a cleared field along with convex mirrors. Two large (6m × 6m) Permaflect$^{\text{TM}}$ reflectance standards were constructed and deployed in the primary scene with a reflectivity of approximately 5% and 50%. These large panels served as reference data in a two-point Empirical Line Method (ELM) for the HS image calibration [3]. Many gray colored felt panels (1m × 1m) were also deployed in the same area for validation of the two-point ELM. Two types of mirrors (for drone imaging) were deployed and placed on black felt covered panels. The black felt helped create a highly uniform and dark background such that the mirror signal could be isolated. Table 1 shows the geometric properties of the mirrors used. The flight parameters include a Digital Elevation Model (DEM) corrected altitude of 103.069 m over the mirrors, a flight speed of roughly 2.0 m/s and a geo-corrected GSD of 6.5 cm. A critical part when using convex mirrors for vicarious calibration is the monitoring of the downwelling irradiance with periodic shading during sensor flyover. Monitoring the direct and indirect illumination during overpass allows for the unique estimate of the Global-to-Diffuse ratio, $G(\lambda)$ [3]. Additionally, convex mirrors suitable for aircraft and satellite imagers were deployed alongside UAV-specific targets for platform intercalibration.

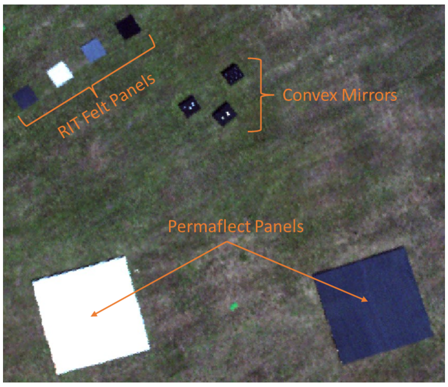

Fig. 1. HS imagery of various calibration targets.

Table 1. Geometric Properties of Drone Mirrors.

	Small	Large
Mirror Diameter	2.54 cm	5.08 cm
Radius of Curvature	5 cm	10 cm
Material	Coated Al	Coated Al
Diameter of Solar Disk	0.22 mm	0.44 mm

3. RESULTS AND DISCUSSION

In this section, we illustrate the unique capabilities mirrors provide when interrogating HS data by comparing radiomet-

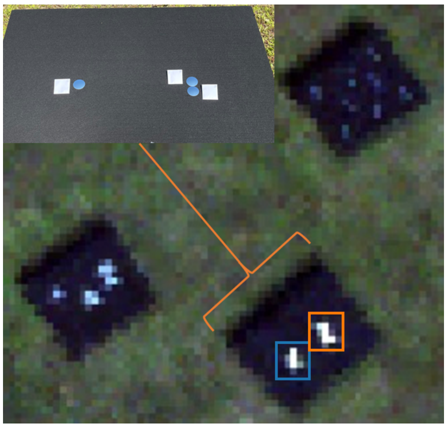

Fig. 2. Zoom of Fig. 1 showing deployment of mirrors. Upper left shows photo of physical mirror layout. Box colors align with the reflectance curves in Fig. 3.

ric performance against traditional methods (*i.e.,* Lambertian panels) and analyzing sub-pixel artifacts.

3.1. Surface Reflectance Comparison of Convex Mirrors

Integrating new technology and methods of vicarious calibration into our UAS capabilities, requires comparison to traditional methods to ensure accuracy and confidence. Fig. 2 shows a close up of the mirrors under test while Fig. 1 illustrates the Lambertian panels. We then computed two mirror reflectances, using Eq. (1), and compared them to reflectances obtained using the ELM approach [3] with Lambertian panels. The Lambertian equivalent reflectance of the mirror targets (Fig. 3, black lines) may be calculated according to Eq. (1). The only field measurement required is the Global-to-Diffuse ratio $G(\lambda)$, used to estimate the diffuse and direct irradiance reflected to the sensor. All other parameters were either measured in the laboratory (*e.g.,* mirror reflectance and radius of curvature) or estimated using publicly available information (*e.g.,* solar zenith angle).

The blue and orange curves in Fig. 3 are the extracted mirror reflectances from the calibrated HS imagery using the respective Permaflect$^{\text{TM}}$ reflectance light/dark standards. One apparent discrepancy seen in Fig. 3 is the reflectances values exceeding 100% in the estimate of the mirror surface reflectance. A property to note when imaging point sources is that the *en-squared energy* is distributed across multiple pixels according to the system's SPSF, reducing the apparent signal on a per-pixel basis (*i.e.,* the enclosed energy can be larger than 100%). More importantly, these mirrors were made for a much larger GSD (greater than 10 cm), but our HSI system had an unexpected problem with the aperture stop size. Because a radiant intensity source is sensitive to the aperture diameter, predicted mirror signals (for a specific GSD) can become buried in the image noise (Fig. 2). Despite this error, we observed agreement between SPARC and Lambertian methodologies for the mirror equivalent reflectance to within measurement uncertainty. Additionally, the mirrors demonstrate an advantage over Lambertian panels in directly identifying potential issues within our imaging chain.

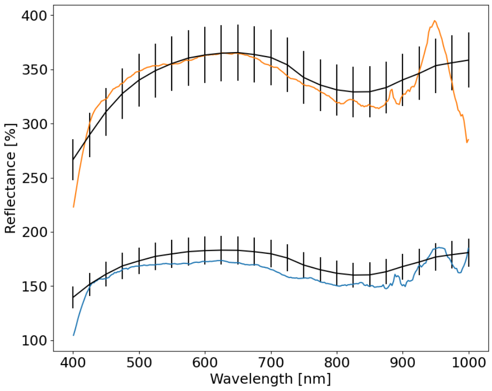

Fig. 3. Predicted surface reflectances for mirrors (black lines) compared to a Lambertian calibrated reflectance (blue and orange curves). Uncertainty estimates also shown.

3.2. Uncertainty Analysis of Surface Reflectance

To achieve confidence in the mirror reflectance and an assessment of the accuracy of the mirror surface reflectance, a first order approximation to the predicted mirror reflectance was derived based on Eq. (2). Table 2 displays the percent uncertainty for the dominant parameters in Eq. (1) along with the combined uncertainty. The dominant term in the combined uncertainty is the GSD or the altitude of the drone and stems from the GPS/IMU system. Without a ground station to correct for various complex issues within GPS systems, the Applanix GPS has an upper limit to the root mean square error in altitude of roughly 3m [4]. The typical digital evaluation mappings used in the geo-rectification was used, but not considered in the uncertainty of the altitude. Finally, motion blur was not considered in this analysis due to complexity in the motion of a fixed-mounted camera system; however, the upper limit in the altitude uncertainty provides enough of a buffer.

3.3. Image and Data Quality Assessment using Convex Mirrors

An advantage of imaging convex mirrors is that one can easily interrogate image and data quality so as to ensure that small target radiometry and spatial integrity (of point sources) is preserved.

Any discrepancies seen in the radiometric representation

Table 2. Uncertainty Budget.

	Percent Uncertainty
Radius of Curvature	2.00%
GSD	2.91%
Mirror Reflectance	2.00%
Total Uncertainty	7.20%

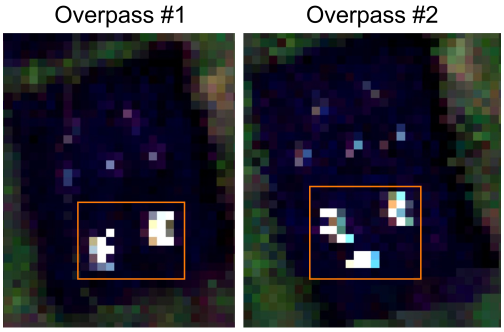

Fig. 4. Two overpasses illustrating inconsistency that can be observed using fixed-mounted HSI systems.

of point sources can provide insight as to how the HSI system is performing. This includes all platform motion, georectification and any post-processing artifacts (*i.e.,* interpolation). Testing radiometric integrity, using convex mirrors, allows for imaging the ideal point-target while simultaneously building confidence in ones instrument for use in small target applications.

Another advantage of using convex mirrors is the ability to probe the spatial integrity of the SPSF formed when imaging point sources. The SPSF formed by an HSI system is a convolution of instrument PSF (including all aberrations), detector sampling, platform motion and post-processing image reconstruction (*i.e.,* geo-rectification). Each element contributes independently to the SPSF. However, platform motion and geo-rectification can often have very profound effects if not properly addressed using a high accuracy GPS/IMU and gimbal-mounted HSI system. Fig. 4 illustrates two different HSI fixed-mounted flights over the same set of mirror targets. There are two noticeable artifacts: in both overpasses, the reconstruction of the point source is poor and in Overpass #2, a single mirror was reconstructed twice due to the complex platform motion. The diagnosis of these problems stem from poor geo-rectification and uncontrollable platform pitching during flight and image acquisition.

Lastly, we examined the complexity of how a point source lands on a detector as a function of wavelength. This is described as co-registration error and all HSI systems have a unique mapping of this error across the FOV [2]. Fig. 5 is a false colored image (using 500, 700 and 900nm bands) which visually illustrates this error. The center of the FOV has very little co-registration error and has a blue appearance due to the high amount of energy in the 500nm spectral channel. The right side of the FOV suffers from major co-registration errors based on the visual color separation and can be described as the SPSF landing in neighboring pixels as a function of wavelength. Vicarious estimates of the co-registration error is the subject of on-going research in our lab.

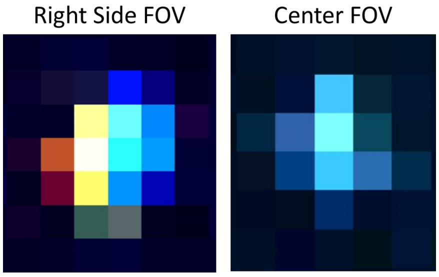

Fig. 5. Two SPSF's at different positions on the focal plane (right side and center) demonstrating how convex mirrors can highlight co-registration errors.

4. CONCLUSIONS AND FUTURE WORK

This paper examined uses of convex mirrors in drone-based HS image analysis. We predicted and extracted reflectances, using mirrors, and showed that predicted and in-scene reflectance agreed within the computed uncertainty. We then used the mirrors to illustrate artifacts, spatial and spectral, from fix-mounted HS imagery. In summary, the DIRS Lab at RIT has been using new convex mirror technology to uniquely interrogate our HS imagery. This has given us new ways to improve our image and data quality. Future work will vicariously probe key spatial/spectral artifacts so as to improve our overall radiometric uncertainty.

5. REFERENCES

[1] S. J. Schiller, "Application of a mirror-based empirical line method for the surface reflectance calibration of earth remote sensing image data," Raytheon Space and Airborne Systems, 2019.

[2] T. Skauli, "An upper-bound metric for characterizing spectral and spatial coregistration errors in spectral imaging," *Optics Express*, vol. 20, no. 2, 2012.

[3] R. Soffer and G. Ifimov, "Experiences learned in the acquisition, processing, and assessment of in-situ point spectroscopy measurements supporting airborne hyperspectral cal/val activities," Calcon, 2019.

[4] Trimble Applanix, *APX-15 UAV v3, Single Board GNSS-Inertial Solution*, 2019.

Appendix B

A Vicarious Technique for Understanding and Diagnosing Hyperspectral Spatial Misregistration

sensors

MDPI

Article

A Vicarious Technique for Understanding and Diagnosing Hyperspectral Spatial Misregistration

David N. Conran * and **Emmett J. Ientilucci ***

Chester F. Carlson Center for Imaging Science, Digital Imaging and Remote Sensing Laboratory,
Rochester Institute of Technology, 54 Lomb Memorial Drive, Rochester, NY 14623, USA
* Correspondence: dnc7309@rit.edu (D.N.C.); ejipci@rit.edu (E.J.I.)

Abstract: Pushbroom hyperspectral imaging (HSI) systems intrinsically measure our surroundings by leveraging 1D spatial imaging, where each pixel contains a unique spectrum of the observed materials. Spatial misregistration is an important property of HSI systems because it defines the spectral integrity of spatial pixels and requires characterization. The IEEE P4001 Standards Association committee has defined laboratory-based methods to test the ultimate limit of HSI systems but negates any impacts from mounting and flying the instruments on airborne platforms such as unmanned aerial vehicles (UAV's) or drones. Our study was designed to demonstrate a novel vicarious technique using convex mirrors to bridge the gap between laboratory and field-based HSI performance testing with a focus on extracting hyperspectral spatial misregistration. A fast and simple extraction technique is proposed for estimating the sampled Point Spread Function's width, along with keystone, as a function of wavelength for understanding the key contributors to hyperspectral spatial misregistration. With the ease of deploying convex mirrors, off-axis spatial misregistration is assessed and compared with on-axis behavior, where the best performance is often observed. In addition, convex mirrors provide an easy methodology to exploit ortho-rectification errors related to fixed pushbroom HSI systems, which we will show. The techniques discussed in this study are not limited to drone-based systems but can be easily applied to other airborne or satellite-based systems.

Keywords: SPSF; keystone; spatial misregistration; hyperspectral; multispectral; imaging; small unmanned aircraft systems; UAS; UAV; convex mirrors

check for updates

Citation: David N. Conran and Emmett J. Ientilucci A Vicarious Technique for Understanding and Diagnosing Hyperspectral Spatial Misregistration. *Sensors* **2023**, *1*, 0. https://doi.org/

Academic Editor:

Received:
Revised:
Accepted:
Published:

Copyright: © 2023 by the authors. Licensee MDPI, Basel, Switzerland. This article is an open access article distributed under the terms and conditions of the Creative Commons Attribution (CC BY) license (https://creativecommons.org/licenses/by/4.0/).

1. Introduction and Background

1.1. Hyperspectral Imaging

Hyperspectral imaging (HSI) utilizes instrumentation that provides a unique perspective for the simultaneous observation of spatial and spectral scene content. Each spatial pixel contains a unique spectrum that is directly proportional to the physical characteristics of the observed material. This is a major advantage over traditional filter-based imaging systems because the measured spectrum can be used more effectively to detect objects, materials, or changes within the scene. For all the usefulness an HSI system promotes in remote sensing applications, the complex optical design of hyperspectral instruments introduces spatial imperfections on the imaged scene, requiring new and innovative ways to diagnose the impact of spatial artifacts related to spectral-spatial information.

A simple design of a pushbroom HSI system can be seen in Figure 1, with the geometric projection of the slit being one-to-one with the detector pixel pitch in the spectral direction. Generally, a pushbroom HSI system only records spatial information in the cross-track direction, where each pixel is dispersed into a spectrum. The remaining spatial component must then be built up by the movement of the HSI system in the along-track direction. Thus, a 3D image of the scene is created, with each pixel containing a spectrum of the 2D spatial scene.

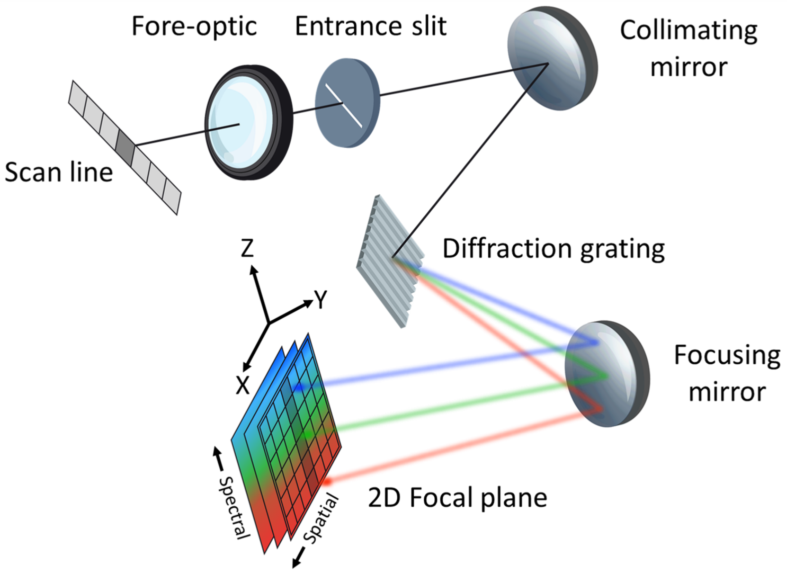

Figure 1. An illustration of a hyperspectral instrument highlighting the various components resulting in a spatial-spectral image of the scan line at the focal plane. The x (cross-track) and z-axis define the internal spectrograph orientation where the scan line is dispersed into a spectrum. The y-axis (along-track) defines the second spatial dimension collected when the instrument is pushed forward.

1.2. Imaging Performance and Spatial Misregistration

Imaging performance of hyperspectral (HS) instruments is a complex topic of discussion because of the unique combination of radiometric, spectral, spatial, and temporal artifacts contaminating the imaged scene. Due to the complex nature of HSI systems, the IEEE P4001 Standards Association committee is currently developing guidelines, definitions, and testing procedures to help the HS community better understand how these systems operate [1]. Figure 1 illustrates an ideal HSI system and for a given spatial pixel within the scan line, the recorded spectrum should only originate from a single pixel without any influence from the surrounding area. However, due to diffraction and various aberrations, a perfect spatial mapping with a unique spectrum is not possible and leads to spatial misregistration [2]. Further degradation in spatial performance is introduced by motion blur and imperfect ortho-rectification, including post-processing artifacts such as nearest-neighbor interpolation. To quantify spatial misregistration, a spectral measurement of the sampled Point Spread Function (SPSF) is required and is further recommended by the P4001 Standards Committee [1]. The SPSF is a culmination of all system imperfections, including optical aberrations, diffraction, grating dispersion, detector pixel blurring, and sampling.

Figure 2 illustrates the main artifacts that contribute to spatial misregistration seen within HSI systems and include the following: *keystone*, SPSF width variability, and SPSF shape differences [2]. The top row shows a well-known distortion called *keystone* that describes the displacement of the SPSF's centroid position as a function of wavelength and can be related back to a variation in the entrance slit magnification when focusing broadband illumination onto the focal plane. The middle row shows a wavelength dependent SPSF width originating from optical diffraction, aberrations, and specifically for HSI systems, the entrance slit and grating diffraction. The last row shows the combination spatial artifacts related to both keystone and SPSF shape differences that are often seen in real HSI systems [3]. What is not shown in Figure 2 are the field-of-view (FOV) dependencies on the various parameters that define spatial misregistration. To fully quantify HSI spatial misregistration, all off-axis behavior is required to be measured as well. In the work presented, we will show that the HSI system under test has degraded performance at the edges of the FOV.

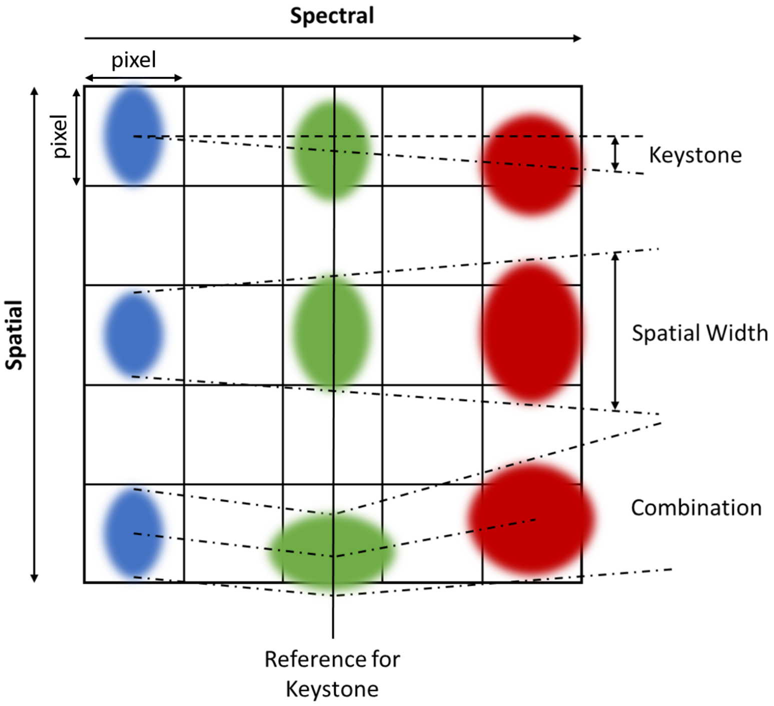

Figure 2. Examples of spatial distortions seen in typical HSI systems. Top row is an example of keystone. Middle row illustrates distortions due to diffraction and aberrations while the bottom row shows a combination of both distortions types.

For the reason that spatial misregistration encompasses multiple spectral measurements of the SPSF's behavior, having a single graph to characterize imaging performance would be more desirable for quick diagnostic checks. To quantify HSI spatial misregistration, a wavelength pair calculation known as *spatial coregistration error* (Equation (1)) can be used to measure differences in the SPSF's keystone, width, and shape across the spectral range [4,5]. The assessment of spatial coregistration error relies on the area normalized difference between two SPSF's for all spectral channel pairs. The spatial coregistration error has a range from 0.0 (i.e., completely overlapping SPSF's) to 1.0 (i.e., completely disjoint SPSF's) and will highlight the behavior of the SPSF at various wavelength pairs and at different locations within the imagers FOV. It should be noted that a smaller spatial coregistration error is ideal (e.g., closer to 0.0 is best) and will lead to fewer errors in applications where spatial and spectral integrity are important. Moreover, for sharp SPSF's, we will show that keystone errors contribute greatly to spatial coregistration error when compared with spatial width variability. The method of understanding spatial misregistration in HSI systems is very important for characterizing the imaging systems spatial performance and has been demonstrated in laboratory experiments using line sources [6].

The calculation of 1D spatial coregistration error ($\epsilon_{i,j}$) for all wavelength pairs i, j is defined as

$$\epsilon_{i,j} = {}^{1}\!/_{2} \int |SPSF_i(x) - SPSF_j(x)| dx \tag{1}$$

where $SPSF$ is an area normalized Gaussian distribution fitted to point targets integrated over the spatial dimension. It is important to note that this calculation is sensitive to enclosed energy, and under estimating enclosed energy will lead to a better estimate of spatial coregistration error [4]. Equation (1) can be easily extended into a second dimension, where the volume normalized SPSF is required.

Laboratory experiments tend to be performed in a static setting by scanning a line source over various parts of the focal plane to extract spatial misregistration. However, extracting spatial misregistration during field experiments using ideal point sources has never been discussed, especially for drone-based imaging platforms. This study fills in the gap for vicarious estimates of HSI spatial misregistration during field experiments by using convex mirror targets and a simple algorithm design for approximating the SPSF response with a 2D Gaussian distribution. However, only the cross-track direction will be assessed since this can be directly tied back to the internal performance of HSI systems, which contributes to the overall coregistration error estimate. More importantly, off-axis behavior can be easily characterized by simply allowing the drone to fly over deployed (convex mirrors) targets until they are no longer in the imagers FOV.

1.3. HSI Application-Based Errors

Spatial coregistration error not only characterizes the spatial misregistration but can also diagnose the ultimate limit on application-based spectral/spatial measurements with HSI systems. When these unknown spatial distortions are present within the HS instruments, small target signatures become mixed in with the background and resemble a problem similar to spectral unmixing with a relationship to the SPSF misregistration.

For example, if we assume the following about an ideal HS instrument: detector-limited SPSF (i.e., width of the optical PSF is equivalent to detector pixel area) with a wavelength-dependent width that varies linearly and a bright sub-pixel target on top of a uniform background. The sub-pixel target will dispense energy into surrounding background pixels, where the energy loss from the target is proportional to the SPSF shape and size. If a spectral unmixing algorithm were applied to this simplistic scenario, energy from the SPSF tails that bleed into surrounding pixels would have a spectral component related to both the sub-pixel target and background. Since the SPSF shape and size are not consistent across the spectral range (or FOV), this would indicate varying degrees of mixture between target and background. The sub-pixel targets impact is no longer contained to a single spatial pixel and adds to the complexity of identifying sub-pixel targets from a background. This example can be expanded upon by now assuming a realistic HSI system with FOV-dependent SPSF characteristics and added keystone, which results in an even more complicated situation. Thus, using convex mirrors to understand an HSI system’s spatial misregistration under field experiment conditions (i.e., complex motion on drone platforms) can now allow scientists to further understand any issues in their scientific results.

Another important application that can suffer from unknown spatial misregistration is small target radiometry and sub-pixel target detection. Target detection relies on the ability to take known spectral signatures and spatially identify unknown sub-pixel target positions with a similar spectral makeup. Depending on the degree of spatial misregistration, the unknown sub-pixel target spectrum can become contaminated by the background, as discussed above, creating a spectrum that does not physically match the defined target. This has large impacts for spectral signatures that were selected from databases containing material properties measured from non-imaging spectrometers (e.g., hand-held point spectrometers). Large spatial misregistration, especially keystone, would corrupt HSI data such that it would not have comparable spectral signatures to the materials in the database. Furthermore, cluttered backgrounds and significant changes in spatial misregistration across the FOV will exacerbate this issue [7,8].

2. Methodology

2.1. Field Experiment Overview

In order to demonstrate the usability of convex mirrors to extract spatial misregistration from HSI systems, a variety of field experiments were performed. Additionally, we performed field experiments with an MSI system to support our ability to extract accurate SPSF estimates. In this section, we will highlight all field experiments while noting the ground sampling distance (GSD) and instantaneous field-of-view (IFOV) for each instrument. Specific imaging system manufacturers will not be discussed so that attention will be focused on the use of the technique instead of quantifying an instrument’s performance.

All imaging systems were fixed mounted to the underside of a DJI Matrice 600 unmanned aerial system (UAS) or drone.

Figure 3 illustrates the field experiment that was conducted to estimate an MSI systems SPSF, utilizing our oversampling technique. Here, only the blue channel with a center wavelength of 475 nm with a bandwidth of 20 nm and an IFOV of 0.694 mrad was used to demonstrate the use of point targets. The drone was flown at an altitude of 57.6 m resulting in imagery collected at 4.0 cm GSD. In Figure 3, there were 16 similar point targets distributed over two black felt-covered panels (each 1.2 m × 1.2 m in size) with an edge target off to the side for comparison, which will not be discussed in this study.

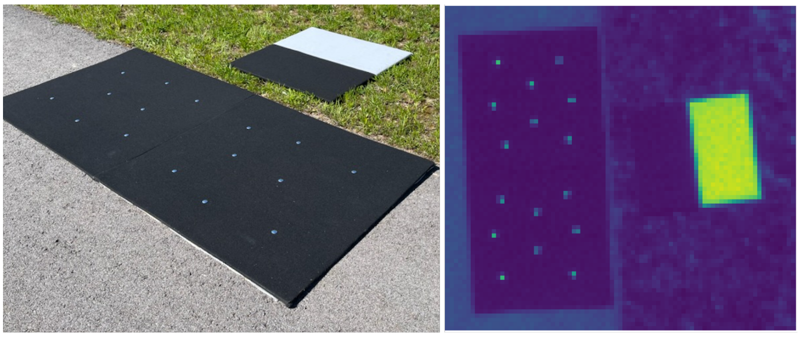

(a) Ground Image **(b)** Drone Image

Figure 3. (**a**) Ground image of the point and edge targets. (**b**) Resulting image of the targets from the MSI system.

The primary data set used to analyze the FOV-dependent spatial misregistration of the HSI system was conducted at two locations during the Ground to Space Calibration Experiment (G-SCALE) [9]. G-SCALE was a joint campaign with the National Research Council of Canada (NRC), Labsphere Inc., MAXAR and the Rochester Institute of Technology (RIT). The HSI system has a spectral range of 400 nm–1000 nm and spectral sampling of 2.23 nm with an average spectral resolution of 5 nm and an IFOV of 0.617 mrad. Figure 4 shows the primary testing site for G-SCALE where the drone flew at an altitude of 103 m resulting in imagery collected at 6.5 cm GSD. The primary site was designed for radiometric and spatial testing [10] and comprised of three black felt-covered panels (1.2 m × 1.2 m in size) with three various mirror configurations. Figure 5 was the secondary site where the drone flew at an altitude of 81.0 m resulting in imagery collected at 5.0 cm GSD. The secondary site was designed for additional spatial testing with large spectral unmixing targets showing two mirror configurations. For both sites, multiple overpasses over the targets were collected and used to analyze spatial misregistration at different parts of the imagers FOV. The spectral unmixing targets were deployed for a separate experiment not to be discussed in this paper.

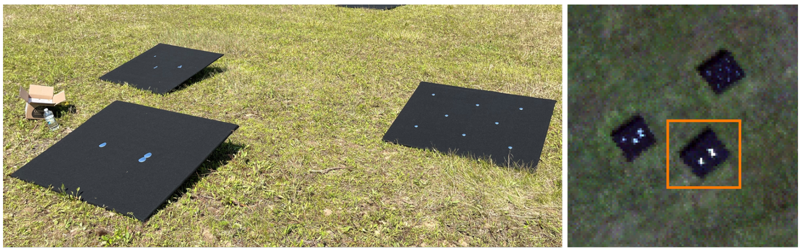

(a) Ground Image **(b)** Drone Image

Figure 4. (**a**) Primary site for G-SCALE where point targets were deployed for radiometric and spatial testing. (**b**) HSI image (RGB bands shown) over the point targets where the orange box highlights the targets used in the analysis.

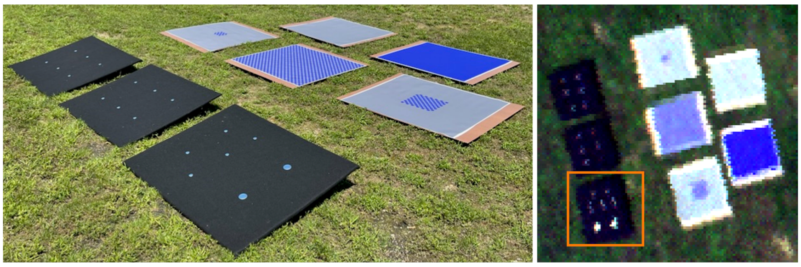

(a) Ground Image **(b)** Drone Image

Figure 5. (**a**) Secondary site for G-SCALE where point and spectral unmixing targets were deployed for additional spatial testing. (**b**) HSI image (RGB bands shown) over the point and spectral unmixing targets where the orange box highlights the targets used in the analysis.

We have been able to extract consistent keystone estimates from a localized region on the focal plane, which demonstrates the repeatability of our presented technique (see the end of Section 3.2). Here, the same HSI system was used as in G-SCALE, but it was flown at an altitude of 63.2 m, resulting in imagery collected at 3.9 cm GSD. Figure 6 shows the deployment area for the various mirror configurations (i.e., single and multiple mirror arrays) on black felt-covered panels. BigMAC was another multi-agency field experiment used to assess the use of HSI systems to validate surface reflectance products for current and future Landsat missions [11]. KBR Wyle, contractor to USGS EROS, South Dakota State University, Rochester Institute of Technology, and Labsphere, Inc. were the main participants in this exercise, where Lambertian panels and convex mirrors were the main field targets.

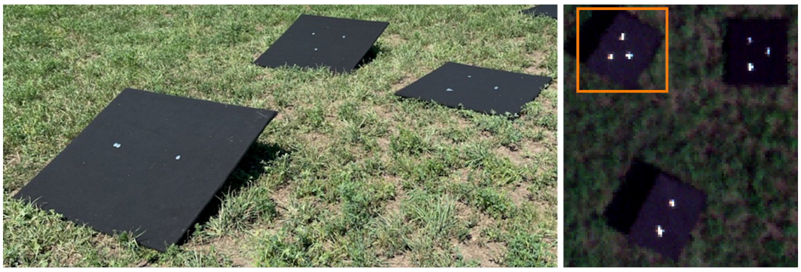

(a) Ground Image **(b)** Drone Image

Figure 6. (**a**) Main site for BigMAC where the primary extraction of surface reflectance for HSI calibration was tested. (**b**) HSI image (RGB bands shown) over the point targets where the orange box highlights the single mirror arrays used in the analysis.

2.2. Sparc Target Overview

To assess spatial misregistration in drone-based HSI systems, the SPecular Array Radiometric Calibration (SPARC) method uses convex mirrors to rely on solar radiation to an imaging system for both radiometric calibration and spatial characterization [12–14]. This paper will have a primary focus on using convex mirrors or point targets for spatial characterization. An initial radiometric assessment of point targets for *drone-based HS imagery* can be found in [9,10]. Spatially, the convex mirrors form a virtual image of the solar disk at the focal plane with a solar-like spectral signature creating a bright, sub-pixel point source. The reflected solar radiation has dependencies on the radius of curvature (R_m) or the focal length ($f_m = R_m/2$), and the solar disk's virtual image can be viewed from any angle within the Field-of-Regard (FOR) [13]. The projected area of the convex mirror (D_m) and R_m define the FOR. Mirror configurations used for all experiments can be found in Table 1. Simple geometric projections of the solar's angular diameter through the convex mirrors can provide estimates of the solar disk's physical diameter (d_{sun}) as seen by an imaging system. Figure 7 illustrates the various geometric relationships for convex mirrors.

Table 1. Mirror configurations used in all field experiments. Various geometrical parameters highlighting the differing properties.

R_m	D_m	FOR	d_{sun}
25 mm	22.9 mm	108.8^o	0.11 mm
50 mm	22.9 mm	52.9^o	0.22 mm
100 mm	45.7 mm	52.9^o	0.44 mm

During the field experiments discussed in Section 2.1, the GSD's at least 3.9 cm or larger, and even for the largest mirror configuration (i.e., R_m = 100 mm), the ratio of d_{sun} to the GSD is 1.1% and smaller for the other mirrors. Thus, when observing the point targets from the drone-based platforms, the resultant image is the SPSF and defines the end-to-end spatial performance of the imaging systems. This includes all blurring factors such as the optical PSF, entrance slit diffraction, the light-sensitive area of a pixel, all forms of motion blur and, any post-processing errors (i.e., interpolation and ortho-rectification inconsistencies). It can be stated that convex mirrors produce an ideal point source and will be the main technique for estimating the spatial misregistration in HSI systems in this study. Furthermore, the SPARC technique will demonstrate the use of multiple points to provide an oversampling technique for multispectral imaging (MSI) systems for more accurate SPSF estimates where ortho-rectification issues are non-existent when compared with the HSI system. For more stable imaging platforms for HSI imaging (i.e., airborne or satellite-based instruments), the oversampling technique can be applied to a localized region within an HS image [15,16].

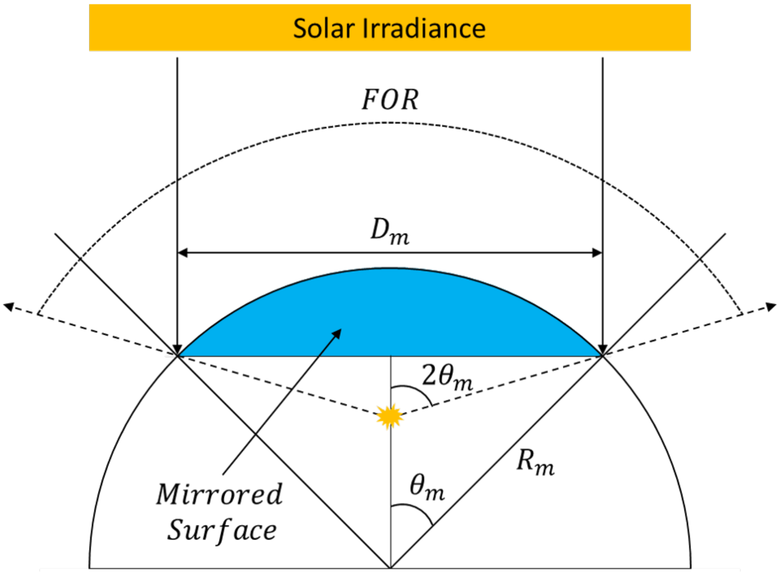

Figure 7. Various geometrical properties of convex mirrors when stimulated by plane waves originating from the sun.

When imaging point targets with pushbroom HSI systems, the second spatial dimension (i.e., the along-track) is captured by platform motion, and GPS/IMU data is used to ortho-rectify a final 2D spatial image where each pixel contains a spectrum. When pushbroom HSI systems are fixed mounted to the moving platform (e.g., the HSI system in this study), the scene reconstruction can be plagued with ortho-rectification errors over areas where complex roll and/or pitch can be experienced. The response time on the GPS/IMU will be the ultimate limit on how much roll/pitch can be experienced without causing massive errors in the final image product. For the reason that motion can plague the imagery used in this study and unrealistic reconstruction can be experienced, using the presented oversampling technique to estimate a more accurate SPSF shape will limit the spatial coregistration error to just keystone and SPSF width. Thus, the proposed solution will be to approximate the HS instruments SPSF with a 2D Gaussian distribution and only focus on the cross-track spatial performance. The HSI system's cross-track performance is related to the instrument's internal imperfections with small amounts of motion blur within the short integration time (e.g., 6 milli-seconds).

2.3. Data Processing and Spatial Analysis Techniques

Most, if not all, of the data examined in this study has been ortho-rectified by 3rd party software that came standard with the HS VNIR instrument under test. This software will, of course, be in question for some of the reasoning behind the artifacts seen in the results; however, uncorrected hyperspectral imagery was assessed to provide confidence in the technique of extracting spatial misregistration from point targets. We observed that for multispectral imaging, multiple mirror targets produced a well-behaved SPSF and errors in ortho-rectified imagery of single mirror targets were mainly due to the instrument and not the software processing over localized regions on the focal plane. There are two procedures for estimating the SPSF, depending on the imaging modality and number of mirrors used in the estimation algorithm. A 2D Gaussian distribution is the main assumption used for modeling the spatial response of aliased imaging systems (i.e., detector-limited imaging). This function is used widely throughout the processing of both multispectral and hyperspectral imagery. However, only the cross-track direction will be discussed, as previously mentioned, for the HSI example.

For multispectral imaging, ortho-rectification of the scene is not required, and all 2D spatial information is captured during the quick integration time (e.g., 4 milli-second integration time). Without the worry of ortho-rectification, multiple mirror targets can be used to oversample the spatial response to form an estimate of the SPSF. The use of multiple mirrors provides the missing information lost when an aliased imaging system observes a scene. The sample phasing of the mirror targets (i.e., sub-pixel location of the point source relative to the square pixels) is taken advantage of in the algorithms proposed by Schiller and Silny [12,14]. On our work here, the algorithm (outline shown in Figure 8) was re-created in Python to perform a multi-point analysis where multiple mirror targets produced an aliased spatial response that can collectively estimate the imaging system SPSF under the assumption of a 2D Gaussian distribution. The double-loop algorithm [12] optimizes a pair of x and y Full-Width at Half Maximum (FWHM) estimates that will minimize the sum of the root mean square error (RMSE) from all target responses. The inner loop uses an initial guess of the x and y FWHM to estimate the center positions of all target responses, then calculates the resulting RMSE. The outer loop varies the directional FWHM for the inner loop and minimizes the sum of RMSEs that fit best with all the target responses. This minimized x and y FWHM defines the 2D Gaussian distribution that fits the collective data best. It will be shown that for aliased imaging systems, the 2D Gaussian distribution produces a well-behaved SPSF estimate for multispectral modalities.

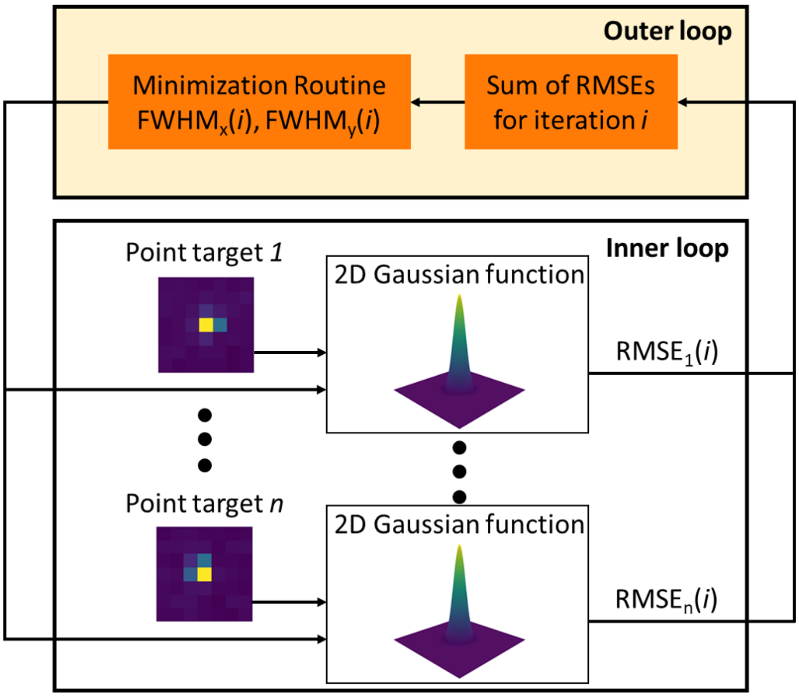

Figure 8. The double-loop algorithm estimates the x and y FWHM by minimizing the sum of the RMSE's from all target responses. The inner loop estimates the targets center position with a fixed x and y FWHM and the outer loop optimizes the directional FWHM until a solution is found.

For hyperspectral imaging, the luxury of using multiple points becomes more complex due to the uniqueness of the spatial response as a function of FOV and the errors that arise related to ortho-rectification. Thus, the mixture of multiple-point targets for any fixed mounted HSI systems cannot be fully justified (see Section 3). Using the 2D Gaussian distribution and a single point target, the first-order approximations to the spatial misregistration of any HSI systems can be calculated. The SPSF signals are fitted using a non-linear optimization function where wavelength-dependent FWHM and center positions are estimated, relieving the spatial misregistration within the HSI system under test, including any FOV dependencies. Only cross-track directional estimates will be the primary focus of this study since this can be tied directly to the instrument's performance with little ortho-rectification dependencies.

Using this fitting routine, the information depicted in the third row of Figure 2 can be dissected into two important parameters defined in the previous two rows. Keystone can be estimated by analyzing the center position in thee cross-track direction as a function of wavelength. When HSI systems image point targets, all wavelengths are measured simultaneously, where displacements in the point target's centroid position can be measured relative to a reference wavelength. In this analysis, all centroid positions are measured relative to the position at wavelength 700 nm because this is the midpoint of the spectral range. Since all point targets are represented by rows and columns with the origin at the top left (i.e., coordinate (0,0)), a positive displacement means the point target was displaced to the right, and a negative value means the point target was displaced to the left.

The SPSF width variability as a function of wavelength can also be assessed from the fitting routine. During the fitting routine, a strict lower limit on the FWHM of 1 pixel can be set based on the limiting blur factor of a single pixel size. For example, an infinitely rst orrst order appr sharp optical PSF convolved with a rectangular pixel will merely blur the edges, and the resulting shape will still resemble a rectangular pixel. However, fixed mounted HSI systems do not strictly follow these rules because ortho-rectification can corrupt and reconstruct unrealistic SPSFs when motion is too complex during flight. This will be demonstrated with various data sets over point targets, where it will be shown that fix mounted HSI systems can undersample scenes that can cause further reconstruction inaccuracies.

Because the SPSF signal is modeled by a 2D Gaussian distribution, a metric for estimating the spatial misregistration (see Section 1) within HSI systems can be easily calculated using only cross-track parameters. Each wavelength has a corresponding 1D Gaussian distribution that is area normalized and is used for this first-order approximation to the coregistration error. A 2D mapping will be shown where each wavelength pair (i.e., (400, 401 nm), (400, 402 nm),..., (400, 1000 nm)) has a corresponding spatial coregistration error with an added colorbar. A histogram of the coregistration error for all wavelength pairs will also be displayed to analyze how the errors are distributed, along with an FOV-dependent observation to understand how they differ.

3. Results and Discussion

Defining a vicarious technique to assess the spatial misregistration is important for understanding the end-to-end spatial performance and application-based limitations of HSI systems. A quantitative analysis of the spatial response of an HSI system to a point source will be discussed with parameters specific to keystone and SPSF width variability. This evaluation will also provide a first order approximation to the spatial coregistration error and a means to evaluate any FOV dependence on the SPSF for cross-track performance only. As previously mentioned, cross-track analysis in pushbroom HSI systems ties directly back to internal performance. Before assessing HSI spatial performance, a multispectral imaging system with a similar IFOV will demonstrate the use of point targets without the need to ortho-rectify the imagery.

3.1. Multispectral Imaging Results—Example

To demonstrate the use of convex mirrors as ideal point targets for extracting an estimate of the SPSF, a simplified experiment was conducted using an MSI system. This experiment will provide confidence in extracting the SPSF when ortho-rectification is not an issue. More importantly, under the assumption that both systems are spatially aliased (i.e., detector-limited imaging), the multi-point analysis of the multispectral system will demonstrate the similarity between the Gaussian distribution and the extracted SPSF. With trust in using the Gaussian distribution for the HSI system, simplifying the experiment (i.e., using only one mirror for spatial performance) can be achieved.

With many observations of the SPSF, sampling artifacts such as aliasing can be mitigated and estimates of the SPSF's unique shape can be extracted and compared with the 2D Gaussian distribution. For this experiment, only the blue channel was used to demonstrate the oversampling technique. The goal of this analysis is to provide reasonable confidence that a 2D Gaussian distribution models an aliased imaging system without the need for ortho-rectification. Figure 9 illustrates our results. Figure 9a shows 16 point targets that were used to build a non-uniformly spaced SPSF. Figure 9b is a 3D representation of the SPSF with the optimized 2D Gaussian distribution.

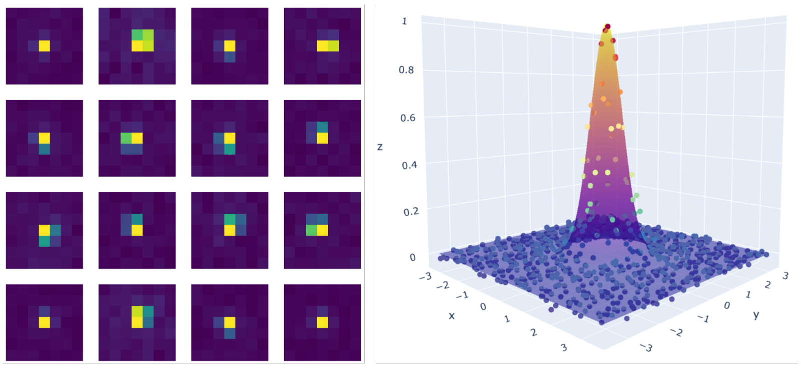

(a) Point Reponses

(b) SPSF

Figure 9. (**a**) The collection of phased point responses used in the creation of the SPSF. (**b**) Final SPSF result when using a 2D Gaussian distribution to centroid multiple point targets into a common reference frame.

To ensure the results focused on the SPSF peak, the image chips were constrained to 7 × 7 pixels and allowed for all enclosed energy to be captured. In addition, a flat-field image derived from an integrating sphere was applied to minimize any Photon-Response Non-Uniformity (PRNU) which slightly improves the RMSE due to the near Lambertian background (black felt). Table 2 contains all the results from this analysis. The major takeaways are the close to unity FWHM, which was expected, the low uncertainty in the FWHM (derived from the fitting routine), and the low RMSE. The small uncertainty in the FWHM can be attributed to the localized region where the point targets were deployed (i.e., only local aberrations and optical PSF) and the fact that the multiple point targets individually represent a collective surface that is the SPSF. A large variation in the FWHM uncertainty would indicate that the individual point responses are in fact different from one another and could not collectively form one SPSF. The low RMSE can be traced back to two factors: the background being uniform with low reflectance and the fact that the unobstructed aperture and detector-limited imaging system can be accurately modelled by a 2D Gaussian surface.

Table 2. Results from estimating the spatial performance of a multispectral imaging system using multiple point targets.

$FWHM\,(Cross-Track)$	$FWHM\,(Along-Track)$	$RMSE$
1.09 ± 0.57%	1.12 ± 0.57%	1.34%

3.2. Estimation of Keystone—Hyperspectral

Keystone has significant impacts on spatially dependent targets, especially when light from the target/background area is spectrally displaced into neighboring spatial pixels. This displacement mixes the spectral components of the target/background such that the resultant spectrum will be non-ideal. More importantly, we will show that keystone error will have FOV dependence such that there is a varying trend across the focal plane, further complicating the issue of spatially separating targets. Figure 10 demonstrates the off-axis behavior of the HSI system under test as the point source moves towards either edge of the focal plane. What can be seen in Figure 10 is that there is very little keystone in the center FOV compared with either edge of the focal plane. These results highlight the problem areas to avoid (i.e., the edge of the focal plane), but also demonstrates the technique's sensitivity in extracting the unique properties of HSI systems.

False-colored images (B-500, G-700, and R-900 nm) were used for displaying the three point targets at the top of Figure 10. Since the solar spectrum peaks around 500 nm, a well aligned system will exhibit a blue tint in the false-colored images. Based on the HSI system's spectral range (400–1000 nm), a reference wavelength of 700 nm was selected to show how the SPSF's relative centroid position varies as a function of wavelength. Major color separation can be seen in the false-colored point target images (at the edges of the FOV), which are reflected by the "S" shaped curves in the plot below the images. A positive value in the graph defines a shift to the right, whereas a negative value defines a shift to the left with respect to 700 nm. An increasing consequence of this analysis is that either side of the focal plane acts oppositely and uniquely, highlighting the usability of mirrors for a vicarious assessment of keystone. Ideally, any imaged point target should not wander about the reference wavelength since this would yield evidence of spatial pixel corruption.

The result at the center part of the FOV illustrates the best scenario since energy is separating minimally from surrounding spatial pixels. This is further highlighted by the overall spread of the SPSF in the images at the top of the graph. Since the fore-optic was more accessible than the internal spectrograph components, the fore-optic data sheet revealed that this particular objective lens suffers from barrel distortion. Objective lenses that suffer from barrel distortion have better on-axis performance than off-axis. This further explains the results seen in Figure 10. Depending on the internal spectrograph design, one can speculate that spherical and/or parabolic mirrors are used to relay the image to the focal plane. These designs can further complicate off-axis behavior [17].

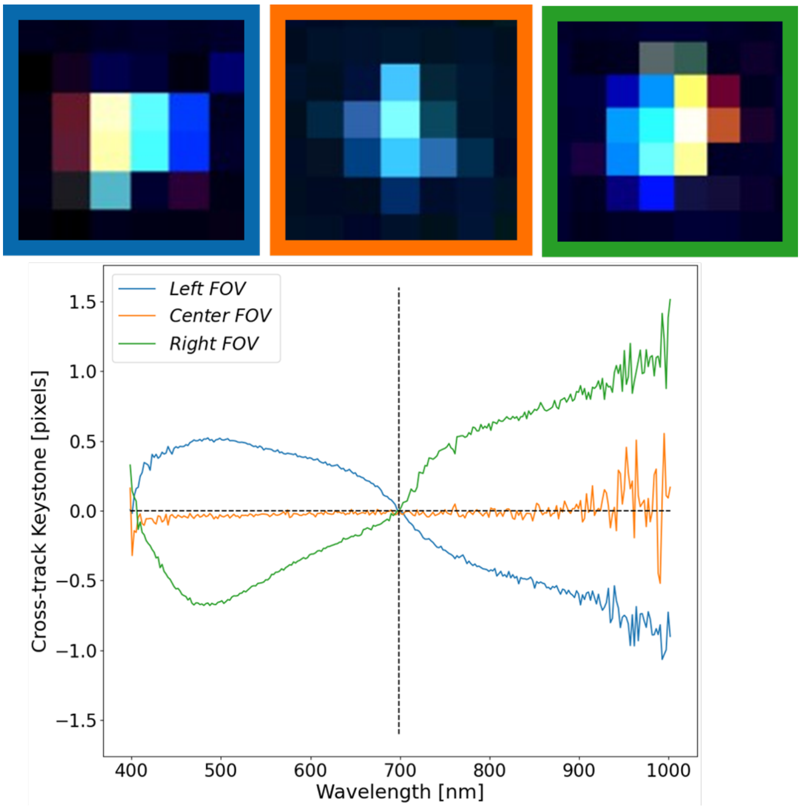

Figure 10. FOV dependency in the cross-track center location (keystone) for three positions of the focal plane. The colored boxes around each SPSF link to the colored curves in the graph below.

Since a pushbroom instrument collects 2D spatial information by forward motion, small regions on the focal plane can be assessed to determine the consistency of the cross-track keystone for well-behaved SPSFs. Figure 11 shows the SPSF keystone between three point targets, all on the right side of the FOV. Even though this is a different data set with unique motion than the data set used in Figure 10, similarities can be easily observed. The slight differences in the cross-track keystone shape seen between Figures 10 and 11 can be attributed to the slight differences where the point targets land on the right side of the FOV. Even with these subtle differences, the consistency in extracting keystone within a localized region and overall trends further demonstrate the uniqueness in using point targets as a method for extracting critical information about instruments used during field experiments .

All three curves trend collectively and demonstrate the repeatability even though the overall shape of the SPSF's look different. Moreover, the ortho-rectification directly impacts the shape of the SPSF's adding error in the cross-track fitting. However, these impacts are inherent in fix mounted HSI systems, where all pixels within a few frames will experience similar behavior. Further investigation needs to be completed on the discrepancies in the along-track center position seen in Figure 11. Since the point sources were offset in the direction of flight, weather impacts and ortho-rectification errors may be deduced from this type of data. An expectation of the along-track center position not being zero and spectrally flat could indicate overall flight and image reconstruction.

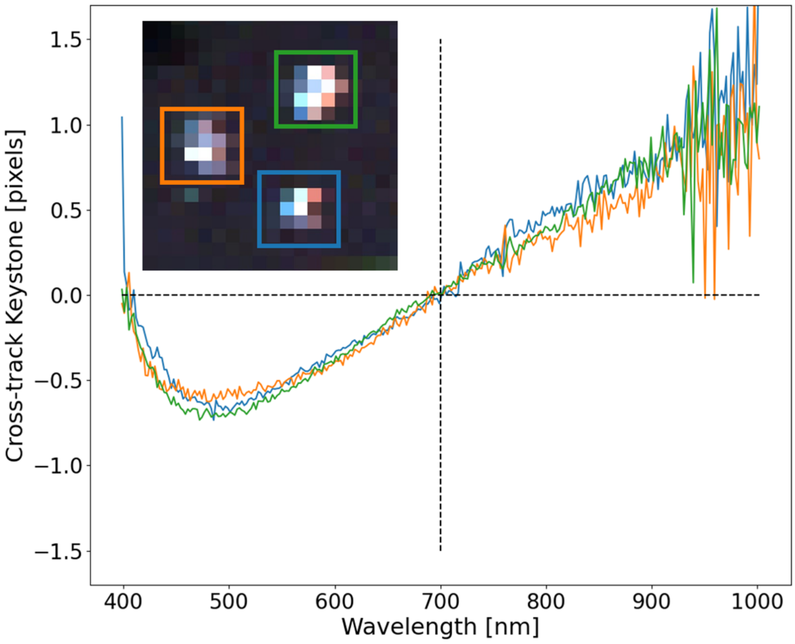

Figure 11. Consistency for the three localized point targets demonstrate the robustness in extracting a vicarious estimate of keystone. Slight ortho-rectification errors can be seen and color separation trends with previous experiments.

3.3. Estimation of SPSF Width Variability—Hyperspectral

The SPSF width is the other important parameter for understanding misregistration in HSI systems. More specifically, for any imaging system, the SPSF width will never be constant due to the nature of diffraction. Moreover, with perfect optics, SPSF width variability will be at best linear and increasing at longer wavelengths (i.e., the Rayleigh criterion). In most HS instrument designs, there tends to be an emphasis on high signal-to-noise ratio (SNR) and spectral separability. Through the analysis of the multispectral imaging system (Section 3.1) and the following discussion, these systems exhibit detector-limited imaging where the SPSF's FWHM is close to unity.

Figure 12 shows the results from extracting the SPSF FWHM at three locations across the focal plane. These are the same point targets from Section 3.2. The FOV center resembles what would be expected for a detector-limited imaging system, where the SPSF's FWHM is close to unity and grows towards 1.5 pixels at longer wavelengths. Noise dominates the estimate of FWHM on either side of the spectral range, but the overall trend demonstrates the SPSF's width variability at the center FOV will dictate spatial resolvability and spectral separability of spatial targets.

When the off-axis point targets are estimated, interesting features can be seen throughout the curves, with similarities and differences between each other. Both off-axis SPSF's have an interesting increase in FWHM around 700 nm, but deviate from each other below

650 nm. The one inconsistency seen throughout all SPSF is within the left FOV FWHM estimate, which dips below 1 pixel. This is physically impossible due to the limiting blur factor of the pixel size (i.e., FWHM cannot be less than 1 pixel) and can be attributed to ortho-rectification errors and an unrealistic reconstruction of the instrument SPSF. This will be further discussed in Section 3.5.

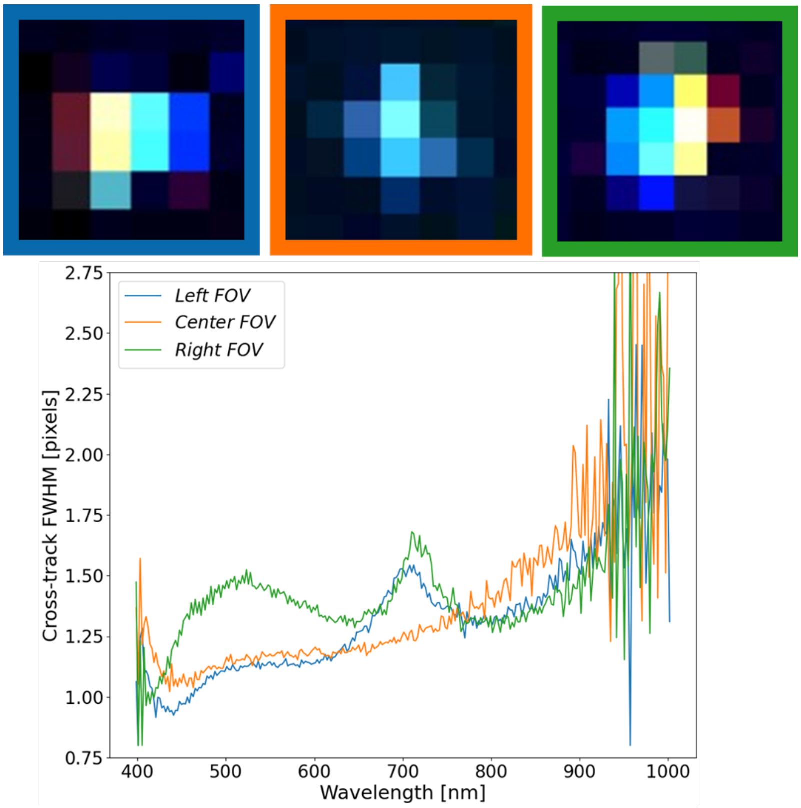

Figure 12. The FWHM of SPSF's at at the FOV edges and center FOV demonstrates uniqueness of the shape and size across the FOV. The SPSF's FWHM at either edge has interesting features around 700 nm, but tend to show that this HSI system is detector-limited with FWHM values close to unity.

The assessment of the FWHM in the cross-track direction as a function of wavelength can highlight the unique behavior of spatial performance and impact scientific applications such as the spectral unmixing of sub-pixel targets. Figure 13 shows the consistency of the cross-track FWHM for two point targets in close proximity with good ortho-rectification. It is important to note that the point target in the orange box is a 2-mirror array aligned in the along-track direction. This has the potential of blurring the along-track FWHM but is still considered a sub-pixel target in the cross-track direction. This result demonstrates the consistency of the SPSF over a small localized region on the focal plane that can be extracted from this technique. These curves trend together between 400 and 800 nm, then slightly deviate after 800 nm due to errors in the fitting procedure and a lack of contrast between the background/target signals.

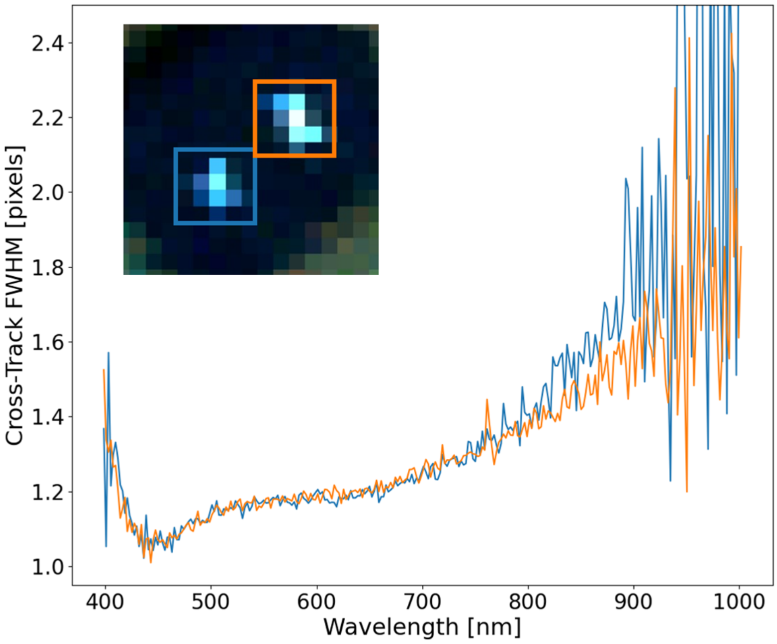

Figure 13. With good ortho-rectification, close point targets exhibit similar FWHM behavior in the cross-track direction and can be tied back to the instruments spatial performance. The colored boxes connect to the curves.

An along-track analysis will not be shown here and will be discussed further in Section 3.5. The fixed mounted HSI system has no active damping, which can drastically manipulate the shape and size of the SPSF in the along-track direction. Furthermore, this can cause inconsistencies in the reconstruction of the SPSF. Moreover, Figure 4a contains a 2-mirror array aligned in the along-track direction, and since the separation between these point sources is 5 cm (image GSD is 6.5 cm), this will elongate the along-track FWHM.

3.4. Estimation of Spatial Coregistration Error—Hyperspectral

As previously discussed in Section 1, spatial coregistration error is a comparative estimate of the shape, size, and location of the SPSF for all wavelength pairs and provides a single metric for HSI spatial misregistration. In this study, only two SPSFs were analyzed (center FOV and the right FOV SPSF) to compare the FOV dependence on misregistration extracted from field experiments. This study was specifically designed to create a fast and simple approximation to estimating the spatial coregistration error using only a single SPSF response and a Gaussian fit. This approximation can highlight the size and location related to spatial misregistration where the unique shape will be (somewhat) lost because only the optimized Gaussian distribution is used. The unique shape is an important parameter since any asymmetry could have a dramatic effect on the spatial coregistration error; however, non-aliased SPSF's require a multi-point analysis, which can be troublesome with fixed mounted HSI systems.

Figure 14 shows an example of quantifying the HSI misregistration for the HSI system under study by calculating the spatial coregistration error. The center and right FOV SPSFs from Sections 3.2 and 3.3 were used to demonstrate how the keystone and FWHM estimates come together into a wavelength pair metric for a more simplistic look at spatial misregistration. The spatial coregistration error was calculated using the FWHM and centroid position (cross-track only) derived from the Gaussian fitting routine, and both were smoothed consistently to lower dependencies on the noise at the longer wavelengths.

Quantifying spatial misregistration (Figure 14) provides a wealth of knowledge about the end-to-end performance of the HSI system by characterizing how well a point source is deposited onto the focal plane and is directly linked to the instrument's spatial performance. These single metrics provide a user with a fast and simple calculation to assess how the

HSI instrument focuses light originating from a sub-pixel point source. The small image chips in Figure 14 show the false-colored image (B-500, G-700, and R-900 nm) for visually understanding why the right FOV is worse than the center FOV. The overall color separation is indicative of misregistration, and the neighboring spatial pixels are corrupted more at the right FOV than at the center FOV.

Initial observations of the similarly scaled heat maps in Figure 14 clearly highlight optimal performance of the HSI system at the center part of the FOV. Spatial coregistration error calculated from single point targets clearly demonstrates the uniqueness of this technique for assessing spatial misregistration during field experiments. Small targets are greatly affected by spatial misregistration because optical features such as keystone distort their spectra unrealistically and make it more difficult to compare with materials extracted from spectral libraries or, in this case, extracted from differing parts of the FOV. This technique provides a user-friendly solution to assess trouble areas of the FOV where optical features could corrupt application performance. Skauli (2012) provides the initial theoretical framework for including spatial coregistration error into an example involving the difference between two spectra and how this can influence the perceived spectral signature. The use of spatial coregistration error in applications can provide additional thresholds that are unique to the instrument's capability to spatially resolve spectral targets from background or cluttered areas.

There are many important features in the spatial coregistration heat maps and histograms that require further discussion. The main takeaway is that the ideal performance of the HSI system is on-axis based on the low average spatial coregistration error, where the spatial width is the limiting factor. Performance will smoothly vary and gradually get worse as one images closer to the edges of the FOV, as demonstrated. The apparent bounding box seen in the Right FOV heat map example is entirely due to keystone dominating the spatial coregistration error calculation (to be further explored in Figure 15).

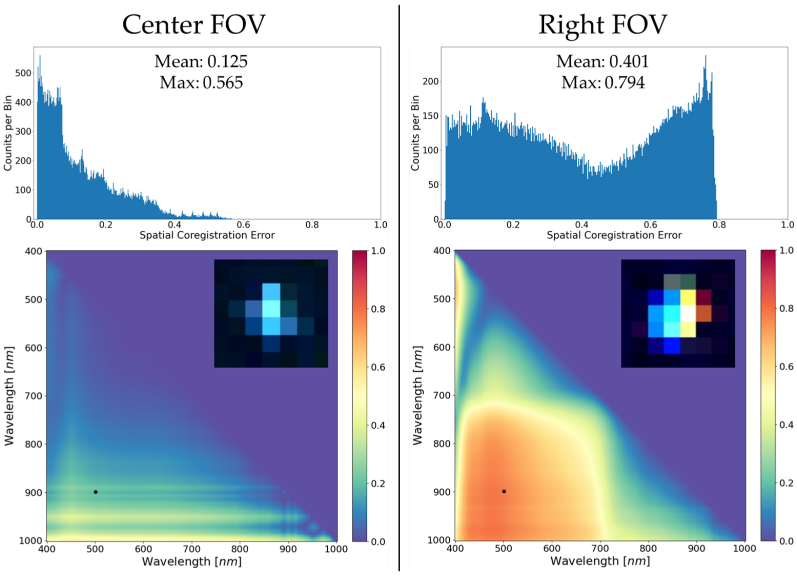

Figure 14. Examples of spatial coregistration error and how off-axis effects greatly degrade the image resolution and separability of targets from background in the area surrounding the SPSF's. The histograms summarize the range and spread of the spatial coregistration errors with mean and max values. The heat maps at the bottom are a visual representation of spatial coregistration error for all wavelength pairs and is mirrored about the $y = x$ axis (i.e., wavelength pair (400, 401 nm) is equivalent to (401, 400 nm)). Black dots within the heat maps represent a specific wavelength pair to be discussed.

To further highlight features within the spatial coregistration error example (i.e., Figure 14), example plots of Gaussian distributions used in the error calculation (Equation (1)) for wavelength pair (500, 900 nm) are seen in Figure 15. For the reason the Center FOV example contains differing spatial misregistration than the Right FOV example, Figure 15 also highlights why large spatial coregistration error is experienced at the edge of the focal plane.

Illustrated in Figure 15 are the area normalized Gaussian distributions for wavelength pairs of 500 nm and 900 nm derived using the parameters estimated in Figures 10 and 12. Since the Center FOV example contains mainly spatial width dependence, the distributions are overlapping and only vary in height and width (i.e., SPSF at 900 nm is wider than SPSF at 500 nm). Whereas in the Right FOV example, there is over 1 pixel of keystone, but both distributions have similar spatial widths. If we observe Equation (1), the spatial coregistration error is a difference between area normalized SPSFs (i.e., in this case, Gaussian distributions fitted to point targets). By observation, the disjointed SPSF's Figure 15b of similar width will lead to a larger error than the overlapping SPSFs Figure 15a of varying width.

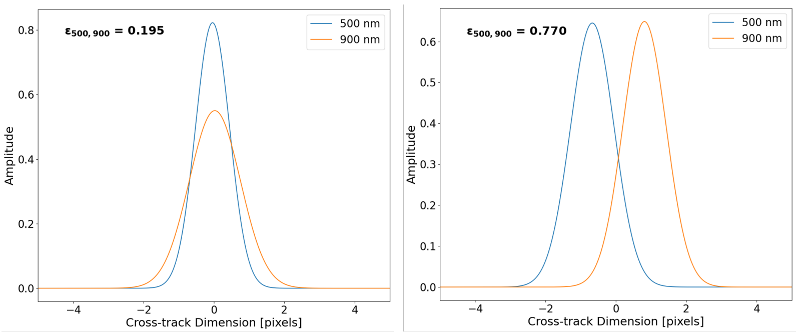

(a) Center FOV **(b)** Right FOV

Figure 15. Two examples of area normalized Gaussian distributions for wavelength pair (500, 900 nm) extracted from the spatial coregistration error example with their respective error values in bold text. (**a**) Due to small keystone, the leading contributor to spatial misregistration is FWHM differences. (**b**) Large keystone error contributes greatly to the spatial coregistration error for wavelength pairs with similar FWHM.

3.5. Ortho-Rectification Impacts—Hyperspectral

As with all pushbroom HSI systems, ortho-rectification is required to reconstruct the observed scene. This process is extremely dependent on the stability of the airborne platform, GPS/IMU accuracy, and Digital Elevation Mapping (DEM). Unless the HS instrument is actively damped with a gimbal mount, the ground targets of interest can be oversampled or undersampled based on the drone's pitch and roll. The results in this section will highlight observations made on point targets that were not correctly reconstructed and provide further insight on what a pushbroom HSI system is observing. Using point targets (i.e., convex mirrors) provides an easy technique to assess ortho-rectification impacts in all imagery collected and has the potential to highlight the loss of scene content.

Before displaying corrupted imagery, a short study on the impacts of ortho-rectification on a well-behaved point target will be assessed. Figure 16 represents the comparison between a raw, uncorrected image and its ortho-rectified version. Due to the fixed mounting of the HSI system under test, this is not always possible because, as will be discussed at the end of this section, the imaging system can roll and/or pitch aggressively as it images point targets, which corrupts the target in the unortho-rectified imagery. Figure 16 demonstrates that the ortho-rectification process can preserve the instruments spatial performance for well-behaved SPSF's. There is slight deviations at the lower wavelength range that can originate from a tighter SPSF being more susceptible to motion throughout the imaging process than a wider SPSF.

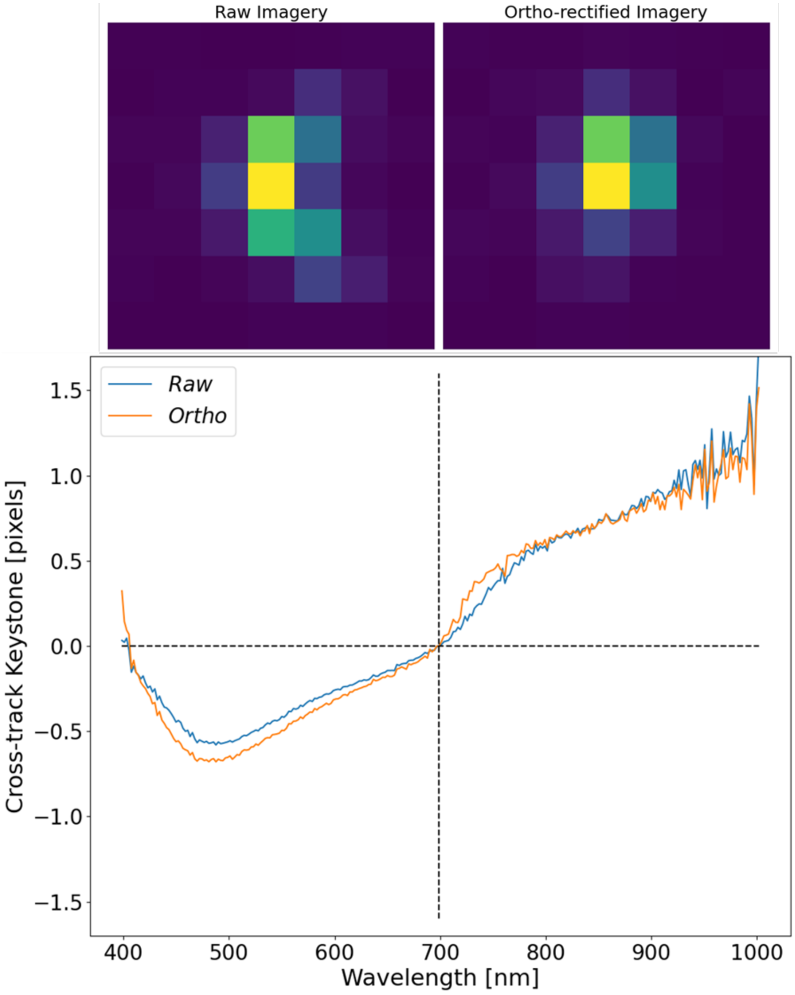

Figure 16. The top of the graph shows images of the same SPSF (raw and ortho-rectified) displayed at a single wavelength of 550 nm. The results from estimating keystone with respect to 700 nm show how minimal impacts from ortho-rectification affect the displacement of the SPSF as a function of wavelength.

To show the inconsistent ortho-rectification, due to complex motion blur, a side study was conducted with two similar point sources imaged multiple times within a small time period, as seen in Figure 17. What this image shows are two separate flight lines over the same target with dramatic differences in shape, size, and extent of the SPSF. Chaotic pitching of the drone can under or oversample the scene, causing severe smearing and issues in the ortho-rectification that cannot be completely fixed without active damping. These issues are always present in fixed mounted HSI systems and will impact the spatial/spectral separability of in-scene targets.

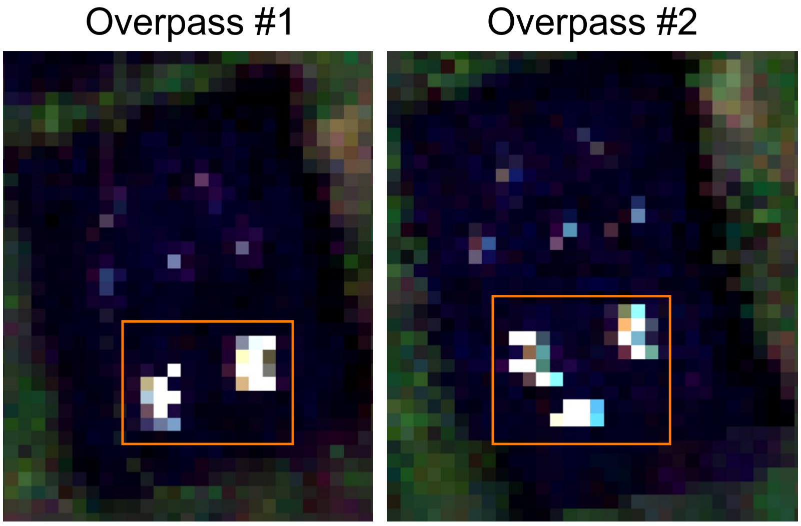

Figure 17. Inconsistent ortho-rectification over the same point targets from two different flight lines. The orange boxes highlight the targets of interest and only two mirrors were present, but Overpass #2 falsely contains three. Reprinted/Adapted with permission from Ref. [10]. © 2022 IEEE.

For fix mounted HSI systems, motion can cause scenes to be under- or oversampled and can be easily observed when imaging sub-pixel spatial targets (i.e., convex mirrors). Ortho-rectification is always required to create 2D square pixel imagery, but this can be misleading because ground coverage is highly dependent on frame rate and motion between frames. Missing ground coverage requires interpolation, and without additional information, this is, at best, guesswork when creating the final HS imagery. Figure 18 shows an example of undersampling the image scene that was highlighted in Figure 4. The three main targets were not sampled properly due to aggressive pitching and rolling over that area (Figure 18a) where the targets seemed squashed and the targets in the orange box only have a single row of data. The ortho-rectified image (Figure 18b) contains about 2× more pixel data over the same area with the targets inside the orange box being elongated in the cross and along-track direction.

Ortho-rectifying undersampled scenes inherently requires interpolation to recover the missing area in the along-track direction. The recovered pixels, therefore, cannot be directly linked to the scene's physical quantities due to the lack of observed photons. This has major implications when the imagery is used for scientific applications such as small target detection or sub-pixel spectral unmixing. The interpolation process alone cannot recover the lost information, and these artifacts can be hidden without sub-pixel calibration targets (i.e., convex mirrors). The radiometric and spatial interpretation of this imagery cannot be trusted, and the point targets described in this paper provide a method to understand this process due to their sub-pixel nature. As more applications move towards sub-pixel detection, it is critical that these artifacts are understood, and the only method for doing this is using the presented convex mirrors.

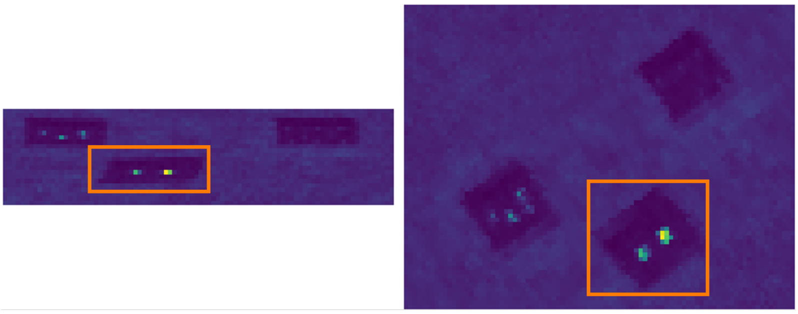

(a) Raw Imagery **(b)** Ortho-rectified Imagery

Figure 18. A comparison between raw and ortho-rectified imagery for a scene that was undersampled due to the motion of the drone and fix mounted setup of the HSI system. (**a**) Raw imagery showing the undersampled area in the orange box. (**b**) The resulting ortho-rectified image of the same area.

Oversampling the image scene presents the other end of motion-induced artifacts. This issue is not as damaging to the underlying physics because there is an excess of information or duplication that requires reduction. The problem with too much information is that the ortho-rectification process has to deal with reducing the imagery without over-fitting. Figure 19 shows an example of when point targets are oversampled and is highlighted by the orange boxes. The small point targets begin to resemble line sources in the raw imagery because the change in pitch/roll angle synchronizes with the forward motion of the drone. Furthermore, the point targets in the raw imagery highlight how a sub-pixel target would be reconstructed in the ortho-rectified image. Thus, the method provides for quality checks over targets of interest.

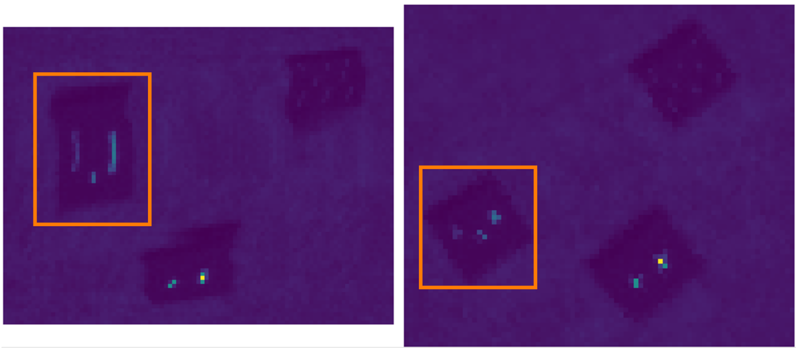

(a) Raw Imagery **(b)** Ortho-rectified Imagery

Figure 19. An example of a small area over the point targets that was oversampled by the drone motion. (**a**) Raw imagery with a small area that was oversampled highlighted in the orange box. (**b**) The ortho-rectified version with the orange box highlighting the same target area.

For any fixed mounted HSI systems, motion will plague the image scene with the potential of misrepresenting the physical properties to be observed. The point targets provide a method for understanding how the raw imagery was collected for quality assurance checks. For the reason that these mirrors represent a sub-pixel target having absolute radiometric and spatial properties, there is a potential to unitize point targets as a vicarious technique for diagnosing ortho-rectification errors over an area containing scientific targets of interest. Future research efforts are focused on using the unique capability of convex mirrors, which have a known spectral radiance signature, as a technique to address ortho-rectification errors.

4. Conclusions

Estimating the spatial performance of an HSI system requires extensive laboratory equipment, including collimators, bright illumination sources, and high-accuracy translation stages. The SPARC technique was proposed for estimating the spatial performance of HSI and MSI systems during field experiments without an expensive laboratory setup. In this study, the novel approach to assessing hyperspectral misregistration, using mirror targets, was demonstrated during UAV field experiments of varying altitudes and GSD's. It was shown that spatial parameters such as SPSF width and keystone that contribute to spatial misregistration, can be easily extracted from field data using only a single mirror target. Not found in previous literature is a vicarious technique to bridge the gap between laboratory and field-based HSI performance testing and comparison, with a focus on extracting hyperspectral spatial misregistration. Diagnostic testing, spatial validation, and FOV dependencies are an added benefit to the deployability of point targets during field experiments. In addition, this technique can provide vital information about the ortho-rectification process and its limitations for scientific applications requiring sub-pixel detection methods. An awareness as to how imaging systems perform during field experiments is critical for advancing the understanding of collected data quality for all scientific applications. The experiments and analysis presented in this paper are also directly applicable to airborne or satellite-based imaging platforms where point targets provide a sub-pixel spatial response.

Author Contributions: Conceptualization, D.N.C. and E.J.I.; methodology, D.N.C.; software, D.N.C.; validation, D.N.C. and E.J.I.; formal analysis, D.N.C.; investigation, D.N.C.; resources, D.N.C.; data curation, D.N.C.; writing—original draft preparation, D.N.C.; writing—review and editing, D.N.C. and E.J.I.; visualization, D.N.C.; supervision, E.J.I. All authors have read and agreed to the published version of the manuscript.

Funding: This research received no external funding.

Data Availability Statement: All relevant data can be requested by contacting corresponding authors.

Conflicts of Interest: The authors declare no conflicts of interest.

Abbreviations

The following abbreviations are used in this manuscript:

SPSF	Sampled Point Spread Function
HSI	Hyperspectral Imaging
MSI	Multispectral Imaging
HS	Hyperspectral
m	meters
cm	centimeter
nm	nanometers
mrad	milliradians
GSD	Ground Sampling Distance
IFOV	Instantaneous Field-of-View
FWHM	Full Width at Half-Maximum
FOV	Field-of-View
1D	One Dimensional
2D	Two Dimensional
3D	Three Dimensional
VNIR	Visible Near-Infared
CMOS	Complementary Metal–Oxide–Semiconductor
SPARC	SPecular Array for Radiometric Calibration
RMSE	Root Mean Square Error
GPS	Global Positioning System
IMU	Inertial Measurement Unit
B, G, R	Blue, Green, Red

References

1. Ientilucci, E.J.; Conran, D.N.; Soffer, R.J.; Perry, D.L.; Skauli, T.; Gilchrist, J.R.; Durell, C. Development of test methods for hyperspectral cameras characterization in the P4001 standards development. In *Proceedings of the Algorithms, Technologies, and Applications for Multispectral and Hyperspectral Imaging XXVIII*; Velez-Reyes, M., Messinger, D.W., Eds.; International Society for Optics and Photonics: Bellingham, WA, USA, 2022; Volume PC12094, p. PC1209402. https://doi.org/10.1117/12.2623490.
2. Høye, G.; Fridman, A. Spatial misregistration in hyperspectral cameras: Lab characterization and impact on data quality in real-world images. *Opt. Eng.* **2020**, *59*, 084103. https://doi.org/10.1117/1.OE.59.8.084103.
3. Qian, S.E. *Optical Satellite Signal Processing and Enhancement*; SPIE: Bellingham, WA, USA, 2013. https://doi.org/10.1117/3.1000981.
4. Skauli, T. Quantifying coregistration errors in spectral imaging. In *Proceedings of the Imaging Spectrometry XVI*; Shen, S.S., Lewis, P.E., Eds.; International Society for Optics and Photonics: Bellingham, WA, USA, 2011; Volume 8158, p. 81580A. https://doi.org/10.1117/12.894699.
5. Skauli, T. An upper-bound metric for characterizing spectral and spatial coregistration errors in spectral imaging. *Opt. Express* **2012**, *20*, 918–933. https://doi.org/10.1364/OE.20.000918.
6. Torkildsen, H.E.; Skauli, T. Full characterization of spatial coregistration errors and spatial resolution in spectral imagers. *Opt. Lett.* **2018**, *43*, 3814–3817.
7. Mouroulis, P.; Thomas, D.A.; Chrien, T.G.; Duval, V.; Green, R.O.; Simmonds, J.J.; Vaughan, A.H. *Trade Studies in Multi/Hyperspectral Imaging Systems Final Report*; Technical Report: Jet Propulsion Laboratory: La Cañada Flintridge, CA, USA, 1998.
8. Casey, J.T.; Kerekes, J.P. Misregistration impacts on hyperspectral target detection. *J. Appl. Remote Sens.* **2009**, *3*, 033513.
9. Russell, B.J.; Soffer, R.J.; Ientilucci, E.J.; Kuester, M.A.; Conran, D.N.; Arroyo-Mora, J.P.; Ochoa, T.; Durell, C.; Holt, J. The Ground to Space CALibration Experiment (G-SCALE): Simultaneous Validation of UAV, Airborne, and Satellite Imagers for Earth Observation Using Specular Targets. *Remote Sens.* **2023**, *15*, 294. https://doi.org/10.3390/rs15020294.
10. Conran, D.; Ientilucci, E.J. Interrogating UAV Image and Data Quality Using Convex Mirrors. In Proceedings of the IGARSS 2022-2022 IEEE International Geoscience and Remote Sensing Symposium, Kuala Lumpur, Malaysia, 17–22 July 2022; pp. 4525–4528.
11. Hedler, D.; Maddox, E.; Mann, J.; Leigh, L.; Raqueno, N.; Gerace, A.; Rehman, E.; Conran, D.; Bauch, T.; Falcon, L.; et al. Landsat Surface Product Validation Instrumentation: The BigMAC Exercise. *Remote. Sens. Environ.* **2023**, *In review*.
12. Schiller, S.J.; Silny, J. The Specular Array Radiometric Calibration (SPARC) method: A new approach for absolute vicarious calibration in the solar reflective spectrum. In *Proceedings of the Remote Sensing System Engineering III*; Ardanuy, P.E., Puschell, J.J., Eds.; International Society for Optics and Photonics: Bellingham, WA, USA, 2010; Volume 7813, p. 78130E. https://doi.org/10.1117/12.864071.
13. Schiller, S.J. Specular Array for Radiometric Calibration and Method. U.S. Patent 8158929 B2, Apr. 17, 2012 .
14. Silney, J.F.; Schiller, S.J. Method and System for Vicarious Spatial Characterization of a Remote Image Sensor. WO 2013/019180 AL, Feb. 7, 2013.
15. Schiller, S.; Silny, J. *Using Vicarious Calibration to Evaluate Small Target Radiometry*; CALCON; Raytheon Company: Waltham, MA, USA, 2016.
16. Ortiz, J.D.; Avouris, D.; Schiller, S.; Luvall, J.C.; Lekki, J.D.; Tokars, R.P.; Anderson, R.C.; Shuchman, R.; Sayers, M.; Becker, R. Intercomparison of Approaches to the Empirical Line Method for Vicarious Hyperspectral Reflectance Calibration. *Front. Mar. Sci.* **2017**, *4*, 296. https://doi.org/10.3389/fmars.2017.00296.
17. Bentley, J.; Olson, C. *Field Guide to Lens Design*; Field Guides; SPIE: Bellingham, WA, USA, 2012.

Disclaimer/Publisher's Note: The statements, opinions and data contained in all publications are solely those of the individual author(s) and contributor(s) and not of MDPI and/or the editor(s). MDPI and/or the editor(s) disclaim responsibility for any injury to people or property resulting from any ideas, methods, instructions or products referred to in the content.

Appendix C

Small Target Radiometric Performance of Drone-based Hyperspectral Imaging Systems

Article

Small Target Radiometric Performance of Drone-based Hyperspectral Imaging Systems

David N. Conran [1,*], Emmett J. Ientilucci [1,*], Timothy D. Bauch [1] and Nina G. Raqueno [1]

[1] Chester F. Carlson Center for Imaging Science, Digital Imaging and Remote Sensing Laboratory, Rochester Institute of Technology, 54 Lomb Memorial Drive, Rochester, NY 14623, USA
* Correspondence: dnc7309@rit.edu (D.N.C); ejipci@rit.edu (E.J.I)

Abstract: Hyperspectral imaging systems frequently rely on spectral rather than spatial resolving power for identifying objects within a scene. A hyperspectral imaging systems response to *point targets* under flight conditions provides a novel technique for extracting *system-level radiometric performance* that is comparable sub-pixel spatial unresolved objects. The system-level analysis not only provides a method for verifying radiometric calibration during flight, but also allows for the exploration into the impacts on small target radiometry, post orthorectification. Standard Lambertian panels do not provide similar insight due to the insensitivity of orthorectification over a uniform area. In this paper, we utilize a fix mounted hyperspectral imaging system (radiometrically calibrated) to assessment 8 individual point targets over 18 drone flight overpasses. Of the 144 total observations, only 18.1% or 26 instances were estimated to be within the uncertainty of the predicted entrance aperture-reaching radiance signal. For completeness, the repeatability of Lambertian and point targets were compared over the 18 overpasses where the effects of orthorectification drastically impacted the radiometric estimate of point targets. The unique characteristic point targets offer, being both a known spatial and radiometric source, is that they are the only field-deployable method for understanding the small target radiometric performance of drone-based hyperspectral imaging systems.

Keywords: Small target radiometry; radiometric performance; point targets; hyperspectral; imaging; small unmanned aircraft systems; UAS; UAV; convex mirrors

Citation: Conran, D.N.; Ientilucci, E.J.; Bauch, T.D.; Raqueno, N.G. Small Target Radiometric Performance of Drone-based Hyperspectral Imaging Systems. *Remote Sens.* **2023**, *1*, 0. https://doi.org/

Received:
Accepted:
Published:

Publisher's Note: MDPI stays neutral with regard to jurisdictional claims in published maps and institutional affiliations.

Copyright: © 2024 by the authors. Submitted to *Remote Sens.* for possible open access publication under the terms and conditions of the Creative Commons Attribution (CC BY) license (https://creativecommons.org/licenses/by/4.0/).

1. Introduction

For drone-based imaging platforms, radiometric calibration is accomplished using Lambertian targets (*i.e.*, Empirical Line Method (ELM) [1,2]) or a physics-based approach (*i.e.*, At-Attitude Radiance Ratio (AARR) [3,4]). Both techniques have the goal of compensating and calibrating remote sensing imagery to surface reflectance. The transformation of remote sensing imagery to surface reflectance more readily aids in the identification of materials.

During typical field data collection campaigns, the relative reflectance of Lambertian calibration targets are measured with respect to reference panels of high reflectivity (*e.g.*, 99% Spectralon^{TM}). Absolute radiometric information of these panels, albeit calibration targets or reference panels, requires additional effort and complexity, however. The complexities resides in the understanding of the *true reflectance* of any Lambertian panel (in the field) in the presence of directional and hemispherical sources of illumination, for example [5]. That said, an advantage of field-deployed Lambertian targets is their large spatial extent where statistical averaging can be employed to improve the signal-to-noise (SNR) of calibration curves for reflectance transformation. Even though high SNR can be achieved over Lambertian targets, these calibration curves are blindly applied to *spatially unresolved targets* and often *not Lambertian* [6]. Assessing the small target radiometric performance from Lambertian calibration targets can not be achieved due to their needed size and many sub-pixel limitations are hidden within their high uniformity.

A physics-based approach to reflectance calibration uses remote sensing principles to transform imagery from entrance aperture-reaching spectral radiance to surface reflectance without in-scene calibration targets. The AARR technique uses the fundamental assumption that all objects in the scene are Lambertian reflectors such that the instantaneous measurements of the downwelling spectral irradiance (with a spectroradiometer) and object spectral radiance (with HSI system) can be used to estimate surface reflectance [4]. An advantage of this technique is the ability to correct hyperspectral (HS) imagery without in-scene calibration targets. However, this heavily relies on the calibratability of both instruments and ability to accurately match different instruments (*e.g.,* spectroradiometer to an HSI system). This calibration approach is limited to surface reflectance transformation and no research has demonstrated the ability to examine HS radiometric performance.

Key design trade-offs for HSI systems prioritize radiometric sensitivity and spectral resolution over spatial acuity resulting in spatially aliased imagery [6]. This puts more reliance on the spectral identification of spatially unresolved objects within the scene. The application space that challenges HSI systems is within the detection of sub-pixel or *small targets* [7]. Within this application space, small targets can not be averaged over multiple pixels like an extended target (*e.g.,* Lambertian calibration target). Furthermore, extracting small target radiometric performance from Lambertian targets does not provide adequate analysis in comparison to the application space [8]. Thus, an emphasize now exists on radiometric performance of HSI systems in the presence of sub-pixel or small targets. The deployment of point targets allows users the ability to radiometrically examine collected imagery for troubleshooting both their instrument and post-processing techniques (*e.g.,* orthorectification process). From what we have seen, no other vicarious technique can support the analysis and understanding of HS imagery for applications involving small targets. Furthermore, there is a lack of vicarious techniques for assessing the radiometric accuracy and performance of orthorectified products at the pixel level for drone-based HSI systems.

The only vicarious method that can investigate the radiometric performance of HSI systems to radiometrically known small targets is the SPecular Array for Radiometric Calibration (SPARC) technique [9]. The SPARC technique produces a radiometrically accurate *point target* for assessing the small target radiometric performance of imaging systems. More importantly, when assessing the small target radiometric performance of a drone-based HSI system, we note that orthorectification is required as a post-processing step for mapping pixel location to a true ground position at a uniform pixel scale. Unfortunately, there are inaccuracies within this post-processing step from interpolation schemes (*e.g.,* nearest-neighbor) related to the assumption of uniform pixel scale (*i.e.,* that every pixel is square) [10]. Furthermore, inaccuracies accumulate from platform motion, HS mounting schemes, boresight offsets, sensor models, resolution scales within Digital Elevation Models (DEM), and the absolute accuracy of Global Positioning Systems (GPS) / Inertial Measurement Units (IMU). All these inaccuracies manifest into an aggregate system level problem that requires evaluation utilizing field experiments and can not be addressed separately due to the unforeseen correlations. Testing, characterizing, and understanding these system level effects, using the SPARC method, as it relates to small target radiometric performance, is thus the subject of this paper.

This paper is outlined as follows. Section 2 gives a background overview of our drone-based imaging platform and laboratory validation efforts of the HSI system. It then goes into detail about the theory behind the quantities that formulate the SPARC technique from a radiometric and spatial perspective. Section 3 speaks to the experiment overview including methodologies used in field measurements and extraction of the radiometric signals related to Lambertian and point targets. Section 4 presents results where Lambertian and point targets are assessed over the entire experiment. In this section, radiometric performance of small targets, after orthorectification, is scrutinized. Lastly, Appendix A and Appendix B outlines a full derivation of the SPARC equation (*i.e.,* entrance aperture-reaching spectral radiance) and the propagated uncertainty.

2. Background

2.1. Equipment Overview

The Digital Imagery and Remote Sensing (DIRS) Laboratory at the Rochester Institute of Technology uses a revolutionary multi-modal UAV payload for remote sensing applications. This includes the simultaneous observation of four different imaging modalities which includes Visible-Near Infrared (VNIR) hyperspectral and multispectral cameras, a Long-Wave Infrared (LWIR) camera and a Light Detection and Ranging (LIDAR) sensor (see Figure 1). This drone-based payload provides for an indispensable resource for solving challenging remote sensing problems includes those which are the subject of this paper. Specifically, the hyperspectral drone mounted instrument under investigation was the VNIR HSI systems. Raw imagery was collected and pre-processed which accounts for dark offsets, dark currents, and dark signal non-uniformity. Flat-fielding was performed after dark corrections. This includes photon response non-uniformity, irradiance fall-offs and signal non-linearity. The final pre-processing step includes a radiance correction that converts digital numbers (DN) to spectral radiance. Lastly, all HS imagery was orthorectified and interpolated [11].

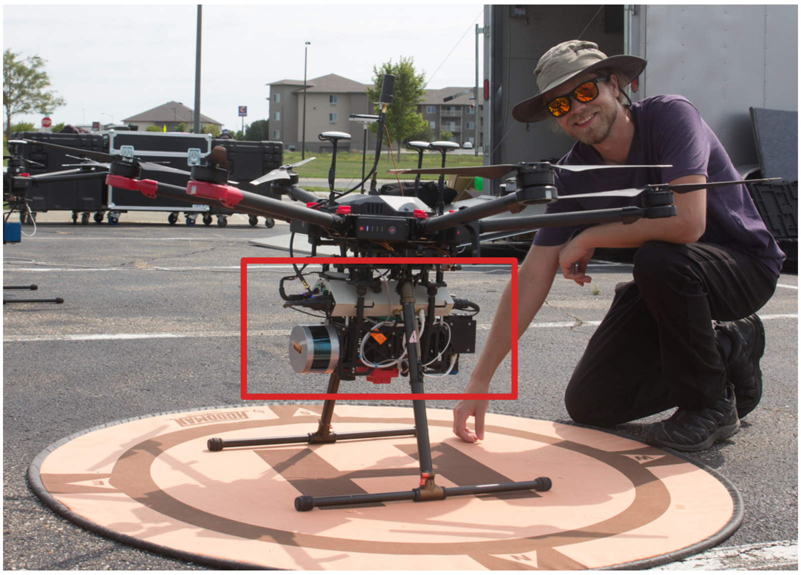

Figure 1. The MX1 imaging payload, highlighted within the red box, is fix mounted to a DJI Matrice 600 PRO UAV.

As is standard practice within the DIRS Laboratory, all radiometric instruments are internally verified with a NIST-traceable Labsphere Inc. 20-inch integrating sphere. The typical routine for validating radiometrically calibrated instruments involves observing the NIST-traceable Quartz-Tungsten Halogen (QTH) lamp ($\sim \pm 1\%$ (k=2) in the VNIR) at four different light levels [12]. The radiometric validation demonstrates that the HSI system under investigation in this paper is well calibrated to spectral radiance within the expected uncertainty (see Figure 2). The absolute uncertainty of the HSI system under test in this study was not known at the time of validation, however, based on the knowledge of our integrating sphere, the spectral radiance measured with the HSI system can be accurately estimated to be within $\pm$ 5%. During all our outside experiments, we assumed that our HSI system holds this uncertainty and is consistent across the Field-of-View (FOV).

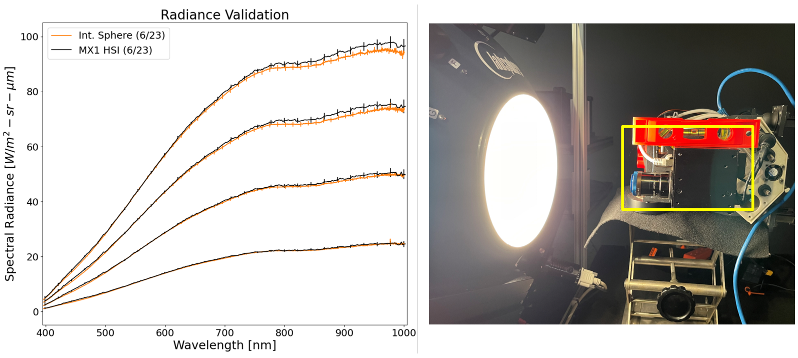

Figure 2. Validating the HSI system against the NIST-traceable integrating sphere at four different light levels. Agreement is within the expected uncertainty as can be seen in the plot.

Other field equipment (*e.g.*, an ASD field spectroradiometer) was also used during our experiments for predicting the at-aperture reaching spectral radiance of point targets. The ASD was also cross-validated using our integrating sphere and holds an absolute uncertainty of approximately ± 2% across the VNIR spectrum. The ASD instrument was used to measure the total downwelling spectral irradiance (utilizing an advanced cosine corrector) and provides atmospheric monitoring capabilities that ensures consistency of the point target predictions.

2.2. Field Irradiance Measurement Theory

Predicting the entrance aperture-reaching spectral radiance from point targets relies on both the total downwelling irradiance and the amount of diffuse sky contributing to the measured signal [5]. In this section we define the field irradiance measurement followed by the formal spectral radiance description of a point targets in Section 2.3.

The ASD field spectroradiometer uses an advanced cosine corrector (*i.e.*, optical diffuser with a collecting solid angle of 2π steradians) to measure the total downwelling irradiance, $E_T(\lambda)$. This can be represented mathematically as

$$E_T(\lambda) = E_{solar}(\lambda) + E_{sky}(\lambda) \tag{1}$$

where $E_{solar}(\lambda)$ is the direct solar irradiance and $E_{sky}(\lambda)$ is the sky irradiance. We assume no additional scattering from surrounding objects such as vegetation or man-made objects. To account for the contribution from the sky irradiance into the point targets spectral radiance signal, the sky irradiance term must be estimated. Without a precise instrument to perform this task (*i.e.*, rotating shadowband radiometer which performs shading), the sky irradiance can be estimated manually by blocking (*i.e.*, shading) the solar disk with a black object attached to a pole [13]. Even though this provides a good estimate of the Global-to-Diffuse Ratio, a side shaded measurement would improve the accuracy. Side shading corrects for the signal lost during the sun-blocked measurement. This method was not implemented, however, we did take into account conservative estimates of uncertainty [14].

With estimates of the total downwelling irradiance and the sky irradiance (*i.e.*, the shaded measurement), the *Global-to-Diffuse Ratio* ($G(\lambda)$) can be defined as

$$G(\lambda) = \frac{E_{sky}(\lambda)}{E_T(\lambda)} = \frac{E_{sky}(\lambda)}{E_{solar}(\lambda) + E_{sky}(\lambda)} \tag{2}$$

Equation (2) is the fractional contribution of the sky irradiance to the total downwelling irradiance and includes the instantaneous scattering properties of the atmosphere [15].

2.3. Imaging Point Targets: Radiometric and Spatial Response

Imaging point targets (*i.e.,* SPARC) with remote sensing instruments has been in development since 2010 [8,9,15,16] with more recent engineering advances, by Labsphere Inc., to bring an automated calibration service to the satellite community [17–21]. Further advancements have been explored by the Rochester Institute of Technology on the application of point targets for drone-based HSI systems [22,23]. In this section we will summarize the radiometric and spatial response of an imaging system to a point target. A full derivation related to the radiometric properties of convex mirrors is presented in Appendix A.

A point target is created by the virtual image of the solar disk created by a convex mirror. The convex mirror has intrinsic properties defined by the surface reflectance ($\rho_m(\lambda)$), radius of curvature (R_m) and clear aperture diameter (D_m). For remote imaging systems, a convex mirror (*i.e.,* point targets) gives us both a radiometric and spatial calibration target which is discussed below.

When downwelling irradiance ($E_T(\lambda)$) illuminates a convex mirror, a virtual solar image is formed at the focal length (*i.e.,* $f = -R/2$). In addition to reflected solar irradiance, a considerable amount of sky irradiance (defined by $G(\lambda)$) is observed. A point target is radiometrically defined by its spectral radiant intensity, $I_m(\lambda)$, off the surface of the mirror. The mirror's spectral radiant intensity is propagated to entrance aperture-reaching spectral radiance ($L_{EAR}(\lambda)$) as

$$L_{EAR}(\lambda) = {}^{1}\!/_{4}\rho_m(\lambda)R_m^2\left[1 - G(\lambda)\cos\left(2\theta_m\right)\right]\frac{E_T(\lambda)}{GSD^2} \tag{3}$$

where $G(\lambda)$ is the Global-to-Diffuse Ratio, $2\theta_m$ defines the angle between virtual solar image and optical axis and GSD is the imaging systems ground sampling distance. This equation has the following assumptions: the atmospheric transmission loss from target to sensor is assumed to be negligible for UAV altitudes [3], both the solar irradiance and $G(\lambda)$ are measured throughout the experiment, and the ground sampling distances are related to square pixels. In addition, path radiance is negated from a point targets signal during the image extraction and will be further discussed in Section 3.3. Note that if $\cos\left(2\theta_m\right)$ goes to zero (*i.e.,* the mirror reflects the entire hemisphere), there is no need to measure the sky irradiance or estimate $G(\lambda)$ because the ASD field spectroradiometer will be measuring the same solid angle that the mirror reflects.

An imaging systems spatial response to point targets is defined by the Sampled Point Spread Function (SPSF). Because the SPSF can be measured with convex mirrors during field experiments, the SPSF estimate will include not only the optical system and detector contributions, but also motion blur, jitter and post-processing artifacts from orthorectification. Post-processing artifacts will be defined as orthorectification radiometric errors and will contribute to the small target radiometric performance analysis. Theoretically, the SPSF has an infinite spatial extent, but the imaging systems Noise-Equivalent Irradiance (NEI) and point target signal intensity will ultimately limit the spatial extent of the SPSF. As long as the observed signal from a point target is bright enough, the energy lost to noise will be negligible.

3. Methodology

3.1. Experiment Overview

In this section we will estimate the spectral radiance of point targets (with a fix mounted HSI system) so as to demonstrate the usability of convex mirrors to understand the energy conservation (or lack thereof) within orthorectified imagery.

Our experiment was designed to use industry standard Lambertian targets and point targets to investigate the radiometric properties of orthorectified HSI imagery. The Lambertian targets include three field-deployable Permaflect panels, manufactured by Labsphere Inc., with an average hemispherical reflectance factor of 7% (dark gray), 25% (gray) and 50% (white). The point targets were protective aluminium coated convex mirrors with a

12.5mm radius of curvature (-50mm focal length) and average specular reflectance (*i.e.,* spectrally flat) greater then 85% from Edmund Optics. All properties related to the mirrors were identical (*i.e.,* radius of curvature and reflectance) and independently measured by Labsphere Inc.

During collection the drone made simple down and back overpasses with all targets deployed close to the center of the sensors FOV. The drone flew at a nominal height of 32m resulting in a nominal GSD of 2.1cm. The integration time was optimized (*i.e.,* spectral signal peaks around 75% saturation) to 5.5ms from a nadir observation of a secondary 50% Permaflect panel prior to take-off. The overpasses began at 11:15 am local time with all 18 overpasses completed within 8 minutes. The solar zenith at the time of collection was 42 degrees. All images used were orthorectified using the same DEM, instrument calibration data, and processing software.

Both the point target configuration and Lambertian target layout can be seen in Figure 3. The Lambertian panels were placed off to the side of the point targets. The larger dark gray and white panels were 1m x 1m in size whereas the gray panel was 0.5m x 1m. With a GSD of 2.1cm, there is a minimum of 23 full pixels on the panels. The point targets are identified by a mirror ID. For example, the label 12.5MM-2 denote a mirror number 2 with a radius of 12.5mm. The point targets were deployed on a low reflectance (roughly 2%) background panel (0.9m x 1m) in groupings of four with a minimum of 14 pixels between mirrors. The ASD field spectroradiometer, not shown in this image, was placed nearby in the middle of a cleared field away from the experiment area.

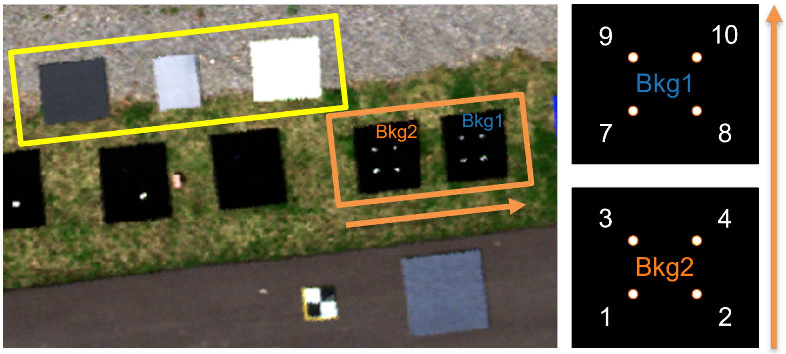

Figure 3. The Lambertian targets are within the yellow box and the point targets (*i.e.,* convex mirrors) are within the orange box. The orange arrow in both images helps define mirror placement within the imagery. The image on the right depicts mirror placement and assigned mirror ID which is linked to descriptive mirror properties and subsequent results (*e.g.,* 12.5MM-2).

3.2. Field Irradiance Measurements

The spectral radiance from a point target is dependent on two field measurements: the the total downwelling irradiance (Figure 4a) and the sky irradiance (Figure 4b). The sky irradiance measurement will be used to estimate the Global-to-Diffuse Ratio, as previously mentioned. Both the field measurements contained a 2% uncertainty on the radiometric calibration and additional contributions from variations in illumination over the duration of the experiment. The illumination variation was estimated by assessing the deviation of both measurements during the 8 minute experiment. This was a small contribution to the field measurement uncertainty compared to the assumed 2% calibration uncertainty. As can be seen in Figure 4, the black curves demonstrate a low percent variation in total downwelling irradiance and atmospheric conditions during the experiment. Any changes in atmospheric conditions, such as clouds or particulate scattering, would be captured in both measurements.

As mentioned in Section 2.2, the sky irradiance was measured by shading the ASD's cosine corrector from the solar disk. The shadowing device was a square piece of wood covered in black felt (similar to the mirror background material).

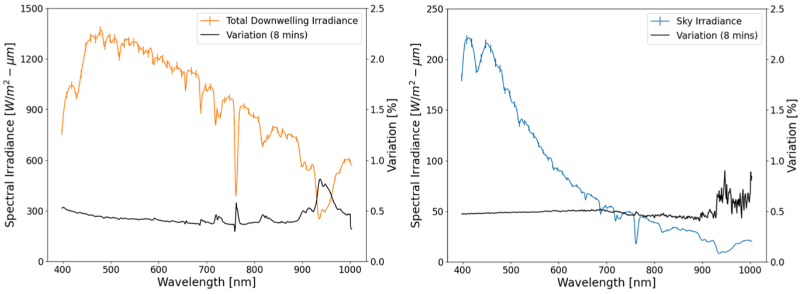

(a) Total Downwelling Irradiance **(b)** Sky Irradiance

Figure 4. The total averaged downwelling irradiance **(a)** and averaged sky irradiance **(b)** were measured during the experiment at 1 second intervals. The black curves are variation estimates of both signals over the 8 minute experiment.

Estimating the point targets entrance aperture-reaching spectral radiance was defined in Eq. (3). The total downwelling irradiance can be used directly whereas Eq. (2) defines the Global-to-Diffuse Ratio. Figure 5 contains the two field measurements used to estimate the predicted point target spectral radiance (*i.e.*, Eq. (3)). Depending on the amount of diffuse sky reflected into the sensors FOV, the point targets will have a similar spectral shape as the total downwelling irradiance. The convex mirrors merely act as an attenuator of the reflected energy as a function of mirror coating and mirror geometry. Since all mirrors were in close proximity, all point target signal estimates use the same total downwelling irradiance and Global-to-Diffuse Ratio. The only difference is in the modification of the Global-to-Diffuse Ratio based on the unique mirror geometries (*i.e.*, θ_m).

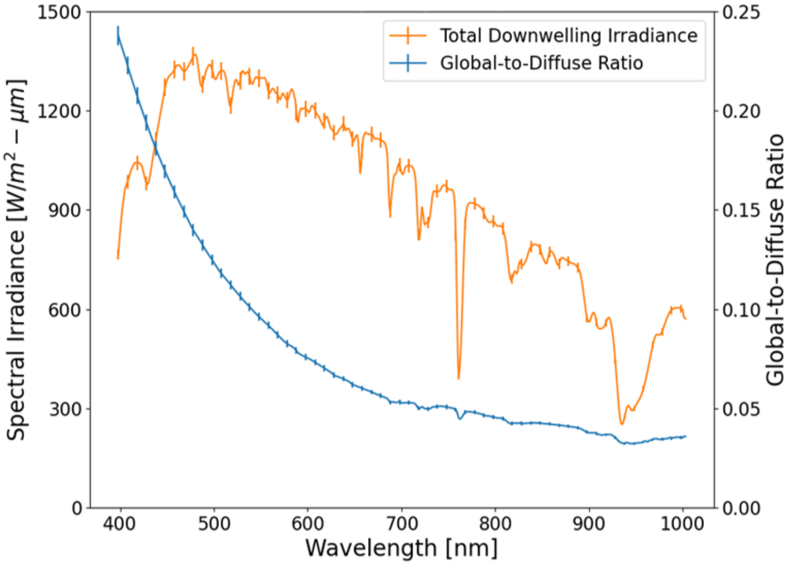

Figure 5. The Total Downwelling Irradiance and the Global-to-Diffuse Ratio are used to make an estimate of the point target spectral radiance. The corresponding uncertainties are shown as vertical error bars for each plot.

3.3. Data Processing and Analysis

For each mirror, we predict the entrance aperture-reaching spectral radiance, using Eq. (3), which is then compared to the collected HS, radiance calibrated, imagery. The uncertainty of Eq. (3) can be derived and evaluated by following the Guide to Uncertainty Measurement framework [24]. This requires taking the partial derivative of Eq. (3) with respect to all variables assuming small variations about the mean and negligible non-linear behavior. When all the variables have an estimated absolute uncertainty, the combined uncertainty for the entrance aperture-reaching spectral radiance from a point target can be estimated. The derivation of uncertainties, related to Eq. (3), can be found in Appendix B. Table 1 provides an example of the maximum relative uncertainty of all input variables as well as the predicted entrance aperture-reaching spectral radiance.

Table 1. Example of relative uncertainties for all input variables, left of vertical bar, along with the estimated relative combined uncertainty (*i.e.*, predicted entrance aperture-reaching spectral radiance), right of vertical bar.

$\frac{u(\rho_m)}{\rho_m}$	$\frac{u(R_m)}{R_m}$	$\frac{u(D_m)}{D_m}$	$\frac{u(G)}{G}$	$\frac{u(E_T)}{E_T}$	$\frac{u(GSD)}{GSD}$	$\frac{u_c(L_{EAR})}{L_{EAR}}$
3%	2%	2%	2.06%	2.05%	3%	8.01%

The predicted entrance aperture-reaching spectral radiance (Figure 6a) and its respective uncertainty (Figure 6b) is plotted for each mirror. Mirror-to-mirror variations are less than 4% across the VNIR spectrum. It was determined that the mirror reflectance and radius of curvature were the main contributors to this difference. In this investigation, when comparing two different mirrors, we should not observe differences in radiometric signal more than the mirror-to-mirror variation. The assumed 2% uncertainty in the radiometric calibration of the ASD field spectroradiometer results in the uncertainty resembling the point target signal. The relative combined uncertainty of the spectral radiance predictions is around 8%, as seen in Table 1.

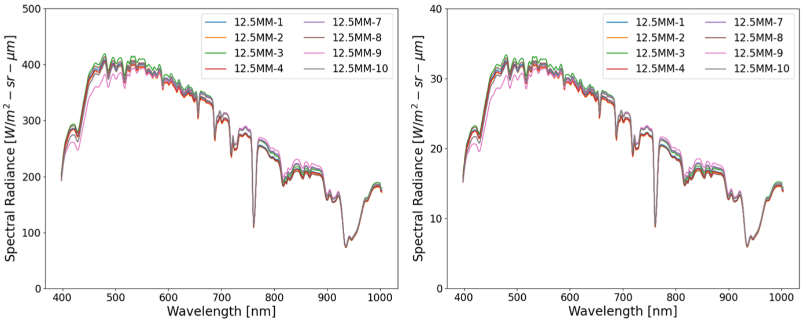

(a) Predicted $L_{EAR}(\lambda)$ **(b)** Predicted $u_c(L_{EAR}(\lambda))$

Figure 6. The predicted entrance aperture-reaching spectral radiance **(a)** and the combined uncertainty **(b)** for all mirrors examined in this experiment. The point target entrance aperture-reaching spectral radiance represent the energy reflected to the sensor.

The permaflect panels shown in Figure 7 demonstrate two key concepts about the experimental conditions, consistency and repeatability. The consistency and repeatability of the spectral radiance reflecting off the panels from the 18 overpasses demonstrates the stability of the atmosphere and the HS instrument. It is important that the stability of the atmosphere is well-understood with measurements from the ASD field spectroradiometer and reflected signals off the Lambertian targets. The measurement variation observed in Figure 4 (*i.e.*, black curve) and the tight signal variations reflected off the Lambertian targets over the 18 overpasses (Figure 7) demonstrates this stability. It is critical that the HS instrument and atmosphere are stable during this investigate so as to eliminate these factors that could potentially contribute to additional variation in the predicted entrance aperture-reaching spectral radiance of point targets.

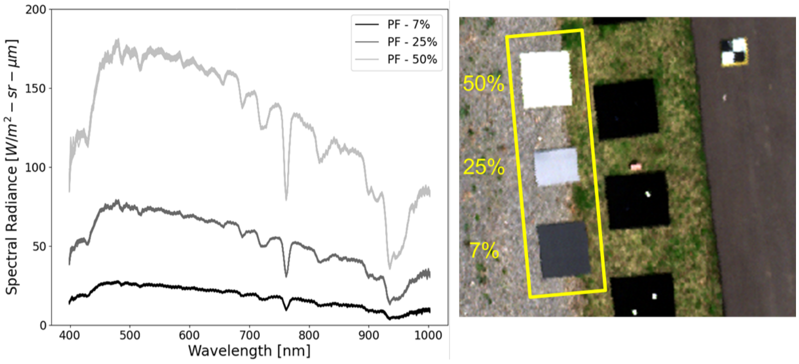

Figure 7. The spectral radiance from each Permaflect panel observed during the experiment is displayed as a grouping of the 18 overpasses. The signal variations reflected off each Permaflect panel is indistinguishable for a given panel reflectance.

The mirror background signal is an additive contribution to the point targets signal and is subtracted during the point target extraction process. The mirror background spatial uniformity and reflectance contributes to the ability to accurately isolate the point target predicted spectral radiance. The low reflectance background (*i.e.*, $\sim$ 2% average hemispherical reflectance) provides the best scenario for optimizing extraction accuracy. It is critical to fully understand the backgrounds stability and spatial variation during the experiment for this could lead to a signal bias in the point target. Figure 8 contains an average spectral radiance measurement of the two mirror backgrounds, “Bkg1” and “Bkg2”. For each overpass, the mirror background is extracted at the center of the panel and averaged over roughly a 5 x 5 pixel box. The black felt material used to construct the multi-layer mirror background provides for excellent spatial uniformity (*i.e.*, has volumetric scattering properties).

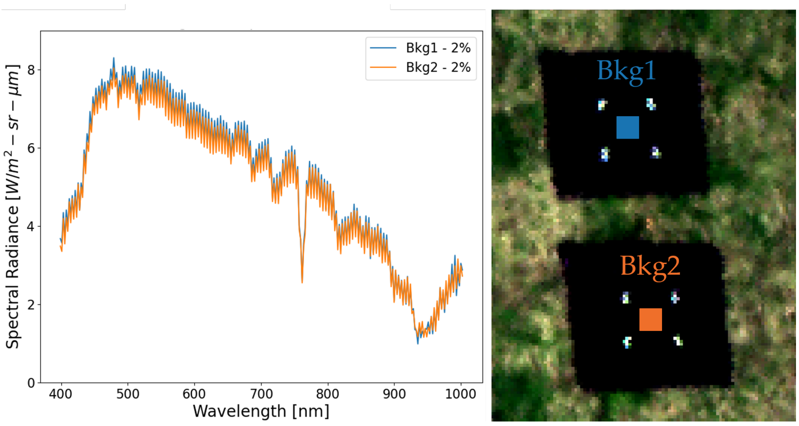

Figure 8. The spectral radiance of the mirror backgrounds (right) are extracted and plotted (left). Even though there is little variation between the background panels, the background subtraction is kept separate. The saw-tooth structure within the spectral radiance is an artifact of the HS sensor and is only observed at low radiance signals where read-noise dominates.

The point target entrance aperture-reaching spectral radiance can be isolated from the backgrounds by defining a small bounding box around the point target that contains all the measurable signal. Equation (4) defines the *ensquared energy* from a point target, over a bounding box with N pixels, after an average background signal is subtracted.

$$L_{mirror}(\lambda) = \sum_{p=1}^{N} \left(L_{img}(p,\lambda) - \overline{L_{bkg}(\lambda)} \right) \tag{4}$$

An overlooked feature within Eq. (4) is the averaged background subtraction. This process is critical for extracting only the point targets signal. We also note that background subtraction process additionally eliminates the path radiance, including adjacency effects. Because the point target produces a spatial response of the imaging system, the ensquared energy is spread over the SPSF and only the ensquared energy can be compared to the predicted entrance aperture-reaching spectral radiance as defined in Eq. (3). Figure 9 illustrates the result of Eq. (4) where a point target within an optimized bounding box highlighted in orange is summed after background subtraction. If the background signal is accurately estimated, a varying bounding box will not contribute to the ensquared energy, but will only impact the noise within the signal (*i.e.,* Bienaymé's identity). Because small targets will be assessed in a similar way as the point targets, the ensquared energy defines the *limit of radiometric target detection from a background.*

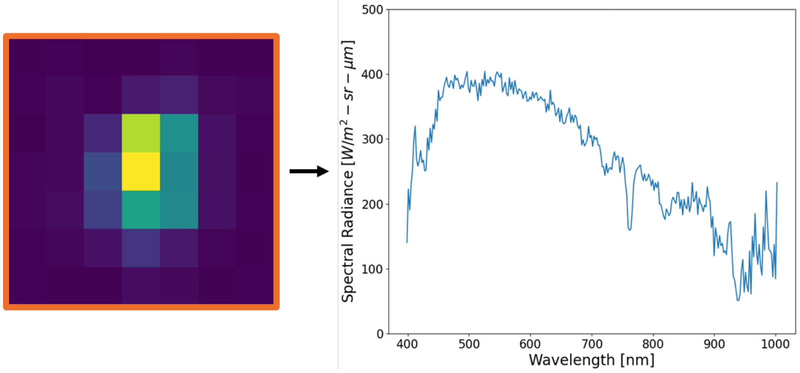

Figure 9. The summation of a point target over the SPSF (left) defines the ensquared energy and can be connected to the predicted entrance aperture-reaching spectral radiance. The spectral radiance for the observed ensquared energy on the left is plotted on the right.

4. Results and Discussion

In this section we discuss three main aspects of our results. Firstly, we compare the standard deviation of all 8 point targets to all Lambertian targets across all 18 overpasses. This provides the first glimpse into the radiometric stability between the two methods. This is then followed by examining how a point target (*i.e.,* convex mirror) manifests itself before and after orthorectification across all 18 overpasses. Next, we focus the attention on radiometric accuracy concerns for a handful of point target observations. Lastly, we investigate the spectral inconsistencies introduced into point target spectral radiance after orthorectification.

In our analysis below, standard orthorectification processes were assumed. However, the exact process and interpolation schemes are irrelevant to fully understand and quantify the results because point targets provide for a "black box" approach. In fact, instrument and post-processing anonymity further demonstrates the usefulness of the SPARC technique. Nothing more than the ground sampling distance (GSD) is required to characterize small target radiometric performance. Analyzing the unorthorectified imagery provides a baseline to determine how much energy was originally collected for comparison to orthorectified results. More importantly, the observed spatial pattern of point targets helps to aid in the discussion of the observed results.

The experimental design was key for extracting two types of results discussed in this section and are highlighted in Figure 10. When the small point target is imaged over multiple frames (*e.g.,* over 18 overpasses), the *radiometric repeatability* of small targets can be examined, see Figure 10a. Whereas, when two similar point targets are imaged together, as in Figure 10b, over a small region, the radiometric stability from orthorectification can be assessed. Both assessment strategies will allow for the investigation of radiometric errors induced on point targets by platform motion and orthorectification. Over the entire experiment, 8 point targets were imaged during 18 overpasses, this accounts for 144 point target observations in total. Of the 144 observations, only 26 point targets (or 18.1%) were within the uncertainty of the predicted entrance aperture-reaching spectral radiance, at a 95% confidence level.

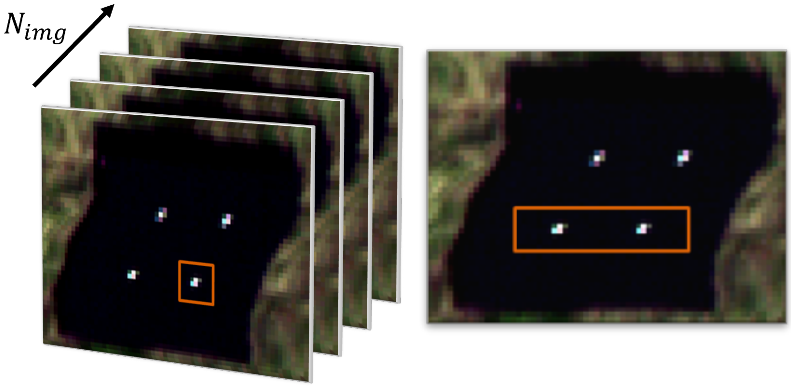

(a) Multiple Images **(b)** Single Image

Figure 10. Point targets were examined from two perspectives: **(a)** tracking a single mirror over the 18 overpasses and **(b)** comparing mirror pairs from a single image.

4.1. Overall Point Target Performance

When assessing the use of new technology (*i.e.,* point targets) for the use of investigating the radiometric accuracy of drone-based HSI systems, it is critical to compare results to standardize methods (*i.e.,* Lambertian targets). In the experimental plan, Lambertian panels were deployed that spanned roughly 2% to 50% reflectance to compare image-to-image radiometric stability. Figure 11a illustrates the spectral radiance standard deviation of each mirror given 18 observations (*i.e.,* overpasses). Figure 11b illustrates the spectral radiance standard deviation of a single pixel, for each of the four Lambertian panels, given 18 observations. Even though all the point targets are similar (*i.e.,* mirror-to-mirror variation less than 4%), their standard deviations are significantly greater than the Lambertian targets that span the detectors dynamic range (*i.e.,* HSI system was optimized for a 50% reflector).

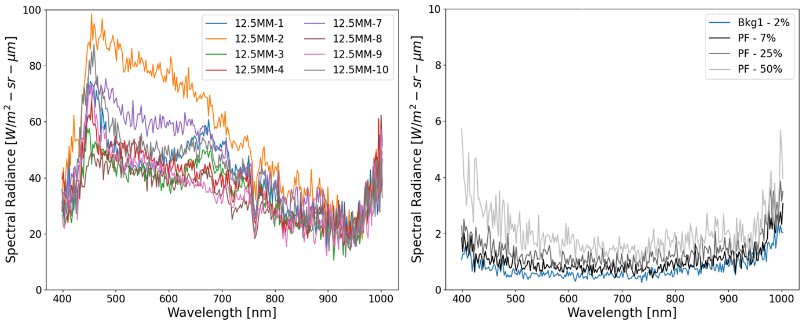

(a) Point Targets **(b)** Lambertian Targets

Figure 11. Assessing the measurement dispersion within orthorectified imagery of each point target **(a)** and the Lambertian targets **(b)** across the 18 overpasses. The Lambertian targets shown little variation compared to the point targets.

Within Figure 11, the general spectral shapes requires further explanation. Excluding values at both ends of the wavelength range (*i.e.,* close to 400 nm and 1000 nm), we see a significant trend of worsening measurement dispersion at the bluer wavelengths for point targets. We speculate the reasoning for this is the interplay between orthorectification and the wavelength dependent SPSF sharpness (Figure 12) [23]. Depending on how the point target is imaged, the orthorectification struggles with sharper targets compared to targets having a larger spatial extent. This trend continues until the target becomes much larger than the SPSF or, in this comparison, a Lambertian target where the image-to-image repeatability is small (see Figure 11b). Radiometric errors induced by orthorectification on small targets not only exists for the point targets, but will manifest in any small target within the scene. Insight on these observations and the ability to extract radiometric inconsistencies of small targets is only possible with high contrast point target (i.e., mirrors). Further wavelength dependent orthorectification errors will be discussed in Section 4.3.

A lesser known effect that may account for the unreal spectral features seen in the point target results in Figure 11a, is the potential for polarization sensitivity. As mentioned in Section 2.3, the point targets are convex mirrors coated with protected aluminium. The aluminium layer is a metal thin film and has the potential to reflect polarized light up to the sensor at specific solar zenith angles. Since the HSI system has a reflective holographic grating, there is inherent grating efficiency for the various polarization states. If the HSI system re-imaged the point target at various polarization states and orthorectified to a single target, the observed spectral features could potentially exist in the results shown in Figure 11a [15,25].

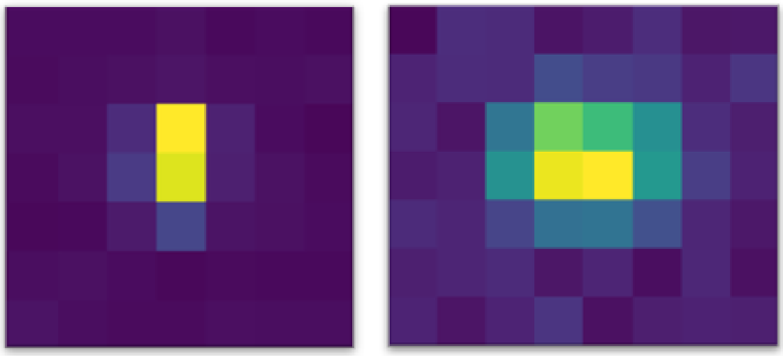

(a) 443 nm **(b)** 844 nm

Figure 12. Orthorectified point response at **(a)** 443 nm and **(b)** 844 nm illustrates the wavelength dependent SPSF size for convex mirror, 12.5MM-2. The sharpness of the SPSF impacts the radiometric performance after orthorectification.

Figure 13 is a observation of a single mirror's spectral radiance across the 18 over-passes. When observing the difference between the unorthorectified (top) and orthorectified (bottom) imagery, a general trend exists: the absolute radiometric signal of small targets is generally over-estimated for a fixed mounted HSI systems. This observation is seen for all the point targets with the exception of a few outliers, to be discussed in Section 4.3, even though the spectral radiance is underrepresented in the unorthorectified image. The main contribution to this over-estimation is orthorectification errors induced by platform motion (*e.g.*, re-imaging the same point target) and interpolation artifacts within the orthorectification process (*e.g.*, pixel values manipulated).

A concluding thought on the results and statements presented in this section relate to the predicted entrance aperture-reaching spectral radiance and the GSD dependence. Equation (3) has an inverse squared dependence on the GSD. This is important to recognise because of the inherent roll/pitch and motion smear from the drone. This physically manifests in a larger GSD compared to the orthorectified pixel. For a predicted entrance aperture-reaching spectral radiance, this would result in an over-predication compared to the observed data. However, Figure 13 displays the reversed, all the observed data is larger than the predicted entrance aperture-reaching spectral radiance. This puts further emphasize on the dependence of the orthorectification process. The sensitivity between the mirrors signal and the GSD is shadowed by the orthorectification and interpolation errors.

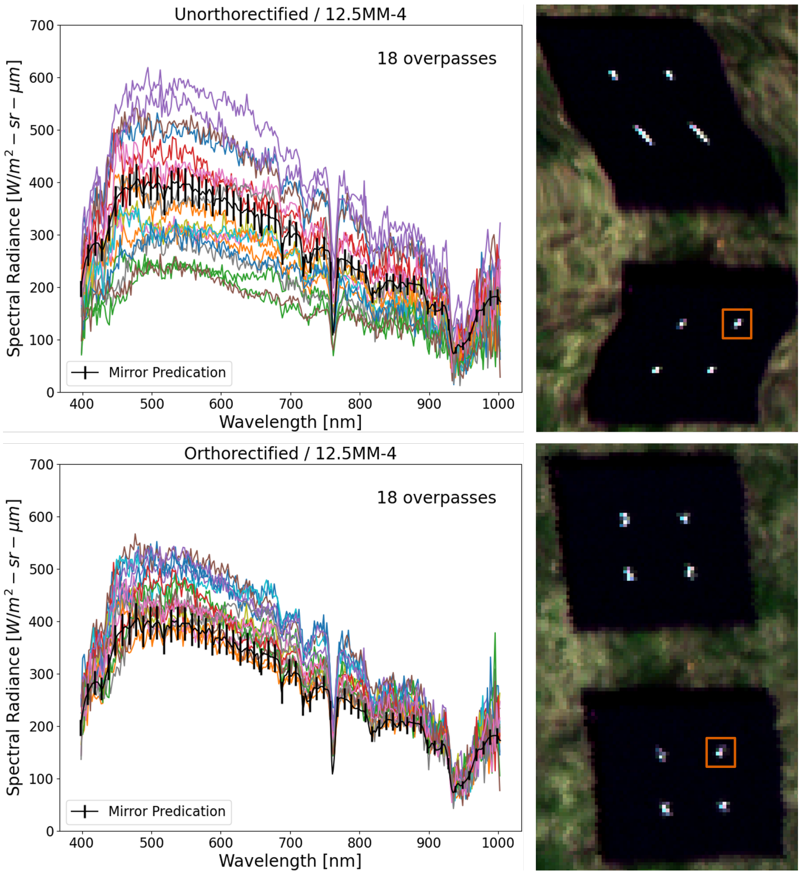

Figure 13. When the fix mounted HSI system images the ground scene, platform motion can impact the ground sampling. Point targets are an ideal calibration target to observe such an effect. From unorthorectified (top) to orthorectified (bottom) imagery, the overall predicted radiance is immense. The ensquared energy captured in the unorthorectified imagery varies significantly above and below the predicted entrance aperture-reaching spectral radiance. Whereas, in the orthorectified imagery, most of the curves over-estimate the ensquared energy (*i.e.,* nearest neighbor interpolation scheme). The orange box within the picture highlights the point target that was analyzed over the 18 overpasses.

4.2. Radiometric Accuracy Concerns

In the previous section, the measurement dispersion (*i.e.,* standard deviation) of each mirror was independently assessed across the 18 overpasses. Figure 14 takes a closer look at two instances of the same point target (mirror ID: 12.5MM-4) imaged within 2 minutes or 3 overpasses apart. The solid blue curve represents the point target imaged on the second overpass of the experiment and provides a mirror signal estimate within the uncertainty. However, not even 2 minutes later, the same mirror (now in solid orange curve) is estimated to be 25% brighter. It has already been demonstrated that the atmosphere and HSI instrument stability can not explain this drastic increase in perceived energy from the point target. The only difference between the imaged point targets is the platform motion (fixed mounted HSI) and resulting orthorectification.

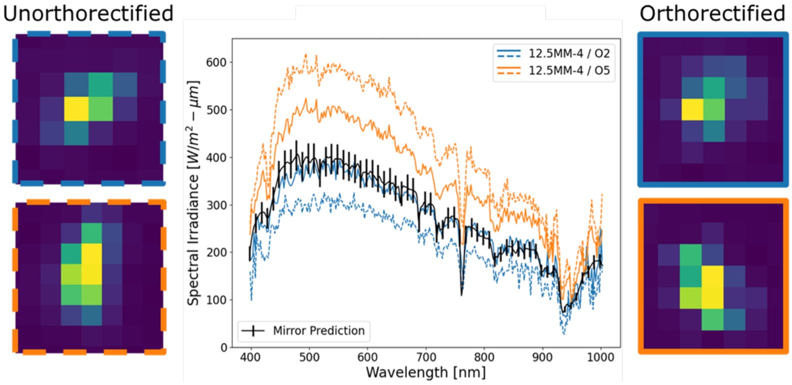

Figure 14. The same point target (12.5MM-4) imaged at overpass #2 and overpass #5 signifies the radiometric inconsistency when observing a point target in quick secession. The blue curve is measured within the uncertainty whereas the orange curve is over-predicted. Platform motion and orthorectification contribute to these inconsistencies. The dotted and solid curves correspond to the unorthorectified and orthorectified point targets, respectively.

If the unorthorectified curves (and point target imagery) are examined more closely, we can begin to form definitive conclusions on the reasoning for such drastic difference in the perceived spectral radiance. When the mirror was imaged on the second overpass, the perceived energy was lower than expected even though the orthorectified signal was accurate to the prediction. In this instance, the orthorectification properly interpolated the scene to add the adequate amount of energy back that was never physically observed. This is one of the largest contributors to the large measurement dispersion seen in the point targets. There is nothing within the post-processing algorithm that provides enough information to accurately inject the correct amount of energy that was never observed due to inconsistent sampling of the ground during imaging. For the orange dashed curve, the HSI system actually imaged the target or ground location too many times and the orthorectification cannot realistically dispose of the excessive amount of energy from the point target. This is also observed in Figure 15 as well. This observation provides a missing link within orthorectification algorithms that can be easily seen when imaging high contrast point targets (i.e., convex mirrors) of a known radiometric signal. If information is not observed or in excess, orthorectification algorithms can only use IMU/GPS and interpolation schemes to correct the scene.

If we focus attention to a mirror pair, as represented in Figure 10b, an examination of oversampling the observed scene can be discussed further. Figure 15 demonstrates a major issue imaging point targets with a fix mounted pushbroom HSI system encountering significant platform motion. As mentioned before, orthorectification does not have the correct information to correctly dispose of excess collected energy when the point target is re-imaged. As Figure 15 shows, the point target pairs are similarly affected in the unorthorectified imagery where both record roughly 2x the expected mirror signal. However, a difference between the point targets can be seen after orthorectification where the point targets no longer overlap. Even though the point targets were aligned in the across-track direction, the orthorectification affected the spectral radiance curves differently, further highlighting the volatility in localized regions.

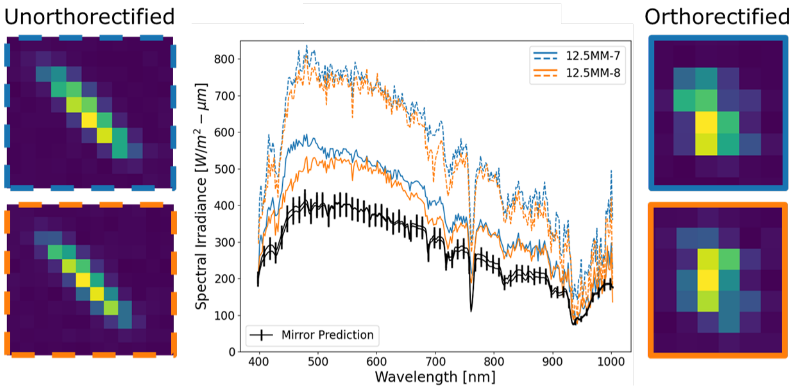

Figure 15. When point targets are re-imaged over multiple frames due to platform motion, the measured radiometric response will always be over-estimated. The comparison between mirror pairs shows that orthorectification can be different over a small region on the ground. The dotted and solid curves correspond to the unorthorectified and orthorectified point targets, respectively.

These results demonstrate a clear lack of realism in orthorectifying algorithms for pixel level details, for fix mounted HSI systems. Multi-modal imaging capabilities and constrained budgets are situations where radiometric accuracy of the HSI system is sacrificed for payload configuration. At a minimum, convex mirrors provide a *low cost solution* for assessing the radiometric performance for any payload configuration. The most optimal mounting solution for HSI systems is a gimbal mount. The reduction in the HS instruments relative motion to the drone will reduce the motion-induced radiometric errors as seen in the results. A gimbal mounting solution will not fully remove all orthorectification errors. However, using the technique illustrated in this paper, the radiometric performance for small targets can be estimated.

4.3. Spectral Inconsistencies

The previous examples demonstrated the inconsistent radiometric performance of orthorectification on the overall signal level. For most HSI applications, the overall signal accuracy has less of an impact on algorithm performance compared to the spectral shape. For sub-pixel target detection or spectral unmixing algorithms, the reliance on the repeatability of the spectral component is critical to identify spatially unresolved objects. Significant issues can arise within algorithms if the spectral component of small targets is not conserved over all images. In the following examples, spectral distortions from the orthorectification process will be examined.

The primary contribution to spectral distortions related to the point target signal is the orthorectification process and the interpolation scheme. During the orthorectification process, nearest neighbor or linear interpolation is implemented to construct the scene, but both these schemes have there issues when encountering a point target. Nearest neighbor interpolation has the issue of replicating or replacing pixels within a scene. For point targets, this can drastically modify the radiometric and spectral integrity due to the inherent SPSF sharpness. Linear interpolation has a lesser affect on signal level because it has an averaging effect, but has significant issues by creating "unphysical" spectra [11]. In addition, both interpolation schemes will have differing performance when HS instrument defects are present (*i.e.,* smile and keystone). HS keystone will produce the worst effects for small, spectral targets because pixels of varying spectral quantities will be replicated or replaced and will produce a modified spectrum. To further complicate this problem, polarization sensitivity of HS instruments will add to spectral inconsistencies.

Figure 16 illustrates a mirror pair after orthorectification where we can see that the observed spectral radiance has changed. Mirror 1 (blue curves) is a perfect example of linear interpolation positively affecting the mirror's spectral radiance. During imaging, the ground was not sampled adequately and resulted in missing energy from the point target. However, during orthorectification, the linear interpolation derived more energy and spatially modified the point target. The red arrows illustrate where the energy was inserted. Most of these pixels where not found in the unorthorectified image.

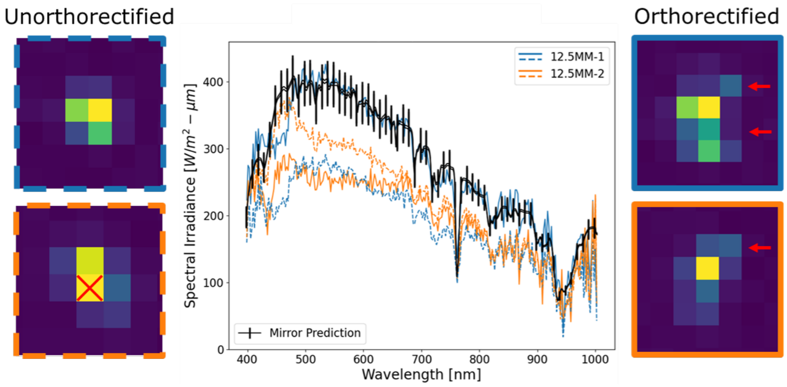

Figure 16. When a scene is not imaged properly (*i.e.,* along-track is spatially undersampled), orthorectification can accurately represent the radiometric signal from a point target or inadvertently eliminate energy. Interpolation contributes heavily to ensquared energy being added to the point target that was never captured. The dotted and solid curves correspond to the unorthorectified and orthorectified point targets, respectively.

The orange curves within Figure 16 exhibited a more complicated orthorectification process that spectrally modified the mirror signal. Again, during imaging, the mirror's signal was not fully captured by improper sampling of the ground. But instead of adding energy to the mirror's signal, this is one of the few cases where the orthorectification caused a massive under-prediction of the mirror's spectral radiance. The main cause is the complete elimination the pixel highlighted with the red "X" as seen in the left side of the Figure. Because of the wavelength dependent SPSF sharpness, the amount of energy missing after orthorectification affects the shorter wavelengths more. Furthermore, the red arrow (bottom right of Figure), indicates a row of pixels that were linearly interpolated, but does not fully account for all the missing energy in the blue end of the spectrum.

The final result in Figure 17 highlights issues when only single pixels are linearly interpolated. When entire rows are interpolated (Figure 16), the instrument defects (*i.e.,* keystone) can have negligible effects to the point targets overall signal because all keystone artifacts are replicated in the interpolation. This is not true when single pixels are interpolated as seen in Figure 17. More importantly, the signal reconstruction will be further impacted if the observed spectral radiance experiences a polarization dependence. The red boxes (right side of Figure) highlight pixels that never existed in the unorthorectified image. Since these pixels are a weighted linear combination of their surroundings, the added energy does not combine to realistically replicate the predicted energy defined by the black spectral curve.

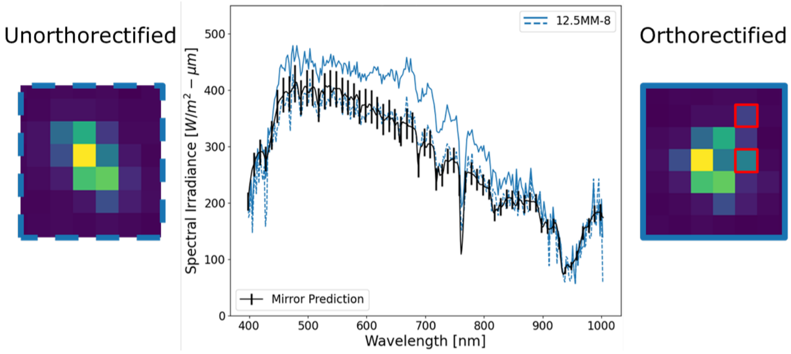

Figure 17. Single pixel interpolation can increase ensquared energy by forming linear combinations of surrounding pixels that do not spectrally match the target. The ensquared energy collected in the unorthorectified imagery was within the predicted uncertainty (black line), but the orthorectification process added new pixels (red boxes on right of Figure) that spectrally changed the overall shape. The dotted and solid curves correspond to the unorthorectified and orthorectified point targets, respectively.

Since the mirror's energy is a summed quantity, any instrument defects should not impact the overall spectral signature, even though single pixels may have a spectrum that has been modified by keystone effects. This is true as long as the ensquared energy for all wavelengths is captured in the bounding box. The important conclusion from this analysis is that single pixel modification *drastically effects the the spectral component of small targets* compared to entire rows being added. Spectral changes of unknown small targets will have more consequences on an algorithms performance because these routines tend to key off spectral shape. The well-known (solar-like spectrum), and the ability to predict the radiometric signal from convex mirrors, lends itself to the only method, that we know of, for understanding spectral impacts linked to the HS orthorectification process.

5. Conclusions

In this paper, the radiometric performance assessment on small targets was assessed for a fix mounted drone-based hyperspectral imaging system. Convex mirrors were used to create point targets that were radiometrically connected to the solar spectrum. Point targets provide the ultimate radiometric test in reconstructing an accurate radiometric signal from orthorectified HS imagery. Results demonstrated the lack of physical realism in the orthorectification process when analyzing point targets. In retrospect, Lambertian targets showed excellent repeatability and self-consistency over multiple overpasses compared to point targets. There was an 18.1% chance that a point target was accurately predicted using radiometric equations defining the spectral radiance of a point target. Major issues originated from both the mounting of HSI systems and the orthorectification process itself. A radiometrically accurate HSI system tends to over-estimate the true spectral radiance of small targets based on the nearest-neighbor interpolation scheme used when orthorectifying imagery. Due to the sub-pixel response of the imaging system to a point target, the orthorectification and interpolation can be assessed for deriving radiometrically accurate HS images for the most difficult object, a small target.

Author Contributions: Conceptualization, David Conran and Emmett Ientilucci; Data curation, David Conran, Timothy Bauch and Nina Raqueno; Formal analysis, David Conran; Investigation, David Conran; Methodology, David Conran, Timothy Bauch and Nina Raqueno; Resources, David Conran, Timothy Bauch and Nina Raqueno; Software, David Conran and Timothy Bauch; Supervision, Emmett Ientilucci; Validation, David Conran and Emmett Ientilucci; Visualization, David Conran; Writing – original draft, David Conran; Writing – review & editing, David Conran and Emmett Ientilucci.

Funding: This research received no external funding.

Data Availability Statement: All relevant data can be requested by contacting corresponding authors.

Conflicts of Interest: The authors declare no conflicts of interest.

Abbreviations

The following abbreviations are used in this manuscript:

DIRS	Digital Imagery and Remote Sensing
VNIR	Visible-Near Infrared
LWIR	Long-Wave Infrared
LIDAR	Light Detection and Ranging
HSI	Hyperspectral Imaging
GSD	Ground Sampling Distance
QTH	Quartz-Tungsten Halogen
SPSF	Sampled Point Spread Function
NEI	Noise-Equivalent Irradiance
FOV	Field-Of-View
m	meters
cm	centimeter
NIR	Near Infrared
HS	Hyperspectral
SPARC	SPecular Array for Radiometric Calibration
GPS	Global Positioning System
IMU	Inertial Measurement Unit

Appendix A

The following appendix derives the entrance aperture-reaching spectral radiance originating from a point source and defines the radiometric signature of a point target used in field calibration efforts [15]. A point source is defined by light originating from an unresolved object. The natural radiometric quantity that defines a point source is radiant intensity, I and has units of power per solid angle (W/sr). Figure A1 provides two visualizations of convex mirrors used to create point source targets for remote imaging systems.

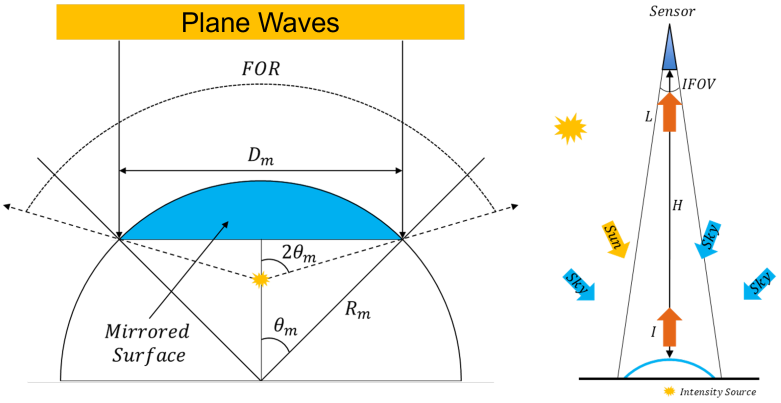

(a) Convex Mirror **(b)** Point Target

Figure A1. **(a)** Defines key geometric parameters that are used to derive radiometric quantities of convex mirrors under plane wave illumination (Reprinted from [23]). **(b)** Under solar and sky irradiances, the spectral radiance observed at the sensor is derived from the radiant intensity of a point source.

Under the assumptions of plane waves (*i.e.*, originating from an irradiance source) fully illuminating a convex mirror, a virtual image is formed at half the radius of curvature or at the focal length. The mirror's spectral radiant intensity, $I_m(\lambda)$ leaving the surface can be described as

$$I_m(\lambda) = \frac{\rho_m(\lambda)E(\lambda)A_m}{\Omega_i} \tag{A1}$$

where ρ_m is the mirror's specular reflectance, $E(\lambda)$ is the irradiance striking the mirror's surface, A_m is the mirror's projected area, and Ω_i is the solid angle of the virtual image form by the mirror. The mirror's geometric angle, θ_mb is defined as the angle from the optical axis to the mirror's edge when viewed from the center of curvature.

$$\theta_m = \sin^{-1}\left(\frac{D_m}{2R_m}\right) \tag{A2}$$

The mirror's geometric angle is a physical quantity that can be easily measured. The mirror's projected area, A_m, is a circle defined by the viewable diameter, D_m.

$$A_m = \pi D_m^2 = \pi(R_m \sin\theta_m)^2 = \frac{\pi R_m^2}{2}(1-\cos 2\theta_m) \tag{A3}$$

The solid angle, Ω_i, is defined by the virtual image since this is viewed by an imaging system. The focal point of a convex mirror creates an angle with respect to the optical axis that is twice as large as the geometric angle, θ_m. The solid angle for a unit spherical cone can be evaluated over the 2π azimuthal angle and $2\theta_m$ polar angle.

$$\Omega_i = \int_0^{2\pi} d\phi \int_0^{2\theta_m} \sin\theta \, d\theta = 2\pi(1-\cos 2\theta_m) \tag{A4}$$

For simplification purposes, it is convenient to rewrite A_m in terms of $2\theta_m$ using the double angle trigonometric identity. This will be apparent when formulating the radiant intensity equation. Before continuing in the derivation of the mirror's spectral radiant intensity, the mirror's field-of-regard, *FOR* should be discussed. The *FOR* defines he total angle at which the virtual image can be viewed from. This quantity is used in pre-planning to ensure the point source can be viewed during an overpass. That is,

$$FOR = 4\theta_m = 4\sin^{-1}\left(\frac{D_m}{2R_m}\right) \tag{A5}$$

The area (A_m) and solid angle (Ω_i) terms within I_m can be simplified as

$$I_m(\lambda) = \frac{\rho_m(\lambda)E(\lambda)A_m}{\Omega_i} = \rho_m(\lambda)E(\lambda)\frac{R_m^2}{4} \tag{A6}$$

where the spectral radiant intensity of a convex mirror is dependent on the surface reflectance, radius of curvature and the irradiance striking the mirror's surface. When mirror's are deployed outside, there are multiple source of energy striking the mirror's surface is a combination of both direct solar and diffuse sky irradiance. The solar component is the primary irradiance and has a small angular extent such that all that energy is reflected. The diffuse sky contribution has a dependence on the solid angle of the virtual image formed at the mirror's focal point. The fractional amount of diffuse sky, f_{sky} reflected to an imaging system can be described by taking the ratio of Ω_i and solid angle of the hemisphere (*i.e.,* 2π sr).

$$f_{sky} = \frac{\Omega_i}{2\pi} = 1 - \cos 2\theta_m \tag{A7}$$

The spectral radiant intensity of a convex mirror deployed outside under nominal field conditions (see Figure A1b) can be described by the following equation

$$\begin{aligned} I_m(\lambda) &= {}^1\!/\!_4\rho_m(\lambda)R_m^2\left[E_{solar}(\lambda)+f_{sky}E_{sky}(\lambda)\right] \\ &= {}^1\!/\!_4\rho_m(\lambda)R_m^2\left[1+f_{sky}\frac{E_{sky}(\lambda)}{E_{solar}(\lambda)}\right]E_{solar}(\lambda) \end{aligned} \tag{A8}$$

where the irradiance was split into two components, the solar and sky contributions. The sky irradiance is modified by the fractional amount of sky irradiance reflected to the imaging system. If $\theta_m = 45$ degrees, the convex mirror reflects the entire hemisphere (*i.e.*, $f_{sky} = 1$). In Section 2.2, the total downwelling irradiance (solar and sky) and the sky irradiance are the only direct measurements using a field spectroradiometer device configured with a cosine corrector. The ratio of the sky and suns contribution to the total downwelling irradiance, $G(\lambda)$ and $1 - G(\lambda)$ respectively, can be expressed by the following equations

$$G(\lambda) = \frac{E_{sky}(\lambda)}{E_T(\lambda)}, \qquad 1 - G(\lambda) = \frac{E_{solar}(\lambda)}{E_T(\lambda)} \tag{A9}$$

where both equations can be used to further simplify Eq. (A8) with two field measurements, the solar irradiance and the Global-to-Diffuse Ratio. The following equation now defines the spectral radiant intensity of a convex mirror under nominal daylight conditions that accounts for both solar and sky irradiances.

$$I_m(\lambda) = {}^1\!/\!_4\rho_m(\lambda)R_m^2\left[1+f_{sky}\frac{G(\lambda)}{1-G(\lambda)}\right]E_{solar}(\lambda) \tag{A10}$$

For imaging systems viewing the point source at altitudes much larger than the focal length of the convex mirror, the spectral radiant intensity can be propagated a distance H to the imaging system. Assuming isotropic behavior, the entrance aperture-reaching spectral irradiance, $E_{EAR}(\lambda)$ is described by

$$E_{EAR}(\lambda) = \frac{I_m(\lambda)}{H^2} = {}^1\!/\!_4\rho_m(\lambda)R_m^2\left[1+f_{sky}\frac{G(\lambda)}{1-G(\lambda)}\right]\frac{E_{solar}(\lambda)}{H^2} \tag{A11}$$

where the inverse-square law defines the relationship between the spectral radiant intensity and entrance aperture-reaching spectral irradiance. For remote sensing systems recording a pixel-level spectral radiance, it is convenient to describe the mirror's signal in the form of entrance aperture-reaching spectral radiance, $L_{EAR}(\lambda)$ by incorporating the sensor's solid angle.

$$L_{EAR}(\lambda) = \frac{I_m(\lambda)}{H^2\,\Omega_{sensor}} = {}^1\!/\!_4\rho_m(\lambda)R_m^2\left[1+f_{sky}\frac{G(\lambda)}{1-G(\lambda)}\right]\frac{E_{solar}(\lambda)}{H^2\,\Omega_{sensor}} \tag{A12}$$

The factor $H^2\,\Omega_{sensor}$ in the denominator of $L_{EAR}(\lambda)$ can be re-written in terms of the directional ground sampling distance (GSD) of the imaging system. The GSD is the area of a pixel projected onto the ground and is a standard parameter for Earth observing imaging systems.

$$H^2\,\Omega_{sensor} = H^2\,(IFOV_x \cdot IFOV_y) = \left(\frac{p_x}{f}\right)H \cdot \left(\frac{p_y}{f}\right)H = GSD_x \cdot GSD_y \tag{A13}$$

where $IFOV$ and p define the directional components to the the instantaneous field for view and pixel pitch, respectively and f is the imaging systems focal length. The entrance aperture-reaching spectral radiance can be generalized for any remote sensing system by incorporating the upwelling atmospheric transmission (*from target to aperture*) and path radiance including adjacency effects. The equation assumes that the solar irradiance is measured at the Earth's surface such that downwelling atmospheric transmission is incorporated. Thus we have,

$$L_{EAR}(\lambda) = {}^{1}\!/\!_{4}\rho_m(\lambda)R_m^2\left[1 + f_{sky}\frac{G(\lambda)}{1 - G(\lambda)}\right]\frac{\tau_{\uparrow}(\lambda)E_{solar}(\lambda)}{GSD_x \cdot GSD_y} + L_a(\lambda) \tag{A14}$$

The equation used in this experiment is a modified form of Eq. (A14) for drone-based experiments. Due to the altitude (*i.e.*, less than 400 ft or 121.92 m), the upwelling atmospheric transmission, $\tau_{\uparrow}(\lambda)$ is negligible [3]. Under post-processing of point targets within HS imagery, the path radiance, $L_a(\lambda)$ is removed by background subtraction. The final assumption is that the orthorectified imagery contains square pixels and the individual GSD is combined into one term. That is,

$$L_{EAR}(\lambda) = {}^{1}\!/\!_{4}\rho_m(\lambda)R_m^2\left[1 - G(\lambda)\cos\left(2\theta_m\right)\right]\frac{E_T(\lambda)}{GSD^2} \tag{A15}$$

The final modification of Eq. (A14) stems from the direct measurements of field quantities. The direct irradiance measurements from a field spectroradiometer is not the solar irradiance component, but is the total downwelling irradiance, $E_T(\lambda)$ that contains both the solar and sky components. Equation (A14) can be modified such that the total downwelling irradiance and Global-to-Diffuse Ratio is used directly such that the uncertainty can be derived explicitly. Equation (A15) is the final form of the entrance aperture-reaching radiance used in this paper to predict the point targets radiometric signal.

Appendix B

The following appendix outlines the methodology used to derive the uncertainty for Eq. (A15). The uncertainty derivation involves taking first-order partial derivatives with respect to all the variables. Equation (A15) requires the substitution of the mirror's geometric angle, θ_m. Equation (A16) defines the main function for uncertainty propagation.

$$L_{EAR}(\lambda) = {}^{1}\!/\!_{4}\rho_m(\lambda)R_m^2\left[1 - G(\lambda)\cos\left(2\sin^{-1}\left(\frac{D_m}{2R_m}\right)\right)\right]\frac{E_T(\lambda)}{GSD^2} \tag{A16}$$

The uncertainty propagation follows the Guide to Uncertainty Measurement framework [24] where the combined uncertainty for a generalized function, $y = f(x_1, x_2, ..., x_N)$. Each variable is a mean estimate, $\overline{x_i}$ with an associated uncertainty, $u(x_i)$. The generalized form of the combined uncertainty, $u_c^2(y)$ with a covariance, $u(x_i, x_j)$ associated to each pair of correlated variables.

$$u_c^2(y) = \sum_{i=1}^{N}\left(\frac{\partial f}{\partial x_i}\right)^2 u^2(x_i) + 2\sum_{i=1}^{N-1}\sum_{j=i+1}^{N}\frac{\partial f}{\partial x_i}\frac{\partial f}{\partial x_j}u(x_i, x_j) \tag{A17}$$

For the uncertainty analysis performed for this investigation, the generalized combined uncertainty equation is reduced by assuming all variables are uncorrelated. Equation (A18) defines the uncertainty propagation for uncorrelated variables. The partial derivatives, $\partial f/\partial x_i$ defines the sensitivity of y to small changes in each variable.

$$u_c^2(y) = \sum_{i=1}^{N}\left(\frac{\partial f}{\partial x_i}\right)^2 u^2(x_i) \tag{A18}$$

It should be understood that Eq. (A18) has limitations and approximation to the uncertainty. In the assessment of the combine uncertainty, $u_c(y)$, the first-order partial derivative assumes linear behavior over the mean estimate of each variable. Any significant deviation from linearity requires either the addition of high-order terms or a Monte Carlo approach to estimate the combined uncertainty. The following equations outline the partial derivatives of each variable with Eq. (A16). The equations were derived by using the Python symbolic mathematics library, *SymPy* [26].

$$\frac{\partial L_{EAR}}{\partial \rho_m} = {}^1\!/\!_4 R_m^2 \left[1 - G(\lambda)\cos\left(2\sin^{-1}\left(\frac{D_m}{2R_m}\right)\right)\right]\frac{E_T(\lambda)}{GSD^2} \tag{A19}$$

$$\frac{\partial L_{EAR}}{\partial R_m} = {}^1\!/\!_4 \rho_m(\lambda)\left[2R_m\left(1 - G(\lambda)\cos\left(2\sin^{-1}\left(\frac{D_m}{2R_m}\right)\right)\right)\right. \tag{A20}$$

$$\left. - \frac{D_m G(\lambda)\sin\left(2\sin^{-1}\left(\frac{D_m}{2R_m}\right)\right)}{\sqrt{1-\left(\frac{D_m}{2R_m}\right)^2}}\right]\frac{E_T(\lambda)}{GSD^2} \tag{A21}$$

$$\frac{\partial L_{EAR}}{\partial D_m} = {}^1\!/\!_4 \rho_m(\lambda) R_m \left[\frac{G(\lambda)\sin\left(2\sin^{-1}\left(\frac{D_m}{2R_m}\right)\right)}{\sqrt{1-\left(\frac{D_m}{2R_m}\right)^2}}\right]\frac{E_T(\lambda)}{GSD^2} \tag{A22}$$

$$\frac{\partial L_{EAR}}{\partial G} = -{}^1\!/\!_4 \rho_m(\lambda) R_m^2 \cos\left(2\sin^{-1}\left(\frac{D_m}{2R_m}\right)\right)\frac{E_T(\lambda)}{GSD^2} \tag{A23}$$

$$\frac{\partial L_{EAR}}{\partial E_T} = {}^1\!/\!_4 \rho_m(\lambda) R_m^2 \left[1 - G(\lambda)\cos\left(2\sin^{-1}\left(\frac{D_m}{2R_m}\right)\right)\right]\frac{1}{GSD^2} \tag{A24}$$

$$\frac{\partial L_{EAR}}{\partial GSD} = -{}^1\!/\!_2 \rho_m(\lambda) R_m^2 \left[1 - G(\lambda)\cos\left(2\sin^{-1}\left(\frac{D_m}{2R_m}\right)\right)\right]\frac{E_T(\lambda)}{GSD^3} \tag{A25}$$

The combined uncertainty is expressed by evaluating the above sensitivity coefficients at the mean estimates for all variables. The relative uncertainty values for each variable can be found in Table 1. The absolute uncertainty for each variable, $u(x_i)$ can be estimated by multiplying the mean value by the relative uncertainty. The combined uncertainty for L_{EAR} can be estimated by taking the square root of Eq. (A26) and the result can be found in Table 1.

$$\begin{aligned} u_c^2(L_{EAR}) &= \left(\frac{\partial L_{EAR}}{\partial \rho_m}\right)^2 u^2(\rho_m) + \left(\frac{\partial L_{EAR}}{\partial R_m}\right)^2 u^2(R_m) + \left(\frac{\partial L_{EAR}}{\partial D_m}\right)^2 u^2(D_m) \\ &+ \left(\frac{\partial L_{EAR}}{\partial G}\right)^2 u^2(G) + \left(\frac{\partial L_{EAR}}{\partial E_T}\right)^2 u^2(E_T) + \left(\frac{\partial L_{EAR}}{\partial GSD}\right)^2 u^2(GSD) \end{aligned} \tag{A26}$$

References

1. Smith, G.M.; Milton, E.J. The use of the empirical line method to calibrate remotely sensed data to reflectance. *International Journal of Remote Sensing* **1999**, *20*, 2653–2662. https://doi.org/10.1080/014311699211994.
2. Baugh, W.; Groeneveld, D. Empirical proof of the empirical line. *International Journal of Remote Sensing* **2008**, *29*, 665–672. https://doi.org/10.1080/01431160701352162.
3. Mamaghani, B.G.; Sasaki, G.V.; Connal, R.J.; Kha, K.; Knappen, J.S.; Hartzell, R.A.; Marcellus, E.D.; Bauch, T.D.; Raqueño, N.G.; Salvaggio, C. An initial exploration of vicarious and in-scene calibration techniques for small unmanned aircraft systems. In Proceedings of the Autonomous Air and Ground Sensing Systems for Agricultural Optimization and Phenotyping III; Thomasson, J.A.; McKee, M.; Moorhead, R.J., Eds. International Society for Optics and Photonics, SPIE, 2018, Vol. 10664. https://doi.org/10.1117/12.2302744.
4. DeCoffe, L.J.R.; Conran, D.N.; Bauch, T.D.; Ross, M.G.; Kaputa, D.S.; Salvaggio, C. Initial Performance Analysis of the At-Altitude Radiance Ratio Method for Reflectance Conversion of Hyperspectral Remote Sensing Data. *Sensors* **2023**, *23*. https://doi.org/10.3390/s23010320.

5. Schaepman-Strub, G.; Schaepman, M.E.; Painter, T.H.; Dangel, S.; Martonchik, J.V. Reflectance quantities in optical remote sensing—Definitions and case studies. *Remote sensing of environment* **2006**, *103*, 27–42.
6. Eismann, M. *Hyperspectral Remote Sensing*; Press Monographs, Society of Photo Optical, 2012.
7. Bioucas-Dias, J.; Plaza, A.; Camps-Valls, G.; Scheunders, P.; Nasrabadi, N.; Chanussot, J. Hyperspectral Remote Sensing Data Analysis and Future Challenges. *Geoscience and Remote Sensing Magazine, IEEE* **2013**, *1*, 6–36. https://doi.org/10.1109/MGRS.2013.2244672.
8. Schiller, S.; Silny, J. Using Vicarious Calibration to Evaluate Small Target Radiometry. *CALCON* **2016**.
9. Schiller, S.J. Specular Array for Radiometric Calibration and Method, US 8158929 B2, 2012.
10. Inamdar, D.; Kalacska, M.; Arroyo-Mora, J.P.; Leblanc, G. The directly-georeferenced hyperspectral point cloud: preserving the integrity of hyperspectral imaging data. *Frontiers in Remote Sensing* **2021**, *2*, 675323.
11. Schläpfer, D.; Richter, R. Geo-atmospheric processing of airborne imaging spectrometry data. Part 1: Parametric orthorectification. *International Journal of Remote Sensing* **2002**, *23*, 2609–2630. https://doi.org/10.1080/01431160110115825.
12. Labsphere Inc.. ISO 17025 NVLAP Accreditation. Accessed Jan. 28, 202024.
13. Soffer, R.; Ifimov, G. Experiences learned in the acquisition, processing, and assessment of in-situ point spectroscopy measurements supporting airborne hyperspectral cal/val activities. *CALCON* **2019**.
14. Hodges, G.B.; Michalsky, J.J. Multifilter Rotating Shadowband Radiometer (MFRSR) Handbook With subsections for derivative instruments: Multifilter Radiometer (MFR) Normal Incidence Multifilter Radiometer (NIMFR). *DOE ARM Climate Research Facility* **2016**. https://doi.org/10.2172/1251387.
15. Schiller, S.J.; Silny, J. The Specular Array Radiometric Calibration (SPARC) method: a new approach for absolute vicarious calibration in the solar reflective spectrum. In Proceedings of the Remote Sensing System Engineering III; Ardanuy, P.E.; Puschell, J.J., Eds. International Society for Optics and Photonics, SPIE, 2010, Vol. 7813, p. 78130E. https://doi.org/10.1117/12.864071.
16. Silney, J.F.; Schiller, S.J. Method and System for Vicarious Spatial Characterization of a Remote Image Sensor, WO 2013/019180 AL, 2013.
17. Durell, C. Top-of-Atmosphere reflectance calibration of satellite and airborne sensor systems using FLARE vicarious calibration network. Technical report, Labsphere, Inc., 2019.
18. Russell, B.; Scharpf, D.; Holt, J.; Arnold, W.; Durell, C.; Jablonski, J.; Conran, D.; Schiller, S.; Leigh, L.; Aaron, D.; et al. Initial results of the FLARE vicarious calibration network. In Proceedings of the Earth Observing Systems XXV; Butler, J.J.; Xiong, X.J.; Gu, X., Eds. International Society for Optics and Photonics, SPIE, 2020, Vol. 11501, p. 115010F. https://doi.org/10.1117/12.2566759.
19. Pinto, C.T.; de Carvalho e Oliveira, P.V.; Aaron, D.; Holt, J.; Russell, B.; Durell, C.; Leigh, L. Preliminary evaluation of the mirror-based empirical line method using FLARE system. In Proceedings of the Earth Observing Systems XXVII; Butler, J.J.; Xiong, X.J.; Gu, X., Eds. International Society for Optics and Photonics, SPIE, 2022, Vol. 12232, p. 1223214. https://doi.org/10.1117/12.2633107.
20. Russell, B.J.; Soffer, R.J.; Ientilucci, E.J.; Kuester, M.A.; Conran, D.N.; Arroyo-Mora, J.P.; Ochoa, T.; Durell, C.; Holt, J. The Ground to Space CALibration Experiment (G-SCALE): Simultaneous Validation of UAV, Airborne, and Satellite Imagers for Earth Observation Using Specular Targets. *Remote Sensing* **2023**, *15*. https://doi.org/10.3390/rs15020294.
21. Hedler, D.; Maddox, E.; Mann, J.; Leigh, L.; Raqueno, N.; Gerace, A.; Rehman, E.; Conran, D.; Bauch, T.; Falcon, L.; et al. Landsat Surface Product Validation Instrumentation: The BigMAC Exercise. *Remote Sensing of Environment* **In review 2023**.
22. Conran, D.; Ientilucci, E.J. Interrogating UAV Image and Data Quality Using Convex Mirrors. In Proceedings of the IGARSS 2022-2022 IEEE International Geoscience and Remote Sensing Symposium. IEEE, 2022, pp. 4525–4528.
23. Conran, D.N.; Ientilucci, E.J. A Vicarious Technique for Understanding and Diagnosing Hyperspectral Spatial Misregistration. *Sensors* **2023**, *23*. https://doi.org/10.3390/s23094333.
24. BIPM.; IEC.; IFCC.; ILAC.; ISO.; IUPAC.; IUPAP.; OIML. Evaluation of measurement data — Guide to the expression of uncertainty in measurement. Joint Committee for Guides in Metrology, JCGM 100:2008.
25. Breckinridge, J.B.; Oppenheimer, B.R. Polarization effects in reflecting coronagraphs for white-light applications in astronomy. *The Astrophysical Journal* **2004**, *600*, 1091.
26. Meurer, A.; Smith, C.P.; Paprocki, M.; Čertík, O.; Kirpichev, S.B.; Rocklin, M.; Kumar, A.; Ivanov, S.; Moore, J.K.; Singh, S.; et al. SymPy: symbolic computing in Python. *PeerJ Computer Science* **2017**, *3*, e103.

Appendix D

A New Technique to Define the Spatial Resolution of Imaging Sensors

IGARSS 2021 - 2021 IEEE International Geoscience and Remote Sensing Symposium | 978-1-6654-0369-6/21/$31.00 ©2021 IEEE | DOI: 10.1109/IGARSS47720.2021.9554436

A NEW TECHNIQUE TO DEFINE THE SPATIAL RESOLUTION OF IMAGING SENSORS

David Conran[1], *Emmett J. Ientilucci*[1], *Stephen Schiller*[2], *Brandon Russell*[3],
Jeff Holt[3], *Chris Durell*[3], *Will Arnold*[3]

[1]Rochester Institute of Technology, Center for Imaging Science, Rochester NY, 14623
[2]Raytheon Space and Airborne Systems, [3]Labsphere, Inc., North Sutton, NH USA

ABSTRACT

Defining resolution within satellite imagery is normally achieved through the observation of edge targets or is visually graded (*e.g.,* National Imagery Interpretability Rating Scale (NIIRS)) for the level of detail observed. These methods are significantly disadvantaged by not directly measuring fundamental quantities related to the imaging system. Recently, ground mirror-based systems have been developed which can mimic an ideal point source observable by satellite systems allowing *direct observation* of an imaging system point response function (PRF). This fundamental quantity of an imaging system defines the end-to-end performance of the optics and detector. In this paper, we illustrate the use of the PRF in a new approach called the point-pair resolution technique (PPRT) which characterizes separability between two ideal point sources. We compare real and simulated point-pairs to demonstrate validity.

Index Terms— Point Response Function, Resolution

1. INTRODUCTION AND BACKGROUND

Traditional satellite image quality has been historically evaluate through two main metrics: Line Response Functions (LRF) of edge targets and the National Imagery Interpretability Rating Scale (NIIRS) [1]. Both methods have been adopted by the image quality community due to the ease of implementation, years of experimental data, and well-defined procedures outlined by the International Organization for Standardization (ISO). Even though the satellite community has adopted these metrics for image quality, the subjective nature of NIIRS combined with the amount of data exceeds the ability of human analysts to characterize spatial quality in a timely, actionable fashion. Moreover, the inherent disadvantage of using a non-ideal impulse response as a target (*i.e.,* a Lambertian edge target) requires a refined procedure for assessing image quality.

A newer technique for assessing image quality involves utilization of the SPecular Array Radiometric Calibration (SPARC) method defined by Schiller [2]. SPARC is a simple but powerful method for calibrating electro-optical sensors, both radiometrically and spatially, by directly reflecting solar energy off convex mirrors into the field-of-view (FOV) of the satellite. The spatial component of SPARC stems from the mirrors forming an image of the sun at the focal point producing an unsaturated ideal point source when imaged from space. When an imaging system is presented with an ideal point source and discretely sampled by the detector, a Point Response Function (PRF) is created. This is an inherent result of the optical Point Spread Function (PSF) convolved with the pixel response function (PixRF) which is then discretely sampled. Note, if the number of samples under the PSF is below the Nyquist sampling frequency, the resultant PRF will be under-sampled (uPRF). The added benefits of SPARC over traditional methods (*i.e.,* edges) can be summarized as: a full 2D spatial analysis, full spectrum resolution analysis (UV to midwave infrared), non-destructive post-processing such as numerical derivatives and more practical solutions for large GSD satellites (>30 km).

Two ideal point sources (*i.e.,* two PRF's when imaged), enable spatial resolution metrics similar to those traditionally studied (*e.g.,* Rayleigh Resolution Criteria or RRC [1]). In this paper we explore using the SPARC method to generate a number of point-pairs, separated by a distance, directly observed by a satellite in overpass and evaluated against these resolution metrics. Further, we explore using the SPARC method to generate a number of single-point sources within a scene allowing the generation of an oversampled PRF. The oversampled PRF allows us to simulate point-pairs at any separation and orientation for evaluation using the same contrast metrics described above (*i.e.,* PPRT).

We compare these point-pair simulations with those found in real data through statistical analysis and demonstrate close parity. Based on this work we introduce a new Point-Pair Resolution Technique (PPRT). Our PPRT has advantage over traditional resolution evaluation methods by directly deriving from a measured full-system response using ideal point stimuli such as SPARC. Further, PPRT has an advantage over physical point-pairs which are sensitive to and constrained by precise distance and orientation, with respect to the imager under test.

Authorized licensed use limited to: Rochester Institute of Technology. Downloaded on January 26,2023 at 18:16:09 UTC from IEEE Xplore. Restrictions apply.

2. METHODOLOGY

2.1. Point-Pair Resolution Technique (PPRT)

The image forming capability of an imaging system is best described by the PRF and illustrates how an objects energy is distributed on the focal plane. Assuming a Linear-Shift Invariant (LSI) system, the PRF can be used to accurately estimate true resolvability. More directly, how close two objects can be positioned while still being separable in an observation. The impact of the optical PSF, PixRF and other blurring factors, when imaging an ideal point source, will cause energy to be displaced from the central pixel which inherently degrades image quality. Our new process, PPRT, is based on the separability of two ideal point sources in close proximity and is theorized to be directly related to the oversampled PRF. An overview of this process can be seen in Fig. 1.

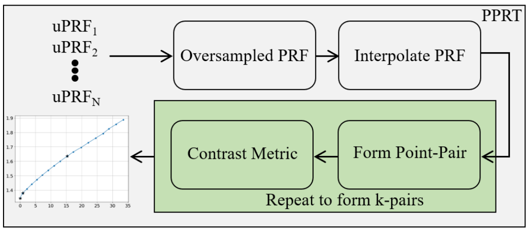

Fig. 1. The Point-Pair Resolution Technique (PPRT). Observed image uPRF's (from SPARC targets) are used to formulate image pairs for spatial resolution assessment.

The PPRT relies on the construction of the oversampled PRF which will be used to simulate contrast metrics such as the RRC. The oversampled PRF is derived from the observation of multiple uPRF's being co-registered to a generalized origin [3]. The uPRF can be represented mathematically as

$$g_{sampled}(x, y) \quad = \quad S(f_{scene}(x, y) * h_{sys}(x, y)) \qquad (1)$$

where $g_{sampled}(x, y)$ is the undersampled image of the scene, $f_{scene}(x, y)$ describes the scene radiance, $h_{sys}(x, y)$ is the culmination of all blurring effects contained within the imaging chain, and S represents detector sampling (*i.e.,* the 2D $COMB$ function). The oversampled PRF can then be approximated as

$$g_{oversampled}(x, y) \approx f_{scene}(x, y) * h_{sys}(x, y). \qquad (2)$$

The goal of Eq. (2) is to isolate $h_{sys}(x, y)$ such that $g_{oversampled}(x, y)$ defines the end-to-end performance of the imaging system under test. An ideal point source is best represented as a delta function displaced within the focal plane. Thus, when an imaging system observes an ideal point source, the signals are directly related to the image performance and represented by the oversampled PRF as

$$g_{oversampled}(x, y) \approx \delta(x, y) * h_{sys}(x, y) = h_{sys}(x, y) \qquad (3)$$

In the construction of an oversampled PRF, the spacing between consecutive x,y coordinates is non-linear, complicating further processing. To overcome this challenge a 2D, linear Radial Basis Function (RBF) interpolation technique was implemented (Fig. 2). Interpolation techniques, such as linear or cubic splines, can not deal with theses effects leading to major artifacts where additional smoothing is required. Creating a well-defined, smooth, non-parametric surface representation of the oversampled PRF is critical for achieving consistent results in the proposed resolution technique.

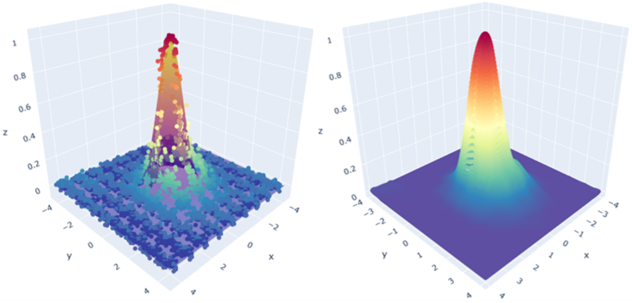

Fig. 2. (Left) Actual oversampled PRF overlaid with an optimized Gaussian surface fit. (Right) The RBF interpolated PRF with linear spacing.

Point-pairs can be described as a superposition of two delta functions. For example, the cross-track direction can be determined by

$$\begin{aligned} g_{point-pair}(x, y) &\approx \frac{1}{|x_0|}\delta\delta\left(\frac{x}{x_0}, y\right) * h_{sys}(x, y) \\ &= h_{sys}(x \pm x_0, y) \end{aligned} \qquad (4)$$

where the symmetric pair of delta functions creates a superposition of $h_{sys}(x, y)$ separated by a distance of $2x_0$ on the detector. To form k-pairs (as noted in Fig. 1), the superposition of $h_{sys}(x, y)$ is stepped through a range of distances based on knowledge of the GSD and/or estimates of the LRF. The point-pairs are then evaluated through use of a contrast metric, M. That is $M = (P_{min} - P_{tr})/(P_{min} + P_{tr})$ where P_{min} is the lower magnitude of the pair and P_{tr} is the corresponding trough. Common interpretation of a contrast metric (*i.e.,* Sparrow, Rayleigh, Ground Spot Size (GSS), etc.) can be found in the literature [1]. Finally, we can use the stepped distances to generate the 1D resolvability map shown in Fig. 1.

2.2. Validation of Point-Pair Imagery

During an experiment conducted in January 2020, point-pairs (*i.e.,* Fig. 3) with a separation of roughly two pixels were deployed in the field for a targeted series of satellite overpasses. In addition, single mirror arrays were deployed to allow for the creation of the oversampled PRF in the same scene as the

Authorized licensed use limited to: Rochester Institute of Technology. Downloaded on January 26,2023 at 18:16:09 UTC from IEEE Xplore. Restrictions apply.

point-pairs. Real and simulated image point-pairs, as a function of separation, were then compared to provide confidence in the oversampled PRF used in the PPRT. An overview of this comparison or validation process can be seen in Fig. 3.

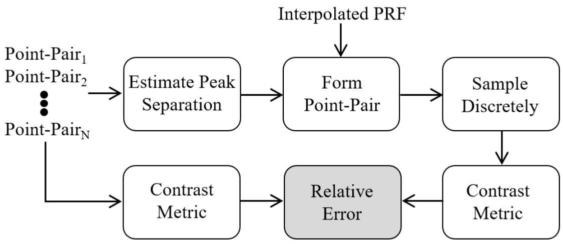

Fig. 3. Overview of the PPRT validation process.

For this validation study, the point-pair separation distance (on the detector) was determined by experimental measurements of pair-point separation. The point source imagery contains features related to the sub-pixel location of the optical PSF on the detector causing aliasing so the appearance of features become sensitive to phasing. In order to minimize the effects of phasing within both the real and simulated point-pair images the contrast was averaged between the peaks. The method used to investigate the validation in the point-pair simulation uses the discrete version of the oversampled PRF and involves a direct contrast comparison to all the separable point-pairs from the satellite imagery (*i.e.,* contrast metric input to the error box in Fig. 3). For constancy, point-pairs with centers laying outside the perceived row or column connecting the point sources were rejected which constrains the data set to the *best point-pair* source candidates.

Evaluating the error between simulated and real image point-pairs is crucial for validating the use of the oversampled PRF in the PPRT. The validation will determine if the contrast metric between the simulated point-pairs and real image pairs is statistically similar based on a two-sample t-test. To be more specific, a pivot, or the measure of how far the estimate (simulation) is from the known value (imagery) in standard error (SE) units, was assessed. The error box of Fig. 3 is the difference between the two contrast results for all the real image input point-pairs. Passing the t-test will provide merit for accepting the hypothesis that the oversampled PRF describes the performance of the imaging system and thus, the PPRT provides a *unique approach* for estimating spatial resolution, unlike other techniques.

3. RESULTS AND DISCUSSION

3.1. Results from the PPRT

Deriving a technique for assessing resolution for remote image sensors begins with the development of the oversampled PRF and ends with a metric of resolvability. The 1D resolvability trend describes the change in separation distance as two oversampled PRF's merge along the x- and y-directions. This 1D resolvability trend can be seen in in Fig. 4 and is a direct result of Fig. 1. The ultimate limit of separability for a point-pair is the Sparrow Limit and is defined by the non-separability of point-pair sources [1]. The 1D resolvability trend highlights all the minute details contained within the PRF including asymmetric features as well as unique characteristics at the base of the peak. These important details are lost when single number metrics are used in the analysis of satellite image quality, including FWHM of LRF or assuming an analytic surface for PRF fitting. Visual differences between the cross- and along-track resolution trends can be seen in Fig. 4. The along-track resolution contains more blurring effects due to motion of the satellite while the cross-track resolution defines the ultimate limit of the system.

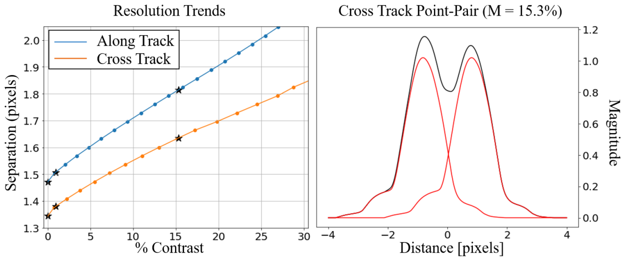

Fig. 4. (Left) Merging two 1D oversampled PRF's and calculating the contrast at each step forms this trend of resolvability. The three stars in each plot mark specific contrast metrics defined as the RRC, GSS and Sparrow Limit. (Right) An instance of resolvability where the black line indicates the addition of the point-pairs.

3.2. Point-Pair Validation Results

Building confidence that the oversampled PRF accurately describes the image performance of a satellite is a critical step in defining the new resolution technique. As mentioned in Sect. 2.2, estimating the center positions of the various satellite point-pairs provides the information needed to simulate them with the oversampled PRF. The collection of center locations displayed in Fig. 5 outlines the sub-pixel locations found in the fitting process described in Sect. 2.2. These locations are used to separate the oversampled PRF's when forming the point-pairs and are unique to each point-pair formed in the comparison.

The validation study illustrates the importance of accurately representing image performance of the satellite. A simulated point-pair created with the observed oversampled PRF, can be seen in Fig. 6. The simulated point-pair was estimated almost perfectly with the expectation of noise. This highlights the main objective of this paper which is to simulate point-pairs with the observed oversampled PRF for defining spatial resolution.

Authorized licensed use limited to: Rochester Institute of Technology. Downloaded on January 26,2023 at 18:16:09 UTC from IEEE Xplore. Restrictions apply.

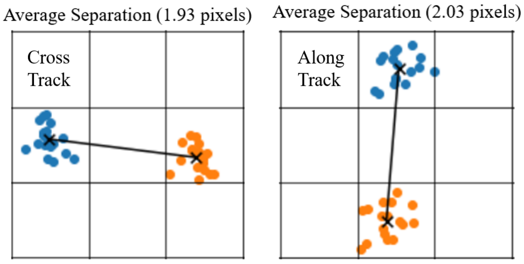

Fig. 5. Point-pair centers from satellite imagery. The average center location for each point-pair is indicated by the x-mark.

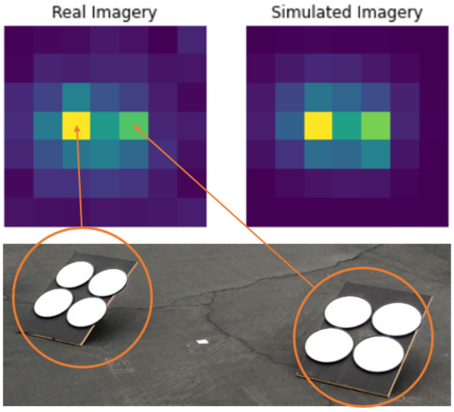

Fig. 6. Comparison of simulated to real image point-pairs from satellite imagery.

Both the cross- and along-track point-pair contrast metrics were analyzed with the statistical inference described in Sect. 2.2 to determine the significance of similarity. This result can seen in Fig. 7. The average difference is very close to zero with a slight positive bias meaning that the simulated point-pairs slightly under estimate contrast. As reported, this bias is small and may be an acceptable trade-off especially when considering this new technique is easier to execute, omni-directional, and based more closely on imager first-principle performance as compared to evaluation using real point pairs or traditional techniques. Lastly, this bias can be attributed to various aspects in the validation study including the estimate of the peak separation, the implemented interpolation, or the simplified assumption of the imaging chain (*i.e.,* the process in simulating the point-pairs).

The statistical inference results for the validation related to the cross- and along-track is highlighted in Table 1. The mean and standard errors (SE) of both the simulated and real point-pairs were used in the analysis of the t-test with both passing the test based on the t-value being smaller than the t-statistic. Although both passed the t-test, there seems to be more ambiguity in the along-track contrast validation as can be seen in Fig. 7.

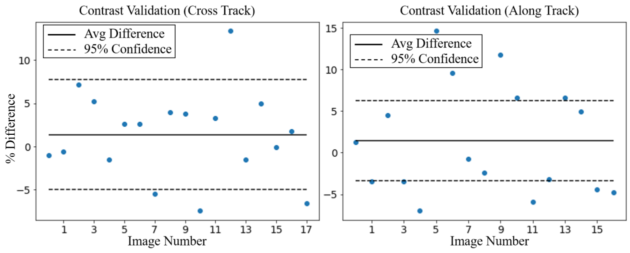

Fig. 7. The mathematical difference between simulated and real point-pair contrast metrics highlights the ability for the oversampled PRF to accurately predict contrast in real imagery.

Table 1. Statistical results for contrast metric differences.

	Cross-Track	Along-Track
Mean Image Contrast	30.6%	19.4%
Mean Simulated Contrast	29.2%	18.0%
Image Contrast SE	2.3%	1.5%
Simulated Contrast SE	2.1%	1.8%
Combined Contrast SE	3.1%	2.3%
t-value	0.4379	0.6122
t-statistic (95%)	2.0322	2.0369

4. CONCLUSIONS AND FUTURE WORK

A new technique for estimating satellite resolution, called the Point-Pair Resolution Technique (PPRT), was developed on ideas related to the RRC. Resolution trends were assessed based on point-pair separation and contrast. Statistical analysis demonstrated that the use of the oversampled PRF in a point-pair simulation can accurately predict the contrast in real imagery. More importantly, point-pair simulations are easier to generate and more powerful due to their inherent omni-directionality and ease of practical implementation. Future campaigns will be conducted to further evaluate this resolution technique based on a variety of imagers found in the remote sensing community (*e.g.,* satellite, airborne, drones, in-lab measurements, etc.).

5. REFERENCES

[1] A. Q. Valenzuela and J. C. G. Reyes, "Basic spatial resolution metrics for satellite imagers," *IEEE Sensors Journal*, vol. 19, no. 13, 2019.

[2] S. J. Schiller, "Specular array for radiometric calibration and method, patent no. US 8158929 B2," 2012.

[3] J. F. Silney and S. J. Schiller, "Method and system for vicarious spatial characterization of a remote image sensor, patent no. WO 2013/019180 AL," 2013.

Authorized licensed use limited to: Rochester Institute of Technology. Downloaded on January 26,2023 at 18:16:09 UTC from IEEE Xplore. Restrictions apply.

Bibliography

Smith, Geoffrey M. and Edward J. Milton (1999). “The use of the empirical line method to calibrate remotely sensed data to reflectance”. In: *International Journal of Remote Sensing* 20.13, pp. 2653–2662. DOI: 10.1080/014311699211994.

Baugh, W. and David Groeneveld (Feb. 2008). “Empirical proof of the empirical line”. In: *International Journal of Remote Sensing* 29, pp. 665–672. DOI: 10.1080/01431160701352162.

Schiller, Stephen and John Silny (2016). “Using Vicarious Calibration to Evaluate Small Target Radiometry”. In: *CALCON*.

Eismann, M.T. (2012). *Hyperspectral Remote Sensing*. Press Monographs. Society of Photo Optical. ISBN: 9780819487872. URL: https://books.google.com/books?id=yW2TtgAACAAJ.

Schiller, S. J. (2012). *SPECULAR ARRAY FOR RADIOMETRIC CALIBRATION AND METHOD, Patent no. US 8158929 B2*.

Gilchrist, John, Torbjorn Skauli, and Christopher Durell (2018). *Standard for Characterization and Calibration of Ultraviolet through Shortwave Infrared (250 nm to 2500 nm) Hyperspectral Imaging Devices*. URL: https://standards.ieee.org/ieee/4001/7314/.

Ientilucci, Emmett J., David N. Conran, et al. (2022). “Development of test methods for hyperspectral cameras characterization in the P4001 standards development”. In: *Algorithms, Technologies, and Applications for Multispectral and Hyperspectral Imaging XXVIII*. Vol. PC12094. SPIE, PC1209402. DOI: 10.1117/12.2623490.

Trim, Simon A., Kimberley Mason, and Andreas Hueni (2021). “Spectroradiometer spectral calibration, ISRF shapes, and related uncertainties”. In: *Appl. Opt.* 60.18, pp. 5405–5417. DOI: 10.1364/AO.425676.

Teillet, P.M., K. Staenz, and D.J. William (1997). “Effects of spectral, spatial, and radiometric characteristics on remote sensing vegetation indices of forested regions”. In: *Remote Sensing of Environment* 61.1, pp. 139–149. ISSN: 0034-4257. DOI: `10.1016/S0034-4257(96)00248-9`.

Bachmann, Charles M. et al. (2012). “A dual-spectrometer approach to reflectance measurements under sub-optimal sky conditions”. In: *Opt. Express* 20.8, pp. 8959–8973. DOI: `10.1364/OE.20.008959`.

Kramida, Alexander (2009). *Handbook of Basic Atomic Spectroscopic Data*. URL: `https://www.nist.gov/pml/handbook-basic-atomic-spectroscopic-data`.

Jablonski, Joseph et al. (2016). “Best practices in passive remote sensing VNIR hyperspectral system hardware calibrations”. In: *Hyperspectral Imaging Sensors: Innovative Applications and Sensor Standards 2016*. Vol. 9860. SPIE, p. 986004. DOI: `10.1117/12.2224022`.

Janesick, James R (2007). “Photon transfer”. In: SPIE. DOI: `10.1117/3.725073`.

Ewald, F. et al. (2016). “Design and characterization of specMACS, a multipurpose hyperspectral cloud and sky imager”. In: *Atmospheric Measurement Techniques* 9.5, pp. 2015–2042. DOI: `10.5194/amt-9-2015-2016`.

Bohndiek, Sarah E. et al. (2008). “Comparison of Methods for Estimating the Conversion Gain of CMOS Active Pixel Sensors”. In: *IEEE Sensors Journal* 8.10, pp. 1734–1744. DOI: `10.1109/JSEN.2008.2004296`.

Fiete, R.D. (Jan. 2010). *Modeling the Imaging Chain of Digital Cameras*, pp. 1–208. DOI: `10.1117/3.868276`.

Mouroulis, Pantazis et al. (1998). *Trade Studies in Multi/hyperspectral Imaging Systems Final Report*. Tech. rep. Jet Propulsion Laboratory.

Schiller, Stephen J. and Jeffery J. Puschell (2017). *Vicarious calibration of moderate resolution sensors using the specular array radiometric calibration (SPARC) method*. CEOS WGCV IVOS workshops and meetings. College of Optical Sciences, University of Arizona: Raytheon Space and Airborne Systems.

Torkildsen, Hans Erling and Torbjørn Skauli (2018). “Full characterization of spatial coregistration errors and spatial resolution in spectral imagers”. In: *Opt. Lett.* 43.16, pp. 3814–3817. DOI: `10.1364/OL.43.003814`.

Bentley, J.L. and C. Olson (2012). *Field Guide to Lens Design*. Field Guides. SPIE. ISBN: 9780819491640. URL: `https://books.google.com/books?id=sd7wMwEACAAJ`.

Conran, David, Emmett J. Ientilucci, et al. (2021). “A New Technique to Define the Spatial Resolution of Imaging Sensors”. In: *2021 IEEE International Geoscience and Remote Sensing Symposium IGARSS*, pp. 8158–8161. DOI: `10.1109/IGARSS47720.2021.9554436`.

Holt, J. and D. Conran (2022). *Systems and Methods for Determining a Minimum Resolvable Distance of an Imaging System, Patent no. US 11228699*.

Valenzuela, Álvaro Q. and Juan Carlos G. Reyes (2019). “Basic Spatial Resolution Metrics for Satellite Imagers”. In: *IEEE Sensors Journal* 19.13, pp. 4914–4922. DOI: `10.1109/JSEN.2019.2902512`.

Storm, Shannon L. (1998). *Absolute Specular Reflectance Measurements at Fixed Angles*. Tech. rep. Labsphere, Inc.

Schaepman-Strub, G. et al. (2006). “Reflectance quantities in optical remote sensing—definitions and case studies”. In: *Remote Sensing of Environment* 103.1, pp. 27–42. ISSN: 0034-4257. DOI: `10.1016/j.rse.2006.03.002`.

Harms, Justin (2016). “The Design and Implementation of GRIT-T: RIT’s Next generation Field-Portable Goniometer System”. PhD thesis. Rochester Institute of Technology, Rochester, NY.

Schiller, Stephen J. (2019). *Application of A Mirror-Based Empirical Line Method for the Surface Reflectance Calibration of Earth Remote Sensing Image Data*. Tech. rep. Raytheon Space and Airborne Systems.

Ruddick, Kevin G. et al. (2019). “A Review of Protocols for Fiducial Reference Measurements of Downwelling Irradiance for the Validation of Satellite Remote Sensing Data over Water”. In: *Remote Sensing* 11.15. ISSN: 2072-4292. DOI: `10.3390/rs11151742`.

Mamaghani, Baabak G. et al. (2018). “An initial exploration of vicarious and in scene calibration techniques for small unmanned aircraft systems”. In: *Autonomous Air and Ground Sensing Systems for Agricultural Optimization and Phenotyping III*. Ed. by J. Alex Thomasson, Mac McKee, and Robert J. Moorhead. Vol. 10664. International Society for Optics and Photonics. SPIE. DOI: `10.1117/12.2302744`.

Ientilucci, Emmett J. and Steven Adler-Golden (2019). “Atmospheric Compensation of Hyperspectral Data: An Overview and Review of In-Scene and Physics-Based Approaches”. In: *IEEE Geoscience and Remote Sensing Magazine* 7.2, pp. 31–50. DOI: `10.1109/MGRS.2019.2904706`.

Yeom, Jong-Min et al. (2017). “Initial Radiometric Characteristics of KOMPSAT 3A Multispectral Imagery Using the 6S Radiative Transfer Model, Well-Known Radiometric Tarps, and MFRSR Measurements”. In: *Remote Sensing* 9.2. ISSN: 2072-4292. DOI: `10.3390/rs9020130`.

Easton Jr, Roger L (2010). *Fourier Methods in Imaging*. The Wiley-IS&T Series in Imaging Science and Technology. Hoboken, NJ: Wiley.

Viallefont-Robinet, Françoise et al. (2018). “Comparison of MTF measurements using edge method: towards reference data set”. In: *Opt. Express* 26.26, pp. 33625–33648. DOI: `10.1364/OE.26.033625`.

Burns, Peter D. (2000). “Slanted-Edge MTF for Digital Camera and Scanner Analysis”. In: *PICS 2000: Image Processing, Image Quality, Image Capture, Systems Conference, Portland, OR, USA, March 2000*. IS&T - The Society for Imaging Science and Technology, pp. 135–138. URL: `http://www.imaging.org/IST/store/epub.cfm?abstrid=1621`.

Kabir, Sakib, Larry Leigh, and Dennis Helder (2020). “Vicarious Methodologies to Assess and Improve the Quality of the Optical Remote Sensing Images: A Critical Review”. In: *Remote Sensing* 12.24. ISSN: 2072-4292. DOI: `10.3390/rs12244029`.

Kohm, Kevin (2004). “Modulation transfer function measurement method and results for the Orbview-3 high resolution imaging satellite”. In: *Proceedings of ISPRS*. Vol. 35, pp. 12–23. URL: `https://www.isprs.org/proceedings/xxxv/congress/comm1/comm1.aspx`.

Tabatabai, Ali J. and O. Robert Mitchell (1984). “Edge Location to Subpixel Values in Digital Imagery”. In: *IEEE Transactions on Pattern Analysis and Machine Intelligence* PAMI-6.2, pp. 188–201. DOI: `10.1109/TPAMI.1984.4767502`.

Schiller, Stephen J. and John Silny (2010). “The Specular Array Radiometric Calibration (SPARC) method: a new approach for absolute vicarious calibration in the solar reflective spectrum”. In: *Remote Sensing System Engineering III*. Ed. by Philip E. Ardanuy and Jeffery J. Puschell.

Vol. 7813. International Society for Optics and Photonics. SPIE, 78130E. DOI: 10.1117/12.864071.

Silney, J. F. and S. J. Schiller (2013). *METHOD AND SYSTEM FOR VICARIOUS SPATIAL CHARACTERIZATION OF A REMOTE IMAGE SENSOR, Patent no. WO 2013/019180 AL*.

SSI and AFRL (2016). *MODerate resolution atmospheric TRANsmission computer code*. URL: http://modtran.spectral.com/.

Holt, Jeff et al. (2021). "FLARE network performance: automated on-demand calibration for space, airborne and UAV assets". In: *Autonomous Systems: Sensors, Processing, and Security for Vehicles and Infrastructure 2021*. Vol. 11748. SPIE, 117480K. DOI: 10.1117/12.2587963.

Conran, David and Emmett J. Ientilucci (2022). "Interrogating UAV Image and Data Quality Using Convex Mirrors". In: *2022 IEEE International Geoscience and Remote Sensing Symposium IGARSS*, pp. 4525–4528. DOI: 10.1109/IGARSS46834.2022.9883984.

Stetson, Peter B. (1987). "DAOPHOT: A Computer Program for Crowded Field Stellar Photometry". In: *Publications of the Astronomical Society of the Pacific* 99.613, p. 191. DOI: 10.1086/131977.

Anderson, Jay and Ivan R. King (2000). "Toward High-Precision Astrometry with WFPC2. I. Deriving an Accurate Point-Spread Function". In: *Publications of the Astronomical Society of the Pacific* 112.776, pp. 1360–1382. DOI: 10.1086/316632.

Lauer, Tod R. (1999). "The Photometry of Undersampled Point-Spread Functions". In: *Publications of the Astronomical Society of the Pacific* 111.765, pp. 1434–1443. ISSN: 1538-3873. DOI: 10.1086/316460.

Faran, Sagi et al. (2009). "Estimation of the MTF of a satellite imaging-system from celestial scenes". In: *2009 IEEE International Geoscience and Remote Sensing Symposium*. Vol. 2, pp. II-452-II–455. DOI: 10.1109/IGARSS.2009.5418114.

Russell, Brandon J. et al. (2023). "The Ground to Space CALibration Experiment (G-SCALE): Simultaneous Validation of UAV, Airborne, and Satellite Imagers for Earth Observation Using Specular Targets". In: *Remote Sensing* 15.2. ISSN: 2072-4292. DOI: 10.3390/rs15020294.

Conran, David N. and Emmett J. Ientilucci (2023). “A Vicarious Technique for Understanding and Diagnosing Hyperspectral Spatial Misregistration”. In: *Sensors* 23.9. ISSN: 1424-8220. DOI: `10.3390/s23094333`.

Hedler, D. et al. (2023). “Landsat Surface Product Validation Instrumentation: The BigMAC Exercise”. In: *In Review*.